Doctoral Dissertation
Doctoral Program in Civil and Environmental Engineering (37th Cycle)

Experimental investigation on the effects of CO_2 and acid exposure on the hydro-mechanical behavior of a clayey caprock

Hidayat Ullah

* * * * * *

Supervisors
Prof. Guido Musso
Prof. Renato Maria Cosentini

Doctoral Examination Committee:
Prof. Alessio Ferrari, Universita degli Studi di Palermo (Italy)
Prof. Jubert Pineda, University of Newcastle (Australia)
Prof. Marta Castelli, Politecnico di Torino (Italy)
Dr. Osvaldo Bottiglieri, Politecnico di Bari (Italy)
Prof. Gabriele Della Vecchia, Politecnico di Milano (Italy)

Politecnico di Torino
2025

I hereby declare that the contents and organisation of this dissertation constitute my own original work and does not compromise in any way the rights of third parties, including those relating to the security of personal data.

.....

Hidayat Ullah

Turin, 2025

Abstract

This dissertation deals with the effect of CO_2 and acid exposure on the hydro-mechanical behavior of Italian carbonatic clayey caprocks. The sealing capacity and integrity of the caprock can be affected by the geo-chemo-mechanical processes involved in CO_2 storage. The injected CO_2 might react with the caprock altering its mineralogical composition and ultimately affecting its mechanical properties.

In this context, the effects of CO_2 and acid exposure on the hydro-mechanical behavior of caprocks were investigated in laboratory experiments. The caprocks studied in this study are structured, carbonatic Italian clays from different formations and depths. The exposure to CO_2 and acid was carried out through two different types of tests. In the first type of tests, samples were first exposed to different forms of CO_2, namely dry $scCO_2$, wet $scCO_2$ and CO_2-saturated brine. Mechanical, microstructural, and mineralogical tests were conducted on exposed samples and on twin non-exposed samples. The results were compared to outline the possible effects of CO_2 exposure. The mechanical tests included consolidated undrained triaxial and oedometer tests. The triaxial tests were conducted in high and medium pressure triaxial cells whereas oedometer tests were conducted up to a vertical stress of 25 MPa. The microstructural and mineralogical study involved the determination of equivalent calcite content, mineralogy, pore size distribution and fabric structure. In the second type of tests aimed at studying the short-term effects of CO_2 injection, reconstituted and intact samples were exposed to low pH water solution by diffusion and advection under oedometer conditions, while monitoring induced displacements and determining the induced changes in equivalent carbonate content.

Exposure to dry $scCO_2$ was found to induce specimen drying. The combined effects of geochemical reactions from CO_2 and water evaporation increased the carbonate content. Changes in mineralogical composition were coupled with fabric effects observed through pore size distribution, as a decrease was noted in the frequency of large pore sizes. Mechanically a slight increase in the strength of specimen exposed to dry $scCO_2$ was observed. Some intact samples exposed to wet $scCO_2$ for 30 days showed a reduced peak strength compared to non-exposed samples. This might be due to microfractures detected through post-exposure CT scans. The exposed specimen that did not have microfractures showed a peak strength similar to that of the non-exposed specimen although the failure was not

that brittle. It also showed higher residual strength compared to non-exposed specimen.

Acid exposure of reconstituted and intact samples was carried out in oedometer cells to investigate the short-term effects of CO_2 injection. The response of specimens after exposure, either induced by diffusion or by flowthrough, was compared to that of control specimens, where only mechanical load histories, with some creep stage, were imposed. The acid-exposed reconstituted specimens showed an increase in compressibility attributed to the dissolution of carbonates. Vertical strains due to the chemical reaction were about 0.58% and 0.48% in the advection and diffusion tests respectively, after around one month of acid exposure. In case of acid-exposed intact samples, a rather insignificant reduction in the void ratio was observed during the acid exposure, both in the case of diffusion and advection tests. The dissolution of carbonates was rather modest compared to one of the reconstituted specimens tested in similar conditions. This can be attributed to the structured and tight fabric of the intact specimens which retards transport of dissolved species. The structured fabric not only ensured stiffer behavior but might also affect the effective diffusivity of the sample.

The flowthrough experiments were carried out in an advanced oedometer developed for this study. It can be engaged for electrical resistivity tomography and ultrasonic wave measurements. Initially, the setup and calibration of the advanced oedometer was carried out. A protocol optimizing the sequence of measurements for significant electrical resistivity reconstructions was defined on the basis of lab and numerical measurements. For reconstruction of electrical conductivity maps, ResIPy, an open-source code was used. Overall, the advanced oedometer was effective in monitoring changes in pore fluid using electrical resistivity tomography and ultrasonic wave velocity during flowthrough experiments.

Table of contents

List of Figures

List of Tables

Nomenclature

A	cross sectional area of the sample
B	skempton's pore water pressure parameter
c′	effective cohesion
CIT	Complex Impedance Tomography
CO_2	Carbon dioxide
c	concentration of the species
C_c	compression Index
C_r	recompression index
C_s	swelling index
C_V	coefficient of consolidation
C_α	secondary compression index
CK_0U	consolidated undrained triaxial test
D	diffusion coefficient of the species
De	Effective diffusion coefficient
e	void ratio
e_0	initial void ratio
E_{oed}	oedometer modulus
ECC	Equivalent Calcite Content
ERT	Electrical Resistivity Tomography
FE	Finite Element
GSD	Grain Size Distribution
Gs	Specific Gravity
HCl	Hydrochloric acid
HPTA	High Pressure Triaxial Apparatus
I	Electric current
K	Hydraulic conductivity

K_0	In-situ stress ratio
K_f	Effective bulk modulus
K_g	Stiffness of gas
K_W	Stiffness of water
LL	Liquid Limit
LVDT	Linear Variable Differential Transformer
M	molecular mass
MIP	Mercury intrusion Porosimetry
MPTA	Medium Pressure Triaxial Apparatus
NC	Normally Consolidated
OCR	Over Consolidation Ratio
pH	hydrogen potential
p′	Mean effective stress
pCO_2	Pressure of carbon dioxide
PI	Plasticity Index
PL	Plastic Limit
PSD	Pore Size Density
q	Deviatoric stress
q/p′	Obliquity
R	Electrical resistance
$scCO_2$	supercritical carbon dioxide
SEM	Scanning Electron Microscopy
S_g	degree of saturation of gas
S_r	degree of saturation
T	temperature
t'	creep time
p_{CO2}	carbon dioxide pressure
u	fluid pressure
$\boldsymbol{u}$	seepage velocity
V_P	compression wave velocity
V_S	shear wave velocity

VNM	Vermeer and Neher Model
w	water content
WRC	Water Retention Curve
XRD	X-ray Diffraction
α	smoothing parameter
ΔV	electric potential drop
ϵ_c	total strain
ϵ_c^e	elastic strain
ϵ_c^c	plastic strain
$\dot{\epsilon}$	strain rate
$\dot{\epsilon^e}$	elastic strain rate
$\dot{\epsilon^c}$	plastic strain rate
κ	geometrical factor
ρ	electrical resistivity
ρ_s	soil mass density
ρ_w	water mass density
σ	electrical conductivity
σ_S	electrical conductivity of the sample
σ_L	electrical conductivity of water/liquid
σ_V	vertical stress
σ_V'	effective vertical stress
σ_0'	initial effective pressure
σ'	final effective pressure
σ_{p0}	preconsolidation pressure corresponding to before loading
σ_{pc}	preconsolidation pressure corresponding to end of consolidation state
τ	Tortuosity
τ_c	time to the end of primary consolidation
ϕ	porosity
ϕ'	friction angle

Ψ_d	data misfit
Ψ_m	modal misfit

Chapter 1 Introduction

1.1 Motivation

Global emissions of greenhouse gases have steadily risen since the start of the industrial revolution, nearly doubling since 1970. Among these gases, carbon dioxide (CO_2) is a dominant gas, predominantly produced by human activities such as fossil fuel combustion, deforestation, and various industrial processes. This increase contributes to a range of detrimental effects on our planet, including rising global temperatures, melting glaciers, declining polar ice sheets, and increasing sea levels. Various strategies have been proposed and employed to reduce CO_2 emissions. These include enhancing energy efficiency, increasing renewable energy production, and preservation of existing forests (IPCC 2005).

Another proposed option to mitigate the climate change effects is Carbon dioxide Capture and Storage (CCS). CCS involves the capturing of CO_2 from large point sources, transporting it to a suitable site of storage and injecting it underground so that it will not be released into the atmosphere for at least tens of thousands of years (IPCC 2005). The geological storage of CO_2 includes the injection of CO_2 in depleted oil and gas reservoirs or deep saline aquifers. The depleted reservoirs although are safer but with limited capacity whereas deep saline aquifers are ubiquitous with a capacity of up to 1000-10^4 $GtCO_2$ (IPCC 2005, Dooley et al., 2006).

The captured CO_2 is injected through wells into geological formations at depths typically greater than 800 meters. The host rock must exhibit sufficient injectivity and storage capacity. Another prerequisite is the presence of extensive confining units, such as shale, salt, or anhydrite beds, to prevent the migration of CO_2 to the surface. For successful storage of CO_2 in these formations, the integrity of caprock material is of paramount importance. The CO_2 in its supercritical form has lower density than formation fluid. This difference in densities forces the CO_2 to move upward until it is halted by caprock. Caprock provides stratigraphic containment to the CO_2 in the early stages of storage.

Several hydrological phenomena occur which govern the primary transport mechanism of CO_2 (Niemi et al., 2017). The injected CO_2 might dissolve in the formation fluid which will move it by advection due to pressure gradients created by CO_2 injection or due to its natural hydraulic gradients. The diffusion of CO_2 into caprock and host rock might also occur.

CO2 injections might increase the pore fluid pressure in the reservoir and at the bottom of the caprock. The increased pressure will cause local changes in the effective stress field, which as a result, will induce mechanical deformations, possibly increasing the porosity and permeability. The increased pressure might also affect the mechanical strength of caprock.

Chemically, the CO_2 might react with the host rock, pore fluid, and also the overlying caprock. The extent of such reactions is dependent upon factors such as the composition of the pore fluid and rocks, as well as the in-situ pressure and temperature (Benson & Cole, 2008). The formation fluid acidifies after dissolution of CO_2 and the geochemical reactions with the acidic environment compromise the sealing capacity and integrity of caprock. It might alter the mineralogy and structure of the rock and affect its hydro-mechanical behavior.

1.2 Research objectives

The interaction of caprock and CO_2 is due to the upward movement of the injected CO_2 due to its lower density as compared to the formation fluid. The injection of CO_2 is usually followed by a pressure increase which might affect the caprock's effective stress. Chemical interactions between the injected CO_2 and the caprock occur near the reservoir-caprock interface. The injected CO2 might exist in different forms including dry $scCO_2$, wet $scCO_2$ or CO_2-saturated brine (Vafaie et al., 2023). The CO_2-induced chemical reactions may alter the microstructure and mineral composition of caprock. Chemical interactions can also cause changes in the mechanical properties of rocks, in terms of their strength, stiffness, and fracture thresholds, which can increase the risk of CO_2 leaking from the reservoir.

These effects have been experimentally investigated on various shale formations in batch reaction tests under different exposure conditions. Since the geochemical reactions of minerals with acidic water have slow kinetics, the time scale required for such projects typically spans hundreds to thousands of years (Benson & Cole, 2008). However, the duration of laboratory testing is significantly shorter. To accelerate the process of CO_2 reaction with rock minerals, flowthrough experiments are carried out (Rohmer et al.,

2016). The flowthrough experiments are also effective in studying the short-term effects of CO_2.

The objective of the study was to study the effect of CO_2 and low pH water solutions on the hydro-mechanical behavior of three Italian caprocks (Clay A, Clay B and Clay C) both in intact and reconstituted states. The materials under consideration are structured, carbonatic Italian clays cored from different depths. They all belong to the caprocks of existing gas fields originally exploited for hydrocarbon production.

Caprock samples were preliminarily exposed to different forms of CO_2 in batch reactions and to acid in flowthrough experiments. The batch reactions were carried out in autoclaves to allow for CO_2 related reactions to take place before testing them mechanically. Effects of CO_2 exposure on the microstructure and the mineralogy of caprocks were also studied. The acid exposure of caprock material was carried out in oedometer cells including flowthrough experiment in an advanced oedometer.

In the first sets of experiments two Italian carbonatic clays (Clay A and Clay B), similar in their mineralogical composition, were exposed to CO_2 in batch reactor. The reconstituted and intact samples were exposed to dry $scCO_2$, wet CO_2 and CO_2-saturated brine. The temperature and pressure conditions were 60 °C and 15 MPa. The exposure time of the samples was 14 (Clay-A) and 30 days (Clay-B). Another exposure state where slurry of Clay B was exposed to wet $scCO_2$ for 14 and 30 days was also carried out. The exposed slurry was later used for reconstitution of samples. After exposure to CO_2 the samples were tested mechanically in high pressure and medium pressure triaxial cells. The results of exposed samples were compared to the mechanical tests carried out on non-exposed samples. The main objective of the research was to study the changes in mechanical properties of the material due to CO_2 exposure. Also, the microstructure and mineralogy of the exposed and non-exposed samples were investigated with Scanning Electron Microscopy (SEM), Mercury Intrusion Porosimetry (MIP), X-ray Diffraction (XRD) and Equivalent Calcite Content (ECC) analyses.

In the second set of experiments samples were exposed to low pH Hydrochloric acid (HCl) solutions under sustained loadings for a period of 30-42 days. Reconstituted samples of Clay B and intact samples of Clay C were utilized in these experiments. The samples were exposed in diffusion and advection conditions (flowthrough experiment). Flowthrough experiments were carried out in advanced oedometer. During the flowthrough experiments the electrical resistivity tomography and ultrasonic wave velocities were also monitored.

The advanced oedometer was designed and developed for this study. Initially, the advanced oedometer was set up and calibrated for its different components, i.e.,

electrical resistivity and ultrasonic waves. A protocol of measurement for electrical resistivity recording was determined based on experimental and numerical geometrical factors. For the inversion and reconstruction of electrical conductivity maps ResIPy was used. The potentialities of this code were initially investigated with data obtained from synthetic flushing test simulated in COMSOL.

1.3 Dissertation outline

The dissertation, in Chapter 2 opens with an introduction to the increase in CO_2 emissions into the atmosphere and its adverse effects on climate. The adverse effects of climate change and options to tackle these effects are subsequently discussed. Carbon dioxide Capture and Storage is introduced as a viable option to mitigate climate change impacts. The geo-chemo-mechanical processes and trapping mechanisms involved in CCS are also reviewed.

Chapter 3 presents literature review of the laboratory experiments carried out on reservoir rocks and caprocks in the context of CO_2 storage. The effects of different exposure aspects including temperature, pressure, and exposure period are reviewed. The types of exposure tests, including batch reaction and flowthrough experiments, are reviewed with more focus on caprocks.

Subsequently, Chapter 4 is devoted to the different techniques and equipment utilized in this experimental study. It outlines the equipment used for batch reaction, reconstitution of samples, mechanical testing, microstructure analyses, mineralogical analyses, flowthrough experiments and electrical conductivity measurements.

Chapter 5 summarizes the physical and mineralogical characterization of the materials used in the study.

Chapter 6 examines the effects of CO_2 exposure on the microstructure and mineralogy of the caprock material. Chapter 7 contains the results and comparison of different mechanical tests carried out on the CO_2-exposed and non-exposed samples.

Chapter 8 presents the design and set up of an advanced oedometer used for flowthrough experiments. The calibration process of its different components is outlined in detail. Chapter 9 deals with the results of effects of low pH water solutions on hydro-mechanical behavior of caprock material including flowthrough experiments.

Finally, Chapter 10 presents the principal findings of the research and offers suggestions for future studies.

Chapter 2 An introduction to CO_2 capture and storage

Global emissions of greenhouse gases (GHGs) have steadily risen since the start of the industrial revolution, nearly doubling since 1970. Among these GHGs, carbon dioxide (CO_2) is a dominant gas, predominantly originating from anthropogenic activities such as fossil fuel combustion, deforestation, and various industrial processes. Since the industrial revolution, atmospheric CO_2 levels have experienced a surge, rising from about 280 ppm in the 18th century to over 420 ppm as recorded in 2023 at the Mauna Loa atmospheric observatory (NOAA, 2023). This alarming increase contributes to a range of detrimental effects on our planet, including rising global temperatures, melting glaciers, retreating polar ice sheets, and escalating sea levels.

In this chapter, the consequences of enhanced greenhouse gas concentrations will be examined, along with various strategies to mitigate these impacts. A focal point of the discussion will be Carbon dioxide Capture and Storage (CCS), including an introduction to the relevant hydro-chemo-mechanical processes involved. At the end of the chapter different trapping mechanisms are discussed which are involved in successful storage of CO_2. Through this exploration, the critical role of CCS in the broader context of climate change mitigation and sustainability will be illustrated.

2.1 Effects of greenhouse gases

Climate change represents a critical global challenge, primarily driven by the growing concentrations of greenhouse gases (GHGs) in the atmosphere. According to the International Energy Agency (IEA), this increase is attributed primarily to fossil fuel combustion, which accounted for about 37.2 gigatonnes of CO_2 emissions globally in 2023 as shown in Figure 2.1(IEA, 2024). The resulting increase in global temperatures due to elevated CO_2 levels has led to far-reaching consequences, including intensified weather events, rising sea levels, biodiversity loss, and significant threats to human health and socioeconomic systems. This escalation underscores the critical need for mitigation strategies to reduce GHGs concentrations and combat climate change.

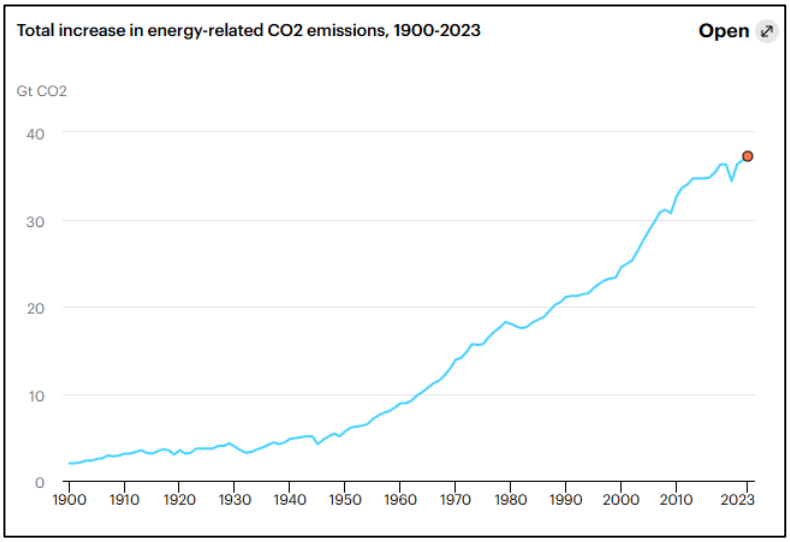

Figure 2.1 Total increase in energy related CO_2 emissions from 1900 to 2023 (IEA, 2024).

Intergovernmental Panel on Climate Change (IPCC) was established by the United Nations Environment Program (UNEP) and the World Meteorological Organization (WMO) in 1988 to provide the world with a clear scientific view on the current state of knowledge in climate change and its potential environmental and socio-economic impacts. In its 2015 Assessment Report (AR5), the Intergovernmental Panel on Climate Change (IPCC) emphasized the catastrophic effects of rising greenhouse gas concentrations (Edenhofer et al., 2015). The report confirmed unequivocal warming of the climate system, with each decade since 1850 being successively warmer than the previous one. Over the last two decades, significant changes have been observed, including mass loss from the Greenland and Antarctic ice sheets and continued worldwide glacier shrinkage. Furthermore, the rate of sea level rise since the mid-19th century has been higher than the mean rate over the preceding two millennia. Another alarming effect is ocean acidification, as seawater absorbs nearly 25% of the CO_2 released annually, altering its chemistry and posing a severe threat to marine life.

2.2 Mitigating climate change impacts

A broad range of strategies has been proposed to mitigate the effects of climate change. Addressing the effects of climate change requires a comprehensive, multi-faceted approach.

One of the first and at hand options is adaptability to the changes occurring due to climate change. The adaptation measures include large-scale infrastructure changes like building a defense to protect against sea level rise or improving the quality of road

surface to withstand the hotter temperatures. This might also include the change in the behavior of individuals. Adaptation aims at reducing the risk of climate change.

There are several technological strategies available for reducing anthropogenic CO_2 emissions (Edenhofer et al., 2015). First, one of the most effective approaches is to reduce the reliance on fossil fuels, which are a primary source of carbon emissions. This can be achieved by substituting less carbon-intensive fossil fuels for more carbon-heavy options; for example, transitioning from coal-based power generation to natural gas, which emits less CO_2. Additionally, a significant shift towards near-zero-carbon alternatives is essential, such as generating power through renewable energy sources like wind, solar, geothermal, and hydro or tidal energy. The adoption of electric-powered vehicles also plays a crucial role in this transition, as they offer a cleaner alternative to traditional fossil fuel-powered cars. Finally, enhancing the capacity of natural systems to absorb atmospheric CO_2 is vital. Forests and soils store CO_2 biologically, helping to mitigate climate change. However, this natural storage may be limited by the already high levels of CO_2 present in the atmosphere, highlighting the need for both technological innovation and sustainable practices.

It is well established that the main mitigation task is to control the emission of greenhouse gases. It includes the adoption of green energy sources, but the current infrastructure and economy are based on fossil fuel consumption. We do not have the ability to change to green energy options at once. Also, the green energy options, for example, solar energy, wind energy and hydropower plants are not enough to support the current energy needs therefore fossil fuels will be used for the next few decades. The continued need for fossil fuels across the world and the relatively slow pace of renewable energy development suggests that the amount of undesired GHGs being emitted into the atmosphere will remain on the rise. In such circumstances, Carbon dioxide Capture and Storage (CCS) is a promising process to decarbonize the industrial sectors (such as iron, steel, cement manufacturing, oil refining, ammonia production, electricity generation plants and hydrocarbon production plants) without significant modification and extra investment in the current infrastructure. In the following sections the concept, relevant processes and trapping mechanisms involved in CCS are presented.

2.3 Introduction to Carbon dioxide Capture and Storage

As the urgent need to combat climate change intensifies, various strategies for storing carbon dioxide (CO_2) have emerged as potential solutions. These methods aim to reduce atmospheric CO_2 emissions and there have been many options for the storage of CO_2. One such strategy is mineral carbonation which is the reaction of CO_2 with calcium or

magnesium hydroxides to form carbonate materials. This is an expensive and slower process of CO_2 sequestration (IPCC 2005).

Another option for the eradication of CO_2 is the oceanic storage of CO_2. It involves the injection of CO_2 into the ocean and the injected CO_2 would be carried by deep water. Ocean sequestration qualifies as the largest possible sink for carbon dioxide storage with an estimated potential storage of 40,000 Gt CO_2 (Leung et al., 2014) and the possibility of storing over 90% of current CO_2 emissions. While this method is relatively easy and economically viable, it poses risks to marine life by potentially acidifying the water (Auerbach et al., 1997). Another downside of this method is that a large fraction of the injected CO_2 will be released into the atmosphere after a few hundred years because of ocean currents and local supersaturation (Jain & Cao, 2005).

Another viable option is geological storage of CO_2. This includes the injection of CO_2 in depleted oil and gas reservoirs, deep saline aquifers, and deep coal seams. These options are illustrated in Figure 2.2.

For hydrocarbon reservoirs, depleted reservoirs can be repurposed for CO_2 storage, whereas in active reservoirs the CO_2 can be used for Enhanced Oil Recovery (EOR). EOR technology has been successfully used in the petroleum industry since the 1970s although the amount of injected CO_2 is less as compared to the emissions (Bachu et al., 2004). Storing CO_2 in depleted hydrocarbon reservoirs is considered safer because of the extensive data available regarding their status and behavior. However, many abandoned wells in mature fields were sealed decades ago using mud-laden fluids and cement plugs, without consideration that they might one day need to contain reactive and buoyant fluids like CO_2. This limits the capacity and safety of the depleted reservoirs. The capacity of depleted reservoirs is around 675-900 $GtCO_2$ (IPCC (2005), Dooley et al., (2006))

The geological storage in deep saline aquifers is another viable option for CO_2 eradication. Saline formations are deep sedimentary rocks saturated with formation water or brine containing high concentrations of dissolved salts. These formations are widespread and contain enormous quantities of water. However, the water in these formations is not suitable for agriculture or human consumption. The deep saline aquifers are ubiquitous and have higher storage capacity (around 1000-10^4 $GtCO_2$) as compared to depleted reservoirs (IPCC 2005). The broader range in storage capacity for deep saline aquifers is due to uncertainties in the estimation process and their relatively unexplored nature compared to oil and gas reservoirs.

The potential for geological storage in coal seams has recently been explored. Storage in coal seams involves replacing methane trapped in the coal structure with CO_2.

This causes methane to be released, which is called CO_2 enhanced coal bed methane recovery (CO_2-ECBM).

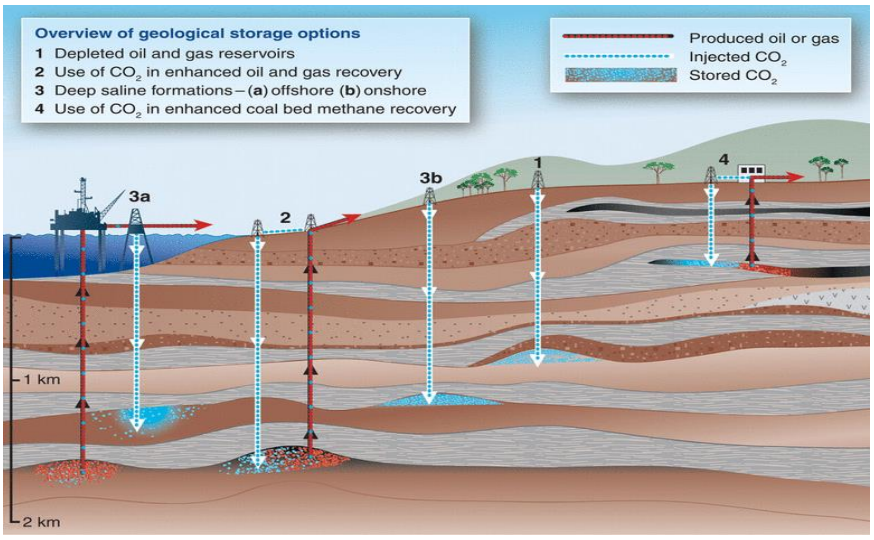

Figure 2.2 Options for storing CO_2 in deep underground geological formations (originally from Cook, 1999)

CCS process involves the capturing of CO_2 from large point sources, transporting it to a suitable site of storage and injecting it underground so that it will not be released again into the atmosphere for at least tens of thousands of years IPCC (2005).

The capturing phase involves separating CO_2 from some of the other gases which are produced as a result of fossil fuel combustion at point sources such as steel, cement, hydrocarbon production plants and others. Capturing CO_2 from other sources such as vehicles, residential and commercial buildings is difficult and expensive therefore, more attention is paid to the large point sources. For mobile sources and buildings, it is prudent to use other green energy options. The capturing of CO_2 can be done with different techniques/systems including post-combustion capturing, oxy-fuel combustion capturing and pre-combustion capture system (IPCC 2005).

The transportation phase is required in cases where the storage site is not the same capture point. The transportation is done in tanks, ships or through pipelines. Finally, the CO_2 is injected unground through wells and is conducted at specific depths within geological formations. To ensure safe and effective injection, monitoring systems are often established to track the pressure, temperature, and seismic activity in the vicinity of the injection site (Mortezaei et al., 2021). Monitoring helps prevent any potential leakage and ensures the long-term integrity of the storage site.

2.4 Projects of geological storage of CO_2

Sleipner in North Sea is the world's first commercial-scale CO_2 storage facility. It began operation in 1996, making use of a deep saline formation under the North Sea (Baklid et al., 1996). Before this, the engineered injection of CO_2 into subsurface was carried out in early 1970s in Texas, USA for EOR projects. By late 90s a number of pilot projects were underway in US, Canada, Japan, Europe, and Australia. Early such projects include Natuna in Indonesia, In-Salah in Algeria and Gorgon in Australia.

Global CCS Institute published a report on the status of CCS facilities in 2024. According to this report in 2024, there were 628 commercial facilities out of which 50 are operational and 44 facilities are under construction. In the pipeline, there are 287 facilities in early development state and 247 facilities in advanced development stage (Global CCS Institute, 2024). These facilities have a storage capacity of around 416 $MtCO_2$ per annum. Figure 2.3 shows the development and CO_2 capture capacity of CCS facilities over the years.

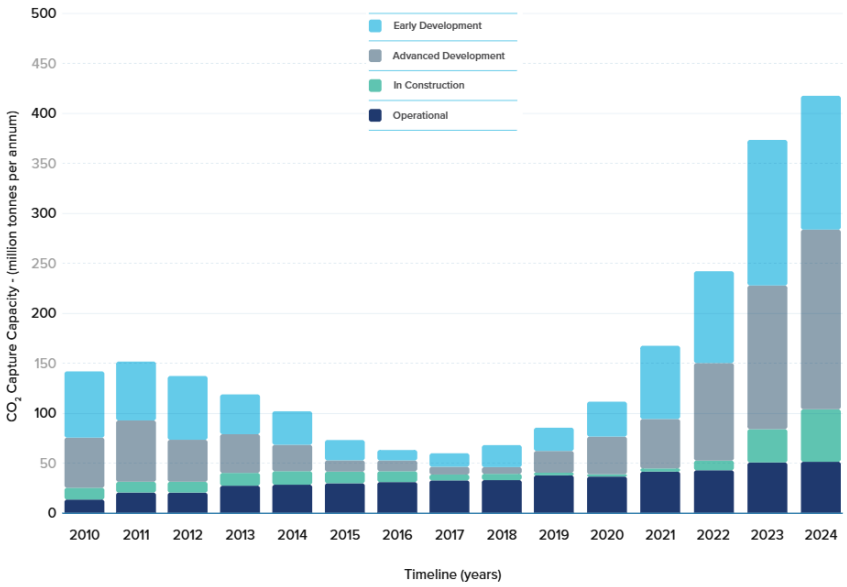

Figure 2.3 CO_2 capture capacity of different types of projects over the years (Global CCS Institute, 2024).

The world map in Figure 2.4 shows the location of all completed and early-stage projects as of 2020. This figure also includes the commercial and pilot projects. With the increase in confidence and availability of technology, the CCS projects have increased manyfold since the first commercial project in 1996.

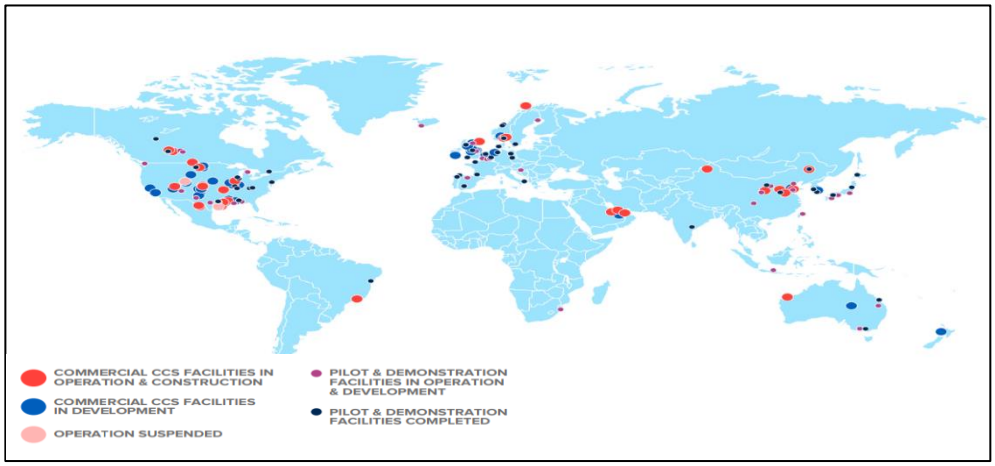

Figure 2.4 World map of CCS facilities at various stages of development as of 2020 (Global CCS Institute, 2020).

2.5 Processes involved in CO_2 geological storage

This section provides an overview of the hydro-chemo-mechanical processes involved in the geological storage of CO_2 in saline formations. In the case of geological storage, CO_2 is injected through wells into geological formations at depths typically greater than 800 meters where the rock exhibits sufficient injectivity and storage capacity. Over these formations, extensive confining units, such as shale, salt, or anhydrite beds, are present acting as sealing to prevent the migration of CO_2 into overlying shallower rock strata and ultimately to the surface. At these substantial depths, CO_2 exists in a supercritical state (T > 32 C and p > 7.2 MPa). In its supercritical form, CO_2 possesses properties between liquid and gas states.

Several physico-hydro-chemo-mechanical processes occur once CO_2 is injected. Firstly, due to low density of CO_2 at reservoir depth (600-750 kg/m^3 at a depth of 1 km) as compared to the formation fluid (1200 kg/m^3) the injected CO_2 moves upward due to the effect of buoyancy forming a plume as shown in red color in Figure 2.5. Additionally, the lower viscosity of CO_2 ($\mu_{CO2} = 0.1$ mPa·s) compared to the formation fluid (μ_{brine} =1.1 mPa·s) leads to a hydrological phenomenon known as viscous fingering (Green & Ennis-King, 2009). In this case, instead of the CO_2 front advancing uniformly like a piston into the injection formation, certain sections of the front move significantly faster, resulting in finger-like projections. Furthermore, the heterogeneity of the injection formation gives rise to the channeling effect in which the injected CO_2 will be channelized to follow the most permeable paths because of the spatial variation of permeability. This means that the CO_2 will preferentially flow through the most permeable zones, further complicating predictions about its behavior within the reservoir. The following are some

of the primary transport mechanisms that govern the flow of CO_2 into the geological formation (Niemi et al., 2017).

- fluid flow as a result of pressure gradients created due to CO_2 injection;
- fluid flow due to natural hydraulic gradients;
- buoyancy of CO_2 due to density difference between CO_2 and formation fluid;
- diffusion of CO_2 in native formation fluid;
- dissolution of CO_2 in the formation fluid;
- dispersion and fingering caused by difference in viscosity between CO_2 and formation fluid;
- pore space trapping of CO_2;
- adsorption of CO_2 onto organic material.

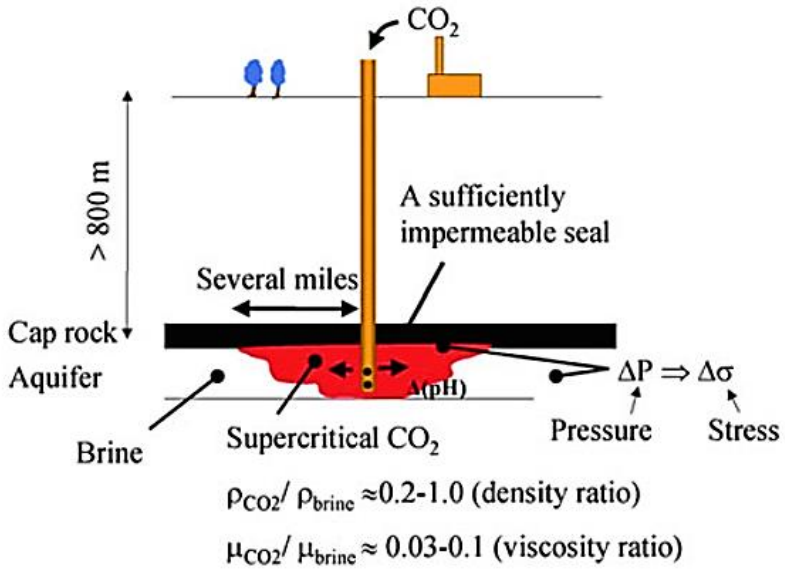

Figure 2.5 Schematic diagram of CO2 geosequestration in saline formation (Niemi et al., 2017)

The CO_2 plume generated by the density differences between CO_2 and brine is effectively contained by the caprock material, which exerts a counteracting pressure. For safe and efficient operation of the storage system, it is crucial that the buoyancy pressure remains significantly lower than the gas entry pressure into the caprock pores. The dynamics of the CO_2 plume i.e., its size and spatial distribution, are influenced by several factors, including the rate of injection, the permeability of the geological formation, and its overall capacity to store CO_2. Once the CO_2 reaches the uppermost layer of the formation, its vertical ascent is effectively halted, while lateral movement may continue. This horizontal migration persists until the plume encounters a sealing fault or the boundaries of the geological formation.

CO_2 injection will increase the pore fluid pressure in the reservoirs and at the bottom of the caprock. Under high pressures, CO_2 displaces the in-situ formation fluids

generating higher stresses near the injection well. This will possibly lead to changes in effective stresses locally, affecting the porosity, permeability and eventually reducing the pressure and increasing the injectivity of the CO_2. At the same time, this might also induce some irreversible changes, giving rise to fracturing in the reservoir rock. In the case of caprock, the increased pressures might compromise its integrity.

The injection of CO_2 into a sedimentary formation will give rise to stress increases not only near the injection zone but far beyond. Some of the geomechanical responses to the CO_2 injection might be ground surface uplift or heave, microseismical events, faults reactivation, and fracturing of caprock (Rutqvist, 2012). These geomechanical processes of CO_2 injection are illustrated in Figure 2.6.

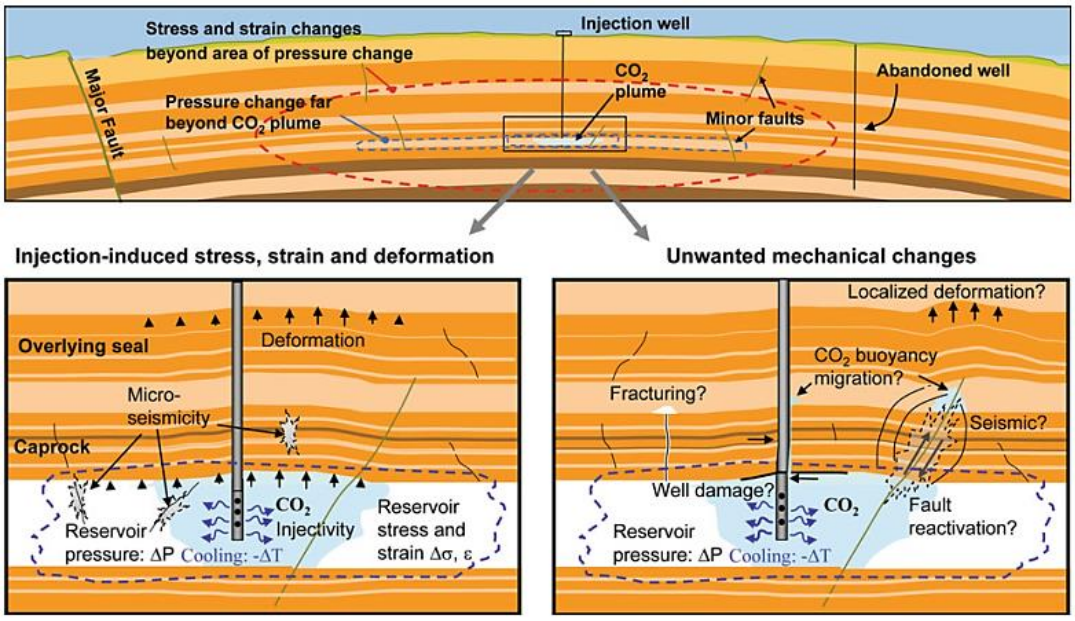

Figure 2.6 Geomechanical processes and key technical issues associated with CCS in deep sedimentary formations (Rutqvist, 2012).

In addition to these mechanical processes, replacing the host formation fluid with CO_2 may cause changes in the rock's mechanical properties through chemical-mechanical interactions between the CO_2 and the host rock, or through desiccation of fractures.

Chemically, at the CO_2 front where CO_2 is dissolved in water, the acidity of the groundwater is increased and many minerals comprising the host rock matrix minerals such as calcite, may dissolve readily, leading to an increase in permeability and porosity along the flow channel. These chemical changes might impact porosity and ultimately the strength of the reservoir rock (Rimmelé et al., 2010). In some cases, carbonate precipitation might occur, especially near the injection well reducing the injectivity of the CO_2 and affecting its mechanical properties. Moreover, the injected CO_2, due to its

buoyancy interacts with caprock and might induce additional chemical reactions that alter the mechanical properties of the caprock. A detailed review of hydro-chemo-mechanical processes and changes in reservoir and caprock, due to different forms of CO_2 (dry, wet and CO_2-saturated brine) is presented in Chapter 3.

2.6 CO_2 trapping mechanisms in geological formations

Once injected into the storage formation, the fraction of CO_2 retained in the geological formations depends on a combination of physical and geochemical trapping mechanisms. In saline formations, the injected CO_2 is sequestrated mainly through four different trapping mechanisms. These mechanisms are structural/stratigraphic trapping, hydrodynamic/residual trapping, solubility trapping, and mineralization/ chemical trapping. In the following sections, these mechanisms are discussed.

2.6.1 Structural/stratigraphic trapping

Structural trapping refers to the physical containment of CO_2 within the pore spaces of geological formations, a process critical to the effectiveness of geological carbon storage at early stages. This mechanism depends on the presence of impermeable caprocks, such as shale or anhydrite, which serve as a barrier to upward migration, effectively sealing the CO_2 within the storage site. The integrity of the caprock is paramount; even minor fractures or faults could jeopardize containment by providing pathways for CO_2 escape. Studies have shown that suitable caprocks possess permeability values as low as 10^{-18} m^2, ensuring robust sealing properties (IPCC 2005).

Faults and folds within the geological formation can significantly impact stratigraphic containment. Faults, depending on their permeability and orientation, may act as either conduits for CO_2 leakage or barriers that enhance containment. For example, sealed faults with low permeability can trap CO_2 effectively, while faults with high permeability could compromise the storage site's integrity (Benson & Cole, 2008). Similarly, folds in the rock layers can create structural traps that provide additional containment for the injected CO_2. Anticlines are particularly favorable for CO_2 storage as they create natural reservoirs where gas can accumulate beneath impermeable layers. However, proper assessment of these features is required otherwise it may lead to leakage risks.

2.6.2 Hydrodynamic/residual trapping

Residual trapping, also known as hydrodynamic trapping, is a critical mechanism in CO_2 storage, involving the immobilization of CO_2 within the pore spaces of the host rock through capillary forces. This is due to phase interference between immiscible CO_2 and

brine. When CO_2 is injected into a formation it displaces the formation fluid (drainage of the formation rock). Since the density of CO_2 is smaller than the one of the formation water, the injected CO_2 will migrate upward (imbibition of the formation rock). Due to hysteresis effect, the saturation of the nonwetting phase for a given capillary pressure is small during drainage, but large during imbibition. For very low capillary pressure, this might also lead to a significant residual CO_2 saturation.

The effectiveness of residual trapping is influenced by several factors, including the porosity and permeability of the reservoir rock, which dictate the capacity and ease of CO_2 movement, and the wettability of the rock, which affects how CO_2 interacts with formation water (Kumar et al., 2005).

2.6.3 Solubility trapping

Solubility trapping occurs when CO_2 dissolves into the formation water. This process significantly enhances the security of CO_2 storage by transforming the gas into an aqueous phase, thereby reducing its buoyancy and mobility. The dissolution process depends on several factors, including pressure, temperature, and salinity of the reservoir. The CO_2 solubility in formation water decreases as temperature and salinity increase (Bachu & Adams (2003), Green & Ennis-King, (2009)).

2.6.4 Mineral trapping

Mineral trapping occurs when CO_2 reacts with rock minerals to form carbonates and bicarbonates. Dissolved CO_2 in water produces a weak acid, which reacts with the minerals in reservoir rock to form bicarbonate ions by chemical reactions (Rochelle et al., 1999). The residual and dissolved CO_2 may undergo secondary reactions with surrounding rocks and formation water, contributing to mineralization and trapping the CO_2 permanently (Gunter et al., 2004). Once dissolved, the injected CO_2 will not be available for leakage in gas phase and will become immobile. Figure 2.7 illustrates the different types of trapping mechanisms.

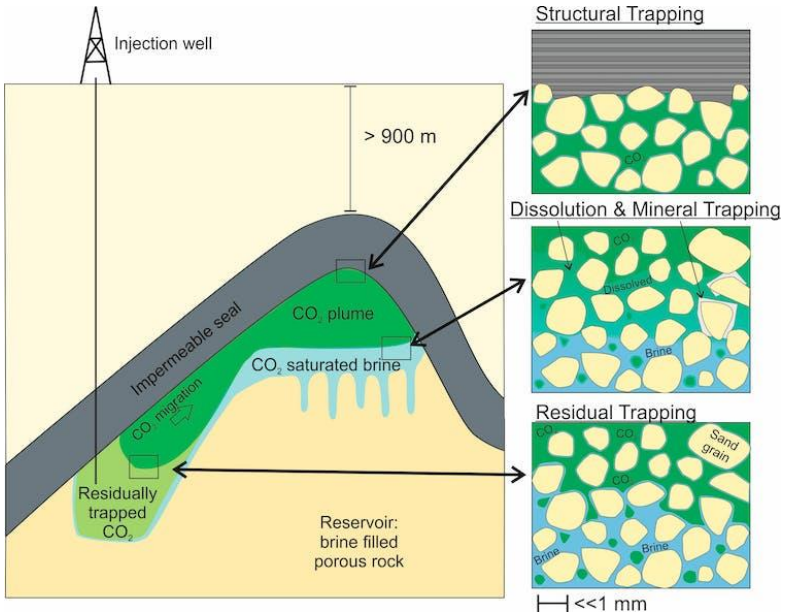

Figure 2.7 Different types of trapping mechanisms of injected CO_2 (Flude & Alcade, 2020)

Among these four trapping mechanisms, structural/stratigraphic trapping is important for the early stages of the storage. The storage site therefore is selected carefully. A storage site in general should have enough capacity, adequate injectivity and a satisfactory sealing caprock at the top which will hold the injected CO_2 and sustain the stresses generated due to CO_2 injection. It should not be close to any faults. Faults may offset stratigraphic layers, bringing permeable formations above the caprock and the storage formation closer together. They may also be either hydraulically conductive, providing a migration path, or sealed, providing a barrier. Thus, they play a significant role in potential migration, or conversely, in flow compartmentalization and storage capacity.

The effectiveness of geological storage depends on a combination of the trapping mechanisms. The most effective storage sites are those where CO_2 is immobile because it is trapped permanently under a thick, low-permeability seal or is converted to solid minerals through a combination of physical and chemical trapping mechanisms. For a storage site at the initial stages, structural trapping is of more importance contributing around 80% of CO_2 trapping. Over time the contribution from residual trapping and solubility trapping increases as shown in Figure 2.8. According to the IPCC special report on CCS (2005), the contribution of mineral trapping is evident around 100 years after the end of injection.

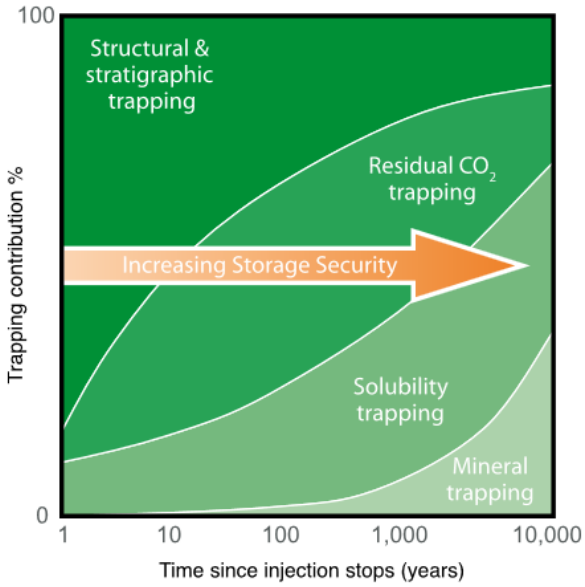

Figure 2.8 Increase in storage security over time. With time the contribution of residual CO_2 trapping, solubility trapping and mineral trapping increase (IPCC 2005).

Chapter 3 Geochemical and chemo-mechanical processes involved in CO_2-water-solid interactions

3.1 General introduction

As discussed in Chapter 2, geological storage of CO_2 is one the most viable options in terms of capacity of storage among the Carbon dioxide Capture and Storage (CCS) options. Geological storage sites include depleted hydrocarbon reservoirs and deep saline aquifers which are not useful for any human use (Bernstein et al, 2008). The depleted hydrocarbon reservoirs have an important advantage. They have been adequately characterized previously during the production period. Additionally, the safe and secure nature of these formations which have been able to store oil and gas over a long period makes them premier candidates but with limited capacity. The capacity of depleted oil and gas reservoirs is indicated between 675 and 900 billion tonnes of carbon (GtC). On the other hand, saline aquifers sequestration capacity spans between 1000 and 10,000 GtC (Bernstein et al, 2008). Unfortunately, despite there has been some progress in defining standard methodologies for capacity estimation and improving regional estimates over the last few years, predictions of sequestration capability for saline aquifers are indeed very questionable (Bachu, 2008).

For storage, a suitable geological site must meet at least three main conditions: large capacity, high injectivity, and strong containment (Bachu 2008, Ajayi et al., 2019). The requirement of the capacity for a site ensures that the selected site possesses adequate pore volumes to store large amount of CO_2. Injectivity of CO_2 is assured if the selected site permeability is high enough so that the desired injection rate of CO_2 is maintained. The candidate site must also contain a sealing top named "caprock". Caprock is an integral part of a geosequestration project. It should be at a desired depth to keep the CO_2 in supercritical state and at the same time it should be away from any major penetrations like faults or wells to avoid leakage (Shukla et al., 2010). The caprock should be dense and intact and should possess low permeability so as to keep the injected CO_2

from seeping through it over a long period. Also, the caprock must have high strength under compression and, to a certain extent, also along tensile paths so to be able to sustain the change in stress field during and after injection. A sealing fault (if any) should not have large opening and ensure that no CO_2 escapes to the surface or groundwater above. Some researchers (e.g., Hepple and Benson, 2005) suggested that the sealing should be effective enough that leakage does not exceed 1% of the stored amount of CO_2 in 1000 years.

When CO_2 is injected into saline aquifers several physico-chemical processes are involved (Niemi et al., 2017) detailed in Chapter 2. First, due to the density difference between CO_2 and brine, buoyancy of CO_2 occurs and moves upwards towards the caprock. Other hydrological factors also come into play, for example, an increase in permeability due to the dissolution of reservoir rock. In chemical processes, injected CO_2 will generally react with reservoir rock. This could result in an increase in porosity in case of dissolution of formation minerals and a decrease in porosity when precipitation occurs. These reactions forming new minerals can be the inception of mineral trapping (Bernstein et al, 2008).

Both the injection and buoyancy provide an increase in formation fluid pressure, which cause local changes in the effective stress field, and then mechanical deformations. Through geochemical reactions, porosity and permeability changes are anticipated as well. As the injection pressure is increased, the hydraulic load on the caprock increases as well, which can result in mechanical failure or overcoming the so-called threshold capillary pressure of the caprock, with leakage of CO_2.

In this Chapter, the geomechanical processes involved in CCS are discussed. In the first section, a general overview of geomechanical and geochemical processes is provided. Consistently with the aims of the Thesis, the following sections narrow the review of the existing literature regarding experimental studies on geochemo-mechanical interactions between CO_2- water (or brine) – rock. Studies on reservoir rocks are reviewed first. Studies on caprock materials are then introduced, with more emphasis on the different forms of CO_2 used in the experiments.

3.2 General overview of geomechanical processes associated with CO_2 sequestration

Geomechanical processes associated with CCS received initial attention in the late 1990s. Some initial modeling studies and discussions indicated that geomechanics plays a central role in CCS was to be expanded to a commercial scale (Rutqvist and Tsang 2002). Both large scale (reservoir or basin) or more local (wellbore) processes might take place.

A significant large-scale concern regarding commercial projects for CCS is their potential to induce micro and macro seismic events and how such events could impact the long-term integrity of a CO_2 repository (Rutqvist, 2012). Consequently, it is crucial to approach large-scale commercial CCS projects with great caution. Geomechanics plays an essential role in conducting site-specific CCS risk analyses to ensure safe operations. The site scale processes also include the subsidence or heaving of caprock due to vertical pressurization of reservoir. These changes might lead to changes in stress and strains due to changes in pressure and temperature, in reservoir and caprock, near and far from injection well. Micro and macro seismicity can also arise from the CO_2 injection near fault zones.

Local processes involve hydro-mechanical alterations including changes in porosity and permeability due to changes in pressures. Chemical reactions can also take place with carbonate minerals in reservoir matrix and caprocks. The scope of this document is limited to local processes, which can also be recreated at the laboratory scale. The literature review is then restricted to geochemically triggered effects on the mechanical behavior of rocks as observed in laboratory tests.

3.3 General Overview of Geochemical Processes

In this section, a brief overview of geochemical reactions in reservoir rocks and caprocks is discussed. Compared to other engineered geological storage facilities (e.g., natural gas, liquid waste, or nuclear solid wastes), one major difference is that the injected CO_2 is prone to dissolve within the resident reservoir pore fluid. CO_2 molecules can adsorb from the supercritical or water phase onto mineral surfaces. CO_2 adsorption is thought to have little effect on mineral structure, except for swelling clays e.g., montmorillonite (Akono et al., 2019). Although pure dry CO_2 has low reactivity, once it encounters brine, it forms carbonic acid (H_2CO_3). It is a weak acid that will almost immediately dissociate as shown in Equation 3.1.

$$CO_2 + H_2O \leftrightarrow H_2CO_3 \leftrightarrow H^+ + CO_3^- \quad 3.1$$

The release of H^+ ions will cause an imminent drop in pH of the brine, reducing the pH of the formation from almost neutral values to acid pH. The actual pH value depends on the amount of CO_2 dissolved, which in turn is related to CO_2 pressure through Henry's law. However, in reservoir conditions, it is accepted that the pH might range around a value of about 3 (e.g. Liu et al., 2022).

The drop in pH will eventually cause acidic reactions with the minerals of the different rock materials involved. Among the different common rock-forming minerals, calcite

($CaCO_3$) is expected to be the most reactive, because of both high solubility and fast kinetics rates. The dissolution of minerals can result in changes to the pore space and pore space network which might change the transport flow paths. This might also eventually affect the mechanical properties (Rohmer et al., 2016).

The rate of dissolution or precipitation is different for different minerals. It depends not only on the type of mineral and its reactive surface area but also on the transport properties of rock, and properties of formation fluid (Akono et al., 2019). The weak carbonic acid can also react with other cations such as Ca^{2+}, Na^{+}, Mg^{2+} etc. Such cations are found in the formation brine and the reaction with carbonic acid results in insoluble ionic species, as those highlighted in Equations 3.2-3.4 (Ajayi et al., 2019).

$$Ca(OH)_2(aq) + CO_2(g) \leftrightarrow CaCO_3(s) + H_2O(l) \quad 3.2$$

$$Na^+ + CO_{2(aq)} + H_2O \leftrightarrow H^+ + NaHCO_{3(aq)} \quad 3.3$$

$$Mg^{2+} + 2CO_{2(aq)} + 2H_2O \leftrightarrow 2H^+ + Mg(HCO_3)_{2(aq)} \quad 3.4$$

The dissolution rates of calcite, dolomite, and magnesite in CO_2-saturated aqueous solutions at partial CO_2 pressure up to 5.5 MPa (pH between 3 and 6) have been well described by Pokrovsky et al. (2005) and Pokrovsky et al. (2009). Among carbonates, calcite has the highest dissolution rate followed by dolomite, siderite and magnesite respectively (Pokrovsky et al., 2009).

Dissolution of minerals like calcite, siderite, feldspars, and chlorite releases Si, Al, K, Fe, and Ca which can form new compounds. The dissolution of K-feldspar results in the formation of kaolinite (Rezaee and Tingate, 1997; Morad et al., 2000). During K-feldspar dissolution, kaolinite forms and silica is released according to the following reaction:

$$2KAlSi_3O_8 + 2H^+ + H_2O \rightarrow Al_2Si_2O_5(OH)_4 + 4SiO_{2(aq)} + 2K^+ \quad 3.5$$

Phyllosilicate minerals are also susceptible to carbonic acid attack. They present a wide range of chemical constituents, including smectites, kaolinite, serpentine, talc, mica, illite, and chlorite minerals. The common feature of all phyllosilicates is their layered nature. Due to this sheeted structure, their specific surface area is large, which increases their reactivity (Bhuiyan et al., 2020). In most cases, the dissolution of phyllosilicates is sensitive to pH and increases with a decreasing pH i.e., in an acidic environment (Kaszuba et al., 2013). The dissolution of chlorite and other phyllosilicates is a complex reaction, not only due to its structures but the pathways by which the dissolution may take place. Black & Haese, 2014 presented a generalized reaction for phyllosilicate as follows:

$$(Fe,Mg)_5Al_2Si_3O_{10}(OH)_8 + 8H^+ \rightarrow 3SiO_{2(aq)} + 2.5Fe^{2+} + 2.5Mg^{2+} + 8H_2O + 2AlO_2^- \quad 3.6$$

Chlorite dissolution releases silica, iron, and/or magnesium and aluminate ions into the solution. In contrast with other phyllosilicates, the chlorite dissolution rates were found to be independent of pH, with a pH range between 4.2 and 5.3 (Black & Haese, 2014).

In contrast to carbonates and silicates, the dissolution of quartz is a slow process under CO_2 storage or fracturing conditions. According to Knauss & Wolery (1988), the dissolution rates of quartz are independent of pH for pH values lower than 6. This means that increasing CO_2 pressure and thus decreasing pH will not facilitate quartz dissolution (Kaszuba et al., 2013). Liu et al., (2022) have provided more detailed reactions concerning the dissolution reaction of silicates, carbonates, oxides, sulphides, halite etc. in CO_2-acidified water.

3.4 Experimental studies on CO_2-solid interactions

In this Section, the changes in mechanical, mineralogical and microstructural properties of reservoir and caprock samples, observed in laboratory experiments and primarily due to reaction with CO_2 are discussed. The dissolution of carbonate-rich rocks can change the pore geometry, pore connectivity, porosity, permeability, and flow paths, and eventually might affect the mechanical properties of rock. Overall, modifications in mechanical properties depend on several factors, including the degree of saturation, the chemistry of the pore fluid, and the thermodynamic conditions (Akono et al, 2019). The mechanical properties investigated in the literature are Young's modulus, acoustic wave velocities, Poisson ratio, and strength properties including frictional angle and shear strength.

The large scale involved in the geological storage of CO_2 has limited the experimental chemo-mechanical studies to laboratory scale. A large set of laboratory experiments has been developed to study the effect of CO_2 on different types of geomaterials. These experiments are classified into different categories.

Based on the type of geomaterial used, the experiments can be divided into two categories: experiments on reservoir rocks and experiments on caprocks. Some studies (Bemer and Lombard 2010) have also used the transition zone rock which sits between these two rock types.

Based on the approach used, the experimental studies are divided into batch-reaction and flowthrough experiments (Rohmer et al., 2016). The relevant test procedure adopted in different batch reaction experiments is almost similar to each other. The rock samples, either reservoir or caprock are exposed in a batch reactor to dry CO_2, CO_2–water, or CO_2–brine under a controlled pressure and temperature for a given exposure time.

Batch reactors are pressure and temperature controlled cells. After exposure, the samples are brought back to ambient temperature and pressure conditions before mechanical or microstructural tests. Whereas, in flowthrough experiments, the fluid is injected into rock sample with a total volume of up to several pore volumes in triaxial or oedometric cells. The injection is carried out under pressure which induces pronounced chemical reactions. The injected fluid in most cases is CO_2-saturated water/brine (acidic fluids).

The experimental studies also differ on the type of fluid used i.e., dry supercritical CO_2 ($scCO_2$), $scCO_2$ and brine, water-saturated CO_2, etc. The forms of CO_2 can be related to the location and fluid saturation distribution in the storage reservoir. Vafaie et al. (2023) provided the temporal and spatial distribution of CO_2 in storage in its different forms as shown in Figure 3.1.

Zones A1-A4 are formed in the reservoir rock after CO_2 injection. A1 is the near-wellbore zone which is fully occupied by dry CO_2. The injected CO_2 displaces the formation brine. Zone A3 is a two-phase flow zone where CO_2 and brine co-exist. Zone A3 is surrounded by zones A2 and A4. A2 contains water-bearing CO_2 (wet CO_2) and A4 contains CO_2-rich brine, respectively. A5 is the far-field uninvaded zone. Similarly, the caprock is also divided into 3 zones: C1 is the zone invaded by dry CO_2, C2 is the zone invaded by the wet CO_2 and C3 is the CO_2 saturated brine zone.

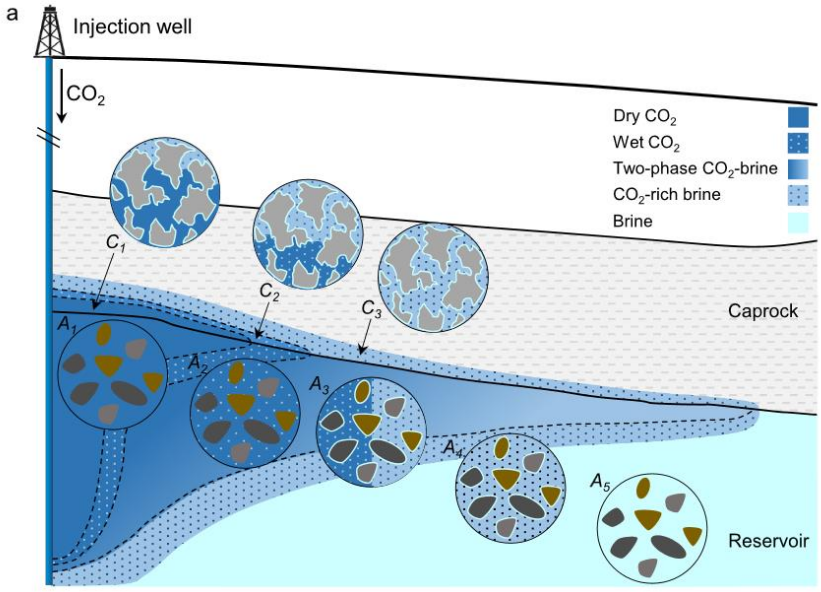

Figure 3.1 Schematic of a geological CO_2 storage site with zones formed around the injection well (Vafaie et al., 2023).

In most of the experiments, the thermodynamic conditions are that of a reservoir at 0.5 km to 5 km depth (e.g., Rimmele et al., 2010, Sterpenich et al., 2009).

The experimental studies also differed on the state of rock samples i.e., in preserved/intact state, fragments, and powder state.

In the following, the main results of these experimental studies are discussed focusing on the type of material i.e., reservoir rock and caprock. First, the studies conducted on reservoir rocks are discussed, followed by those carried out on the caprock.

3.4.1 Effects of CO_2 injection on reservoir rocks

The hosting reservoir rocks are mostly sandstones and carbonates, including chalks (Rohmer et al. 2016). Carbonates are most reactive to CO_2 and dissolve after the formation of weak carbonic acid due to the reaction of injected CO_2 and brine. The dissolution of calcites in reservoir rocks can result in an increase in porosity and eventually a decrease in mechanical properties. The CO_2-enhanced dissolution/ precipitation phenomena mainly occur in the zones A2, A3 and A4 which contain CO_2 in two phases, wet CO_2, and brine-rich CO_2 (Sterpenich et al. 2009). The dissolution patterns might be different based on the injection rates, dissolution kinetics of minerals, and rock heterogeneity. Different studies have investigated the change in mechanical properties like Young's Modulus, compressive strength, and change in ultrasonic wave velocity.

Sterpenich et al. (2009) exposed samples of Lavoux oolitic limestone to CO_2-saturated brine and to dry $scCO_2$ under 80°C and 15 MPa pressure for 7 days. They concluded that massive calcite dissolution did not occur (dissolution of calcite was less than 1% in mass). Furthermore, no significant variation in velocity of ultrasonic waves was observed upon CO_2 exposure. The authors attributed this to the opposing effects of decrease in pH of pore fluid and increased stability of calcites. The increase in CO_2 pressure results in more acidic solution but at the same time the stability of calcite increases due to higher concentration of dissolved carbonates.

Rimmelé et al., (2010) studied two reservoir rocks in batch reactor experiment. They exposed Lavoux limestone and Adamswiller sandstone to wet $scCO_2$ and CO_2-saturated water at 90°C and 28 MPa for one month (thermodynamic conditions corresponding to a depth of approximately 3 km). The authors found no significant change in mechanical properties (Young's modulus, compressive strength, and Poisson's ratio) despite an increase in porosity.

Some authors have followed the protocol of Egermann et al. (2005) of using retarded acid treatment (RAT), which is activated at specific temperature. The samples are saturated with retarded acid at ambient temperature. Once the sample is completely saturated the temperature is increased to 60° C for the retarded acid activation. The sample is then flushed with brine for the next cycle of acid exposure. RAT is used for the

homogeneous alteration of rock samples and to avoid the formation of wormholes (discussed in Section 3.4.2). The formation of wormholes is not desired as it might result in inaccurate measurements of porosity and permeability. Such studies aim at investigating the worst-case impact of acid attack on carbonate samples. Bemer and Lombard (2010) analyzed the alteration of elastic moduli and strength parameters of two host rocks (Comblanchian and Lavoux limestones from Paris basin) and one transition zone rock. The Lavoux limestone (host rock) is almost exclusively made of calcite whereas the transition zone limestone consists of about 5% clay fraction, 90% calcite and 5% pyrite and gypsum.

They found a decrease in porosity of about 1-2.1% without any significant increase in permeability. Both carbonate rocks showed a decrease in elastic moduli. Isotropic loading stress-controlled drained triaxial tests on intact samples before and after chemical alteration showed a decrease in reservoir formation failure strength (Figure 3.2). The transition zone samples (bottom right of Figure 3.2) were apparently not affected by the exposure.

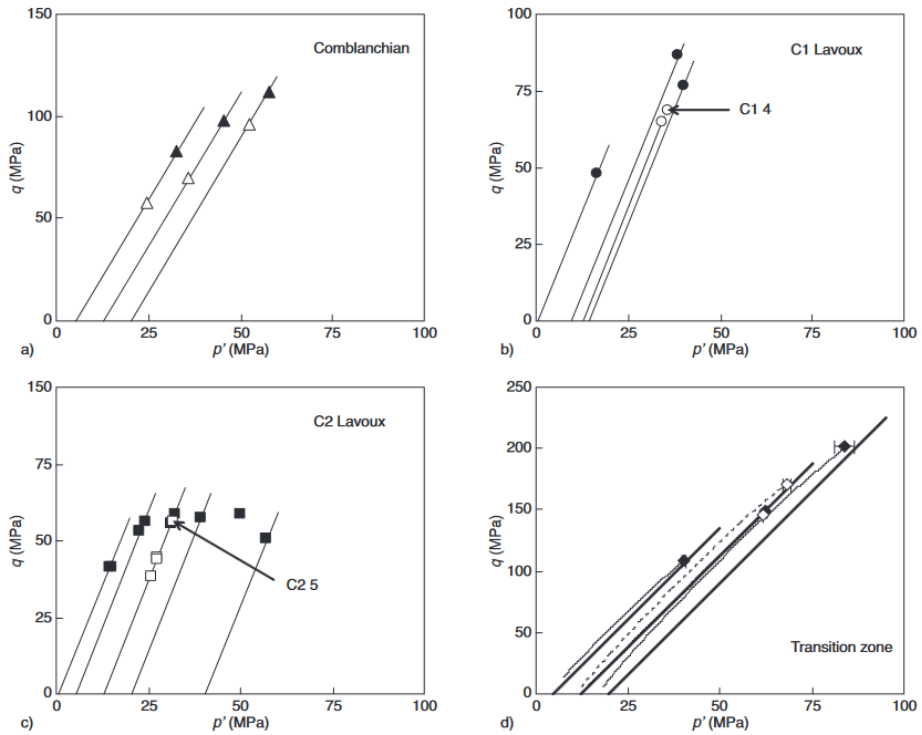

Figure 3.2 Failure points of intact (filled shapes) and altered samples (open shapes) for different formations. (Bemer and Lombard 2010)

The authors correlated the elastic moduli to the change in porosity as shown in Figure 3.3. Comblanchian limestone falls out of the general trend, showing a higher sensitivity of this rock to chemical alterations. The authors concluded therefore that a decrease in

strength and elastic stiffness cannot be explained by just porosity changes.

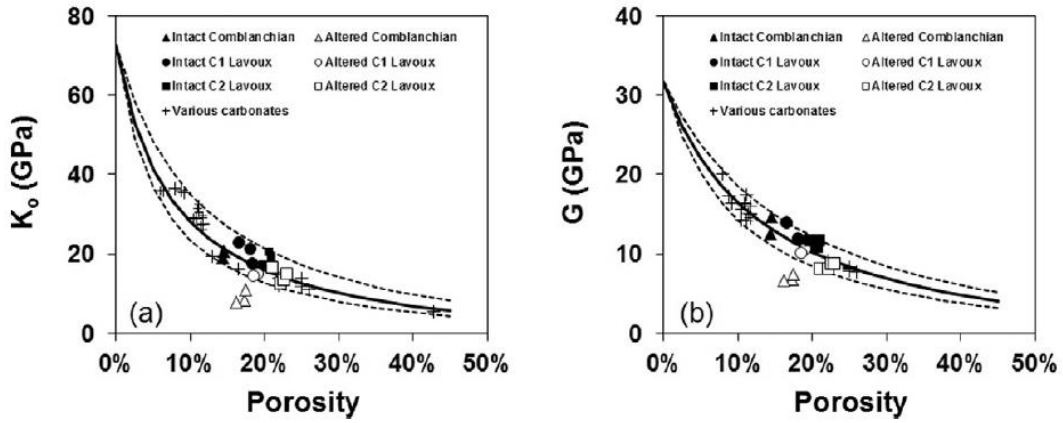

Figure 3.3 Trends of drained elastic moduli as a function of porosity for pristine and CO_2-altered carbonate core samples. (Bemer and Lombard 2010)

Xie et al. (2011) studied the change in porosity of Oolitic limestone which has calcite content of 97%. The samples were saturated for 6 hours and then separated into two groups, i.e., one being tested 'as is' (without exposure to chemicals), the other being immersed in a strong acid (ammonium nitrate solution, 6 mol/l), for one year and then tested (degraded samples). Exposure to acid led to an increase in porosity from 23 to 27%.

Such a porosity increase was mostly related to degradation of the intergranular cementation, combined with the formation of connected wormholes. Results of mechanical tests showed that the elastic properties were significantly altered as the drained bulk modulus decreased from ~5 GPa to ~1 GPa, whereas the plastic volumetric strain threshold (i.e., the volumetric yield stress) was also reduced from ~30 to 20 MPa. This means that the degraded materials become more prone to collapse, as shown in Figure 3.4, where σ_m is the mean stress and σ_{eq} is the deviatoric stress.

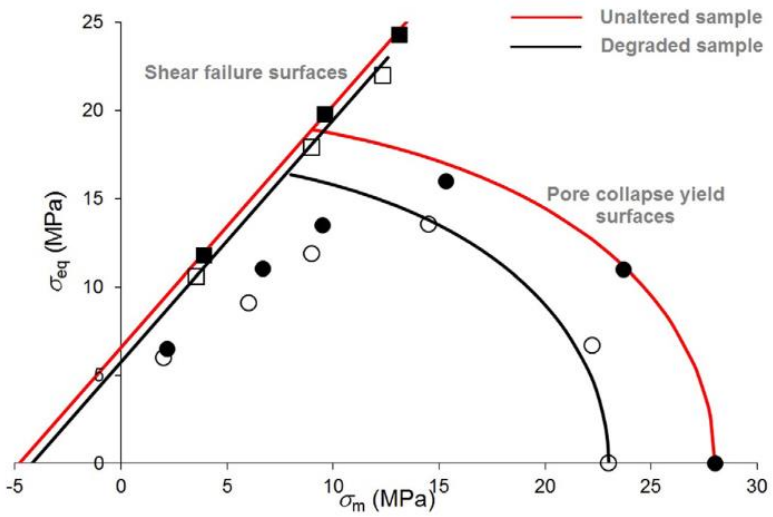

Figure 3.4 Comparisons of pore collapse yield surfaces and shear failure surfaces between unaltered samples (red lines) and degraded samples (black lines). Filled squares and circles respectively correspond to failure stresses and to the initial yield stress of unaltered samples. Open squares and circles respectively correspond to failure stresses and initial yield stress of degraded samples. (Xie et. al., 2011)

3.4.2 Flowthrough experiments on reservoir samples

Flowthrough experiments are conducted to study the enhanced effect of CO_2 injection. In these experiments the sample is maintained under reservoir conditions and CO_2 (either CO_2-saturated brine or brine and $scCO_2$) is injected at different injection rates. The alterations also depend on initial microstructure, leading to heterogenous dissolution process at the core sample scale. The higher injection rate in flowthrough experiments using acidic fluids might result in the development of wormholes in carbonate rocks, an example is shown in Figure 3.5. In the context of CO_2 injection into reservoir rock, a wormhole refers to a network of highly conductive channels that form within the rock matrix due to the dissolution of soluble minerals by the injected fluid. The high injection rate experiments are relevant to reproduce fast processes occurring mainly near the injection well, or the breakthrough of supercritical CO_2 in the caprock.

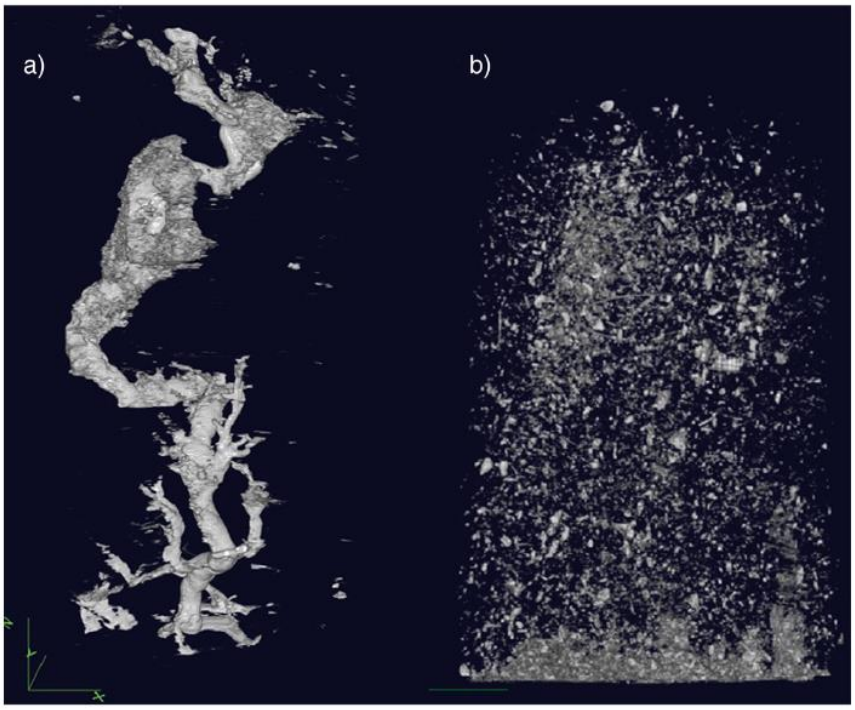

Figure 3.5 Observed void space via X-ray computed micro-tomography analysis after injection of brines equilibrated with pCO_2=3 MPa at T=60° for (a) a heterogeneous limestone and (b) a homogeneous dolostone (from Carroll et al., 2013)

Vialle and Vanorio (2011) investigated different carbonate rocks (white chalky mudstones, brownish calcite limestone, calcite/dolomite limestone) for coupled physical and chemical effects of injecting CO_2-rich water with a pH of about 3.2. The samples, of 1 inch in length and diameter, were held in a vessel under constant confining pressure. The authors monitored the elastic and transport properties of six carbonate rocks along with calcium content and pH at the outlet. The elastic properties of samples, both saturated and dry samples, were measured in terms of P wave and S wave velocity. The authors registered a maximum of 24.7% decrease in P-wave and 21.2% decrease in S-wave velocity in chalk samples. The increase in permeability and porosity in chalk was 495% and 19% respectively. SEM analyses showed that the dissolution was more extensive on the sample side of fluid injection with respect to the other one.

Alam et al. (2014) investigated samples from chalk formations, as they have high porosity-but also high specific surface, which makes them highly vulnerable to chemical changes. Samples from two different formations were studied: a) from Ekofisk Formation (fraction of non-carbonate minerals above 12%), and b) Tor Formation (fraction of non-carbonate minerals below 5%). Dry $scCO_2$ was injected for 8 days in 1.5 inches brine saturated samples. The injection experiments were conducted at 38 MPa pore pressure, 50 MPa hydrostatic confining pressure and a temperature of 115°C. The authors found

that the effect of CO_2 injection on both the petrophysical and mechanical properties of chalk depends on carbonate content. Pure chalk with high carbonate content (Tor Formation) was found to be vulnerable to mechanical weakening due to CO_2 injection, whereas, no significant mechanical effect was observed in the impure chalk of Ekofisk Formation as shown in Figure 3.6.

A 1-2% increase in porosity of Ekofisk formation samples and a 2–3% increase in Tor formation sample were observed. A minor decrease in specific surface and a small increase in permeability for most cases was also reported.

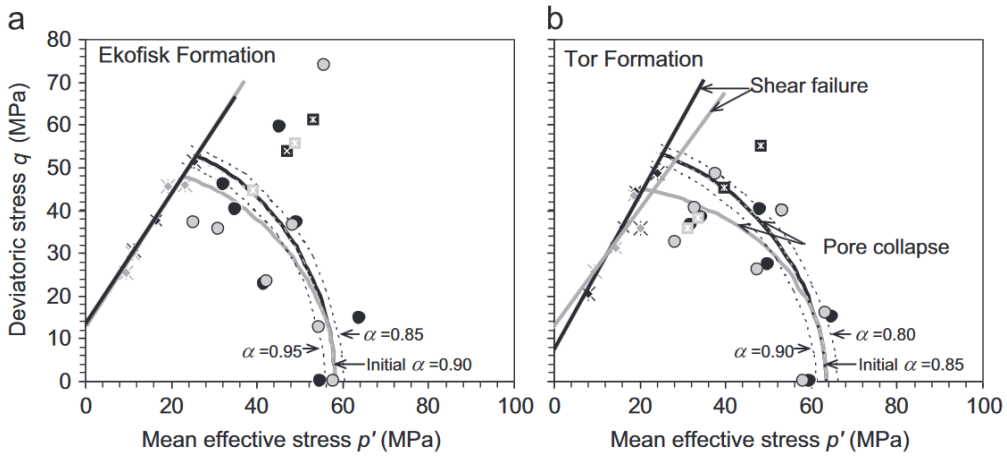

Figure 3.6 The p′–q plots of reference (black) and CO_2 flooded set of samples (gray) reveal the effect of injection of supercritical CO_2 on the mechanical strength of (a) Ekofisk Formation and (b) Tor Formation chalk. (Alam et al. 2014)

In Figure 3.6 the circles indicate the so-called 'compaction strength' (i.e. the volume yielding away from failure) whereas the stars indicate shear failure points. Pore collapse stress for the second or third cycle with the same stress ratio is indicated by squares with a cross. The dotted lines indicate the failure curve when a different Biot's coefficient, α is adopted.

3.5 Effects of CO_2 exposure on mineralogy and mechanical response of caprock samples

Caprocks have very low permeabilities and high threshold capillary pressures. Evaporite and shale caprocks are the two main categories of caprocks (Rohmer et al., 2016). These caprocks have low permeabilities ($<10^{-18}$ m^2). They have porosity in the range of 10-15%, although in general clay-rich caprocks have somewhat higher porosity than evaporite caprocks (Fitts and Peters 2013). When the caprock is intact CO_2 penetration may occur either through diffusion, with or without reactions, or by overcoming the capillary pressure of the caprock. The interaction of caprock and CO_2 is due to the upward

movement of the injected CO_2 due to its lower density as compared to the formation fluid. CO_2–brine–caprock interactions can cause changes in the mechanical properties of rocks, in terms of strength, stiffness, and fracture thresholds, which can increase the risk of CO_2 leaking from the reservoir. These effects have been experimentally investigated on various shale formations and under different exposure conditions aspects including form of CO_2 (gaseous, dry $scCO_2$), with or without brine, temperature, pressure, and the time of reactions (Lyu et al., 2016, Hangx et al., 2010, Mouzakis et al., 2016, Choi et al., 2021).

According to the literature, the magnitude of porosity and permeability changes indicate that regardless of caprock type and considering modelling times up to 10,000 years, undamaged caprock will only be affected for the first 10 m from the caprock-reservoir interface (Bildstein et al., 2010; Gaus et al., 2005; Hangx et al., 2010b; Tambach et al., 2015). Gaus et al., (2005) studied this in their reactive transport model for Sliepner. They assumed a caprock with porosity of 5% with temperature and pressure of 37 °C and 10 MPa. In the modelling it was assumed that the caprock mineralogy is homogeneous and that diffusion is the only mechanism transporting dissolved CO_2 into the caprock. The model involved a number of minerals found in Sliepner site including albite, anorthite, oligoclase, calcite, illite, kaolinite etc. They found that the reactions of CO_2 were up to 10 m of caprock. This implies that as long as sites are chosen with sufficiently thick caprock, this rate of progress of the reaction front should not, therefore, lead to a breach of site integrity over design time scales.

However, chemical reactions leading to a considerable change in porosity (i.e., large-scale carbonate dissolution, or volume reducing chemical reactions) may induce changes in mechanical strength as well, as an increase in porosity correlates with a decrease in strength. The reactions and their effects might differ if dry or CO_2+brine is used. First, the experimental studies conducted on caprocks with dry $scCO_2$ are presented. Some authors (e.g., Hui et al., 2019; Rezaee et al., 2017) studied the effects of dry $scCO_2$ on the microstructure and mineralogical composition of caprocks whereas others (e.g., Choi et al., 2021; Feng et al., 2019; Dewhurst et al., 2020) have focused on the effects on the mechanical behavior.

3.5.1 Effects of dry $scCO_2$

When dry CO_2 is injected, at the CO_2-brine interface water is adsorbed into CO_2 (i.e. it 'evaporates') and mixes within the CO_2 phase. Under in-situ conditions, this process of evaporation and mixing continues until the CO_2 becomes saturated with water and an equilibrium is reached (Bhuiyan et al., 2020). The absorption of water into the CO_2 results in the drying of the surrounding formation rocks. The drying of near wellbore zone also

occurs due to brine displacement as injection of CO_2 proceeds (Figure 3.1). The continuous drying of brine, filled in the pore spaces in the rock matrix, often leads to the precipitation of different minerals in the matrix. The common mineral that precipitates is halite (Nooraiepour et al., 2018). The precipitation of halite in fractures might have the fracture closing potential and might also induce injectivity problems. In the case of caprocks, the dehydration might lead to structural changes including shrinkage and cracking within the shale matrix (Feng et al., 2019, Espinoza & Santamarina, 2012).

Choi et al., (2021) studied the effect of $scCO_2$ on shale having a mineralogical composition of muscovite (47.1%), quartz (39.3%) and chlorite (13.6%). They investigated an outcrop heterogeneous shale in Boryeong (Chungcheongnam-do, Korea). They highlighted the effect of dry $scCO_2$ and $scCO_2$+brine on the mechanical response of such shale. For $scCO_2$+brine condition, the shale specimens were saturated with a synthetic brine and later placed in reactor chamber along with brine under pressure and temperature conditions of 10 MPa and 50°C. Whereas for dry $scCO_2$ conditions, the shale samples were exposed without brine but under the same temperature and pressure conditions.

Uniaxial compressive tests for each condition were conducted, the results are shown in Figure 3.7. Compressive strength increased in the case of dry $scCO_2$ by 10%. Whereas, in the case of brine+$scCO_2$ a significant decrease of 30% was noted. A similar trend was observed for P and S wave velocities of the exposed samples. In the $scCO_2$ case, an increase in seismic velocities was recorded and for the $scCO_2$+brine case, a decrease was observed. The authors attributed the increase in P and S waves to the self-healing effects, such as cracking closures caused by secondary oxides or sediment precipitation.

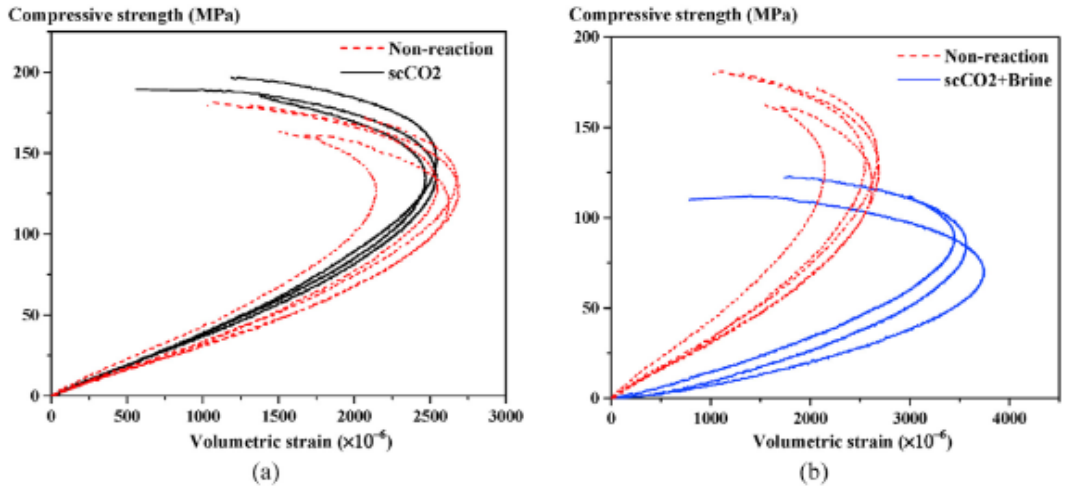

Figure 3.7 Volumetric strain curves difference according to the reaction condition. (Choi et al., 2021)

Among other mechanical properties, Brazilian Split Strength (BSS) has also been

investigated in the literature. Feng et al., (2019) studied black shale from Changning region of the Sichuan Basin in China.

The shale had a total organic carbon content (TOC) around 3.8% and a water content of 1.8%. Mineralogically it was composed of quartz, calcite, and feldspar and also contained small amounts of illite, and iron chlorite. Quartz and calcite were the dominant minerals. Sample with dimensions of Φ50x25 mm were placed in the reaction chamber containing dry $scCO_2$ at 40°C and 10 MPa for 10, 30 and 60 days.

The BSS of the shale gradually decreases as shown in Figure 3.8. The BSS value was 6.37 MPa for non-exposed (control sample) and showed a clear drop of 11.30% after 10 days of adsorption. For samples exposed to 30 days of adsorption, the BSS changed significantly with a value of 3.78 MPa, this was 33.10% lower than the 10-day adsorption value. With an increase in the adsorption time to 60 days, BSS was 3.46 MPa, only 8.47% lower as compared to the 30-day value. According to the authors, the decrease in BSS was slow after 30 days.

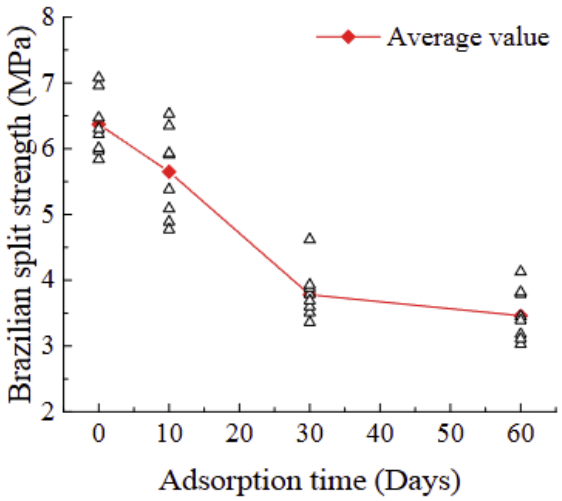

Figure 3.8 Change in Brazilian split strength after different days of dry scCO2 immersion. (Feng et al., 2019)

Dewhurst et al., (2020) studied mudrock samples cored from a depth of around 1800m. The material is a deep marine shale dominated by mudrocks. The main mineral phases were quartz (~30%) and clay minerals, with up to three different clay phases present (~25% mixed layer illite-smectite, ~19% kaolinite, and ~ 15% illite).

Four mudrock samples were exposed to dry $scCO_2$ in batch reactor. The temperature and pressure conditions were 150° C and 29 MPa. The samples were exposed for a total of 6 months before mechanically testing them. Some core chips were obtained during

the exposure for mineralogical and geochemical testing after 1, 4 and 6 months. No significant changes were observed in the mineralogy of these shale samples.

After 6 months the samples were practically dry, and the water content dropped from 5% to <0.5%. The 'initial state' samples were tested in consolidated-undrained triaxial and Brazilian split tests. Whereas the 'aged' samples were tested in dry conditions in consolidated-drained tests since no-pore pressure development was predicted. The results are compared in Figure 3.9.

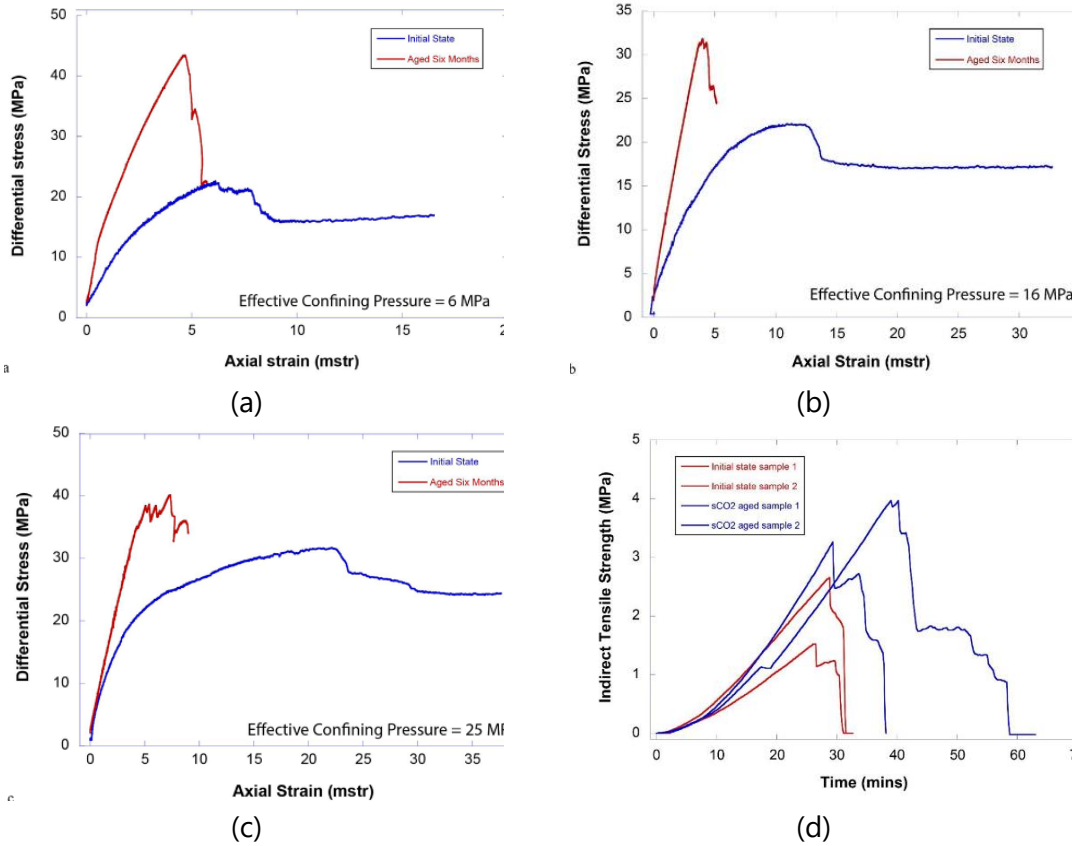

Figure 3.9 Comparison of stress-strain curves for preserved and dry $scCO_2$-exposed samples deformed at effective confining pressures of 6 MPa (a), 16 MPa (b) and 25 MPa (c). Plot (d) shows the result of the Brazilian split test both on exposed and non-exposed samples in terms of indirect tensile strength. (Dewhurst et al., 2020)

Both tests at 6 MPa Figure 3.9 (a) were anomalously strong compared to the other samples in their respective preserved and $scCO_2$ exposed states. The authors deemed this to be the heterogeneity of samples. Strength and stiffness increased after exposure to $scCO_2$. The stress-strain response changed to ultra-brittle, with complete collapse of the $scCO_2$ exposed samples after failure, so that no residual strength was obtained. The results from Brazilian tests suggest a tensile strength for 'initial state' samples somewhere in the range of 1.7–2.6 MPa and for exposed samples of 3.3-4.0 MPa.

The authors concluded that the strength and stiffness increase in exposed samples compared to 'initial state' samples are the result of loss of water from the shales as shown by changes in bulk density. The increase in the BSS was contradictory to that of Feng et al., (2019) shown in Figure 3.8 who noted a decrease in BSS values.

Apart from mechanical studies effects of $scCO_2$ on microstructures including porosity, permeability, pore size network and mineralogical composition of caprocks are also investigated. Hui et al., 2019 studied the effect of $scCO_2$ exposure on three shale samples. Samples were collected from the study area of Sichuan Basin and Ordos Basin in China. The focus of the study was the effect of dry $scCO_2$ adsorption on mineralogy and microstructural changes. The adsorption of CO_2 on untreated and $scCO_2$-exposed shale samples was measured with the ISOSORP-HP Sorption Analysis instruments (Rubotherm Company). The measurements were carried out by gravimetric method. This instrument utilizes the Magnetic Suspension Balance (MSB), which can precisely weigh any sample material in wide pressure and temperature ranges. The moisture content of the samples varied between 1.07 to 2.21%. The shale samples mainly contained quartz, feldspar, carbonate minerals (calcite and dolomite) and clay minerals. Two samples had carbonate content of around 6.5-7% (named TY and ML) while the third sample had higher carbonate content of up to 50% (MW).

The samples reacted with dry $scCO_2$ in batch reactor at pressure and temperature of 60°C and 18 MPa. These samples were reacted in their 'natural state'. The researchers also exposed other dry shale samples to $scCO_2$ at 60°C-18 MPa and 80°C-25 MPa. In all cases the reaction time was 240 hours.

Exposure induced a decrease in the moisture content but no significant mineralogical changes. The Pore Size Distribution (PSD) of exposed and non-exposed samples were compared. For ML and MW samples, it was found that smaller pores were reduced after exposure, leading to a reduction in surface area, while the opposite trend was found for sample TY. The reason for this contradictory behavior of clays was not found. Compared to the raw samples, the maximum CO_2 adsorption capacity of the shale samples was reduced after long-term $scCO_2$ treatment.

Rezaee et al., (2017) studied mudrock samples collected from an average depth of 1482 m from the Latrobe Group in the Gippsland Basin of Australia. Mineralogically the material was clay-rich with no carbonates. They analyzed the microstructural and mineralogical changes in samples exposed to dry $scCO_2$ at 15.17 MPa and 66°C for three months. Different forms of material including core plugs, pebble-size core chips, and crushed/powdered rock particles were used. The samples were saturated with synthetic brine before being exposed to dry $scCO_2$.

The XRD and SEM analyses demonstrated that, for most of the samples, there was no marked change in mineralogy after exposure to $scCO_2$. However, the mixed layer illite/smectite content reduced. According to the authors, this is likely due to the illitization process that may occur at low pH. Illite and mica content increased in most of the samples. The authors also found a 4% increase in porosity and increased pore size.

3.5.2 Effects of CO_2-saturated brine and wet $scCO_2$

The reaction of CO_2 with brine results in weak carbonic acid as shown in Equation 3.1. When shale comes in contact with CO_2-saturated brine the carbonic acid present in the solution starts diffusing into the shale's pore space. In shale's composition, there are always some minerals susceptible to carbonic acid. These minerals may be dissolved and eventually leach out. Some examples of chemical reactions are discussed in Section 3.3. The pH and reaction of acidified brine increase when the temperature and pressure are increased.

Lahann et al., (2013) explored this aspect in their low and high-pressure tests conducted on New Albany Shale from Indiana. Mineralogically the shales were composed dominantly of illite and quartz with 5-15% of total organic content. In low pressure test, 2 g samples were immersed in CO_2 by equilibrating with CO_2 at 3.8 MPa at about 15°C. Later 2 ml of distilled water was added and the resulting paste heated at 150 °C and exposed for 3 to 42 days. For high pressure tests the 2g sample was mixed with 2 ml of NaCl brine. Variable amounts (including none) of solid (dry ice) CO_2 (to simulate various pressures up to 24 MPa) were added to the reaction chamber and the chamber was heated to 80°C for 21 days. After exposure, the shale powder was washed to remove any slats on it. Mineralogy, pore size and fluid of reaction were studied post-exposure.

The authors studied the brine chemistry and SEM analysis indicating that the first response of CO_2 injection is carbonate dissolution. The mineralogical changes in caprock effects under low pressures were negligible compared to the high-pressure tests. Ca^{2+} and Mg^{2+} concentrations in reacted fluids generally increase with the pressure of the CO_2. The authors attributed this increase to the lowered brine pH in response to increased CO_2 solubility in the brine with increased pressure.

Alemu et al. (2011) studied crushed rocks from two caprock samples from Longyearbyen in Svalbard Norway. The two caprocks were carbonate-rich shale and clay-rich shale. Carbonate-rich shale mineralogically contained calcite (29%), illite (26%), chlorite (19%) and quartz (13%) as dominant minerals. The clay-rich shale contained chlorite (38%), illite (22%) and quartz (26%) as dominant minerals.

These shale materials were reacted with a mixture of brine (1M NaCl) and supercritical CO2 in batch reactor. The temperature varied between 80-250°C whereas the pressure was 110 bars. The water to rock ratio was 20:1. The time of exposure was 1–5 weeks. The authors studied the mineralogy of crushed materials and analysed the fluid chemistry after exposure.

SEM and XRD analysis of solid material revealed that the carbonate-rich shale was more reactive at 250°C. At such temperature, the analyses revealed the dissolution of plagioclase and clay minerals (illite and chlorite), dissolution and re-precipitation of carbonates, and the formation of smectite. According to the authors, a contradictory behavior was found in clay-rich shale which did not show major mineralogical alteration.

Chemical analysis showed that the aqueous concentration of major cations (i.e. Ca, Mg, Fe, K, Al) and SiO_2 increased in all experiments. Release rates of Fe and SiO_2 were more pronounced in solutions reacted with CO_2–brine as compared to those reacted with CO_2-free brine. For samples reacted with the CO_2–brine, lower temperature reactions (80°C) released much more Fe and SiO_2 than higher temperature reactions (150–250°C).

The dissolution and precipitation of minerals might open or close the pore throats. Several authors have studied the effects of CO_2-brine-shale interactions on porosity, permeability, and pore size (e.g., Zou et al., 2018, Mouzakis et al., 2016). It has been found that such interactions trigger the dissolution and precipitation of some minerals including carbonates. The migration of fine clay grains and inter-conversion of clay minerals has also been reported. Mouzakis et al., (2016) studied the changes in two caprock porosity and pore network geometry. The two caprock materials were Gothic Shale from Aneth oil field in Utah, and Marine Tuscaloosa shale from Plant Daniel site in Jackson County, Mississippi.

The Gothic Shale is a Pennsylvanian carbonate mudstone mineralogically containing quartz, calcite, dolomite, and mica in a clay matrix of illite and smectite. Total carbonate mineral content typically ranged from 20% to 30%. The porosity ranged between 2.7-4.3%. The Marine Tuscaloosa is a silica-rich mudstone mineralogically containing quartz (60%), feldspar (14%), chlorite (9%), kaolinite (5%), and illite (5%), with trace calcite (5%). The porosity in this case was around 2.2%.

The samples were exposed to brine and brine+CO_2 at 160°C and 15 MPa for 45 days. Both rock fragments and powder were used in the batch reactor. In the case of powder exposure, the rock to brine ratio was 54.

Both the Gothic Shale and Marine Tuscaloosa experienced mineral dissolution. In both sets of experiments, more extensive mineral reactions were observed in the CO_2 experiments compared to the control experiments (only brine exposed). In the Gothic

Shale (carbonate-rich), both total porosity and connected porosity increased whereas, in the Marine Tuscaloosa (silica-rich), total porosity increased slightly but connected porosity decreased.

The reaction time is another important parameter while exposing shales to CO_2-brine. Studies in literature have varying reaction times ranging between few hours to several months. Zou et al., (2018) studied this line of research on shale samples from two different formations, including the Lujiaping (LJP) and the Longmaxi (LMX) shales of Sichuan Basin. The mineralogical composition of the sample included quartz, carbonates and clays as the dominant minerals. The LJP shale contained approximately 44.1%, 24.8%, and 20.4% of these minerals respectively. The LMX shale had a quartz content of 43.3%, a carbonate content of 15.7% and a clay content of 30%. The samples were exposed to CO_2-brine with varying parameters i.e., reaction time (ranging from 0.5 h to 168 h), temperature (ranging from 40 °C to 120 °C), and pressure (at 10, 20, and 30MPa.) The authors studied the changes in porosity/ permeability, and rock mechanical properties (tensile strength and friction coefficient) as result of CO_2–brine–rock interactions.

It was concluded that the CO_2−brine−rock reaction occurred in less than 0.5 h. According to the authors, the geochemical reaction will occur promptly once a large amount of supercritical CO_2 is injected into the formation. The mineralogical analysis revealed that the carbonate dissolution was the most pronounced among all the reactions. Feldspar dissolution was also observed and resulted in clay precipitation within the large pores. A more substantial fraction of kaolinite was observed due to the feldspar dissolution. The reactions were found to become stronger with the increase in temperature or pressure, which was in agreement with the finding that more CO_2 is dissolved in the brine at a high pressure, which results in low brine pH also found by (Lahann et al., 2013). Moreover, in the SEM analysis, it was revealed that more and larger etched pores were created on the surfaces of the LMX shale which was clay-dominant shale. This result contradicted the finding of Alemu et al., (2011), that carbonate-rich shales show relatively high reactivity compared with clay-rich shales. The mineral dissolutions resulted in numerous large pores, which eventually caused a significant increase in porosity and permeability (by up to one order of magnitude).

The mechanical strength of the sample post-exposure was also tested. The tensile strength decreased due to CO_2-saturated brine. For the clay-dominant shale (LMX) shale, the tensile strength decreased by 7.9% after 0.5 h and by 71.3% after 168 h. The tensile strength of calcite dominant shale (NF) decreased by 3.9% after 0.5 h and by 48.2% after 168 h. The decline of dry-surface friction coefficient was up to 9.8%.

The effect of CO_2-water reaction on mechanical properties was also investigated by Lyu et al., (2016) in their study of black shale from Cambrian Niutitang Formation. Mineralogically the major minerals included calcite (9.54%), quartz (58.38%), feldspar (14.57%), muscovite (5.57%), illite (1.42%) and kaolinite (1%). They prepared samples of 60 mm in length and 30mm in diameter. These samples were divided into two groups. One group of samples was saturated in water with CO_2 at 7 MPa (gaseous phase) and the other group at 9 MPa (supercritical state). For each group of tests, the temperature was 40°C and the time of saturation was 10, 20, and 30 days. Two controlled samples were also tested which were not saturated.

The unsaturated or controlled samples had the highest UCS and Young's modulus values of 58.82 MPa and 5.22 GPa shown in Figure 3.10. A significant decrease was observed both in UCS and E values with an increase in the time of saturation. The final value for gaseous CO_2+water of UCS and E, after 30 days reduced by 56%, and 54%. The decrease in UCS and E was 66% and 56% respectively for scCO_2+water setup.

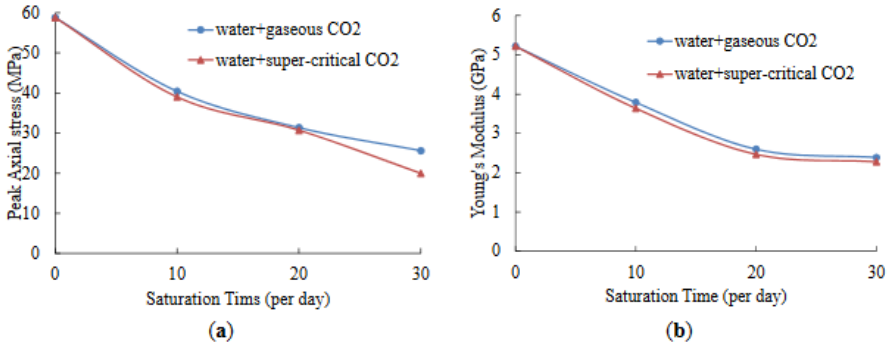

Figure 3.10 Variation of (a) UCS and (b) Young's modulus (Lyu et al., 2016)

The authors attributed the significant decrease in UCS and E to the combined effect of geochemical and geomechanical effects. Shales undergo swelling when exposed to water reducing the young's modulus. The adsorption of CO_2 on shale also influences strength. The higher decrease in the case of scCO_2 was justified because of higher density, viscosity, and dissolution ability in water than gaseous CO_2 therefore the scCO_2 can penetrate more easily into shale samples.

Choi et al., (2021) in their study as discussed in Section 3.5.1, investigated the heterogeneous shale of Boryeong Korea. They found that when exposed to CO_2+brine the compressive strength values decreased more (30% decrease) as compared to dry scCO_2 (10% increase) as shown in Figure 3.7.

In a similar fashion to Lyu et al. (2016), the effects of subcritical and supercritical CO_2 in brine or water were also studied by Zhang et al. (2017). They studied outcrop samples

of the lower Silurian Longmaxi formation located in the Changning region of the Sichuan Basin China. These samples were mainly composed of quartz (44.8%), dolomite (19.8%) and calcite (13.9%). They studied the mechanical properties of the samples after exposure to different fluids. The exposure was carried out in water, brine, dry scCO_2, and brine-CO_2 conditions at 45°C-6MPa (subcritical) and 45°C-12MPa (supercritical) conditions for 7 days.

The authors observed considerable mineralogical structural changes in the shale samples exposed to CO_2-saturated samples and CO_2–brine saturated samples. No significant changes occurred for water-saturated samples. The Ca^{2+} content in the sample exposed to supercritical conditions (dry CO_2 and CO_2-brine) showed 10% decrease compared to the dry sample. The dry sample was a control sample only heated at 45°C for similar testing times. Similarly, the same trend was seen in the element like K, Fe, and Al. However, S, Na and P almost remained unchanged. A noticeable increase in Na concentration was observed in the brine-saturated samples. The authors observed a prominent influence of water saturation and brine saturation on the mechanical behavior of shale. Supercritical CO_2 saturation caused a greater reduction of strength and elastic modulus in shale compared to subcritical CO_2 saturation agreeing with Lyu et al., (2016). The authors attributed this to the higher adsorption capacity of supercritical CO_2 on soil grains. Maximum reduction in strength and elastic modulus of shale was observed in case of CO_2+brine saturation condition.

3.5.3 Flowthrough tests on caprocks

The flowthrough tests where the fluid is injected into caprock samples are less frequent as compared to the flowthrough tests on reservoir rocks. This could be due to their low permeability and higher reaction times. Some authors have studied the change in permeability, porosity and breakthrough pressures as a result of different forms of CO_2 (e.g., Armitage et al., 2013; Favero & Laloui, 2018).

Armitage et al. (2013) studied the permeability of intact caprock samples of 'In Salah', Algeria. The authors flushed the samples with CO_2-saturated water at approximate reservoir pressure conditions (45 MPa confining pressure, 20 MPa pore pressure) for 72 hours. They found a drastic increase in permeability, by a factor of 8. The authors also observed an increase in porosity from 7 to 10% owing to the dissolution of siderite and chlorite.

In their study on Oplinus clay Favero & Laloui (2018) studied the hydro-mechanical properties of intact samples subjected to CO_2 injection in oedometer cell. They studied the effect of liquid CO_2 injection on vertical strain. Mineralogically the samples contained

quartz (13%), calcite (13%) and clay (66%) as dominant minerals. They injected liquid CO_2 (p= 9 MPa and T= 23°C) under constant stress conditions (vertical effective stress of 30 MPa) into the clay samples in normally consolidated and over consolidated state.

The authors found different vertical strains for normally consolidated (test 1) and over consolidated (test 2) as shown in Figure 3.11. Comparatively higher strains were observed for normally consolidated sample, whereas almost negligible strains were measured for over consolidated sample. The authors attributed this to the material structure which is prone to collapse when it is in normally consolidated conditions. In the case of over-consolidation, the microstructural rearrangement has already been observed in previous loadings.

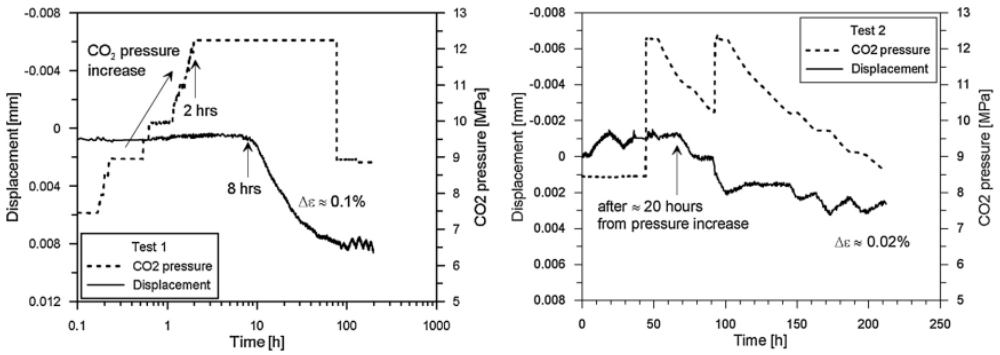

Figure 3.11 Vertical displacement and CO_2 pressure with time during the CO_2 injection phases (Favero & Laloui, 2018)

They also presented the comparison of oedometric modulus (E_{oed}), the coefficient of consolidation (c_v), and the secondary compression coefficient (C_α) before and after the injection of CO_2. The results of the comparison are reported in Figure 3.12 and Figure 3.13. The OPA and BHG represent the non-treated sample data and negligible effects of CO_2 injections were found on these parameters.

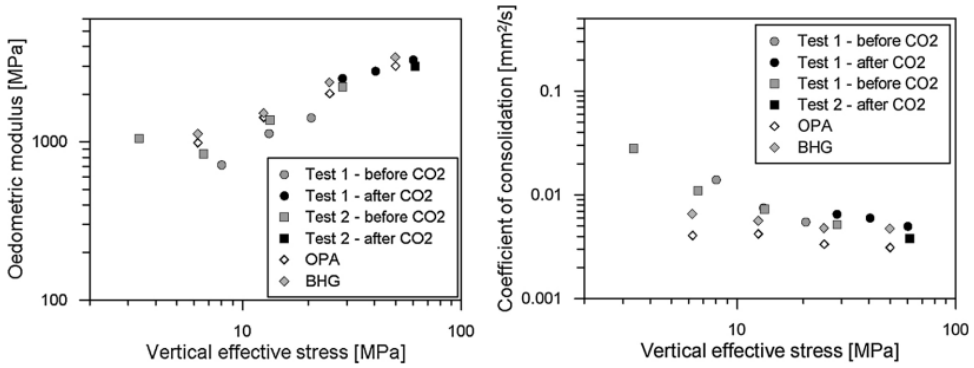

Figure 3.12 Oedometric modulus and coefficient of consolidation as a function of the vertical effective stress for the Opalinus Clay with and without CO_2 contact (Favero & Laloui, 2018).

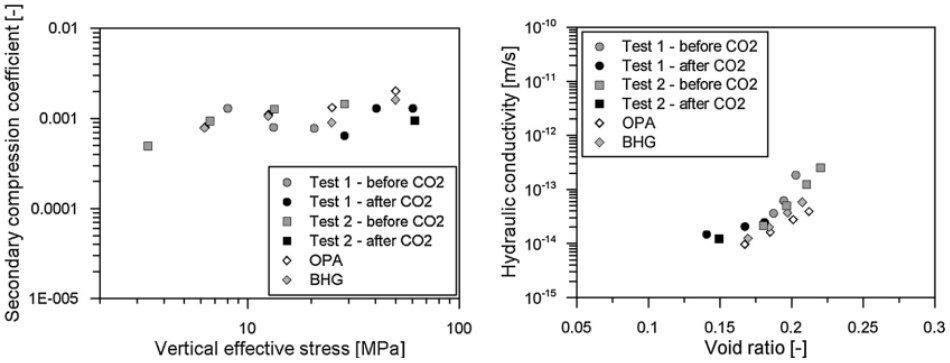

Figure 3.13 Secondary compression coefficient as a function of vertical effective stress and hydraulic conductivity as a function of void ratio with or without CO_2 contact (Favero & Laloui, 2018).

In the flowthrough experiment conducted by Agofack et al., (2019), who studied the change in E and Poisson ratio on a shale sample in triaxial loading conditions. After flooding with CO_2–brine for more than 12 days the authors showed a reduction of the Young's modulus and Poisson's ratio, while the maximum deviatoric stress (axial stress minus confining pressure) increased after exposure to CO_2–brine. A reduction of the undrained bulk modulus after exposure to CO2–brine was also reported.

3.6 Exposure of caprocks to acid solution

The injected CO_2 in the reservoir will dissolve into water (zones A3 and A4 of Figure 3.1) and form carbonic acid (H_2CO_3), which dissociates into protons (H^+), bicarbonate (HCO_3^-) and carbonate (CO_3^{2-}) ions (Gaus, 2010). The H^+ producing reactions lead to a pH drop in the resident brine from approximately 7.0 to an acidic range of 3.5–5.0 (Gaus, 2010). As stated in Section 3.3 the acidic fluid induces chemical reactions with the reservoir and caprock, mainly mineral dissolution and precipitation, with potential pivotal impacts on their hydraulic and mechanical properties discussed in previous sections.

The storage of CO_2 is a long-term process involving tens of thousands of years. The reactions involved are slow and time-consuming. In laboratory testing, sometimes to expedite the processes involved, low pH acid is also used instead of CO_2. Dissolved carbon dioxide in the CO_2-brine system is a weak acid, and reactions with minerals may buffer the fluid and further decrease its chemical reactivity. Therefore, the acid attack is expected to be less severe compared to that induced by a stronger acid, like ammonium nitrate or hydrochloric solution (Rohmer et al., 2016).

Xie et al. (2011) studied the changes occurring in limestone samples exposed to low-pH acids. Samples were immersed in ammonium nitrate solution (6 mol/l), for one year. They found an increase in porosity from 23 to 27%.

Nouailletas et al. (2013) studied the shear behavior of calcareous limestone rock subjected to acid exposure. They studied Campanian Flysch specimens from France. It contained more than 60% calcite. The specimens were immersed in an HCl acid solution (0.6 $mol.L^{-1}$) for 6 hours for chemical degradation whereas, reference samples were immersed in water. Direct shear tests were performed on the degraded and reference samples. Despite an apparent roughness of sample surfaces, the shear stress vs tangential displacement curves of degraded samples exhibited the behavior of a smooth joint. The degraded sample showed less dilatancy compared to reference sample.

Favero & Laloui (2018) studied the mechanical response of Opalinus Clay shale samples under acid environment. They studied the physical properties, including grain density, void ratio and dominant entrance pore size. They also investigated the effect of acid exposure on the retention capacity of the clayey caprock. The samples were exposed to an HCl solution with a pH = 3. The material was exposed to this solution at room temperature and atmospheric pressure conditions, for 40 days. The results show that grain density, pore size density and void ratio are not significantly affected by the contact with the low pH solution. Similar conclusions were drawn for the retention capacity of samples.

Vespo (2024) studied the influence of exposure to an acid environment on the mechanical behavior of carbonatic clay. He investigated the response of reconstituted samples subjected to long-term exposure to HCl solution in oedometric conditions. The acid was used in diffusion condition and flowthrough test where the acid was injected under pressure. A decrease of 3-4% in carbonates was observed after exposure of around 184 days. In total about 140 pore volumes of acid was injected. Mechanically almost no change was observed. Another set of tests with pH = 0 resulted in an extensive decrease in carbonate content and 8-12% deformation due to chemical reactions.

3.7 Conclusions

In this Chapter, different experimental studies in the literature were reviewed, where reservoir and caprock samples were exposed to different forms of CO_2. More attention was paid to the caprock samples which are the interest of this study.

In the case of reservoir rocks, carbonate dissolution was most common in different rocks. Most studies (Alam et al., 2014; Vialle and Vanorio, 2011; Xie et al., 2011) found a decrease in the mechanical properties of exposed reservoir rocks.

In all the studies conducted on caprocks with dry $scCO_2$, the drying of samples was a common theme. Water content in the exposed samples was reduced to almost dry conditions. Although no significant changes were observed mineralogically in most

studies but changes in mechanical behavior were observed in treated samples. Some studies recorded a decrease in mechanical properties (e.g., Feng et al., 2019) while others observed an increase (eg., Dewhurst et al., 2020; Choi et al., 2021).

Dissolution of carbonates was observed in most studies where caprock samples were exposed to CO_2-saturated brine (or water). According to Lahann et al. (2013), carbonate dissolution is indeed the first reaction expected to occur upon injection of CO_2. Some authors have reported the dissolution of other minerals including silicates (Alemu et al., 2011). In many studies the effect of CO_2+brine exposure affected porosity, permeability, pore size and pore network (Zou et al., 2018, Mouzakis et al., 2016). Highlighting a single factor that influences the total porosity, pore diameter, and connective porosity under CO_2 exposure is challenging. The two primary mechanisms that can change the pore structure are dissolution and adsorption-induced expansion. It was found that with increased pressure and temperature, the effects of CO_2 were pronounced (Lahann et al., 2013; Zou et al., 2018).

The flowthrough experiments are more common in reservoir rocks and less frequent for intact samples of caprocks. Flowthrough experiments using acid are used to expedite the chemical reactions.

In conclusion, the impact of CO_2 injection has been extensively researched through experimental investigations. As highlighted in the literature review, the results of these experiments exhibit considerable variability. This variability can be attributed to the inherent dissimilarities in the geomaterial, which encompass variations in mineral compositions at microscales. The effects of CO_2 are very site-specific and complicated. The correlation between the mineralogy, chemistry and mechanical properties is not straightforward. The scatter of results in the literature underscores the necessity for a comprehensive and meticulous examination of each project, with consideration given to the specific mineral characteristics involved.

Chapter 4 Experimental techniques and methods

In this research the effects of CO_2 and low pH water solutions on the hydro-mechanical behavior of caprock samples both in intact and reconstituted state was studied. Caprock samples were preliminarily exposed to CO_2 in batch reactions and to acid in flowthrough experiments. The batch reactions were carried out in autoclaves to allow for CO_2-related reactions to take place before mechanical testing. The temperature and pressure conditions in the autoclaves were relevant to CO_2 storage sites at around 1500 meters. After exposure to CO_2 the samples were tested mechanically in high pressure and medium pressure triaxial cells.

Flowthrough experiments were carried out to study the short term effects of CO_2 on hydro-mechanical behavior of intact and reconstituted caprock samples. CO_2 storage is a long term process and the reactions involved are slow and time consuming. The main expected reactions are related to the acidic environment generated by CO_2 dissolution into water which causes a pH≅3 at reservoir pressures and temperatures. To expedite the chemical reactions, HCl solution with lower pH was injected through the specimens in flowthrough experiments. The flowthrough experiments were carried out in an advanced oedometer, designed and set up at Politecnico di Torino. To complement the mechanical study, the microstructure and mineralogy of the exposed and non-exposed samples were also investigated with Scanning Electron Microscopy (SEM), Mercury Intrusion Porosimetry (MIP), X-ray Diffraction (XRD) and Equivalent Calcite Content (ECC) analyses. This chapter presents an introduction to the techniques and equipment used for mechanical and microstructural analyses.

4.1 Reconstitution procedure and consolidometer

In this research, reconstituted samples were used in both the batch reactions and flowthrough studies. The samples were prepared by consolidating the soil slurry paste in consolidometer under stepwise pressure increments.

4.1.1 Preparation of slurry

The process starts with the preparation of the soil slurry. Initially, the dry soil material is vigorously grinded in mortar and pestled until obtaining a powder. The solid fraction thus obtained was then placed on a Plexiglas surface and mixed with distilled water. This operation was completed, depending on the quantity of material to be prepared, using a spatula or a mechanical mixer. These steps are shown in Figure 4.1.

(a) (b) (c)

Figure 4.1 (a) Grinding of material, (b) mixing of the grinded material with distilled water, (c) making a slurry paste for reconstituted samples.

A high water content is a necessary prerequisite for the workability of the material. Typically, these samples were reconstituted starting from an initial water content $w_0 \cong$ (1.1-1.5)LL. At low levels of stress the position of the compression curve on the vertical stress-void ratio ($\sigma'_v - e$) plane is influenced by the preparation water content (Hong et. al., 2010, Hong et. al., 2012). However, at high-stress levels, such as those of interest in this study, the relationship between vertical stress and void ratio tends to be unique and not so influenced by the adopted w_o.

4.1.2 Preparation in consolidometer and mechanical loads

After mixing, the slurries were left to rest for approximately 24 hours, to allow homogenization of the water content. They were subsequently introduced into a metal cylinder with rigid side walls to allow load application and one-dimensional consolidation. The mixtures were poured into the cylinder by taking care not to leave any spaces filled with air. Two porous stones were placed at the top and bottom of the cylinder for the drainage of water when the vertical load was applied. In order not to clog the porous stones with solid particles, a filter paper was introduced between the slurry and the porous stones. The cylinder with the porous stones was placed on the base of a frame, then a further external cylinder accommodated, wider than the one containing

slurry. The space between the outer and inner metal cylinders was filled with water, to allow the sample to always be kept under a minimum head of water and to avoid desaturation by evaporation. The adopted frame allows imposing an axial force of around 17 kN. Cylinders with two different diameters were adopted: one with a diameter of 38 mm (allowing applying a vertical stress of up to 15 MPa), another one of 50 mm (allowing to applying a vertical stress of up to 8.5 MPa). The base, the cylinder filled with slurry and the external cylinder containing the slurry-filled cylinder are shown in Figure 4.2.

(a) (b) (c)

Figure 4.2 Assembly of the consolidometer. (a) the base with porous stone, (b) cylinder filled with slurry and (c) external cylinder containing the slurry cylinder to be filled with water.

The porous stone at the top of the specimen is connected to a rod, possibly with a load cell, and then to a pump through which the vertical load is applied. The variation of the sample height is measured by connecting an LVDT to the piston rod that applies the load (Figure 4.3 (b)). In Figure 4.3 (c) a specimen having a diameter of 50 mm is shown after the completion of the consolidation process.

(a) (b) (c)

Figure 4.3 Cell assembly (a) cell mounted in the consolidometer (b) 50 mm specimen extracted from the consolidometer (c).

4.1.3 Consolidation under the application of an increased mechanical load

Reconstitution occurs by imposing a series of load increments, up to a maximum vertical stress. Whenever the load, applied by the piston of the consolidometer is increased, a consolidation process is established.

Generally, a new load increment should only be applied when the consolidation is complete under the previous load step. Given the dual aspect of pore pressure dissipation phenomena and the settlement of the specimen, theoretically, the end of consolidation should correspond to the moment in which the settlements stop increasing. However, it is known that the behavior of the soil is always associated to some extent with creep or secondary compression phenomena. By these phenomena the settlement of the top of the specimen continues to occur even for constant effective stress: experimentally it has been observed that this occurs due to a law that relates the increase of settling to the logarithm of time. In the initial time instants after the application of the load the settlement–time (incremental ΔH vs t) curve is governed by the consolidation process, while subsequently it is governed by secondary compression. According to the Casagrande procedure, the time of the end of consolidation, t_{100}, can be identified by the intersection of the straight-line tangent to the central inflection of the curve with the continuation of the line tangential to the part of the curve dominated by secondary compression (Figure 4.4).

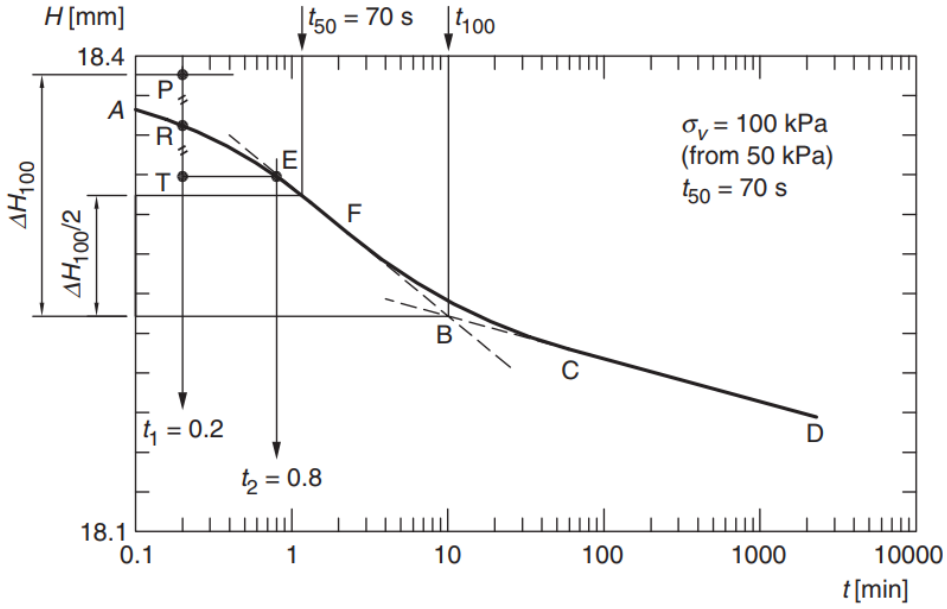

Figure 4.4 Example of settlement versus log time graph (Lancellotta 2008).

At the end of the consolidation, the load is increased until the required vertical pressure is reached. The sample is then extracted from the cylinder and is preserved in plastic and aluminum wrap with wax on the top. This is necessary in cases where the sample is not immediately used to maintain the specimen saturated.

4.2 Sample preservation

All samples, in all states (e.g., non-exposed intact and reconstituted; exposed intact and reconstituted specimens) were preserved in wax for preservation. The process involved application of plastic layer on the sample, followed by aluminum of around two layers. The sample was then covered in waxed at melting temperature. The application of the aluminum layer was to minimize the effects of temperature difference between wax and sample. Although it is known that the temperature difference induces thermal loads, after application of plastic and aluminum layers, this effect was assumed to be negligible.

4.3 Autoclave for batch reaction experiments

Intact and reconstituted specimens were exposed to CO_2 through batch reactions. These samples were exposed to CO_2 in different forms and for different periods. The study also involved the exposure of wet soil powder to CO_2, that was later used for reconstitution of samples. The exposure of the specimens to CO_2 was carried out at Eni E&P laboratories.

4.3.1 Equipment and thermodynamic conditions

The autoclave or reaction chambers used for the exposure of the samples to CO_2 are available at Eni E&P laboratories. These autoclaves are Hastelloy chambers with a volume of around 600 ml, a diameter of 82.55 mm, and a height of 119.38 mm. The maximum temperature that can be imposed in the autoclave is 350°C while the highest pressure is 345 bars (34.5MPa). Two such autoclaves were used in this study. The two chambers are connected to the same pump, which controls the pressure of the CO_2. One of the autoclaves is shown in Figure 4.5.

(a) (b)

Figure 4.5 Autoclave used for the exposure of specimens present at Eni E&P.

The temperature and pressure conditions of exposure were consistent with those of a reservoir at around 1500 m depth. With a temperature gradient of 3°C/100 m (15° at the surface) and hydrostatic pressure gradient of 10 bar/100 m, the CO_2 would be injected at a temperature of T= 60°C and a pressure of p_{CO2}=150 bars (15 MPa). At this temperature and pressure, the CO_2 is in its supercritical state, which is achieved when T≥31.1°C and p≥7.38MPa.

At the end of the exposure period, the chamber was depressurized before removing the sample from the autoclave. Depressurization of the reaction chamber is a critical step in the exposure procedure as the state of CO_2 reverts from supercritical to gaseous, which might affect the structure of the specimen. To depressurize the autoclave the temperature was decreased to 20°C overnight and the pressure was maintained at 150 bars (from point 1 to point 2 in Figure 4.6). The pressure was then reduced from 150 bars to 60 bars stepwise at a rate of 3 bars per 10 minutes. At the temperature of 20°C, the pressure decrease from 60 bars to 50 bars requires more care because of the phase change of CO_2 from liquid to gas. Therefore, between 60 to 50 bars, a continuous decrease of 0.3 bars/min in pressure was adopted, as shown by the dotted line in Figure 4.6. For pressures smaller than 50 bars, the stepwise decrease was imposed at a rate of 3 bars/10 minutes, on the 20°C isotherm shown by the red line from point 2 to point 3 in Figure 4.6.

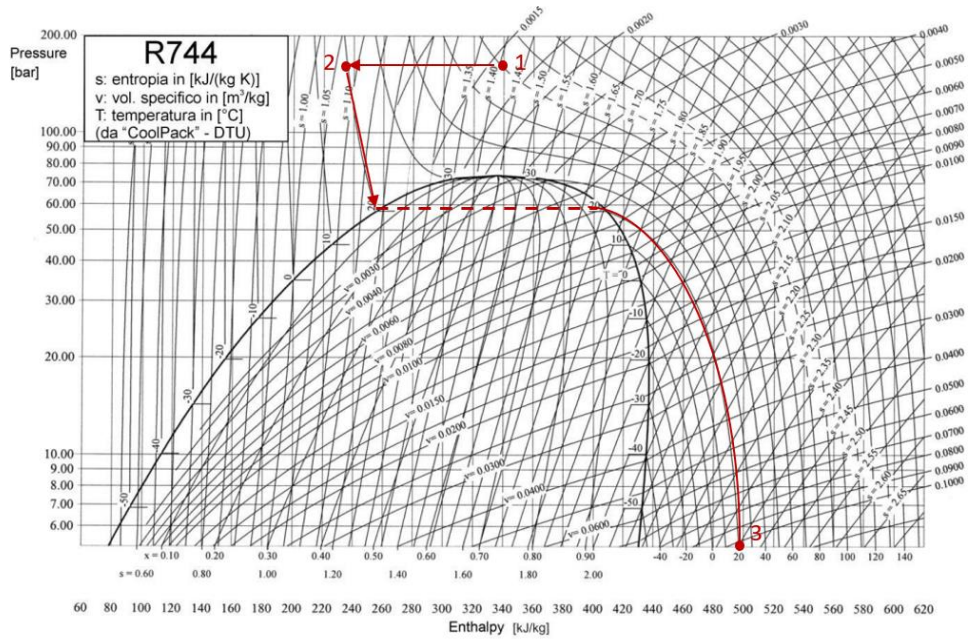

Figure 4.6 P-h diagram for carbon dioxide (Katende 2016) and path imposed in the reaction chamber during depressurization.

The depressurization path is shown in Figure 4.7 on the phase diagram of CO_2. The phase of the CO_2 changes from supercritical to liquid and then to gaseous form.

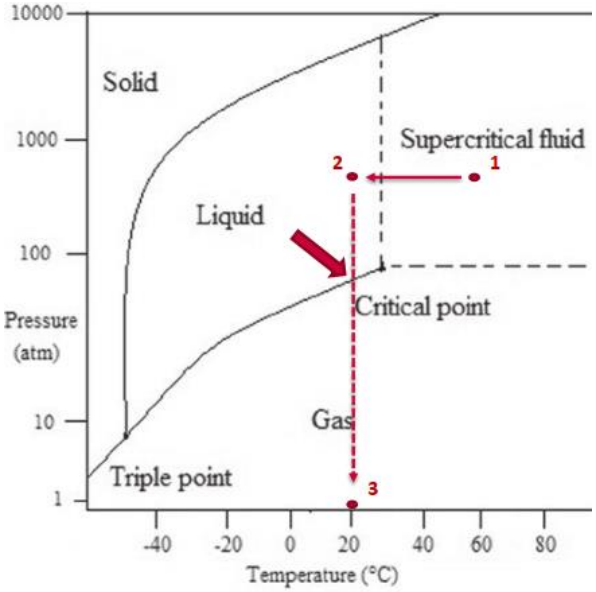

Figure 4.7 CO_2 phase diagram showing the imposed depressurization path.

4.3.2 Exposure procedures

The exposure of the specimens to CO_2 was carried out keeping into account the possible states into which CO_2 and caprock might interact. The samples were exposed to dry $scCO_2$, wet $scCO_2$ and CO_2 saturated brine for 14 and 30 days. Apart from samples, powdered soil material was also exposed to wet $scCO_2$. After being exposed, this powdered material was used to reconstitute other specimens.

Exposure to dry $scCO_2$

Exposure to dry $scCO_2$ was pursued by placing the specimens within the autoclave, where they were immersed into an 'atmosphere' of dry $scCO_2$ at the temperature and pressure declared in the previous Section 4.3.1. Dry scCO2 does not have any water dissolved in it, therefore it causes desaturation of samples. To avoid desaturation, exposure was also done using wet (water saturated) $scCO_2$.

Exposure to wet $scCO_2$

Exposure to wet $scCO_2$ was pursued by placing the specimens within the autoclave, where they were immersed into an "environment" of $scCO_2$ at the temperature and pressure declared in the previous Section 4.3.1. Ideally, water saturated $scCO_2$ could be injected into the chamber. However, the experimental setup does not allow the saturation of the CO_2 outside of the chamber, therefore, some water was put within the chamber in a small baker for this purpose as shown in Figure 4.8 (b). The mass of water used was slightly larger than the amount of water that evaporated from a specimen exposed to dry $scCO_2$ during previous exposures.

Exposure to CO_2 saturated brine

In the case of CO_2-saturated brine, two specimens were first placed into the autoclave. Then, 250 ml of formation water was poured into the autoclave to cover the specimens. The composition of formation water is provided in Table 4.1 below. The content of each mineral is in mg/l.

Table 4.1 composition of formation water used during Clay A exposure.

Na	K	Mg	Ca	HCO_3	Cl	S	Total (NaCl eq.)
11500	117	387	593	536	20474	6.7	33613.7

A few centimeters of the autoclave chamber were left clear of water and specimens. Later $scCO_2$ was injected into this space, to allow its dissolution into the brine. Two specimens and the added brine are shown in Figure 4.8 (c).

(a) (b) (c)

Figure 4.8 Exposure of specimens to different forms of $scCO_2$ in autoclave (a) exposure to dry $scCO_2$ (b) wet $scCO_2$ and (c) CO_2 saturated brine.

4.3.3 Containment of samples during exposure

During the exposures, special attention was paid to avoid undesired effects on the specimen fabric which, instead of being caused by interaction with the CO_2, might depend on how the specimen is subjected to pressure and fluid histories. In particular, it might be expected a soil specimen, though reconstituted at high stress, immersed into brine would 'disaggregate' and turn into mud as the effective stress is null in such conditions. Because of this, during the first experiment where the CO_2-saturated brine was used, two specimens were used. One was immersed into the brine without any containment whereas another one was contained in a 'cage'. After the exposure, it was found disaggregated, so that the soil particles were deposited at the bottom of the solution in the autoclave chamber Figure 4.9 (a). On the other hand, the caged specimen preserved its shape with minimal changes in height and diameter.

The containment/caging was done with a metallic mesh of 250 microns (60 mesh). The mesh was wrapped around the sample and O-rings were placed on the top and bottom of the specimen to hold the mesh. Two porous stones were employed on top and bottom to contain the specimens in the axial direction. Plastic clamps were used to maintain the mesh as shown in Figure 4.9 (b) and (c).

(a) (b) (c)

Figure 4.9 (a) Disintegration of uncaged specimen exposed to CO_2-saturated brine (b) and (c) show caged and uncaged specimens with mesh, O-rings and plastic clamps.

The caging was important in cases where the samples were exposed to CO_2 saturated brine. In the case of dry and wet $scCO_2$, proved not to be necessary but it did not affect the properties of the samples.

4.3.4 Powder exposure to wet $scCO_2$

Soil slurry was prepared at a water content equal to LL by properly mixing it with distilled water. The slurry was then exposed to $scCO_2$ for 14 and 30 days (Figure 4.10). After 14 days of exposure the paste was recovered, underwent mineralogical analysis, and used to prepare reconstituted specimens for triaxial testing. After testing the specimens were dried and grinded again and mixed with distilled water once again to obtain another slurry, which was exposed to CO_2 in the autoclave for another 16 days (in total 30 days of exposure).

Figure 4.10 Placement of powder paste in the reaction chamber before exposure to $scCO_2$.

4.4 High pressure and medium pressure triaxial apparatus

Triaxial testing was performed with the High-Pressure Triaxial Apparatus (HPTA) and the Medium Pressures Triaxial Apparatus (MPTA) of the geotechnical laboratory of Politecnico di Torino. The two triaxial cells differ in terms of the maximum cell pressure and back pressure that can be applied, whereas they have the same working setup. More details about the apparatus can be found in Barla et al. (2010).

4.4.1 Triaxial testing equipment

The experimental apparatuses, made by GDS Instruments Ltd (UK), can be used to conduct triaxial tests on soft rocks and stiff clays following various stress paths, both stress and strain-controlled. The apparatuses are mainly composed of (i) triaxial cell (ii) hydraulic pumps (iii) measurement system and (iv) control and data acquisition system. The different components of the apparatuses are presented in Figure 4.11.

The sample is placed on a cylindrical base with a diameter equal to that of the sample along with porous stones at top and bottom. As for the HPTA, specimens of different diameters can be tested including 38.1, 50, 70 and 100 mm. In the MPTA it is possible to conduct tests on 38.1 mm samples.

(a) (b)

Figure 4.11 (a) Triaxial cell along with the ram (b) hydraulic pumps for cell pressure and back pressure.

The cell pressure is applied with a rigid steel cylindrical chamber filled with oil. The cell

pressure and the pore pressure in the sample are controlled through two hydraulic pumps (Figure 4.11 (b)), connected respectively to the cell and the sample. It is possible to apply a maximum cell pressure of 64 MPa and 20 MPa for HPTA and MPTA respectively. A maximum back pressure of 32 and 20 MPa can be applied for HPTA and MPTA respectively. By controlling the volumes of water and oil exchanged between the pumps and the cell, it is possible to evaluate the volumetric deformations of the sample. For this study, only the change in the volume of water was evaluated for volumetric deformations.

The apparatus is equipped with instruments to measure the stress and strain state inside the sample. The vertical load applied by the press is measured using two load cells: one placed externally, below the ram, and one placed internally, installed on the load rod of the triaxial cell and therefore free from friction phenomena. The external cell of the HPTA is capable of measuring loads up to 250 kN with an accuracy of 60 N. The internal cell has a maximum capacity of 64 kN and an accuracy of 15 N. The MPTA is equipped with an external load cell of 100 kN and an internal one capable of measuring loads up to 64 kN with an accuracy of 15 N. Cell pressure and pore pressures are constantly monitored using pressure transducers.

Advanced High Pressure/Volume Controller (HPDPC) from GDS instruments is utilized for controlling both pressure and volume within the cell. An additional pump is employed to inject water into the sample during the saturation process and to store the water during consolidation, ensuring the continuous recording of pressure and volume. The maximum pressure of these pumps is declared above whereas the maximum volume capacity is 200 ml with an accuracy of 0.1%.

The displacements (and consequent deformations) of the sample are measured both globally and locally. The global deformation can be monitored with an accuracy of 1 μm. The local axial and radial strains can be measured using LVDT (Linear Variable Differential Transformer) glued directly on the membrane of the sample as shown in Figure 4.12.

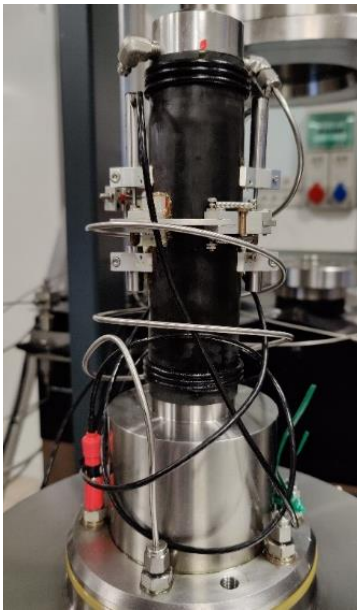

(a)

(b)

Figure 4.12 (a) Local radial and axial transducers placed directly on the sample (b) ultrasonic waves measurement system in MPTA.

The control and data acquisition system allows for control of the different parts of the apparatus using the dedicated software developed by GDS. A computer is connected to the instrumentation via a digital control unit which, in addition to controlling the various displacements and pressures, allows the data recorded by the measurement system to be acquired.

In addition to the previously described measurement systems, the MPTA apparatus is also equipped with ultrasonic transducers. This allows the evaluation of the compression (P) and shear (S) wave velocities of the sample at high confining pressures (Figure 4.12 (b).)

The instrumentation consists of piezoelectric transducers made of piezoceramic material, which allow generating and receiving high-frequency compression and shear waves, the latter polarized along two orthogonal directions. The ultrasonic wave velocity is obtained directly by dividing the length of the sample by arrival time of the transmitted signal along the sample. Piezoelectric sensors are shielded by an outer metal casing embedded in the cell bases, which allows the measurement system to be used even for high confining pressures.

Transducers are present at the top and base. One set is used to generate input, which propagates through the sample and is read as output by the other set of transducers. Measurement can be made by generating waves that propagate from top to bottom and vice versa. The control system has the dual function of generating high-voltage pulses to

energize the transmitter piezoelectric sensors and recording the signal of the receiver piezoelectric sensors. The pulse generator has the capacity to deliver up to ±200 V and the ability to generate pulses in a range of duration between 0.625 μs and 500 μs. The generated pulse can have a positive or negative initial phase. Two types of pulses are possible: 'simple pulse' i.e., a single square wave; 'push-pull pulse' in which the rising and falling edge of the square wave occurs over a certain period, providing a higher pulse to the transmitting transducers.

The high-speed acquisition system makes it possible to amplify signals with a maximum gain of 11 times. The test setup allows for two types of measurements to proceed i.e., single scan and multi-scan. In single scan recording for each measurement, a single input pulse is produced and the corresponding wave is recorded at the receiver, whereas for multi-scan a number of pulses are generated and as many waves are recorded at the receiver, which are summed at the end so that they constructively interfere by improving the signal-to-noise ratio (stacking of signals).

4.4.2 Mechanical testing procedure and protocols

To investigate the effect of CO_2 exposure, in its different states, on the mechanical behavior of the caprock materials, a series of triaxial undrained monotonic tests were carried out. The main purpose was to evidence the possible changes in strength and stiffness; thus, undrained conditions were preferred to keep testing times short. Furthermore, as evidenced also in previous results (Ciancimino et al., 2024) the undrained conditions were proved to be most critical one for failure. Twin samples (same preparation procedure for reconstituted sample, same depth for intact ones) were tested along the same mechanical paths before and after exposure to CO_2. The complete description and results of the mechanical tests are presented in Chapter 7. These triaxial tests were conducted following the protocols of ASTM-D4767-11 (2020) standards. The tests consisted of three phases i.e., sample saturation, consolidation, and shearing phase. These phases are briefly discussed in the following. To speed up pore pressure equilibration, side drains made of filter paper were placed on the specimens' lateral surface. This allowed reducing the drainage length thus also reducing the consolidation times and allowing for higher shearing velocities.

Saturation

The saturation of the samples was imposed through a progressive increase in the back pressure. Both the cell pressure and the backpressure were gradually increased (in drained conditions), keeping the effective pressure p' constant (generally equal to around 300-400 kPa). The cell drains were then closed and Skempton's (1954) coefficient B was

measured. This parameter is the ratio between the increase in pore pressure to the increase in cell pressure in undrained conditions:

$$B = \frac{\Delta u_w}{\Delta p} \quad 4.1$$

Although B=1 would be necessary to ensure full saturation of soft soil, in literature it is found that for materials with high stiffness of the material, a final limiting value of B=0.95 is acceptable (Cook, 1999; Hart and Wang, 1999, Monfarede et. al., 2011). Note that the degree of saturation also increases during the following consolidation stage because of the progressive decrease of the porosity.

Consolidation

Specimen consolidation was induced by imposing an anisotropic stress state, where the ratio between the radial and the axial effective stress was kept identical to the expected in site stress ratio of Clay A ($K_0=\sigma'_{ho}/\sigma'_{vo}$ =0.48) and Clay B samples (K_0=0.50). This phase was carried out by gradually increasing the cell pressure and deviatoric stress until reaching the desired stress state. Stress was increased slowly enough to prevent the development of any excess pore pressure with open drains. For some samples, the condition of Over Consolidation Ratio (OCR) of 1.5 and 3.0 was applied. To this aim the samples were consolidated to 1.5 and 3 times the in-situ stress state and then unloaded to the desired stress condition.

Undrained shearing

Shearing was performed in undrained, strain-controlled conditions. Conventional 'compression/loading' stress paths were applied (the axial displacement was increased while keeping the total radial stress constant). After consolidation, the drainage lines were closed, and a constant rate of axial displacement was applied. To ensure a homogeneous distribution of excess pore pressure within specimens, a sufficiently slow loading/strain rate, which depends on specimen permeability, size, and drainage length, is required (details in Head and Epps, 2014). However, a strain rate of 0.01%/min was applied in this study to ensure consistency with the study of Ciancimino et al. (2024) which was carried out on the same material.

The tests ended after attaining a condition where the values of the deviatoric stress, mean effective stress and pore pressure remained constant as the axial strain increased. In the case of intact specimens, the shearing phase usually implied the development of a shear (or failure) band.

4.5 Oedometer

In this study, mechanical testing included oedometer tests using a standard oedometer apparatus for some of the tests. For intact specimens, high vertical loads were necessary to observe changes in the compressibility. To achieve high stresses, (up to 28 MPa) specimens with small diameters (25.2 mm) were used. Figure 4.13 illustrates the comparison between the sample rings of the standard and small diameter oedometers.

Figure 4.13 Sample rings for the standard oedometer on the left and small diameter oedometer on the right.

4.6 Microstructural investigations

Microstructural analysis was conducted to study the possible effects of CO_2 on the fabric of the material. The microstructural study included Scanning Electron Microscopy (SEM) and Mercury Intrusion Porosimetry (MIP). SEM provides a direct detail of the specimen microstructure and fabric, whereas MIP provides the pore size distribution of the samples. The main difficulty in studying the microstructure of clay minerals is the preservation of the delicate fabrics of the specimen. These techniques require well preserved and dehydrated samples (Smart and Tovey, 1982). When left for air drying or oven drying the microstructure of the soil fabric (especially the one of clays) might change. Therefore, the microstructures resulting from air-dried soil samples may represent a very different structure from the one of the structured soil.

To ensure minimal effects on fabric upon water removal, this was induced through freeze drying.

4.6.1 Freeze drying

Freeze drying is one of the effective techniques to remove the water content from the sample while maintaining the original structure and fabric of the clay specimen (Osipov and Sokolov, 1978).

In this study, freeze-drying was carried out at the chemical labs of Politecnico di Torino (DISAT Department). The specimens of cubic shapes of around 10 mm were prepared. Initially, the specimens were immersed in a baker filled with nitrogen for the first freezing, having a temperature of -196°C. Freeze drying was then completed under vacuum for two cycles. The primary cycle of freezing was carried out at -45°C for 60 minutes and the second cycle of freeze drying was carried out at -10°C overnight. The temperature was then gradually increased to 10°C and 20°C the next morning. After freeze drying, the samples were wrapped in plastic containers and stored in a vacuum jar where salts were present at the bottom of it. The salt at the bottom of the jar creates a suction of around 200 MPa making it completely dry. This is important when the freeze-dried samples are planned to be investigated (e.g., by SEM or MIP) after a certain time.

4.7 Scanning Electron Microscope

A scanning electron microscope (SEM) is a type of electron microscope that produces images of a sample by scanning the surface with a focused beam of electrons. The electrons interact with atoms in the sample, producing various signals that contain information about the sample's surface topography (Goldstein et al., 2017).

Figure 4.14 shows the typical scheme of a SEM setup, which contains the electron gun including an electron source and accelerating anode, electromagnetic lenses to focus the electrons, and a vacuum chamber housing the specimen stage.

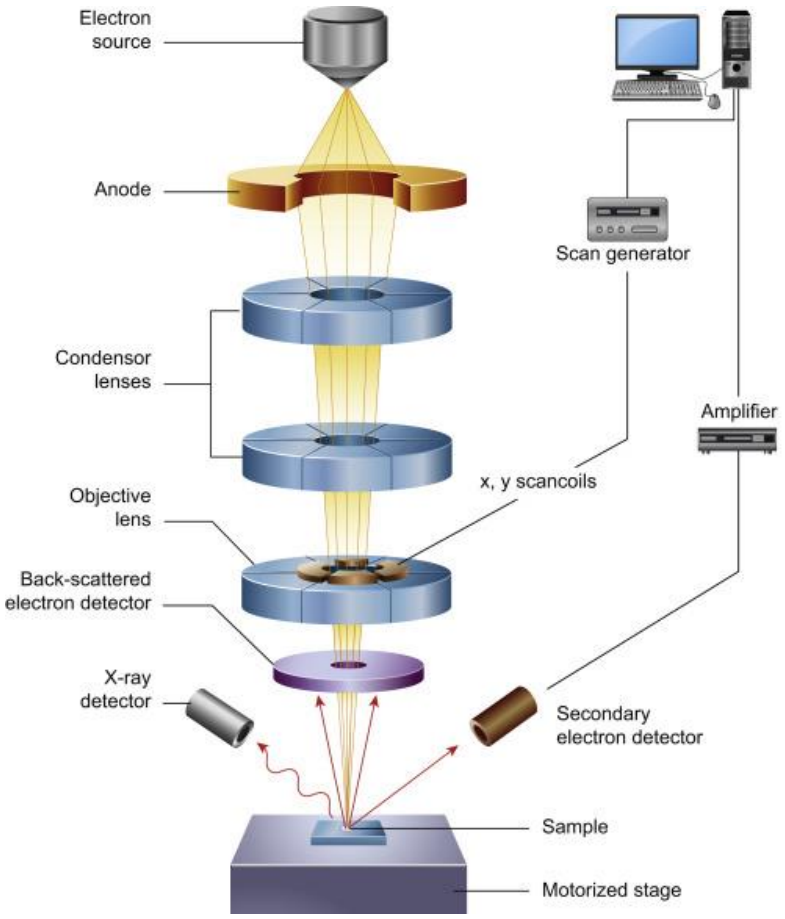

Figure 4.14 Schematic diagram of the core components of an SEM microscope (Inkson, 2016).

The electron microscope can reveal clay particles and their arrangements directly. The smaller object observable with SEM has a size of about 10 nm. However, lesser magnification is sufficient to resolve details of clay particles and other very small soil constituents (Mitchell & Soga, 2005). SEM magnifications range between 20X and 20000X therefore allowing to study the surfaces directly.

Electron microscopy requires an evacuated sample chamber. It is usually necessary to coat SEM sample surfaces with a conducting film to prevent surface charging and loss of resolution. Gold in a very thin layer (20 to 30 nm) in a vacuum evaporator is often used. In this study, gold-coated specimens were studied up to 20000X magnification. The freeze-dried samples with a size of around 8-10 mm were used and SEM photographs were obtained for reconstituted and intact samples after the treatment of CO_2 with the help of thin sections.

4.8 Mercury Intrusion Porosimetry

Mercury Intrusion Porosimetry (MIP) is a widely used technique for characterizing the pore structure of porous materials and providing detailed information on pore size distribution (Sridharan & Venkatappa rao., 1972).

The method relies on the non-wetting nature of mercury, which requires external pressure to penetrate into the pores of a material. By systematically increasing the applied pressure, the volume of mercury intruded into the pores is measured, allowing for the calculation of pore diameter based on the Washburn (1921) equation.

$$P = -\frac{4\gamma \cos\theta}{d} \qquad 4.2$$

where P is pressure, γ is the surface tension of the liquid (mercury in this case), θ is the contact angle of the liquid, and d is the diameter of the capillary. Mercury must be forced using pressure into the pores of a material. The porosimetry measures the total volume of mercury injected into the pores of the sample and the pressure applied to achieve this. Thus, when the pressure is increased, the pore size for each pressure increment is calculated while the volume of mercury required to fill these pores is measured. The pressure applied to the mercury at each increment gives information on the size of the pores and the total volume of mercury injected provides information on the porosity of the sample.

Romero and Simms (2008) presented the main limitations of MIP:

a) isolated pores enclosed by surrounding solids are not measured although this enclosed porosity might not be significant in soils;
b) pores that are accessible only through smaller ones (constricted porosity) are not detected until the smaller pores are penetrated;
c) the apparatus may not have the capacity to enter the smallest pores of the sample (non-intruded porosity);
d) the minimum practical pressure of the apparatus limits the maximum pore size to be detected (non-detected porosity).

In this way, when the clay sample is intruded by mercury, the intruded void ratio estimated under the maximum applied pressure does not coincide with the estimated void ratio of the sample. Differences mainly arise due to the non-intruded porosity. In addition, the intrusion (pressure increase) and extrusion (pressure decrease) cycles do not close when the initial pressure is restored, indicating that some mercury has been permanently entrapped in the constricted porosity.

The MIP analysis for this study was carried out at ENI E&P using AutoPore IV 9500 by micro metrics. It can measure pore sizes from as small as 3 nm to as large as 360 μm with a maximum pressure of up to 414 MPa.

4.9 XRD analysis and mineralogical analysis

X-ray diffraction is a commonly used technique for the identification of fine-grained soil minerals and their crystal structure. XRD provides valuable insights into the mineral composition and structural properties of soils.

Generally, the production of X-rays is achieved by the use of sealed tubes, rotating anodes or synchrotron radiation sources. The production of X-ray radiation in synchrotrons is generated by bunches of electrons or positrons which circulate at relativistic energies close to the speed of light (Epp, 2016). High energy electrons are produced by a high power electron gun and then it is injected into a booster ring for acceleration. The electrons are then introduced in a storage ring where the synchrotron radiation is produced. The high energy range (up to 500 keV or more) permits to measure through samples of several mm or cm in thickness.

Bragg's law (Bragg, 1913) forms the basis for the identification of crystals using X-ray diffraction. Since no two minerals have the same spacings of interatomic planes in three dimensions, the angles at which diffractions occur (and the atomic spacings calculated from them) can be used for identification.

$$n\lambda = 2d \sin\theta \tag{4.3}$$

where λ is the wavelength of striking X-ray at an angle θ to parallel atomic planes spaced at distance d.

X-ray diffraction is particularly well suited for the identification of clay minerals because the spacing is characteristic for each clay mineral group. The basal planes generally give the most intense reflections of any planes in the crystals because of the close packing of atoms in these planes. The common nonclay minerals occurring in soils are also detectable by X-ray diffraction (Mitchell & Soga, 2005). Because the small size of most soil particles prevents the study of single crystals, use is made of the *powder method* and oriented aggregates of particles. In the powder method, a small sample containing particles at all possible orientations is placed in a collimated beam of parallel X-rays, and diffracted beams of various intensities are scanned by a Geiger,

proportional, or scintillation tube and recorded automatically to produce a chart showing the intensity of diffracted beam as a function of angle 2θ.

4.9.1 Sampling and Preparation

The X-ray diffraction analyses were performed at ENI E&P. The X-ray Powder Diffraction (XRD) instrument used for this study is a Panalytical CubiX equipped with a CuKα (λ=1.54178Å) radiation source and a Fast Detector (PANalytical Srl., Lissone Italy). CubiX is specially made for industrial applications providing high-speed phase analysis and high-quality control. The instruments are generally composed of an X-ray source, primary and secondary optics, a goniometer, a sample holder, and a detector (Epp, 2016).

Generally, 5-6 g of rocks or soils are grinded to a fine powder. Then, the powder is pressed in a special sample holder and analysed. It is possible to introduce into the instrument up to 30 samples that can be analyzed in sequence.

Data are collected in two spectral intervals:

(i) bulk analysis: 3°≤2θ≤70° with steps of 0.02°2θ and accumulation times of 25s/step (~12 min/sample).

(ii) clays fraction < 2μm: 2°≤ 2θ ≤ 30° with step of 0.02°2θ and accumulation times of 25 s/step (~5 min/sample).

The diffraction pattern contains plenty of peaks over the complete 2θ range, showing varying and partially overlapped intensity. In order to identify the present phases and quantify their respective amounts, the different methods of qualitative and quantitative phase analysis can be employed. Once a diffraction pattern has been measured, a qualitative phase analysis can be performed. In order to identify the present phases, a comparison of the present diffraction peaks with known data from a database has to be performed.

The phase identification is made by a search-match procedure comparing the position and the relative intensity of the reflections with the data contained in a reference database.

4.10 CT scan

X-ray computed tomography Scan (CT scan) has largely been used in the medical field. It is a powerful nondestructive probing technique for mapping the internal structure of objects. CT scan allows the construction of a three-dimensional density profile inside a material by assembling X-ray radiographic two-dimensional

images taken at different angles (Hanke et al., 2016). In geotechnical engineering, it is possible to investigate the key aspects of soil fabric such as particle orientation, and void ratios e.g., Otani et al., (2000), Desrues et al. (1996) and Vlassenbroeck et al. (2006).

In CT scan an incident beam of electromagnetic radiation (x-rays or gamma rays) passes through an object and is collected with an array of detectors; the object is rotated such that the beam probes from several angles to collect attenuation data and produce the equivalent of a "slice" through the region of interest. The attenuation information collected during the rotation is then used by a computer program to reconstruct a slice image of the internal structure. A general scheme of CT scan equipment is shown in Figure 4.15.

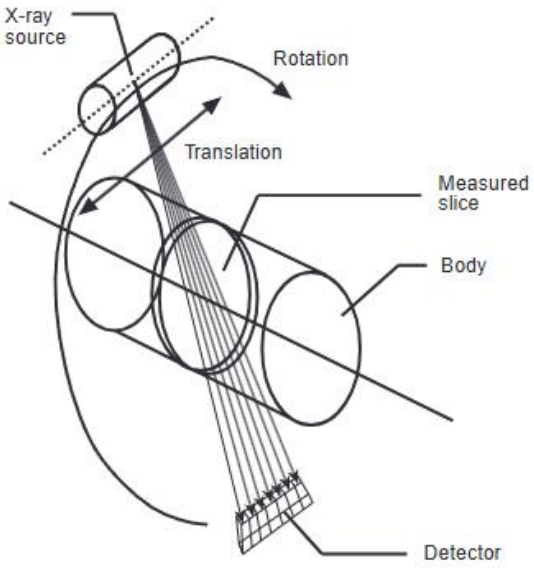

Figure 4.15 CT scan is based on the recording of a set of attenuation profiles of a collimated X-ray beam through a body (Desrues et al., 1996).

The measurement of attenuation which results from CT is predominantly proportional to the electron density of the material under inspection. If the material has a uniform chemical composition, the measurement is proportional to the local mass density of the object. The apparatus can also be calibrated with materials of known densities and a calibration line is obtained for the specific scanner as done by Desrues et al. (1996).

For this study, the CT scans were carried out at ENI E&P. A medical CT scanner from Toshiba Aquilian S16 was used for this purpose. The scanner can take 32 scans per second and generate tomography. The X-ray high-voltage generator is built into the gantry, and the system employs a high-frequency inverter for

generating and stabilizing the high voltage supplied to the X-ray tube. The voltage range is 80-150 kV and current is 10-500 mA. The generator includes electronic circuits for controlling the speed of the rotating anode in the X-ray tube. The use of a high-frequency inverter system results in high power output combined with excellent stability.

4.11 Equivalent Calcite Content tests and equipment

The Equivalent Calcite Content (ECC) (providing a measure of the carbonate minerals in terms of the stoichiometric percentage of calcite, $CaCO_3$) of the samples, both before and after exposure to CO_2 and acid, was determined using a 'calcimeter', following a method similar to ASTM-D4373-21 (acid dissolution). The calcimeter at Geotechnical Laboratory is shown in Figure 4.16. The conjecture of this method is based on the fact that when a soil containing carbonates reacts with Hydrochloric Acid (HCl), CO_2 is generated. The amount of CO_2 generated depends on the carbonate content in the sample, predominantly calcite and dolomite minerals. At first, the calcimeter is calibrated with geomaterials of a known quantity of calcite content at a given temperature. Later these calibration curves are used for the determination of equivalent calcite content of the samples.

The soil sample for ECC determination was prepared through pulverizing and passed through sieve number 40. The sample was inserted into the cylinder shown in Figure 4.16 (labelled as Soil+HCl). The amount of pulverized soil used for each determination was between 0.2-0.6 grams. HCl of 5 molarity (5M) was then added to the cylinder in a small cup to avoid any reaction before air-tightening the cylinder with a cap. After closing the cylinder with the top cap, the soil and HCl present in the cylinder were mixed. This produces CO_2 which passes through the spiral tube and forces the water in the long burette on the right hand side of the stand to move down as shown with red arrows. The soil and HCl were stirred until there was no further movement of the water level in the tube. The burette on the left hand was then brought to the level of water in the burette on the right hand. The volume of water thus displaced by CO_2 was noted. The equivalent calcite content was then determined using the calibration line of the instrument at testing temperature and pressure conditions i.e., T=22°C and p≈101kPa (760mmHg).

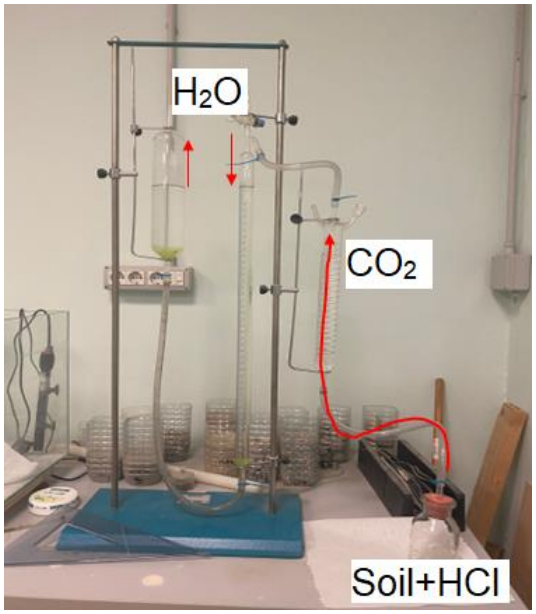

Figure 4.16 Calcimeter used for determining the equivalent calcite content.

4.12 Conductivity and pH meter

The electrical conductivity (σ) and pH of different fluid solutions used in the study were measured using SevenMulti S40, a conductivity meter by Mettler Toledo. The apparatus is a professional-grade instrument designed for precise electrochemical measurements, including pH, conductivity, and ion concentration.

It supports up to five calibration points. The device has also the capability to record data over time. Figure 4.17 shows the conductivity meter with two probes for electrical conductivity and pH. It is important to clean the probes very well with distilled water before using them for the next solution.

Figure 4.17 Conductivity-meter from Meter Toledo used for electrical conductivity and pH measurements.

4.13 Measurements of water potential with WP4C

WP4C Dewpoint PotentiaMeter by Decagon was used to measure the water potential in soil samples and liquids. It uses chilled mirror dew point technique to determine the relative humidity of the air above a soil sample conforming ASTM D6836–16. The WP4C measures the sum of the osmotic and matric potentials in a sample. Figure 4.18 shows the WP4C psychrometer with a digital screen on the left and the sample chamber in the bottom right corner.

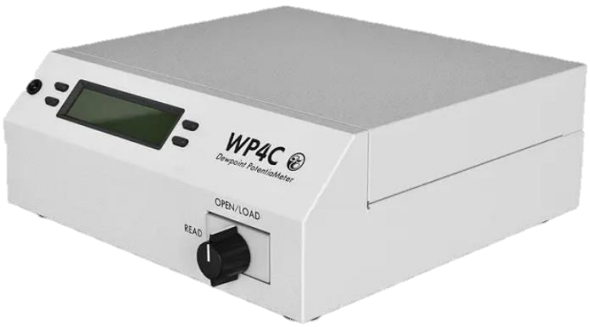

Figure 4.18 Front view of WP4C dewpoint psychrometer used for the total potential of samples.

A liquid of up to 7 ml or soil sample is placed in the sample chamber in a sample cup, which is sealed. Inside there is a sensor block which contains a dew point sensor, a temperature sensor, and an infrared thermometer which measures the sample

temperature. The WP4C measures water potential by equilibrating the liquid phase water of the sample with the vapor phase water in the headspace of the closed chamber, then measuring the vapor pressure of that headspace. The relationship between the sample's water potential (Ψ) and the vapor pressure of the air is:

$$\Psi = \frac{RT}{M} \cdot \ln \frac{p}{p_0} \qquad 4.4$$

where p is the vapor pressure of the air, p_0 is the saturation vapor pressure at sample temperature, R is the gas constant (8.31 J/mol K), T is the temperature of the sample, and M is the molecular mass of water. The vapor pressure of the air can be measured using the chilled mirror, and p_0 is computed from sample temperature.

The WP4C psychrometer has a measurement range between 0.1-300 MPa with a resolution of 0.1 kPa and an accuracy of 1%. The instrument has two modes of measurement. The precise mode has higher accuracy with higher measurement time as compared to the fast mode of measurement. Table 4.2 shows some of the characteristics of the WP4C psychrometer.

Table 4.2 Characteristics of WP4C psychrometer (Decagon Devices, Inc., 2010)

WP4C psychrometer	
Measurement Principle	Chilled-mirror dew point measurement
Measurement Range	-0.1 to -300 MPa
Resolution: Soil Water Potential	0.1 kPa
Resolution: Soil Temperature	0.1°C
Accuracy	±0.05 MPa from 0 to -5 MPa 1% from -5 to -300 MPa
Measurement Time	Precise mode: 10-15 minutes Fast mode: <5 minutes (reduced accuracy)

4.14 Determination of the electrical conductivity of homogeneous soil samples

The electrical conductivity of a homogenous soil sample can be determined using a 1D electrical conductivity measurement. For this purpose, a four-electrode scheme was employed, as shown in Figure 4.19 in which the electric current (I) is injected through a pair of electrodes (A and B) and the potential difference (ΔV) is measured by another pair of electrodes (M and N).

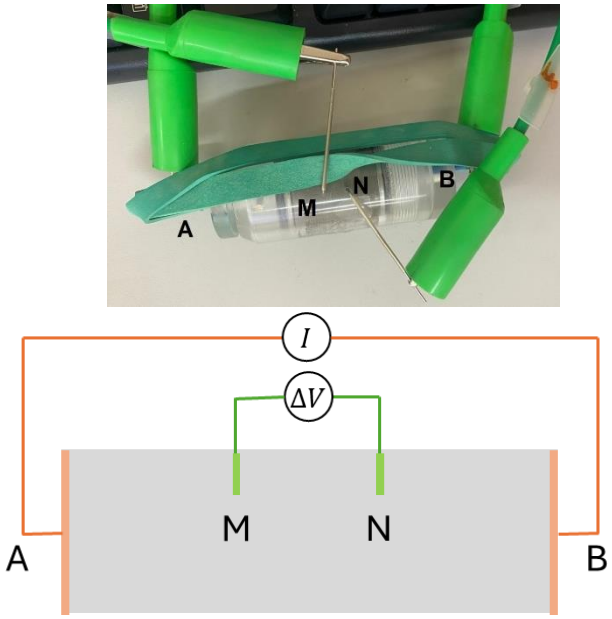

Figure 4.19 1D electrical conductivity measurement with 4 electrodes scheme.

The electrodes A and B are circular and a rubber band was used for a better connection with soil samples. The electrodes M and N are wires which are inserted into the sample as shown in Figure 4.19. The resistance was measured with Complex Impedance Tomography (presented in Section 4.16) and the resistivity ρ determined by Pouillet's law.

$$\rho = R\frac{A}{l} \tag{4.5}$$

where ρ is the resistivity of the material, A is the cross sectional area of the sample and l is the length of the sample between M and N. The electrical conductivity of the sample can be calculated by σ = 1/ρ.

4.15 Advanced oedometer

One of the objectives of this research is to study the effect of geochemical reactions due to CO_2 sequestration on the mechanical behavior of Italian carbonatic stiff clay. An acid solution with a pH of 2 was used to force the chemical reaction, thus enhancing the dissolution that occurs in reduced testing times. A 0.01 M solution of HCl was used to this extent. To study the short-term effect of CO_2 injection an advanced oedometer was designed and developed for the flowthrough experiments. The oedometer is equipped with electrodes for Electrical Resistivity Tomography (ERT) and ultrasonic wave transducers.

The conceptualization and development of the advanced oedometer was carried out at the DISEG department at Politecnico di Torino, and it is an enhanced version of the EIT oedometer described in Comina et al. (2008). The advanced oedometer was built with a corrosion resistant INOX AISI 304, enabling it to withstand the harsh conditions of low pH solutions. The oedometer is equipped with 16 electrodes for Electrical Resistivity Tomography (ERT) and ultrasonic wave transducers and piezoelectric transducers for ultrasonic wave testing. Complex Impedance Tomography (Section 4.16) was used for the injection of current for ERT. The oedometer can host a sample having a diameter of 50 mm and a maximum height of 25 mm. The load is applied through a piston installed on the top cap (Figure 4.20).

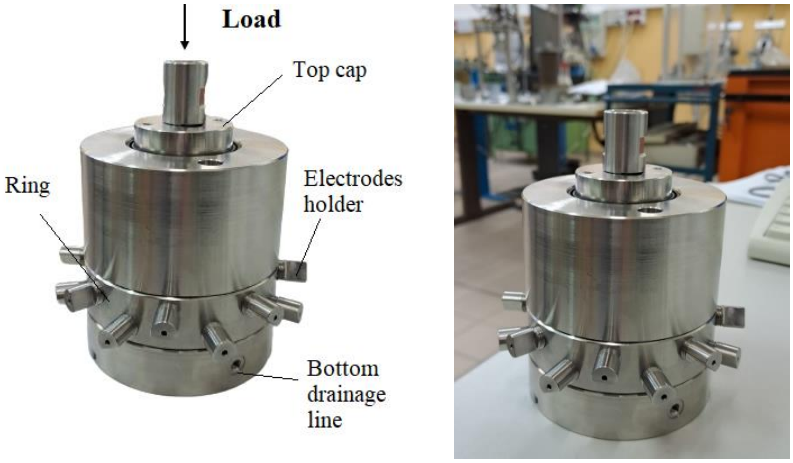

Figure 4.20 Setup of the advanced oedometer.

Drainage paths are provided at the bottom and top of the oedometer for the advection of fluids and pore pressure controls. The setup and calibration of this advanced oedometer are discussed in Chapter 8.

4.16 Complex Impedance Tomograph

Electrical Resistivity Tomography (ERT) is a tomography technique which aims at assessing the electrical conductivity distribution within a body, starting from electrical measurements taken from its periphery using electrodes. ERT can be used to image subsurface soil and rock properties, such as porosity, water content, and clay content. It also has vast applications in environmental geotechnics, hydrology, and other soil sciences such as agriculture. Cosentini et al. (2012) have listed some of the geotechnical engineering applications at laboratory scale, where besides allowing imaging of the sample, ERT can be used to track evolutions of the sample degree of saturation (Cosentini et al., 2012) or changes in the pore fluid composition (e.g. Comina et al., (2011). For the ERT measurements, four electrodes scheme is used where current is injected with two

electrodes and potential is measured at other electrodes.

The Complex Impedance Tomograph (CIT) was used to inject electrical current from two electrodes and acquire the electrical potential from two others (Comina et al., 2008). It is manufactured by Iridium Italy and has the ability to acquire measurements at high rates up to 2.5 kHz. This speed allows precise monitoring of water content or concentration changes during transient laboratory tests. The characteristics of CIT are summarized in Table 4.3.

Table 4.3 Complex impedance tomography characteristics.

Complex Impedance Tomograph	
Maximum output current	±250 mA
Maximum output voltage	± 50 V
Operative frequencies	0.1 to 2500 Hz
Acquisition channels	48
Resolution on phase angles	≈1 mrad
Resolution on voltage	100 μV
Resolution on current	10 μA
Input impedance	200 MΩ

A digital direct synthesiser is used for the generation of the A.C waveform, which is then fed to a voltage-controlled current source and applied via a multiplexer to the pair of driving electrodes. The output impedance of the current source is estimated to be in the range of 200 MΩ, making it possible to drive currents in very resistive media. The tomograph is connected to the oedometer cell through multiplexer as shown in Figure 4.21. In Figure 4.21, CIT is connected to the EIT used in Comina et al. (2008). The tomograph is operated by a computer, which is used to set the excitations and to record experimental data.

For this study, an acquisition rate of 114 Hz was selected because of the low permeability of the samples, changes in the electrical conductivity are expected to occur at a relatively low pace in the tests performed on caprocks.

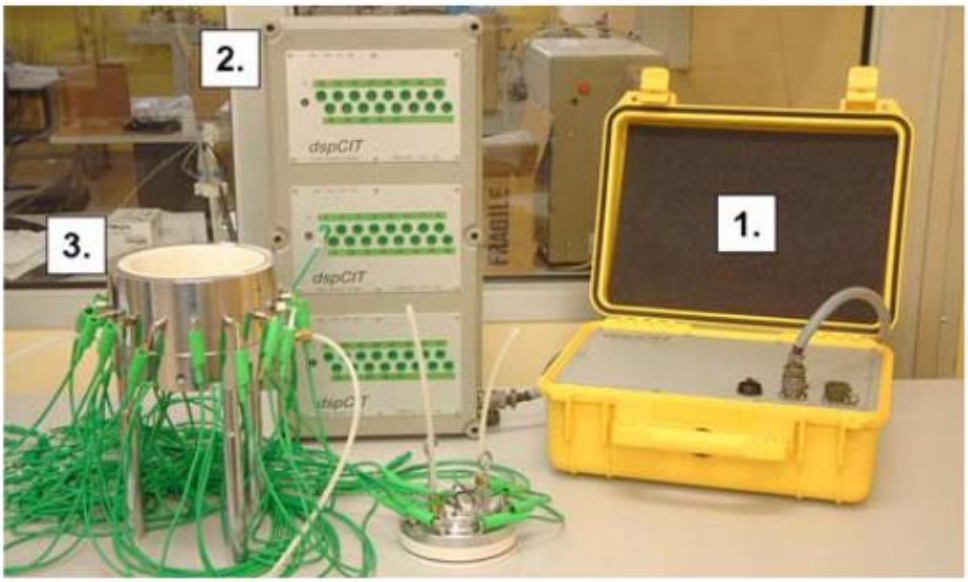

Figure 4.21 Measurement setup of CIT: 1. Complex impedance tomograph. 2. Multiplexers and connection to the cell. 3. EIT oedometer cell from Comina et al. (2008).

Chapter 5 Materials

The response of three Italian clayey caprocks (named Clay A, Clay B and Clay C) to the interaction with CO_2, in various forms, and with an acid solution was studied in this research. The materials under consideration are structured, carbonatic Italian clays from different formations and depths; they all belong to the overburden of existing gas fields originally exploited for hydrocarbon production.

Clay A comes from a field in the onshore Romagna area of Eastern Italy. Clay A was cored from a depth of about 3520 meters: cores were not well preserved, so it was tested only in reconstituted conditions. Clay B was cored from a depth of around 1300 meters from two different wells from a field in the Po Valley. Cores were correctly preserved, so this material was tested both in intact and reconstituted conditions. Clay C was cored from a depth of about 2760 m from a Central Adriatic field, only intact samples were tested from this set of samples. In their intact state, these caprock materials can be described as stiff clays.

Reconstituted samples, in the case of Clay A were tested due to non-availability of intact samples. The study of reconstituted samples could also allow evidencing the role of structure on the coupled chemo-mechanical processes. Therefore, clay B was tested both in natural and reconstituted state.

A series of tests including grain size distribution, Atterberg limits, and XRD analysis were performed for physical characterization. The index properties, equivalent calcite content and mineralogy were determined as well. In this Chapter, the physical and mineralogical characterization of the material is presented.

5.1 Physical and mineralogical characterization of Clay A

5.1.1 Grain size distribution

The Grain Size Distribution (GSD) of Clay A was completed at ENI E&P determined through the laser technique shown in Figure 5.1. The material was obtained by mechanically grinding a disturbed which was not well-preserved sample. According to the British Standard, the GSD revealed a clay fraction of 13%, silt fraction of 72% and

sand fraction of 15 %.

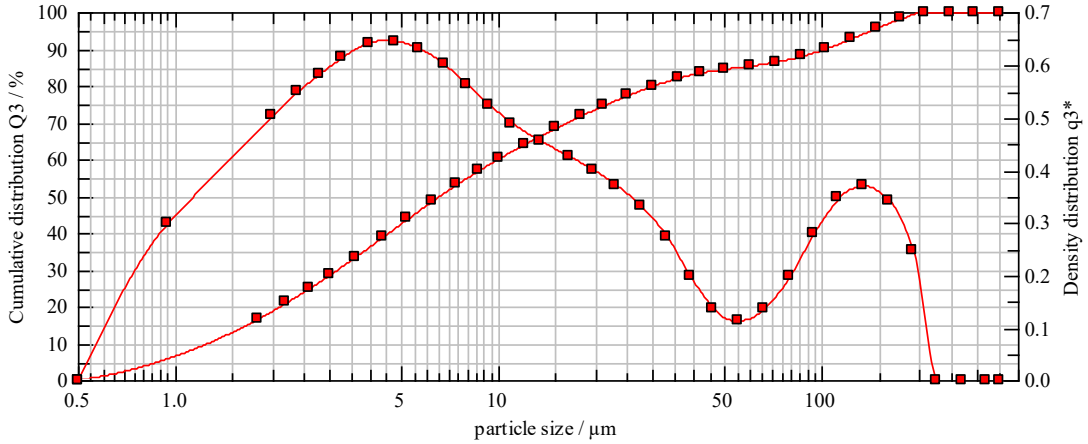

Figure 5.1 Grain size distribution curve for Clay A material.

5.1.2 Index properties and specific gravity

The protocol of ASTM D4318 was used to determine the Liquid Limit (LL), Plastic Limit (PL) and Plasticity Index (PI). The material was oven dried, pulverized to powder and sieved through sieve number 40. The passing fraction was thoroughly mixed with distilled water and a paste was prepared. The liquid limit was determined as LL = 50%, the plastic limit as PL= 28% and the plasticity index as PI = 22%. The activity (A=PI/clay fraction) was determined as A= 1.69.

The specific gravity, G_s, was determined following the protocols of ASTM D792, it was found to be G_s =2.79.

5.1.3 Mineralogy

A representative sample of Clay A was used for X-ray Diffraction (XRD) for mineralogical analysis, performed at the ENI E&P laboratories. Calcite and dolomite were found to be the main minerals, with a mass content of 26.2% and 24.6% respectively. The dominant clay mineral of the sample was illite with a 12.8% mass content, followed by chlorite (6.2%) and kaolinite (3.0%). The results of the mineralogical analysis for Clay A are summarized in Table 5.1 and Figure 5.2. The composition of pore fluid is provided in Table 4.1.

Table 5.1 Mineralogical analysis of Clay A.

Mineral	Mass Content (%)
Kaolinite	3.0
Chlorite	6.2
Illite	12.8
Calcite	26.2
Dolomite/Ankerite	24.6
Quartz	18.4
Plagioclase	6.7
Others	2.1

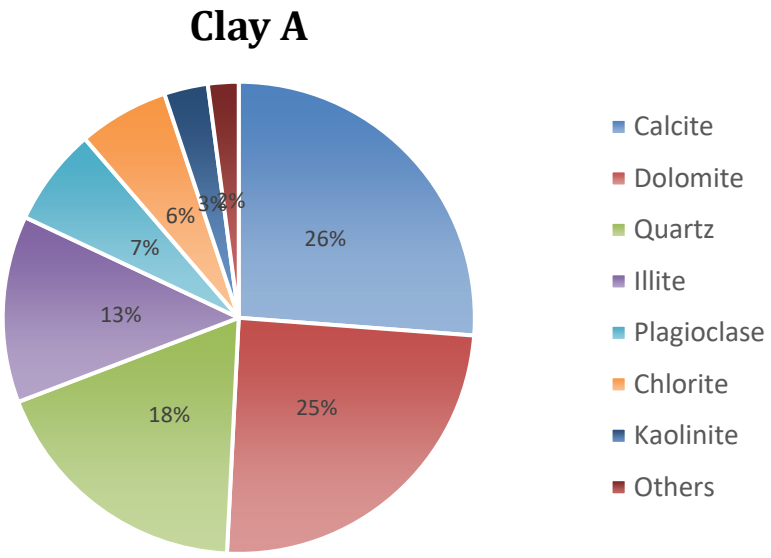

Figure 5.2 XRD analysis of Clay A material.

The Equivalent Calcite Content (ECC) of the samples was determined using the calcimeter introduced in Section 4.11 of Chapter 4. In its original conditions, the ECC of Clay A was found to be 36.8%.

5.1.4 Compression curve of reconstituted Clay A samples

The process of reconstitution was introduced in Chapter 4. The reconstitution was conducted after the clay powder was mixed thoroughly with distilled water at an initial water content of around 1.2-1.5LL. The slurry was then compressed in oedometer conditions to a predefined vertical stress. A sample prepared by this procedure is defined here as "reconstituted", following Burland (1990). Since no intact samples were available for Clay A, therefore, all the samples of Clay A were reconstituted. Figure 5.3 shows as an

example the time-displacement curve for a specimen of Clay A at 8.5 MPa vertical load.

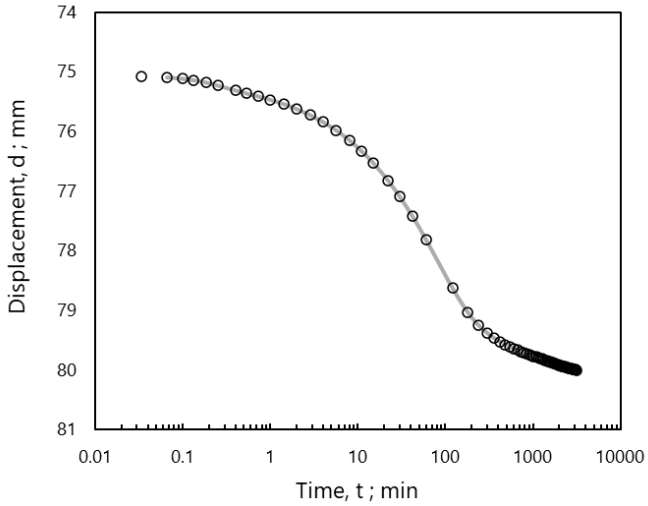

Figure 5.3 Time-displacement curve of Clay A sample at vertical stress of 8538kPa.

Figure 5.4 shows the relationship between void ratio and vertical stress for some of the reconstituted specimens of Clay A. The compression index C_c for Clay A material was found between 0.21 and 0.23.

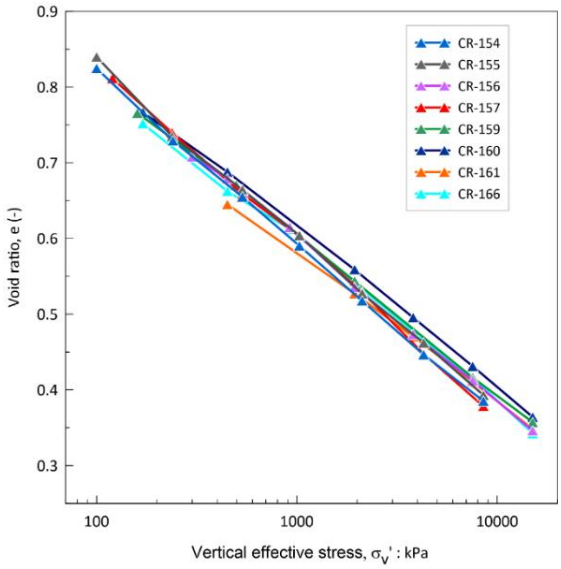

Figure 5.4 Compression curves of reconstituted Clay A samples.

5.2 Physical and mineralogical characterization of Clay B

5.2.1 Initial state of intact Clay B samples

The intact samples from Clay B were analysed for the initial state of the material including

natural water content (w), degree of saturation (S_r), initial suction (ψ) and P, S-wave velocities both from logs and laboratory tests. Ciancimino et. al., (2024) studied the mechanical behavior of intact samples of Clay B in the context of hydrogen storage. The initial state of the samples was determined on cylindrical specimens with a diameter of 10 mm and height of 10 mm which were sub-cored from the undisturbed samples.

Samples were cored so to minimize the disturbance and maintain the original petrophysical and mechanical characteristics of the formation. The coring procedure for this material was detailed by Ciancimino et al. (2024). The coring was performed with a hydrolift-type total closure system, aluminum inner barrels 4 ¾" x 4 ¼" (Outer Diameter x Inner Diameter) x 32 feet with a pressure relief valve suitable for preventing possible damage in the event of undesired gas expansion during extraction. The core bit was of the face discharge type, for soft or moderately consolidated formations. This process minimizes contact between the drilling mud and the core. Additionally, a low invasion PCD (Poly-Crystalline Diamond) core head was used for soft or moderately consolidated formations. After the coring was completed, the cores were immediately stabilized by sealing them with foam. They were then carefully transported to the laboratory, where samples were sub-cored for testing.

Water content of the material was determined by oven-drying samples at 110°C for 24 hours. The natural water content (w_o) was found to vary between 12.8% and 14.3%. The void ratio (e) of the specimens varied between 0.37 and 0.42, with a corresponding initial degree of saturation S_r of 0.92 to 0.98. The composition of pore fluid for Clay B is summarized in Table 5.2.

Table 5.2 Composition of pore fluid of Clay B (mg/l).

Ca	Mg	Cl	Na	K	SO_4	HCO_3
2384	1242	46718	25081	136	23	114

The in-situ stress conditions of Clay B were also investigated by Ciancimino et al. (2024). The authors determined the vertical total stress at the depth of recovery from the integration of density logs and it was found to be σ_v = 25.90 MPa. The in-situ pore pressure was determined from direct borehole measurements (taken at the most permeable soil layers) along with analysis of sonic and density data at the depth of interest by identifying normal compaction trend lines through mathematical regression (Eaton & Eaton, 1997). The final value of pore pressure resulted in 13.62 MPa. The horizontal stress components were determined from leak-off and break-out analyses (Scelsi et al., 2019) and resulted in isotropic values between σ_{h1}=19 MPa and σ_{h2}=20 MPa.

A preliminary check on the sample quality/conservation was run by comparing the sample suction with the one theoretically induced by an ideal coring operation. The ideal undrained coring shall induce a matric suction in the specimen which is roughly equal to the initial mean effective stress (8 MPa). The matric suction, determined with the filter paper technique (ASTM D5298–16), resulted in 6.59 MPa. It is slightly smaller than the predicted one due to coring, which might depend on the fact that an isotropic stiffness was assumed, while the theoretical suction in the presence of stiffness anisotropy might be higher (Doran et al., 2000). The total suction was also determined using the Decagon WP4C psychrometer and a value of 8 MPa was obtained.

Water retention behavior of the intact sample was studied using vapor equilibrium technique (see e.g., Delage et al., 1998). Small specimens were cut from undisturbed sample and placed in sealed containers partially filled with saturated saline solutions. These solutions control the air relative humidity of the sealed containers. A total of five different salts were used for this purpose. The total suction imposed by the saline solutions was verified with the WP4C, and the corresponding values are presented in Table 5.3.

Table 5.3 Salts used to obtain the water retention curve.

Saturated salt solution	**Total suction ψ (MPa)**
K_2SO_4	5.08
$BaCl_2{\cdot}2H_2O$	14.27
KCl	22.72
NaCl	38.73
$NaNO_2$	59.10
$CaCl_2{\cdot}6H_2O$	159.09

The weight of the sample was recorded every day until a constant mass in time is obtained. The gravimetric water content at equilibrium for each suction was used to determine the water retention curve shown in Figure 5.5. The initial condition (ψ = 8 MPa) of the samples lies slightly above the water retention measurements, suggesting that a small hysteretic wetting occurred for the sample exposed to the lower suction. The initial total suction seems, however, associated to a saturated state, i.e., the corresponding matric suction should be smaller than the air entry value. The other part of the retention curve appears to belong to the main drying curve. These results indicate that a limited drying occurred during sample storage. However, the very high degrees of saturation and the fact that initial suction compares reasonably well with the one predicted theoretically, suggest that no significant change has occurred in their fabric during the coring and storage stages (Ciancimino et al., 2024).

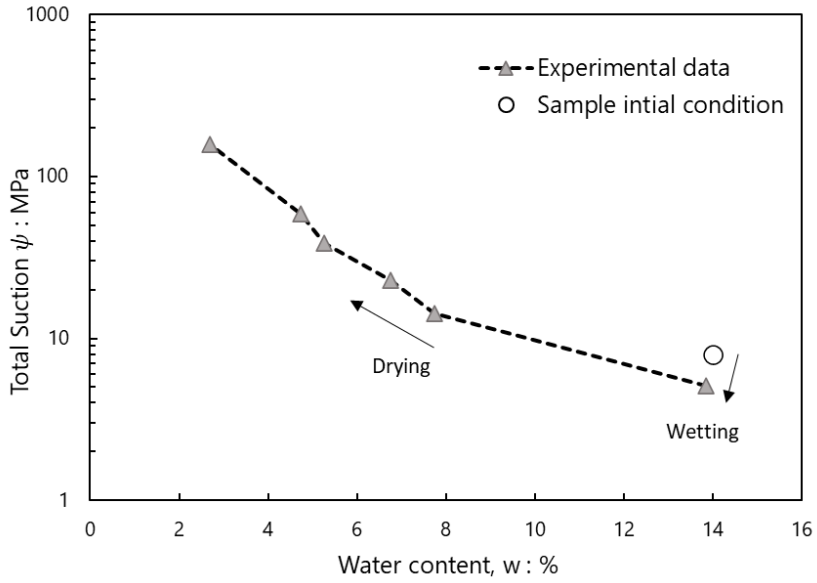

Figure 5.5 Water retention plot of intact sample of Clay B material (Ciancimino et al., 2024).

The sound preservation of the sample was also confirmed by the comparison between P and S-wave velocities at small strains as shown in Figure 5.6. It shows the comparison between in-situ and laboratory ultrasonic wave velocity values. The laboratory waves, shown with filled circles, were measured in Medium Pressure Triaxial Apparatus (MPTA) during triaxial tests at stresses comparable to that of in-situ ones. The in-situ measurement of P and S waves was obtained by sonic logs conducted within the caprock formation, in a well located approximately 150 m from the one from which the samples were taken (Ciancimino et al., 2024).

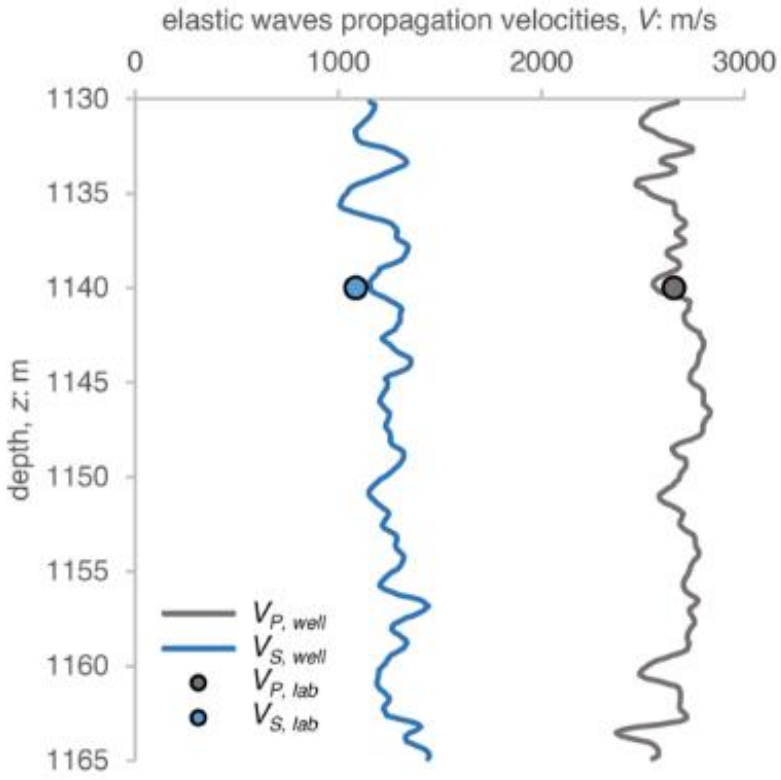

Figure 5.6 Comparison between laboratory P- and S-wave ($V_{P\ lab}$ and $V_{S,\ lab}$) velocities with wellbore sonic logs $V_{P,\ well}$ and $V_{S,\ well}$ (Ciancimino et al., 2024).

5.2.2 Grain size distribution

The GSD of Clay B was conducted at the Geotechnical Laboratory of Politecnico di Torino. The GDS showed a clay fraction of 50%, a silt fraction of 49% and a sand fraction of 1%. The GSD curve of Clay B is shown in Figure 5.7.

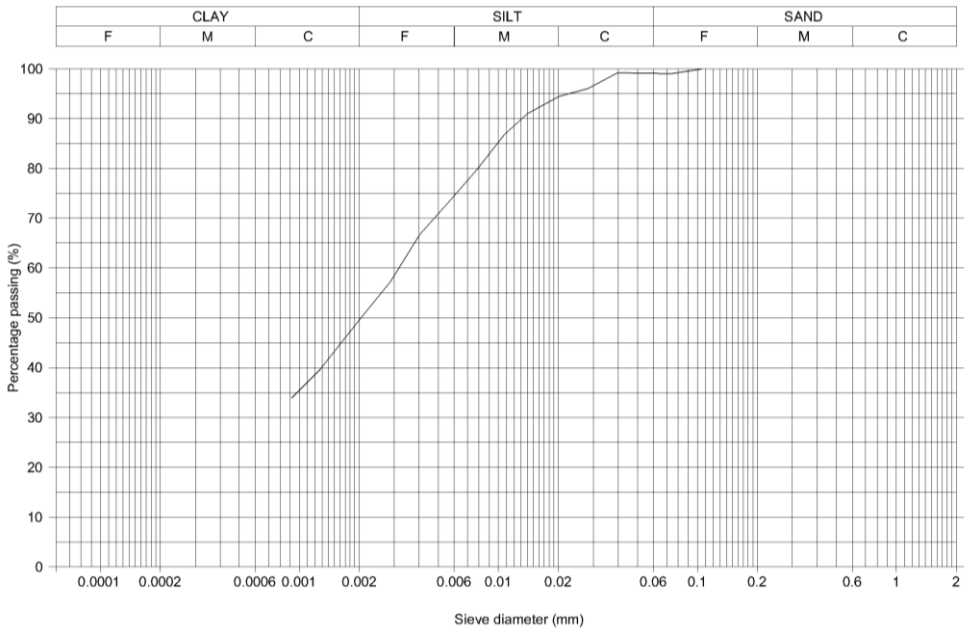

Figure 5.7 Grain size distribution curve for Clay B material.

5.2.3 Index properties and specific gravity

The LL of Clay B was found to be 43%, the plasticity limit was PL=25% and the plasticity index PI=18%. The natural water content measured on the preserved sample was around 14%. The activity was A=0.37.

The specific gravity of Clay B was found to be Gs = 2.78.

5.2.4 Mineralogy

The mineralogical analysis of Clay B was performed on different samples proceeding from depths ranging from 1329 to 1334 m. For these specimens, the dominant clay mineral by mass fraction was illite (26.2%), followed by kaolinite (6.3%) and chlorite (3.8%). The analysis showed a calcite content of 28.1%, dolomite content of 10.7% and quartz of 15.4%. The mineralogical analysis results for Clay B material are summarized in Table 5.4 and Figure 5.8.

Table 5.4 Mineralogical analysis of Clay B

Minerals	Mass content (%)
Calcite	28.1
Dolomite	10.7
Quartz	15.4
Plagioclase	7.3
Illite	26.2
Kaolinite	6.3
Chlorite	3.8
Others	2.2

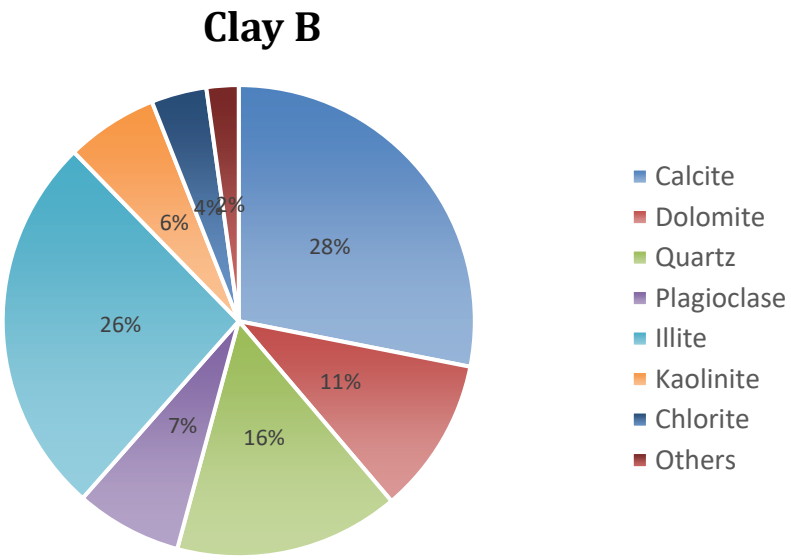

Figure 5.8 XRD analysis of Clay B material.

The ECC of 11 Clay B samples at different depths was found to range between 31% and 44% and is shown in Table 5.5.

Table 5.5 Equivalent Calcite Content of different Clay B specimens.

Well	Depth (m)	ECC (%)
Well 0	1332.5-1332.6	39.3
Well 0	1332.4-1332.5	40.9
Well 0	1334.5-1334.6	32.8
Well 0	1333.5-1333.6	35.6
Well 0	1331.45-1331.55	43.2
Well 0	1332.5-1332.6	41.9
Well 0	1333.5-1333.6	36.6
Well 0	1334.5-1334.6	31.6
Well A1	1299.37-1299.6	34.9
Well A1	1299.37-1299.6	34.3
Well A1	1299.6-1299.8	33.6

5.2.5 Compression curve of reconstituted Clay B samples

Some samples of Clay B were also reconstituted for both batch reactions and flowthrough experiments following the procedure of reconstitution. Figure 5.9 shows the relationship between void ratio and vertical stress for some of the reconstituted Clay B specimens. The compression index C_c for Clay B was found to vary between 0.25 and 0.29.

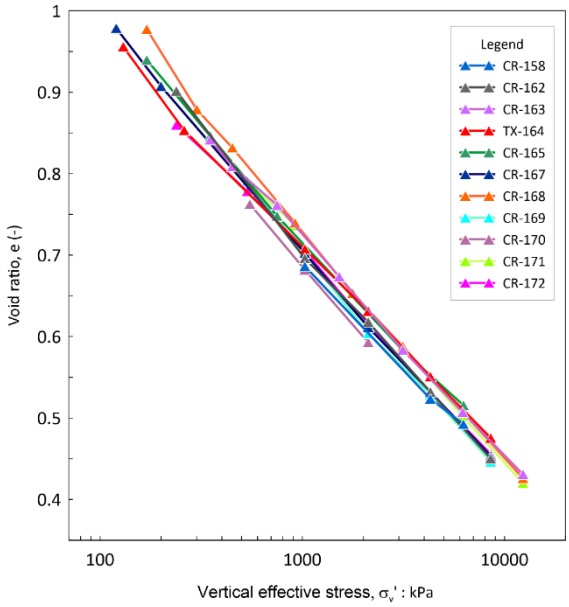

Figure 5.9 Compression curves of reconstituted Clay B samples.

5.3 Physical and mineralogical characterization of Clay C

5.3.1 Initial state of intact Clay C samples

The initial state of intact Clay C samples including natural water content was determined. The water content was determined by oven-drying the specimen at 105° C for around 24 hours and was found to be 13.5%.

5.3.2 Grain size distribution

The GSD of the Clay C was performed on a sample cored from 2754.4 m depth. It was done at ENI E&P determined through the laser technique as shown in Figure 5.10. According to the British Standard, the GSD analyses revealed a clay fraction of 54% and a silt content of 46%.

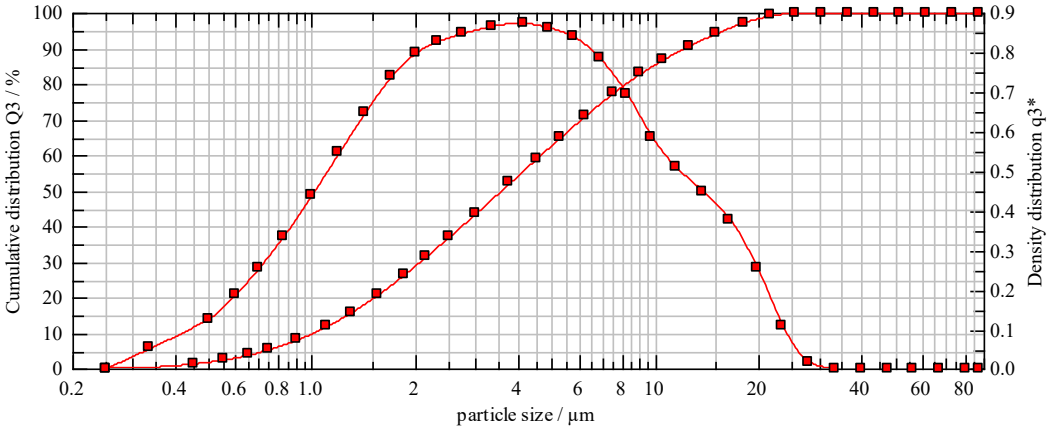

Figure 5.10 GSD of the Clay C performed at material from a depth of 2754.4 m.

5.3.3 Index properties

The LL of Clay C was found to be 48%, the PL 27% and the plasticity index PI=21%. The activity (A=PI/clay fraction) was determined to be A= 0.39.

5.3.4 Mineralogy

A representative sample of intact samples was used for X-ray Diffraction (XRD) for mineralogical analysis, which was performed at the ENI E&P laboratories. Calcite is the most abundant carbonate mineral by mass fraction (39.7%), followed by dolomite (8.8%). Illite is the main clay mineral with 17.0%, followed by muscovite (6.0%) and kaolinite (3.1%). The mineralogical composition of Clay C is summarized in Table 5.6 and Figure 5.11.

Table 5.6 Mineralogical characteristics of Clay C.

Minerals	Mass content (%)
Calcite	39.7
Dolomite	8.8
Quartz	19.1
Plagioclase	2.5
Illite	17.0
Kaolinite	3.1
Chlorite	0.6
Muscovite	6.0
Others	3.3

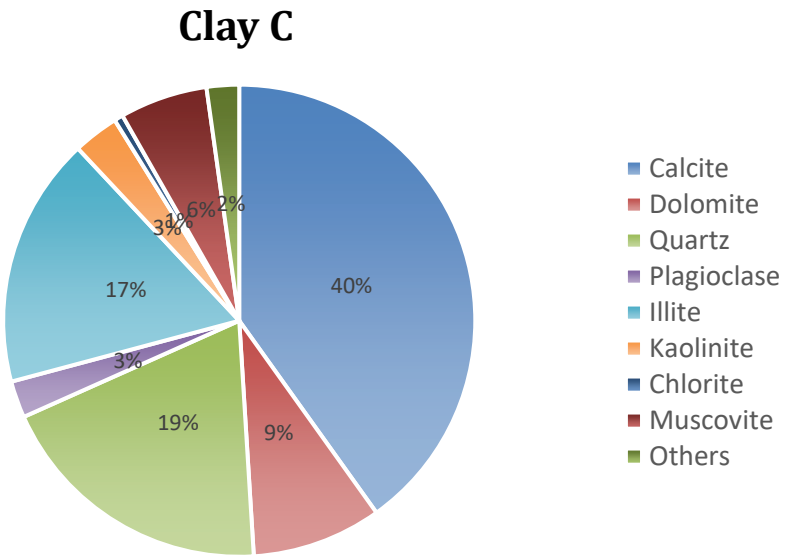

Figure 5.11 Mineralogical analysis of Clay C.

The ECC of the Clay C resulted in a value of 35.1%.

Chapter 6 Effects of CO_2 exposure on mineralogy and fabric

The effects of CO_2 exposure on the microstructure and mineralogy of caprock samples were investigated in this research. Reconstituted and intact samples and soil slurries were exposed to different forms of CO_2 including dry $scCO_2$, wet $scCO_2$ and CO_2 saturated brine. Microstructural and mineralogical analyses were carried out on samples before and after exposure, including the investigation of Equivalent Calcite Content (ECC), mineralogy (XRD analysis), Pore Size Density (MIP analysis) and fabric (SEM analysis).

In this Chapter, the experimental program conducted on Clay A and Clay B samples exposed to CO_2 is first introduced. Later the results on the effects of CO_2 exposure on ECC, mineralogy, Pore Size Density and fabric of Clay A and Clay B are discussed. The impact of CO_2 exposure on the sample's mechanical behavior is outlined and discussed in Chapter 7.

6.1 Experimental program

After injection CO_2 flows through the reservoir rock and approaches the caprock through different transport mechanisms. The pressure gradient created by CO_2 injection displaces the brine in the vicinity of the injection well, and a two phase flow takes place here. CO_2 also dissolves into the formation fluid: the dissolved fraction migrates with the formation water carried by advection. The buoyancy of CO_2 due to the density difference between CO_2 and formation fluid forces an interaction of injected CO_2 with caprock.

The injected CO_2 interacts then with the rock (either reservoir or caprock) in different states. The caprock can be divided into 3 zones depending on the form of CO_2 as shown by Figure 3.1 in Chapter 3 from Vafaie et al. (2023). In the zone near injection well, the brine saturated caprock is in contact with dry CO_2 (here dry indicates that no water is dissolved into the CO_2). Next is the zone where water has dissolved into CO_2 (wet CO_2). In the last zone CO_2-rich brine conditions are prevalent (CO_2 is not a separate phase but it has dissolved into the brine) as discussed in Chapter 3. These different forms of CO_2 were used in the 'batch reaction' tests, so to mimic the position in the CO_2 storage site

with respect to distance from the injection well. Samples of two Italian carbonatic clays (Clay A and Clay B) with similar mineralogic composition were used to this extent.

As for Clay A, only reconstituted samples were used. As for Clay B, intact, reconstituted and slurry samples were used. The samples after exposure to CO_2 were mechanically tested in triaxial and oedometer apparatus. Triaxial undrained tests (CK_0U), consolidated at different stress levels including the in-situ one (in the case of Clay B) were conducted. Two oedometer tests at high vertical stresses (up to 25 MPa) were also conducted on Clay B intact samples. As a complement to the mechanical investigation, the experimental campaign also included the study of the effects of CO_2 exposure on microstructure and mineralogy. Changes in microstructure and mineralogical composition were tracked through Scanning Electron Microscopy (SEM), Mercury Intrusion Porosimetry (MIP), Equivalent Calcite Content (ECC) and mineralogical analysis of the material both pre- and post-exposure. The results of the microstructural analysis are presented in this Chapter whereas the results of mechanical tests are presented in Chapter 7.

6.1.1 Sample nomenclature and ID

To characterize the effects imparted by exposure to CO_2, twin samples were generally tested, one referring to the material original state (pre-exposure) and another to the material state after interaction with the CO_2 (post-exposure).

Each sample was assigned an ID which allowed for faster identification of the specimen state and testing conditions. The ID of a test starts with an indication of the type of material. The first letter of the test would be either "A" or "B" indicating Clay A or Clay B material respectively.

The second letter indicates the type of specimen i.e., intact (I), or reconstituted (R). The letter "I" might have the subscript "MF" indicating an intact specimen which had micro-fissures as evidenced by the results of CT scans. This aspect is further explained in Section 6.3.1. The reconstituted samples of Clay B were prepared at three different Over Consolidation Ratios (OCRs) of 1, 1.5 and 3. Therefore, the letter "R" (reconstituted) also carries information on the value of the over-consolidation ratios. Specifically, "R1" for the normally consolidated samples, "R1.5" for the sample reconstituted at OCR=1.5, and "R3.0" for the sample reconstituted at OCR=3.0.

The third letter of the ID gives information on whether the specimen was exposed to CO_2 or not. "N" is used for a specimen that was not treated (non-exposed) and "T" is used for the sample that is treated with CO_2 (exposed specimens). The same temperature and pressure (T=60 °C and p=15 MPa) were imparted in all the batch reaction tests. The

treatment conditions differed on whether dry $scCO_2$, wet $scCO_2$, or CO_2 saturated brine was used. The term "T" further contains this information on CO_2 conditions. For dry $scCO_2$, in subscript, "DCO2", for CO_2-saturated brine, "BCO2" and for wet $scCO_2$ the subscript of "WCO2" is used.

As stated earlier, two different approaches were used for the exposure of Clay B material. In one approach, the intact or reconstituted specimens were exposed to CO_2 (in this case the letter 'S' is used). In another approach the soil powder was prepared at a slurry state and then exposed to CO_2: after exposure the slurry was taken out of the autoclave and the specimens were reconstituted. In this case, the letter 'P' is used. After TS or TP, the exposure period, in days, is provided. For example:

- $T_{DCO2}S14$: is a reconstituted sample exposed to dry $scCO_2$ for 14 days.
- $T_{WCO2}P30$: powder exposed to wet $scCO_2$ for 30 days and then a sample was reconstituted.

The last part of the name provides information on the effective radial stress of the triaxial test (in MPa) at the end of the consolidation stage, before starting the undrained shearing phase. In cases where tests were carried out in an oedometer, the ID contains the term 'Oed' at the end of the ID.

Following the whole nomenclature, a test ID would be as:

A-R1-T_{DCO2}S14-7.5 indicates a reconstituted Clay A specimen with OCR=1. The specimen was exposed to dry $scCO_2$ for 14 days. The sample was then tested triaxially and the radial stress at the end of the consolidation was 7.5 MPa.

B-R1.5-T_{WCO2}P14-6 is a reconstituted Clay B specimen with OCR=1.5. The specimen was reconstituted from powder that was exposed to wet $scCO_2$ for 14 days. The radial stress in the triaxial test at the end of consolidation was 6 MPa.

B-I-T_{WCO2}S14-Oed is an oedometer test conducted on an intact sample of Clay B which was exposed to wet $scCO_2$ for 14 days.

Table 6.1 contains the list of all the specimen used in this study for CO_2 exposure including the non-exposed ones.

Table 6.1 list of tests conducted on exposed and non-exposed clay A and clay B samples.

Test ID	Caged/Uncaged	Notes
Clay A specimens		
A-R1-N-4.25	-	
A-R1-N-7.5 (1)	-	
A-R1-N-7.5 (2)	-	
A-R1-T_{DCO2}S14-7.5	Caged	
A-R1-T_{BCO2}S14-7.5	Caged	
A-R1-T_{DCO2}S14	Uncaged	Dedicated to post-exposure microstructural and mineralogical analyses
A-R1-T_{BCO2}S14	Uncaged	Uncaged sample-not recovered
Clay B specimens		
B-I-N-6		
B-I-N-12		
B-I-T_{WCO2}S30-6	Caged	Intact specimen with no microfractures
B-I_{MF}-T_{WCO2}S30-6	Uncaged	Intact specimen with microfractures
B-I_{MF}-T_{WCO2}S30-6 (1)	Caged	Intact specimen with microfractures
B-I_{MF}-T_{WCO2}S30-12	Uncaged	Intact specimen with microfractures
B-I-T_{WCO2}S30	Caged	Used for microstructural and mineralogical analyses
B-I-N-Oed		Oedometer test pre-exposure
B-I-T_{WCO2}S14-Oed		Oedometer test post-exposure
B-R1-N-3		
B-R1-N-6		
B-R1.5-N-6		
B-R3.0-N-6		
B-R1-T_{WCO2}S30-3	Caged	
B-R1-T_{WCO2}S30-6	Caged	

B-R1.5-T_{WCO2}S30-6	Caged	
B-R1-T_{BCO2}S30-3	Caged	
B-R1-T_{BCO2}S30-6	Caged	
B-R1-T_{WCO2}P14-6		
B-R1.5-T_{WCO2}P14-6		
B-R1-T_{WCO2}P30-6		
B-R1.5-T_{WCO2}P30-6		

6.2 Effects of exposure to CO_2 on fabric and mineralogy of reconstituted Clay A specimens

This section deals with the effects of the exposure to CO_2 on fabric and mineralogy of reconstituted Clay A samples. The list of the characterization carried out is presented in Table 6.2.

Table 6.2 - Different microstructural and mineralogical analyses done on Clay A samples.

Specimen ID	State	Water content	ECC	XRD	SEM	MIP	CT scan
A-R1-T_{DCO2}S14	Original	Yes	Yes	Yes	Yes	Yes	No
	Exposed	Yes	Yes	Yes	Yes	Yes	Yes
A-R1-T_{BCO2}S14-7.5	Original	No	Yes	No	No	No	No
	Exposed	No	Yes	No	No	No	Yes

6.2.1 Effects of exposure to dry $scCO_2$

One of the two specimens of Clay A material exposed to dry $scCO_2$ for 14 days (A-R1-T_{DCO2}S14) was used for post-exposure microstructural and mineralogical analyses. The post exposure analysis included the analysis of ECC, water content, SEM, MIP and XRD on sub-specimens at different heights of the specimen.

After exposure, the specimen A-R1-T_{DCO2}S14 was divided into 4 different sections shown as a, b, c and d in Figure 6.1. These sections were further divided into small specimens to allow for more local microstructural and mineralogical characterizations.

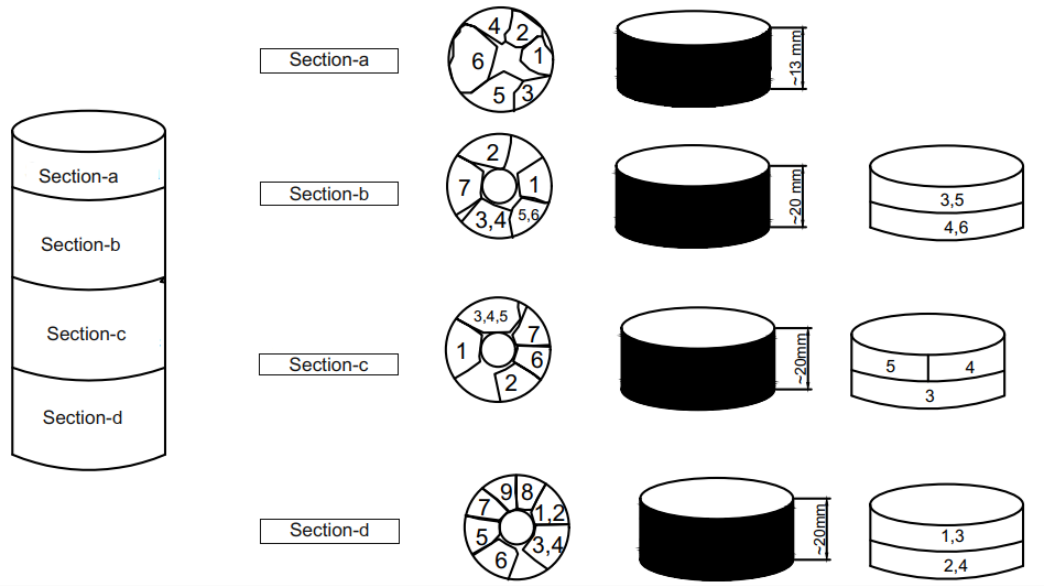

Figure 6.1 Sections and sub-specimens of sample A-R1-T_{DCO2}S14.

The dimensions of the specimens were measured before exposure and post exposure only height of the sample was measured. The vertical strain due to exposure was 0.25%. Similar data on other samples is documented in Appendix D.

Effects on water content and ECC

The gravimetric water content was determined by drying the sub-specimens in the oven at 105°C for around 24 hours. The water content analysis was conducted without considering salt content dissolved in pore fluid. In this case before and after water content was performed on the same sample, neglecting the effects of salts would be pragmatic. After exposure of the specimen to dry $scCO_2$ the water content varied between 4.5% - 5.2%. This represents a significant decrease, as the initial water content of the specimen before exposure was around 14%, as indicated by the dotted line in Figure 6.2. The reduction in water content of the specimen may be due to the introduction of dry $scCO_2$, which evaporates the water from the specimen. The evaporated water at the end of exposure was found at the bottom of the autoclave as shown in Figure 4.8 of Chapter 4.

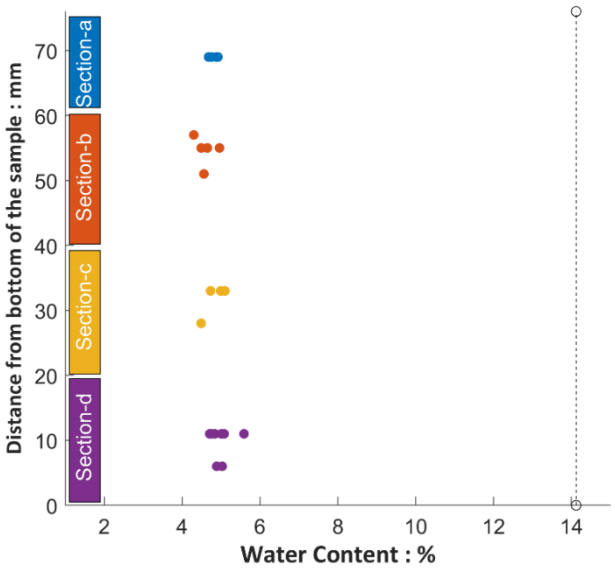

Figure 6.2 Water content along the height of the specimen A-R1-T_{DCO2}S14.

The ECC of the exposed specimen was determined in the calcimeter (Section 4.11). ECC increased passing from the top towards the bottom of the specimen (Figure 6.3). The original ECC of the mixed Clay A powder was around 37%. At the top of the specimen, the ECC values after exposure are about the original, whereas they increase towards the bottom of the sample (ECC=41.6%). It is suggested that the observed trend might be associated to the effects of gravity, evaporation of water and precipitation of carbonates during exposure.

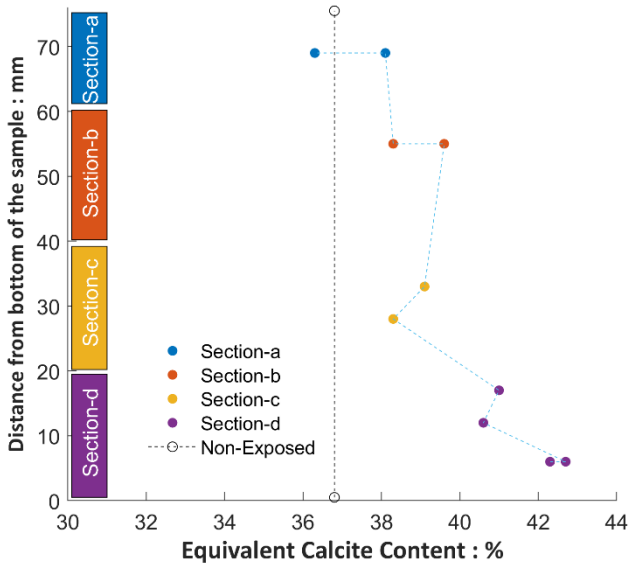

Figure 6.3 Equivalent calcite content along the height of the specimen A-R1-T_{DCO2}S14.

Effects on mineralogy

The XRD analysis of Clay A reconstituted sample (both original and post-exposure) was carried out to outline the possible mineralogical changes taking place during exposure to dry $scCO_2$. The sub-specimens obtained from sections a, b, c and d (Figure 6.1) of specimen A-R1-T_{DCO2}S14 were used for the XRD analysis. The powder used for the reconstitution of the samples was used for the pre-exposure analysis. The results are summarized in Table 6.3.

Table 6.3 Mineralogical analysis of Clay A non-exposed powder and exposed specimen (A-R1-T_{DCO2}S14).

Minerals	Mass content (%)					
	Original	**1a**	**5b**	**5c**	**2d**	**9d**
Kaolinite	1.3	3.6	0.9	1.0	0.5	0.5
Chlorite	1.9	2.6	3.8	3.8	2.7	2.3
Illite Type*	16	10.9	11.3	13.1	13.4	11.9
Calcite	33.6	30.4	29.6	30.4	30.8	34.1
Dolomite/Ankerite	22.5	24.4	24.6	26.2	26.7	27.9
Total Carbonates	56.1	54.8	54.2	56.8	57.5	62.0
Quartz	20.1	23.2	22.8	22.8	21.7	19.7
Plagioclase	3.8	4.2	5.1	3.3	3.2	3.2
Others	2.1	0.7	1.9	1.2	1.0	0.4

*Illite type includes illite and muscovite.

Figure 6.4 compares the calcite, dolomite and total carbonate content in a bar graph for exposed and non-exposed states. Figure 6.4 (a) shows the absolute values of calcites, dolomite/ankerite and total carbonate content whereas Figure 6.4 (b) elucidates the change in these minerals' content with respect to the non-exposed specimen.

Overall, there is an increase in dolomite/ankerite content as compared to non-exposed specimens. This implies that CO_2 exposure may have caused some of the calcite to react with magnesium ions in the water to form dolomite/ankerite. When compared in terms of total carbonate contents (i.e., calcite and dolomite/ankerite for specimens) sub-specimens from the bottom of the specimen (section d) have higher content as compared to the sub-specimen from the top of the specimen (section-a).

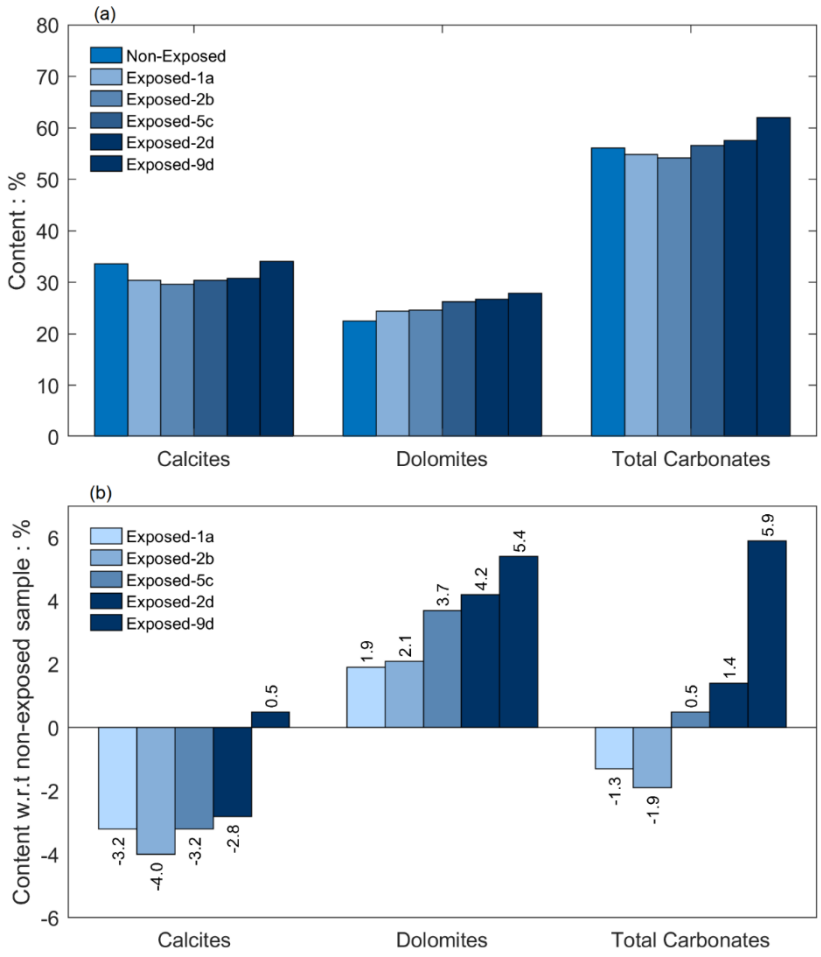

Figure 6.4 (a) Calcite, dolomite/ankerite and total carbonate content obtained by XRD for Clay A non-exposed powder and exposed specimen A-R1-T_{DCO2}S14, (b) change in minerals' content with respect to the non-exposed specimen.

There is indeed an increasing trend of total carbonates from top to bottom. This trend is very similar to the one determined through ECC (Figure 6.3), however the values are different. Different values between the outcomes of the mineralogical analysis and those of the ECC are obtained also with respect to the original powder, as the mineralogical total carbonate content is 56% and the Equivalent Calcite Content (ECC) is 37%, with a difference of 19%. The difference can be explained by accounting for the conventional procedure followed in the determination of the ECC. According to Demars et al. (1983), the accuracy of the acid dissolution method can be around 5%. Furthermore, the tests were carried out by wetting the soil powder with an HCl solution and waiting for the development of gas for about 5 minutes. It was later realized (Demars et al., 1983) that dolomite requires a higher reaction time which can extend up to 35 minutes. It can be observed that the ECC determinations provide a mass content of carbonate which is

slightly higher than the calcite content.

The overall increase in carbonate content (up to 6% as compared to non-exposed material) might result in an apparent decrease in the mass fraction of other minerals. This can be observed in the total clay content as shown in Figure 6.5.

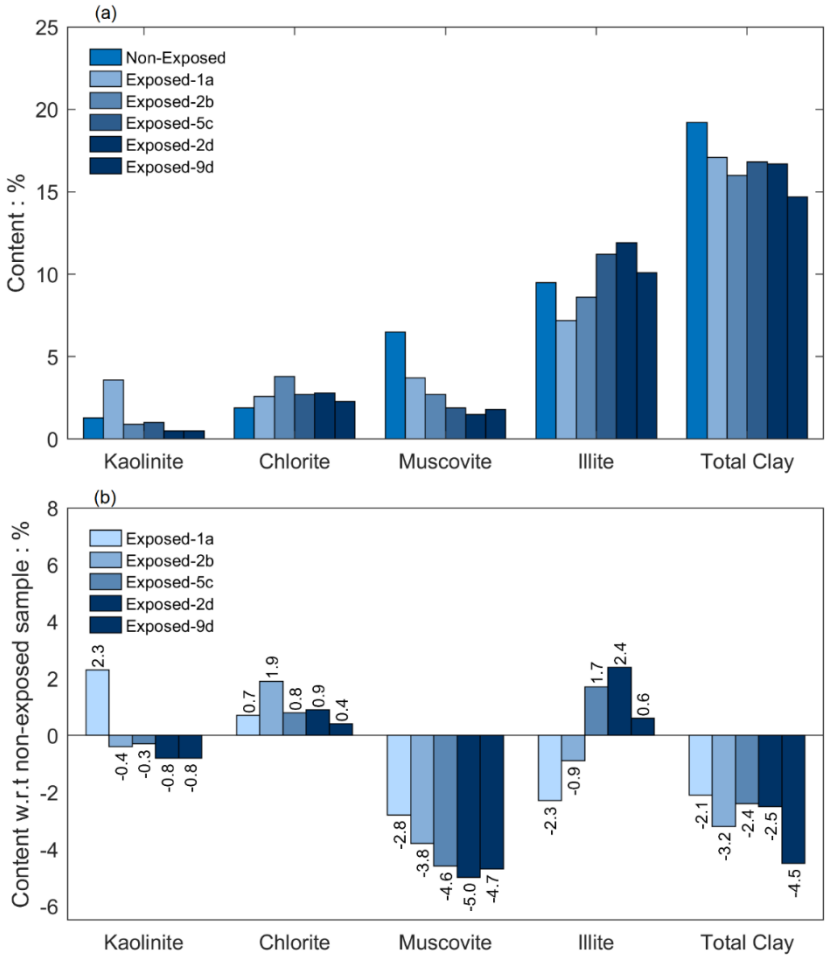

Figure 6.5 (a) Clay minerals contents obtained by XRD for Clay A non-exposed powder and exposed specimen A-R1-T_{DCO2}S14, (b) change in minerals' content with respect to the non-exposed specimen.

Apart from 'section a', the kaolinite content has remained almost constant with slight decrease along the height of the specimen as compared to the non-exposed specimen. Chlorite content shows minimal increase. Muscovite content has decreased significantly along the height of the specimen but illite has shown a mixed trend. Overall, the illite-type clay minerals i.e., muscovite + illite show almost constant values as recorded in Table 6.3.

The total silicate minerals, which include quartz and plagioclase showed an increasing trend apart from specimen 9d which shows a decrease in total silicate content i.e., 22.9% as compared to 23.9% for non-exposed specimens.

Effects on Pore Size Density

The effects of the dry $scCO_2$ exposure on the Pore Size Density (PSD) of Clay A specimens reconstituted to an axial stress of 15 MPa were determined through MIP tests. Figure 6.6 compares the PSD of a specimen which was not exposed to CO_2 (A-R1-N) to the ones of the specimens exposed for 14 days (A-R1-T_{DCO2}14). Different PSDs emerge depending on the height of the specimen as sub-specimens 7b, 7c and 5d come from sections b, c and d of Figure 6.1.

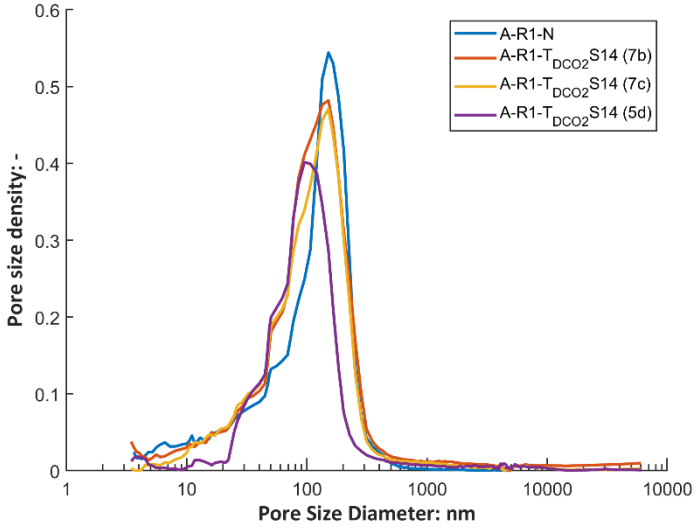

Figure 6.6 Pore size density comparison of non-exposed specimen (A-R1-N) and exposed specimen (A-R1-T_{DCO2}S14).

All the PSDs are characterized by a monomodal distribution, with a peak for pores having diameters ranging between about 80 and 150 nm. It can be observed that the height of the peak (i.e. its relative frequency) is larger in the non-exposed specimen (A-R1-N) than in the exposed one (A-R1-T_{DCO2}S14). Interestingly, the size of the peak and the corresponding pore diameter reduce from proceeding from the upper half of the specimen (section 'b') to its bottom (section 'd'). If compared with the equivalent calcite distribution, these results suggest that carbonates precipitated clogging the larger pores, leaving the smaller pores mostly unaffected, since for the size of the pores smaller than the one of the peak the PSDs mostly overlap.

From the data of MIP analysis, water retention curves were obtained for both exposed and non-exposed specimens which are presented in Figure 6.7. The figure also

shows the matric suction values obtained with vapour equilibrium technique after subtracting osmotic suction values from total suction.

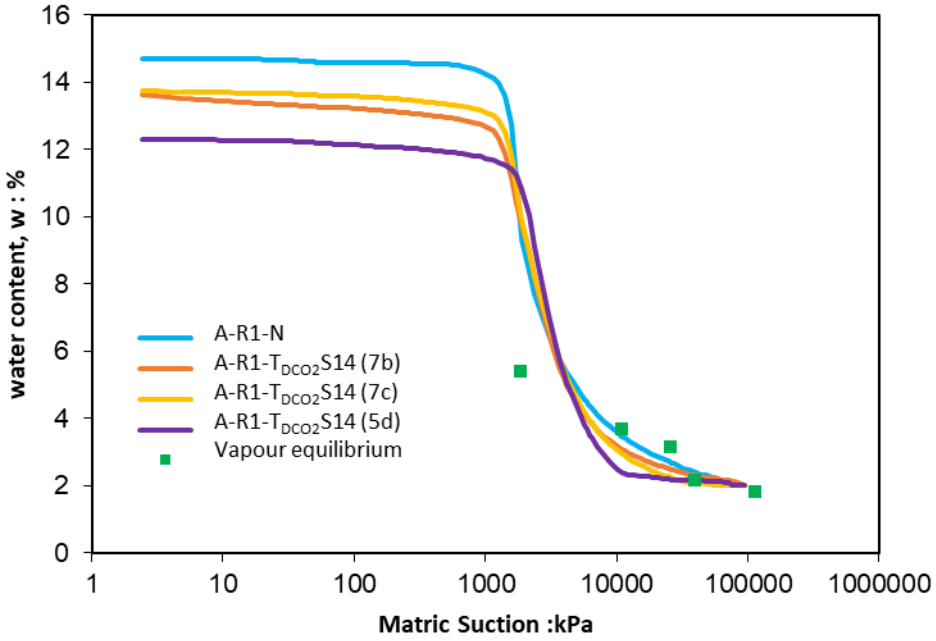

Figure 6.7 Water retention curves comparison for exposed and non-exposed specimens of Clay A.

Threshold pressure is commonly interpreted by a graphical reconstruction of water retention curve. Threshold pressure is obtained from semi-log plot between degree of saturation and matric suction, by extending the tangent line drawn at point of inflection of the curve to the point of intersection of horizontal line drawn at initial degree of saturation. The threshold pressure values for different specimens are summarized in Table 6.4.

Table 6.4 Threshold pressure for exposed and non-exposed specimens of Clay A.

Specimen	Threshold pressure (kPa)
A-R1-N	1360
A-R1-T$_{DCO2}$S14 (7b)	1100
A-R1-T$_{DCO2}$S14 (7c)	1250
A-R1-T$_{DCO2}$S14 (5d)	1600

Effects on fabric

Figure 6.8 shows the SEM results of Clay A reconstituted specimens both before (A-R1-N, left column) and after exposure to dry $scCO_2$ (A-R1-T_{DCO2}S14, right column). As for the exposed conditions, SEM was performed on sub-specimen 3d (specimen bottom). The scale of the magnification varies from 2000 to 10,000 times.

A-R1-N

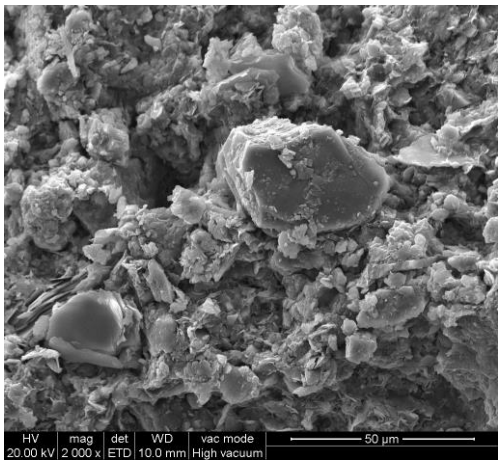

(zoom 2000x)

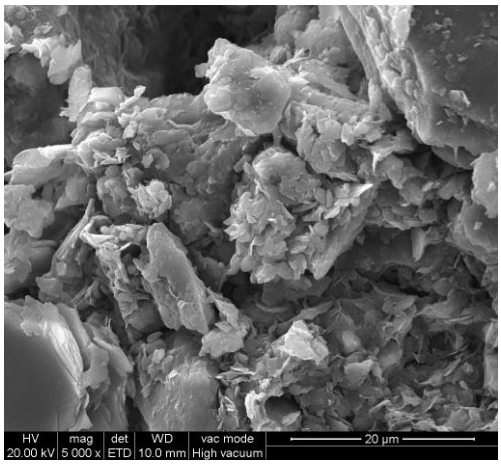

(zoom 5000x)

A-R1-T_{DCO2}S14 (sub-specimen 3d)

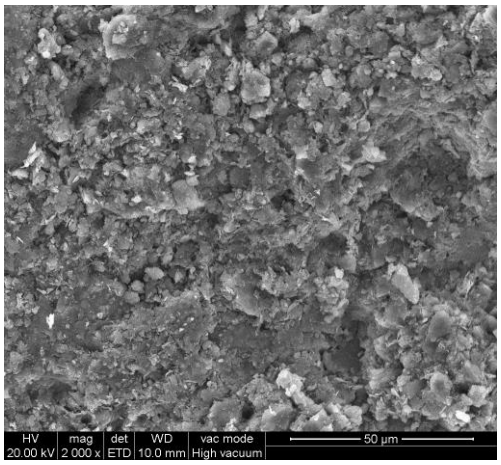

(zoom 2000x)

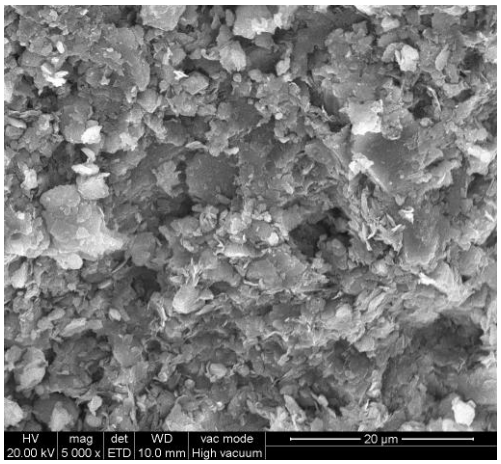

(zoom 5000x)

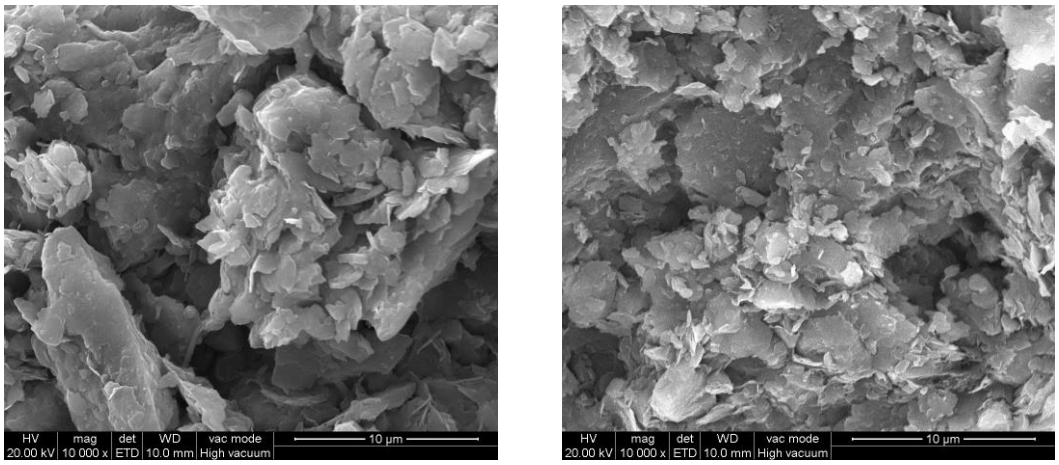

(zoom 10 000x) (zoom 10 000x)

Figure 6.8 SEM images of Clay A specimens at different magnifications before exposure (left column) and after 14 days of exposure to dry $scCO_2$ (right column).

Larger calcite/dolomite grains are appreciated in the images of the original specimen (especially zoom 2000x and 5000x), not in the ones at the bottom of the exposed specimen. For both specimens, aggregations of clay particles (in an edge-to-face arrangement) are easily appreciated.

CT scan analysis

The post-exposure CT scans of the specimen (A-R1-T_{DCO2}S14) show no anomalies or microfractures, as appreciated in Figure 6.9. The specimen is a reconstituted one, therefore it can be assumed that before exposure, in its original state, had a homogenous density. The two figures show the CT scans along two longitudinal planes. Apart from these 2D scans, other scans could not be retrieved from ENI and no 3D reconstruction were developed.

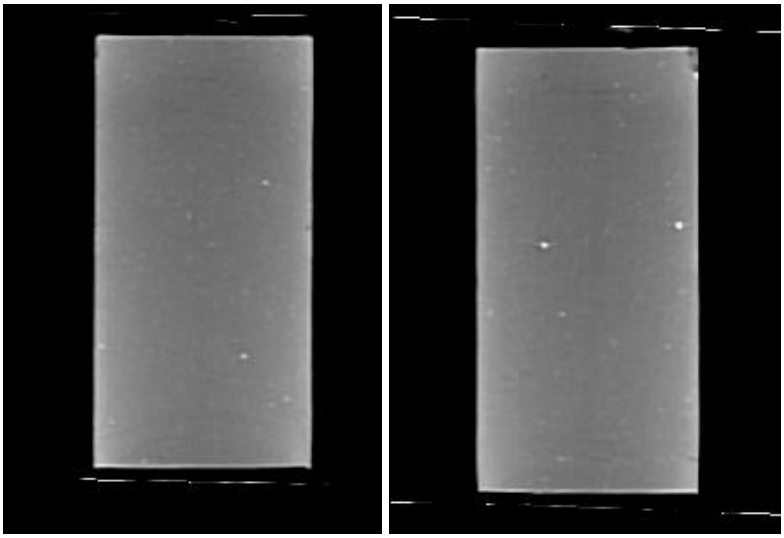

Figure 6.9 CT scan of the post-exposure sample exposed to dry $scCO_2$ (A-R1-T_{DCO2}S14).

The CT scans of the exposed specimen revealed that both the exposure to CO_2 and the pressurization/depressurization histories imposed in the batch test with dry $scCO_2$ did not lead to heterogeneity or cracking, possibly not having a detectable physical effect on the specimen. No cracks after drying can also be related to the low plasticity of the material.

6.2.2 Effects of exposure to CO_2-saturated brine

Effects on equivalent calcite content

The ECC of the Clay A specimen exposed to CO_2-saturated brine (A-R1-T_{BCO2}S14-7.5) was determined after the triaxial test (described in Chapter 7) was completed. Similarly to specimen A-R1-T_{DCO2}S14, this specimen was also divided into 3 sections and ECC was determined on the sub-specimens. The average value of ECC is about constant along the specimen height as shown in Figure 6.10. The average values were obtained from three determinations of ECC. The lowest value of calcite content was around 38% and the maximum value was around 40%. There is an increase of around 2% in the overall calcite content as shown in Figure 6.10.

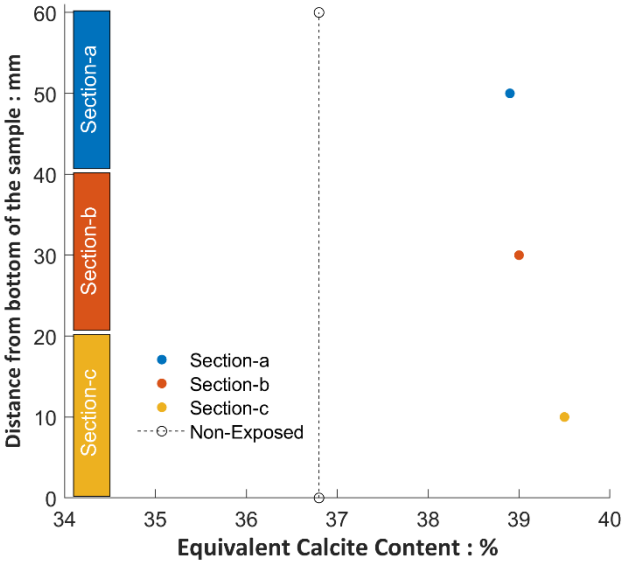

Figure 6.10 Average equivalent calcite content for each section along the height of the specimen (A-R1-T_{BCO2}S14-7.5) exposed to CO_2-saturated brine for 14 days.

Effects on the mineralogy

The samples for the XRD analysis were prepared but the analysis could not be completed due to logistics and time constraints.

Effects on the fabric and pore size density

Two specimens were exposed to CO_2-saturated brine out of which only one specimen was recovered as the other specimen was not caged (Section 4.3.3 of Chapter 4). The recovered specimen (A-R1-T_{BCO2}S14-7.5) was first used for the triaxial test, which led to changes in its fabric and pore size distribution. As a result, the analyses of fabric and pore size distribution will reflect the effects of triaxial testing rather than the CO_2 exposure. Therefore, no SEM or MIP analyses were performed on this specimen.

CT scan analysis

Only post-exposure CT scans were taken for specimen A-R1-T_{BCO2}S14-7.5. The specimen is reconstituted in a consolidometer; therefore, it was assumed that the specimen initially had a homogenous density. The post-exposure CT scans are shown in Figure 6.11, and they showed some fissures and some layering on one end of the specimen. These defects are believed to be caused mainly by the exposure procedure (i.e. by the action of the cage into which the sample was inserted during the exposure period). These layering did not affect the mechanical behavior of the sample as discussed in Chapter 7. Although

these fissures might not have any effect on the mechanical behavior, with higher exposure time the pattern might enhance and extend along the height of the sample.

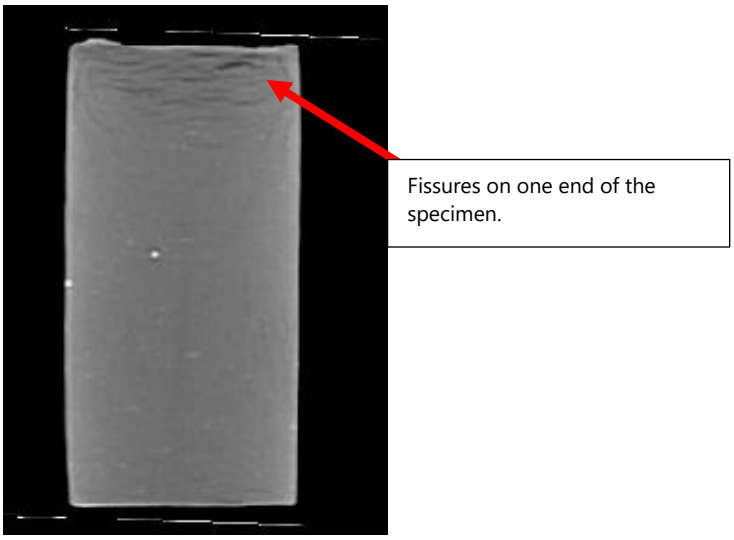

Figure 6.11 CT scans of the post-exposure specimen exposed to CO_2-saturated brine (D-R1-T_{BCO2}S14-7.5).

6.3 Effects of exposure to CO_2 on fabric and mineralogy of Clay B

6.3.1 Effects of exposure to wet $scCO_2$ on intact specimens of Clay B

Similar to that of Clay A material the post-exposure analysis was carried out on intact samples of Clay B material. Five Intact samples were exposed to wet $scCO_2$ for 30 days. One of the specimens (B-I-T_{WCO2}S30) was completely dedicated to microstructural analyses including water content, XRD, SEM, MIP and ECC. The other three specimens (B-I-T_{WCO2}S30-6, B-I_{MF}-T_{WCO2}S30-6, and B-I_{MF}-T_{WCO2}S30-12) underwent mechanical testing before performing ECC and XRD analyses on them. The last specimen (B-I_{MF}-T_{WCO2}S30-6 (1)) was tested only mechanically with no mineralogical and microstructural analysis performed on it. CT scans of the only post-exposure state were obtained for all the specimens, except specimen B-I_{MF}-T_{WCO2}S30-6 (1) which underwent CT scans both before and after exposure. The details of microstructural and mineralogical tests performed on different samples are provided in Table 6.5.

Table 6.5 Different microstructural and mineralogical analyses done on intact Clay B samples.

Sample ID	State	Water content	ECC	XRD	SEM	MIP	CT scan
B-I-T_{WCO2}S30	Original	Yes	Yes	Yes	Yes	Yes	No
	Exposed	Yes	Yes	Yes	Yes	Yes	Yes
B-I-T_{WCO2}S30-6	Original		Yes	Yes			No
	Exposed		Yes	Yes			Yes
B-I_{MF}-T_{WCO2}S30-6	Original		Yes	Yes			No
	Exposed		Yes	Yes			Yes
B-I_{MF}-T_{WCO2}S30-12	Original		Yes	Yes			No
	Exposed		Yes	Yes			Yes
B-I_{MF}-T_{WCO2}S30-6 (1)	Original		No	No			Yes
	Exposed		No	No			Yes

The dedicated post-exposure microstructural analysis specimen (B-I-T_{WCO2}S30) was divided into 3 sections along the height, each of them with a thickness of around 20 mm. For each section, different sub-specimens were obtained as shown in Figure 6.12.

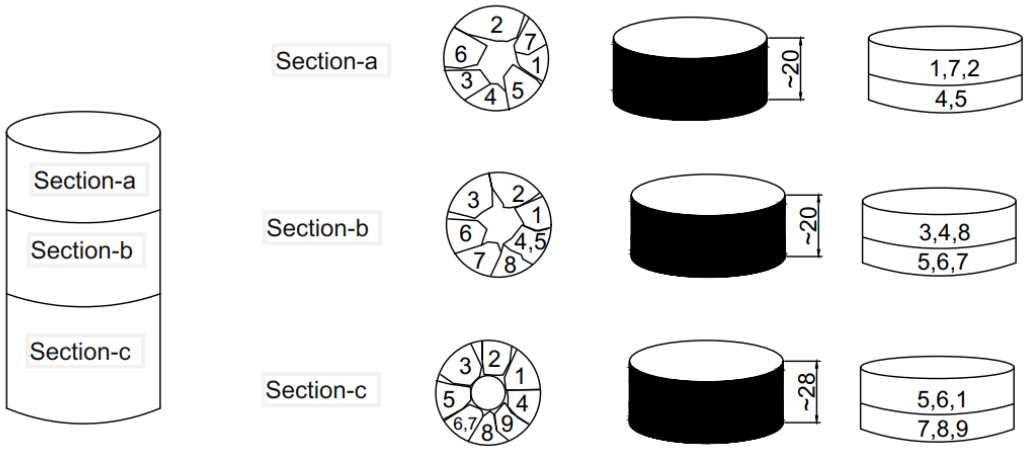

Figure 6.12 Subsections and sub specimens of specimen B-I-T_{WCO2}S30 after exposure to wet $scCO_2$ for microstructural analyses.

Effects on water content and ECC

Water content after exposure to wet $scCO_2$ was determined by oven drying the sub-specimens for 24 hours. The water content profile of specimen B-I-TS30 is shown in Figure 6.13. The average water content was 14.9%, 14.7%, and 14.1% for section-a, section-b and section-c respectively, as shown with purple triangles in Figure 6.13. These water contents are comparable with the original (non-exposed) ones of other similar Clay B intact samples, which were found to be around 14.3%.

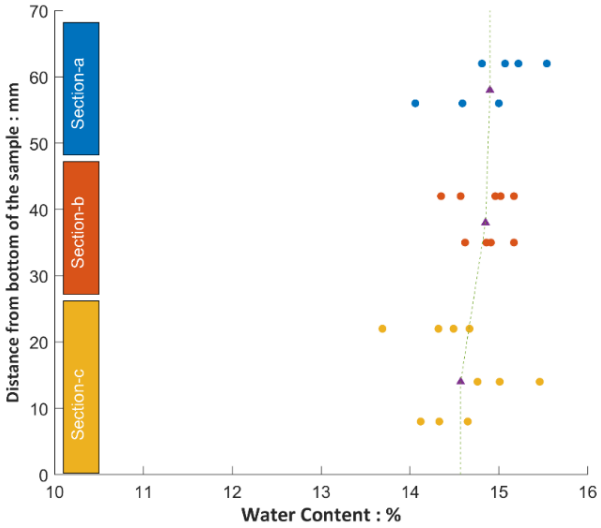

Figure 6.13 Water content along the height of the specimen after exposure to wet $scCO_2$ (B-I-T_{WCO2}S30). The purple triangles show the average water content for each section.

The close values of water content before and after exposure revealed that the wet $scCO_2$ did not evaporate any water from the specimen, as was observed instead in the case of dry $scCO_2$. It also verified that placing water in the baker into the autoclave was enough to saturate the dry $scCO_2$ entering the chamber.

The original ECC of the specimen was determined on the powder obtained during sample preparation and a value of 36.4% was obtained. After exposure, the ECC of the specimen remained unchanged along the sample height. The comparison is shown in Figure 6.14. Notice that in section-c, one sub-specimen had an equivalent calcite content of around 33.8%, which can be an outlier.

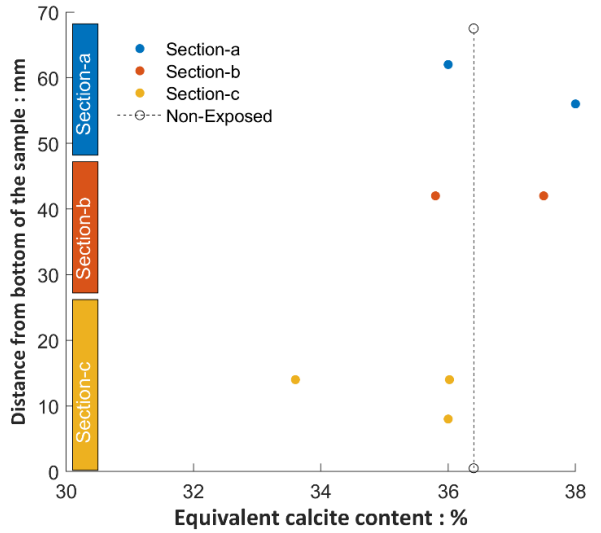

Figure 6.14 Equivalent calcite content along the height of specimen B-I-T_{WCO2}S30 after exposure to wet $scCO_2$.

As stated earlier out of the five exposed specimens, three specimens were triaxially tested. Their ECC was determined after testing. Figure 6.15 shows ECC for the other three exposed intact specimens. Out of these three specimens, two specimens (B-I_{MF}-T_{WCO2}S30-6 and B-I_{MF}-T_{WCO2}S30-12) come from the same depth of 1299.8-1300 m, similar to that of specimen B-I-T_{WCO2}S30. The third exposed specimen, B-I-T_{WCO2}S30-6 is from depth of 1331-1331.2 m. The specimens from similar depth have about the same equivalent calcite content and can be assumed "true twins". The specimen B-I-T_{WCO2}S30 cored from different depth, had slightly higher ECC as compared to post-exposure microstructural analysis specimen B-I-T_{WCO2}S30 (Figure 6.14).

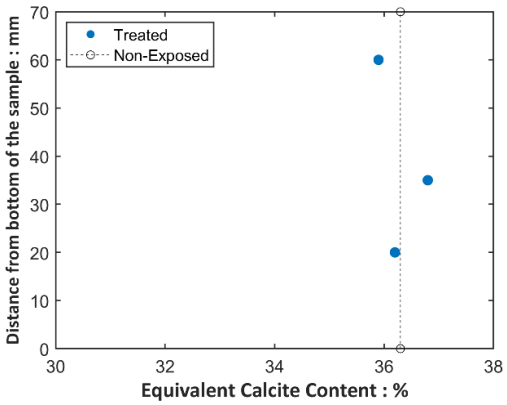

B-I_{MF}-T_{WCO2}S30-6

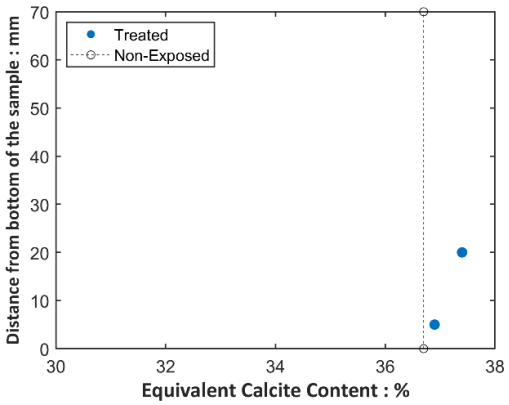

B-I_{MF}-T_{WCO2}S30-12

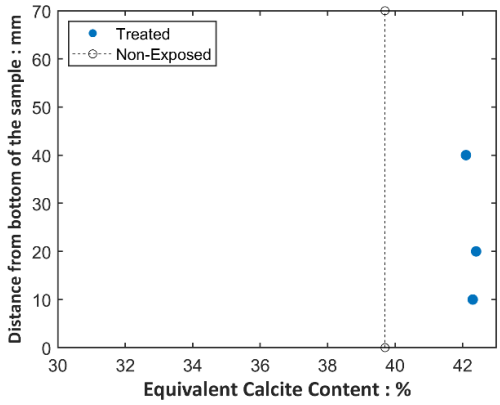

B-I-T_{WCO2}S30-6

Figure 6.15 Equivalent calcite content of specimens B-I_{MF}-T_{WCO2}S30-6, B-I_{MF}-T_{WCO2}S30-12 and B-I-T_{WCO2}S30-6 after exposure to wet $scCO_2$.

Effects on the mineralogy

In the following, the mineralogical analysis of the four intact Clay B samples exposed to wet $scCO_2$ for 30 days is discussed.

Specimen B-I-T_{WCO2}S30

This is the specimen dedicated to post-exposure microstructural analysis. Sub-specimens from different heights of the specimen (1a, 4a from section 'a', 5b, 8b, 9b from section 'b' and 4c, 7c from section 'c') were used for mineralogical analysis and compared with non-exposed powder. The results are compared in Table 6.6.

Table 6.6 Clay, carbonates and silicate contents for Clay B non-exposed powder and specimen exposed to wet $scCO_2$ (B-I-T_{WCO2}S30).

Minerals	Mass content (%)							
	Original	**1a**	**4a**	**5b**	**8b**	**9b**	**4c**	**7c**
Kaolinite	2.3	2.3	1.9	0.9	0.7	1.9	1.6	0.8
Chlorite	3.1	6.3	3.5	5.7	6.6	4.6	3.4	4.1
Illite Type	20.1	17.0	17.8	20.3	19.9	19.6	18.0	17.8
Calcite	37.7	36.5	34.8	37.3	34.5	36.1	36.4	36.6
Dolomite/ Ankerite	11.7	13.6	16.8	12.9	15.4	12.9	17.2	15.7
Quartz	17.1	19.0	19.2	17.5	17	18.4	17.2	18.2
Plagioclase	6.1	4.9	5.6	5	4.2	4.9	5.2	5.7
Others	1.9	0.4	0.4	0.4	1.7	1.6	1	1.1

The calcite content showed a decreasing trend for exposed specimens but the decrease in each section had mixed trends. The dolomite/ankerite content shows higher value at the specimen top (section-a) and bottom (section-c) as compared to section-b. As with the results of the Clay A sample, ECC underestimates the total carbonate content because of the larger reaction times required for dolomite.

The changes in calcite and dolomite content are further highlighted in Figure 6.16: dolomite content has increased as compared to non-exposed specimens, whereas a slight dissolution of calcites seems to have taken place.

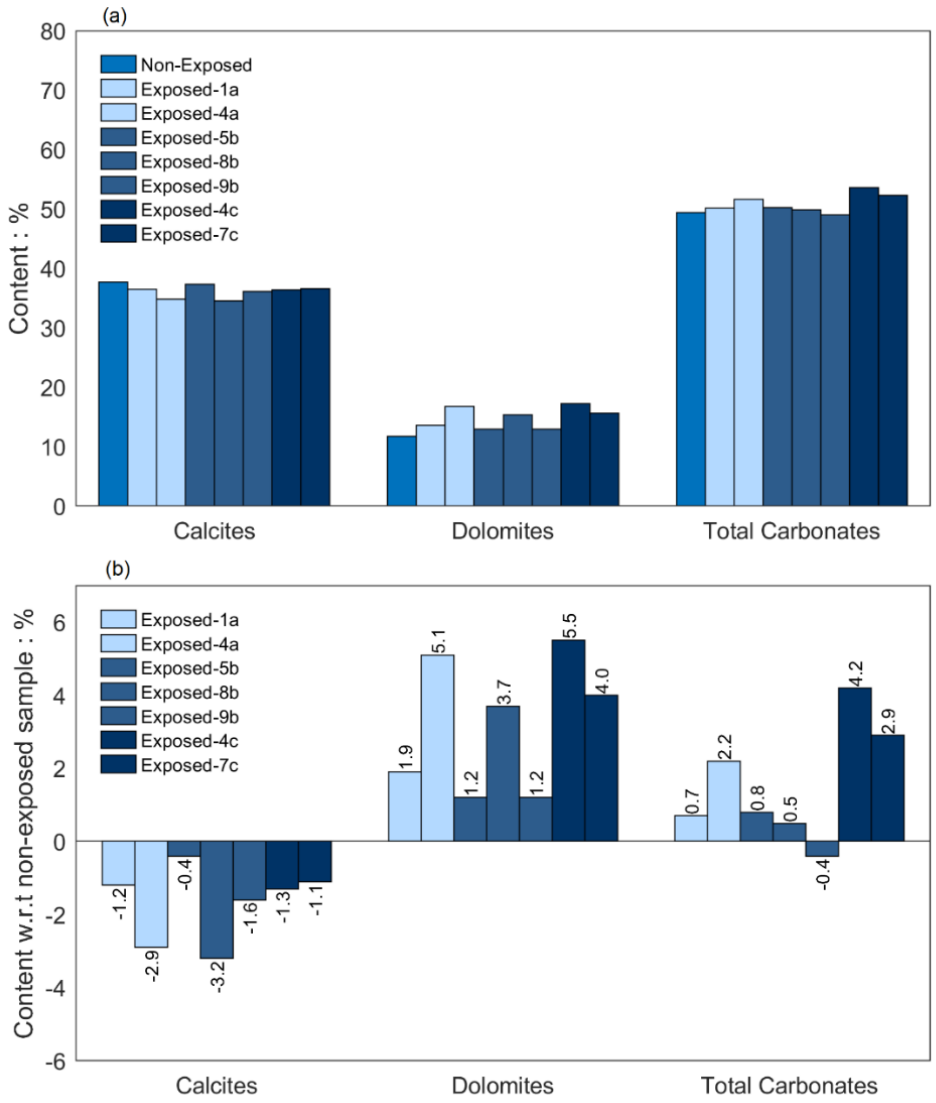

Figure 6.16 (a) Calcite, dolomite/ankerite and total carbonate content obtained by XRD for Clay B non-exposed and exposed specimen B-I-T_{WCO2}S30, (b) change in minerals' content with respect to the non-exposed specimen.

The comparison of different clay minerals for exposed and non-exposed specimens is shown in Figure 6.17. The total clay content decreased for section-a and section-c, whereas for section-b a slight increase can be observed.

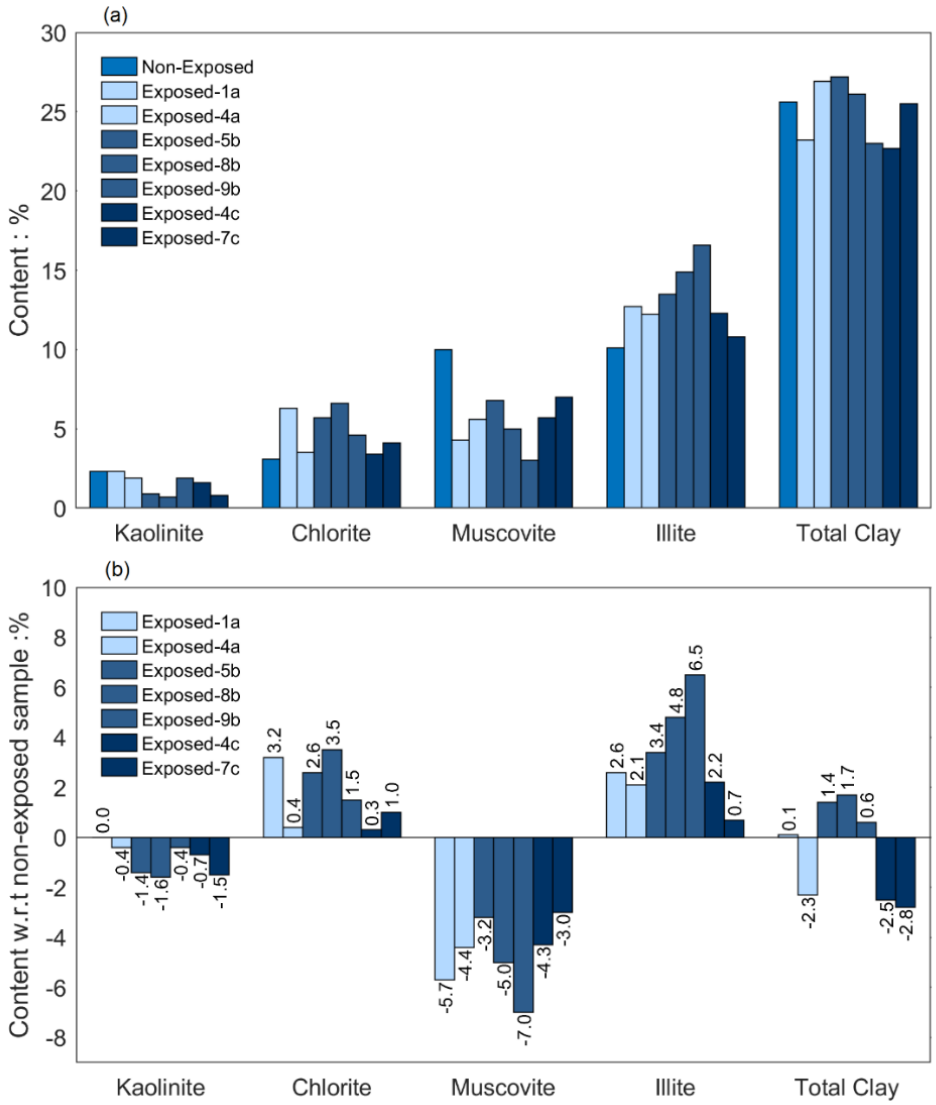

Figure 6.17 (a) Different clay mineral content obtained by XRD for Clay B non-exposed and exposed specimen B-I-T_{WCO2}S30, (b) change in mineral content with respect to the non-exposed sample.

Kaolinite is decreasing whereas chlorite shows an increasing trend for all the sections of the specimen. Muscovite shows a clear decrease as compared to the non-exposed material, but an increase is observed in illite content. The total illite type (muscovite + illite) shows a constant trend as recorded in Table 6.6. The quartz and plagioclase content shows a mixed trend and almost remains constant.

Specimen B-I_{MF}-T_{WCO2}S30-12

The post exposure XRD analysis was determined on a portion from the center of the specimen after the triaxial test. The pre-exposure XRD analysis was performed on powder obtained during the preparation of the specimen. The results, provided in Table 6.7 and

Figure 6.18, suggest a small increase in total carbonate fraction.

Table 6.7 Different clay, carbonates and silicates contents for B-I_{MF}-T_{WCO2}S30-12 specimen before and after exposure.

Minerals	Mass content (%)	
	Original	After exposure
Kaolinite	1.0	1.1
Chlorite	7.2	3.4
Illite Type	18.6	18.8
Calcite	34.5	36.6
Dolomite/Ankerite	15.3	16.6
Quartz	16.3	17.6
Plagioclase	4.5	5.7
Others	2.6	0.2

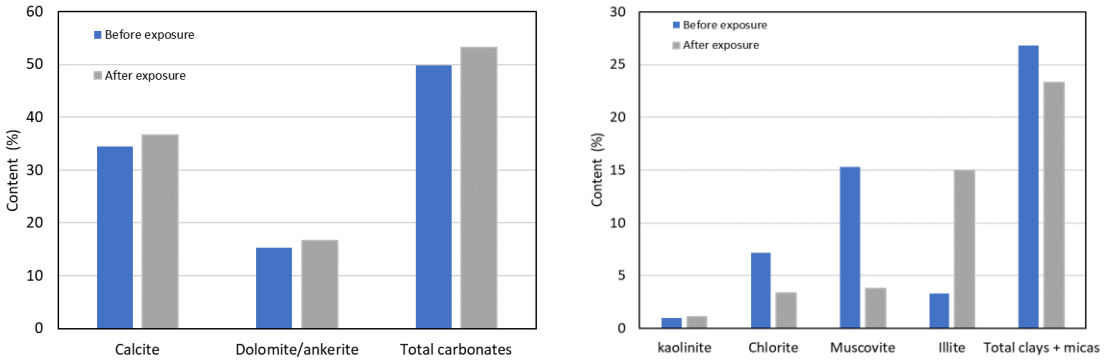

(a) (b)

Figure 6.18 Mineralogy of specimen B-I_{MF}-T_{WCO2}S30-12 obtained by XRD analysis.

Specimen B-I_{MF}-T_{WCO2}S30-6

Similar to the specimen B-I_{MF}-T_{WCO2}S30-12, post exposure XRD analysis on this specimen was performed after mechanical testing (only on a portion from the center of the specimen). The pre-exposure material was obtained during the preparation of the specimen. The results, provided in Table 6.8 and Figure 6.19, suggest a small increase in total carbonate fraction (especially dolomite).

Table 6.8- Different clay, carbonates and silicates contents for B-I_{MF}-T_{WCO2}S30-6 specimen before and after exposure.

Minerals	Content (%)	
	Original	After exposure
Kaolinite	2.3	1.2
Chlorite	3.1	2.8
Illite Type	20.1	19.0
Calcite	37.7	36.6
Dolomite/Ankerite	11.7	17.0
Quartz	17.8	17.1
Plagioclase	5.4	6.1
Others	1.9	0.2

When comparing the total clay minerals of exposed and non-exposed specimens a decrease from 25.5% to 23.0% is observed. The clay mineral which shows a decreasing trend is kaolinite (2.3% to 1.2%) and illite type (20.1% to 19.0%). Illite type is the combined content of muscovite and true illite. Chlorite content remains almost constant (3.1% to 2.8%).

The silicate minerals show a minimal change. Quartz content increased from 17.1% to 17.8% and plagioclase decreased from 6.1% to 5.4%.

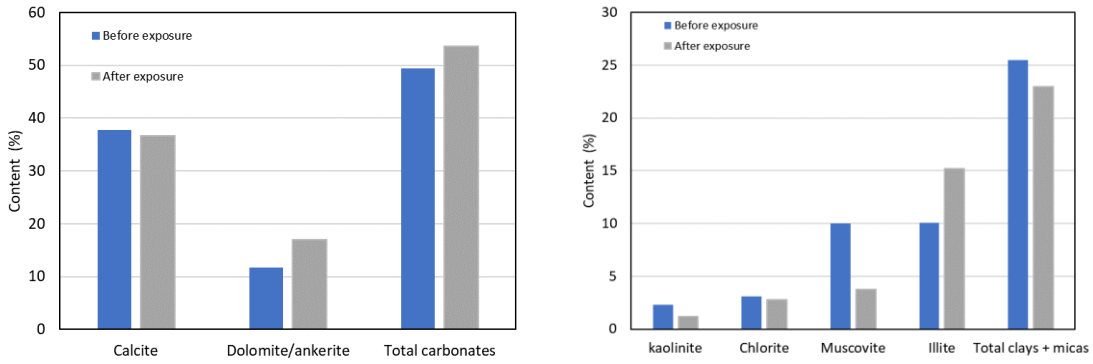

(a) (b)

Figure 6.19 Mineralogy of specimen B-I_{MF}-T_{WCO2}S30-6 obtained by XRD analysis.

Specimen B-I-T_{WCO2}S30-6

The XRD analysis was performed before and after exposure. The post-exposure XRD analysis was performed after mechanical testing. The results, provided in Table 6.9 and Figure 6.20, suggest a decrease in total carbonate fraction (especially dolomite), contrary

to the results of the other exposures.

Table 6.9 - Different clay, carbonates, and silicate contents for B-I-T_{WCO2}S30-6 before and after exposure.

Minerals	Content (%)	
	Original	After exposure
Kaolinite	2.9	1.1
Chlorite	2.4	7.5
Illite Type*	17.1	18.7
Calcite	37.1	33.6
Dolomite/Ankerite	18.0	13.7
Quartz	16.5	17.4
Plagioclase	4.7	5.5
Others	1.3	2.5

The change in mineralogy is graphically presented in Figure 6.20 for specimen B-I-T_{WCO2}S30-6. A decrease in calcite and dolomite content is visible in Figure 6.20 (a). The total carbonate content decreases from 55.1% to 47.3%.

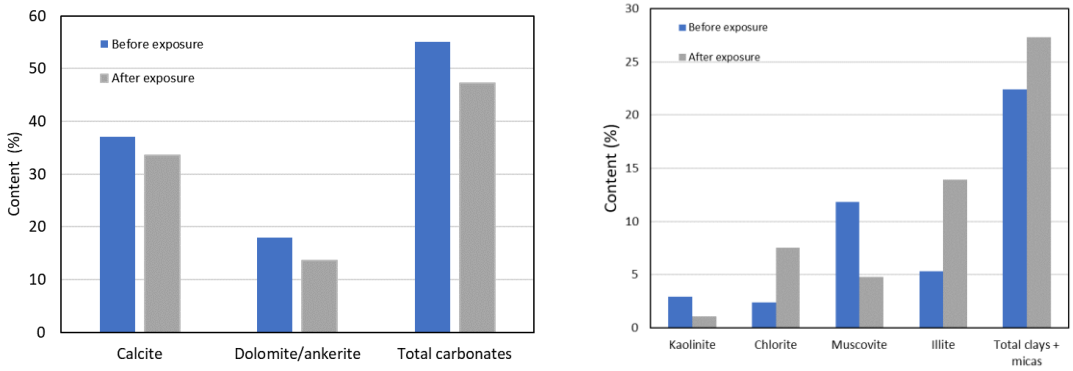

(a) (b)

Figure 6.20 Mineralogy of specimen B-I-T_{WCO2}S30-6 obtained by XRD analysis.

Effects on Pore Size Density

PSDs of Clay B intact samples (both exposed and non-exposed) are compared in Figure 6.21. The PSDs are characterized by a monomodal distribution with a large peak in correspondence with a diameter of about 100 nm. The pore size density functions are identical for all the samples. The sample ending with "2b" and "6c" indicates the sub-specimen from sections b and c from the post-exposure microstructural specimen (Figure 6.12). The sample names with 1 and 1b are two specimens from non-exposed intact specimens.

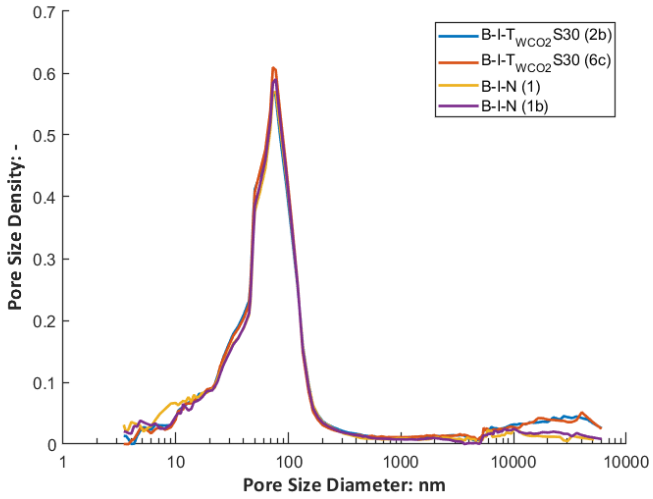

Figure 6.21 Comparison of pore size density of exposed (B-I-T$_{WCO2}$S30) and non-exposed (B-I-N) specimens of Clay B material.

For exposed specimen, more pores between 10-50 microns are visible. These pores might be related to micro-fissures in this specimen as shown in CT scans of Figure 6.25.

Using the MIP data, water retention curves were obtained for exposed and non-exposed specimen of Clay B and is shown in Figure 6.22.

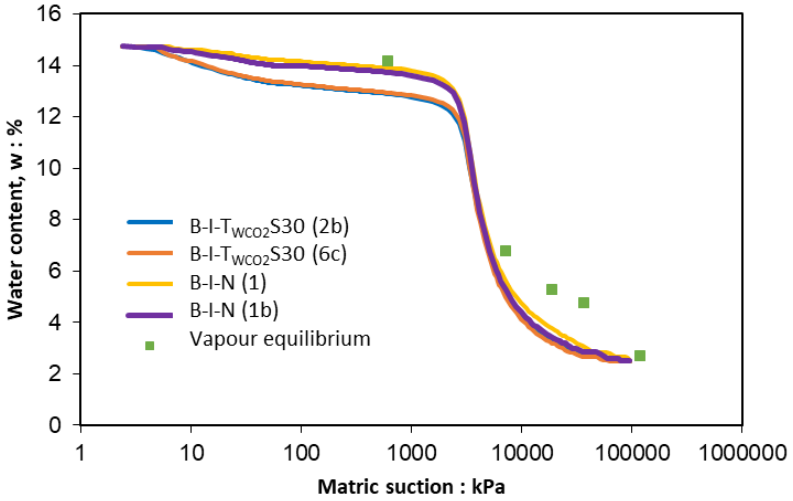

Figure 6.22 Water retention curves comparison for exposed and non-exposed specimens of Clay B.

Threshold pressure of Clay B specimens obtained through tangent method are given in Table 6.10.

Table 6.10 Threshold pressure values for exposed and non-exposed specimens of Clay B.

Specimen	Threshold pressure (kPa)
B-I-T_{WCO2}S30 (2b)	2100
B-I-T_{WCO2}S30 (6c)	2100
B-I-N (1)	2200
B-I-N (1b)	2200

Effects on fabric

The SEM for pre-exposure specimens was conducted at Politecnico di Torino DIATI labs whereas, for post-exposure analysis, the specimens were provided to ENI E&P. The SEM results obtained for pre-exposure specimens from Politecnico di Torino laboratories are presented in Figure 6.23.

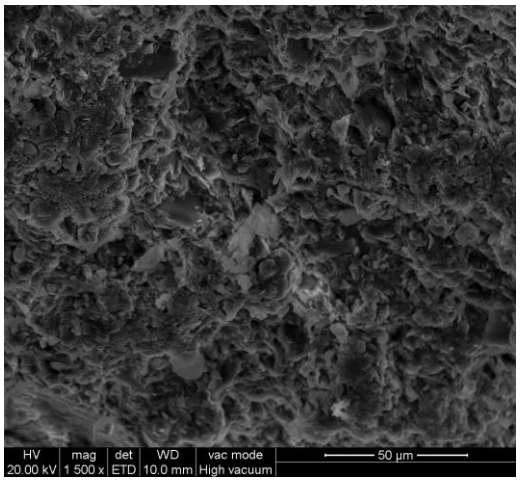

B-I-N (zoom 1500x)

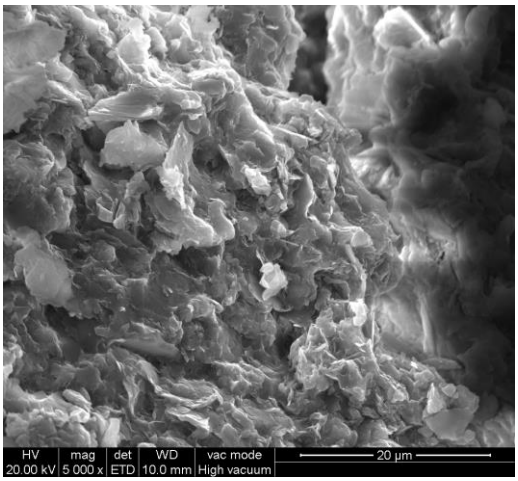

B-I-N (zoom 5000x)

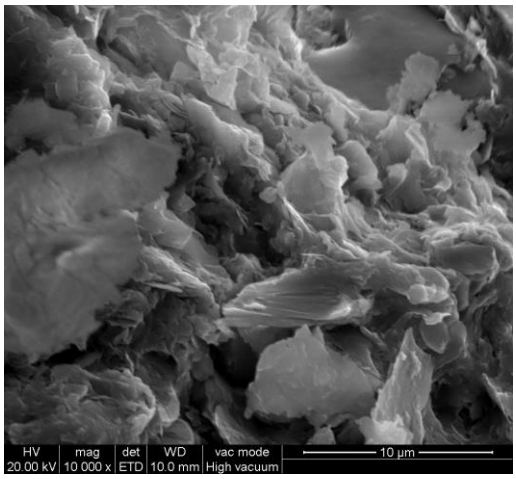

B-I-N (zoom 10 000x)

Figure 6.23 SEM images of non-exposed Clay B intact specimen.

The non-exposed SEM images seem to suggest the typical fabric of a dense, structured silty clay, with several carbonate grains with a massive 3D (parallelepipedal) shape and clay particles mainly iso-oriented (large magnification of the above figure).

The post-exposure SEM analysis was performed and analyzed at ENI E&P. The post-exposure microstructural analysis on sub-specimens of specimen B-I-T_{WCO2}S30 revealed that the CO_2 exposure did not lead to any significant fabric changes. According to the experts of SEM at Eni E&P the matrix (Figure 6.24 (a)) is made up of an illitic-smectitic clay with mica platelets (red arrows in Figure 6.24 (a)) and a high calcium carbonate content. The calcium carbonate content is related to the presence of coccoliths, a calcitic algae (Figure 6.24 (b), red arrows).

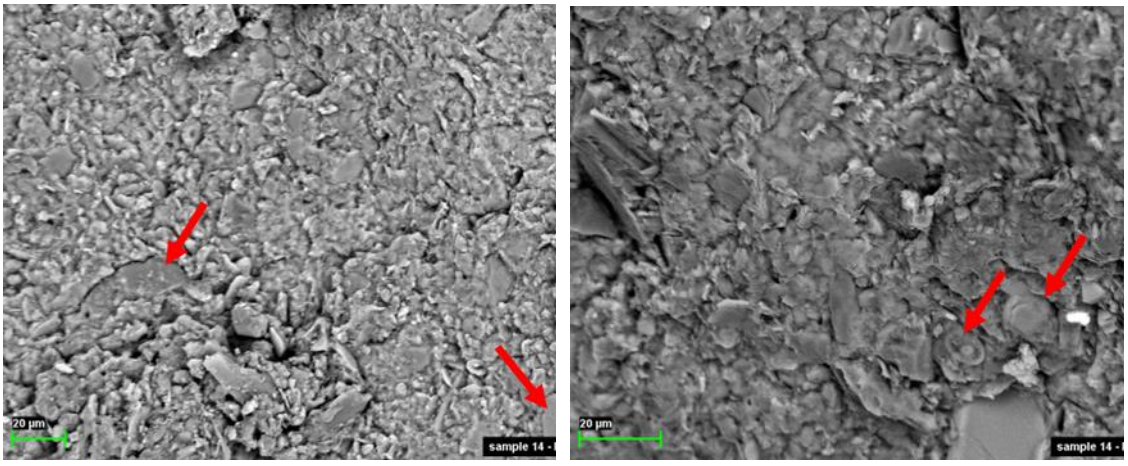

(a) (b)

Figure 6.24 The SEM analysis of specimen B-I-T_{WCO2}S30 done at ENI E&P.

As remarked by ENI E&P geologists, concluded that the sub-specimens are silty clays

with a massive structure made up of an illitic-smectitic clay with a silty fraction made up of calcite grains, coccoliths (a calcitic algae), small micas (mainly muscovite), TiO_2 (possibly rutile) and zircon grains. The calcite content is high, averaging around 30-40%. The diagenetic components are pyrite as an alteration of the organic matter and some dolomite crystals. The samples analysed as polished slabs do not show a visible (at the SEM) alteration of the silty clay structure in terms of texture, porosity or in the overall composition of the samples, which remains a Ca-rich clay. The only possible effect is a very subtle alteration of the pyrite crystals surface.

CT scan analysis

To check the homogeneity of the samples, CT scans were conducted at ENI E&P laboratories. The post-exposure CT scans were performed for most of the samples. The term 'MF' used in the ID of the samples features this aspect of the specimens. It shows whether CT scan detected microfractures or not. These microfractures were not visible on the surface of the sample when observed with the naked eye. Table 6.11 summarizes the CT scan details of samples and their depths.

Table 6.11 CT-scanned specimens along with depths and their state.

Sample	Depth (m)	Original	Exposed
B-I-T_{WCO2}S30-6	1331.00-1331.10		X
B-I-T_{WCO2}S30	1299.80-1300.00		X
B-I_{MF}-T_{WCO2}S30-6	1299.80-1300.00		X
B-I_{MF}-T_{WCO2}S30-12	1299.80-1300.00		X
B-I_{MF}-T_{WCO2}S30-6 (1)	1299.80-1300.00	X	X

The only specimen which did not show microfractures after exposure was B-I-$T_{WC(O2}$S-30-6, which was cored from a depth of 1331-1331.10 meters. Its CT scan results are shown in Figure 6.25 (top left). The other specimens, proceeding from a different depth (1299.80-1300.00 m) showed microfractures after exposure. Figure 6.25 shows the results for specimens B-I-T_{WCO2}S30 (top right), B-I_{MF}-T_{WCO2}S30-6 (bottom left), and B-I_{MF}-T_{WCO2}S30-12 (bottom right).

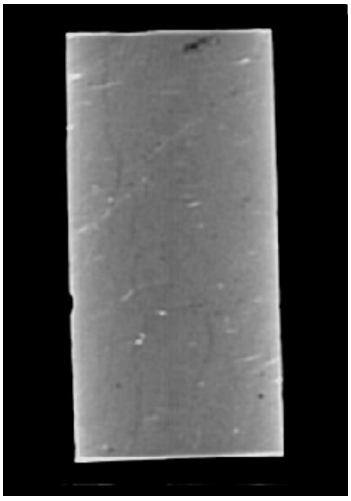

B-I-T_{WCO2}S-30-6

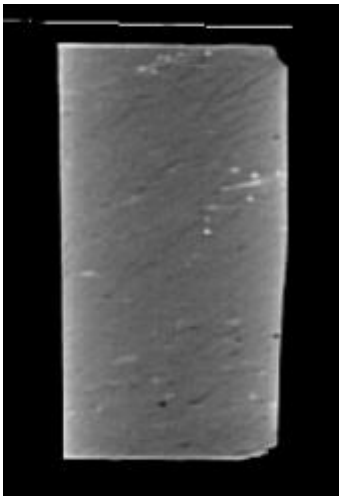

B-I-T_{WCO2}S30 (used for microstructural analyses)

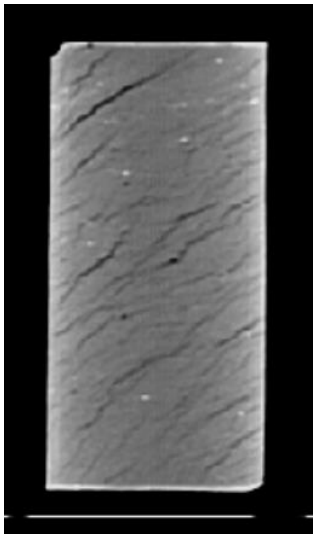

B-I_{MF}-T_{WCO2}S30-6

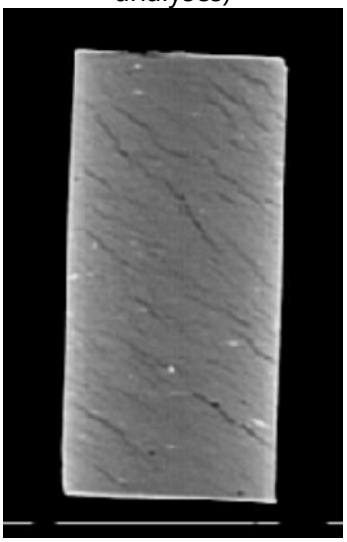

B-I_{MF}-T_{WCO2}S30-12

Figure 6.25 CT scans of post-exposure intact specimens of Clay B material.

Only one specimen (B-I_{MF}-T_{WCO2}S30-6 (1)) was scanned both before and after exposure to wet $scCO_2$. The results of CT scans are shown in Figure 6.26. It can be seen that the microfractures were present even before the exposure.

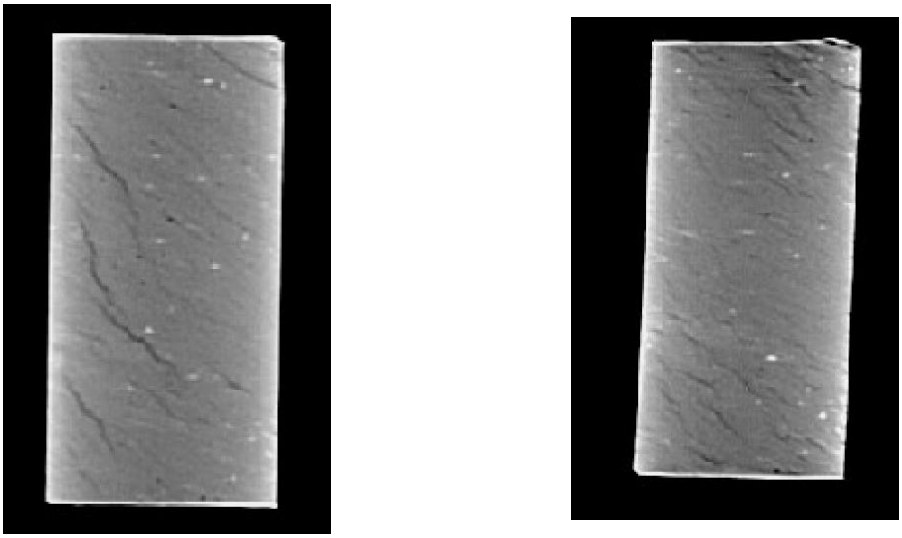

(a) (b)

Figure 6.26 CT scans of pre-exposure (a) and post-exposure (b) for specimen B-I_{MF}-T_{WCO2}S30-6 (1).

No CT scans are available for other specimens before exposure, so it cannot be concluded whether microfractures were induced by CO_2 exposure or were pre-existing. It shall be noticed that unfractured specimen B-I-T_{WCO2}S30-6, comes from a depth of 1331-1331.2 m, whereas all other samples are from the same depth (1299.8-1300 meters). Thus it is possible that the samples from the depth of 1299.8-1300m had these microfractures before exposure.

6.3.2 Effects of wet scCO$_2$ on reconstituted specimens of Clay B

The microstructural and mineralogical analyses done on Clay B reconstituted samples exposed to wet scCO$_2$ are shown in Table 6.12.

Table 6.12 Different microstructural and mineralogical analyses done on Clay B reconstituted samples.

Specimen ID	State	ECC	XRD	SEM	MIP	CT scan
B-R1-T_{WCO2}S30-3	Original		Yes	Yes	Yes	Yes
	Exposed	Yes		Yes	Yes	Yes
B-R1-T_{WCO2}S30-6	Original		Yes			Yes
	Exposed					Yes
B-R1.5-T_{WCO2}S30-6	Original		Yes			Yes
	Exposed					Yes

Effects on equivalent calcite content

Three reconstituted specimens (B-R1-T_{WCO2}S30-3, B-R1-T_{WCO2}S30-6 and B-R1.5-T_{WCO2}S30-6) from Clay B were exposed to wet scCO$_2$ for 30 days. The ECC was determined

only for specimen B-R1-T_{WCO2}S30-3 after performing the mechanical test on it. The other two specimens were contaminated with oil during the exposure process, so they were not utilized for any post-exposure analysis. The specimens were contaminated by the oil of the pump used for the pressurization of the autoclave. This contamination occurred due to some maintenance problem and occurred towards the end of the exposure period.

Three sub-specimens taken from different heights from specimen B-R1-T_{WCO2}S30-3 were analyzed. The value of ECC ranged between 39.6% to 40.6% along the height as shown in Figure 6.27. ECC of non-exposed material was not recorded so it is not possible to compare it with post-exposure specimen.

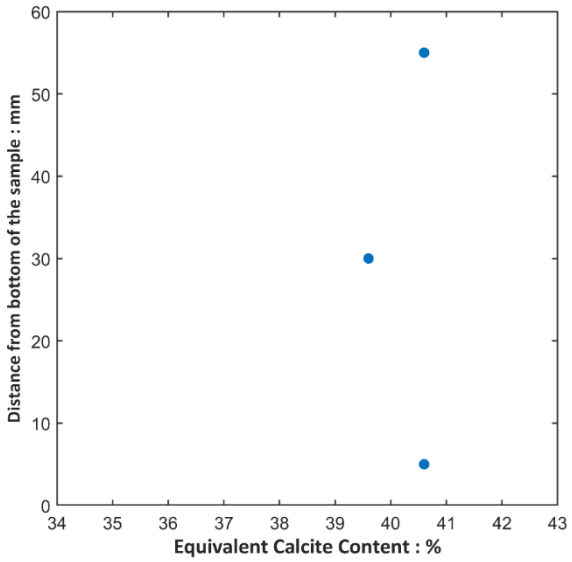

Figure 6.27 Equivalent calcite content of specimen B-R1-T_{WCO2}S30-3 along the height of the specimen.

Effects on the mineralogy

Reconstituted specimens B-R1-T_{WCO2}S30-3 and B-R1-T_{WCO2}S30-6 were prepared from a single batch of powder. The pre-exposure mineralogical analysis is provided in Table 6.13 and Figure 6.28. These mineralogical contents are comparable to that of non-exposed intact specimens discussed in Section 6.3.1.

Table 6.13 The original state (before exposure) XRD analysis of specimens B-R1-T_{WCO2}S30-3 and B-R1-T_{WCO2}S30-6.

Mineral	Mass Content (%)
Kaolinite	2.8
Chlorite	2.8
Illite Type*	16.8
Calcite	37.6
Dolomite/Ankerite	15.0
Quartz	19.0
Plagioclase	5.1
Others	0.9

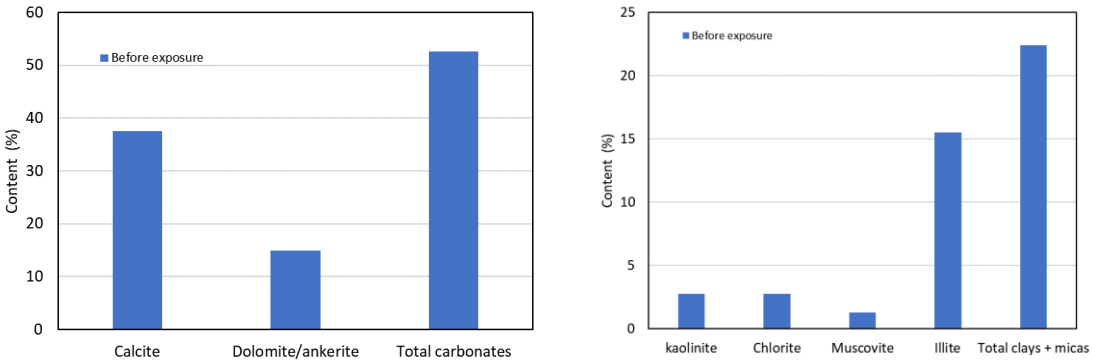

Figure 6.28 Mineralogy of specimens B-R1-T_{WCO2}S30-3 and B-R1-T_{WCO2}S30-6 before exposure.

The total carbonate content is 52.6% with calcite=37.6% and dolomite/ankerite content =15.0%. The total clay and mica content is equal to 22.4% with kaolinite=2.8%, chlorite=2.8, muscovite=1.3%, and illite=15.5%. The illite type would therefore be 16.8%. The silicate minerals are quartz=19.0% and plagioclase=5.1%.

The mineralogical content of specimen B-R1.5-T_{WCO2}S30-6 before exposure is introduced in Table 6.14 and plotted with a bar graph in Figure 6.29.

Table 6.14 XRD analysis of pre-exposure specimen B-R1.5-T_{WCO2}S30-6.

Mineral	Mass Content (%)
Kaolinite	1.5
Chlorite	5.3
Illite Type*	18.5
Calcite	35.2
Dolomite/Ankerite	14.1
Quartz	17.4
Plagioclase	4.0
Others	4.0

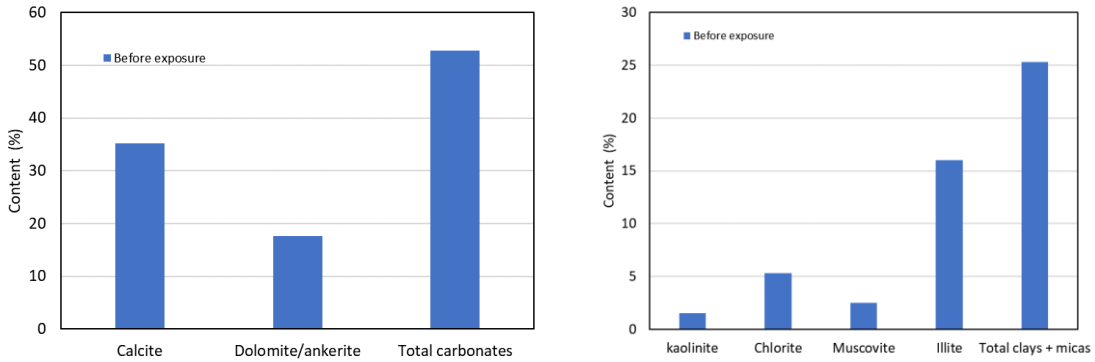

Figure 6.29 Mineralogy of specimen B-R1.5-T_{WCO2}S30-6 before exposure.

For this specimen, the total carbonate content is 49.3% with calcites=35.2% and dolomite/ankerite = 14.1%. The total clay and mica content is 25.3%. The individual clay minerals are kaolinite=1.5%, chlorite=5.3%, muscovite=2.5% and illite=16.0%. The illite type (muscovite + illite) is equal to 18.5%. The quartz content is 17.4% and plagioclase = 4%.

The post exposure XRD analysis of these samples was not conducted. The triaxial test on specimen B-R1-T_{WCO2}S30-3 was performed and specimens for XRD were obtained but due to logistics reasons were not completed.

Effects on the fabric and pore size density

Initially, the samples were intended for mechanical testing, making the SEM and MIP

analyses unnecessary. Additionally, the two specimens were polluted with oil, so no mechanical tests were performed.

CT scans analysis

The CT scans of the reconstituted samples are shown in Figure 6.30. In the pre-exposure samples (left column) the porous stones at the top and bottom, used for the caging of the sample are also visible. In the post-exposure samples, a little wear and tear is visible.

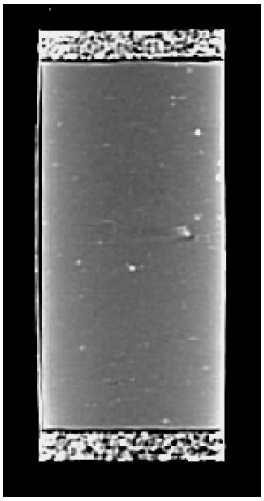

Before exposure- B-R1-T_{WCO2}S30-3

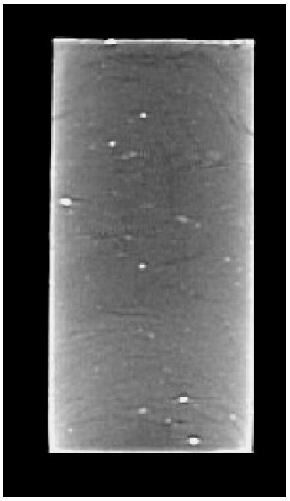

Post exposure- B-R1-T_{WCO2}S30-3

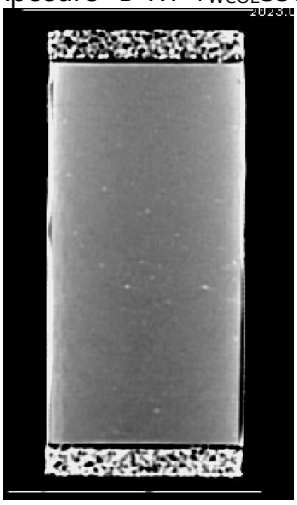

Before exposure- B-R1-T_{WCO2}S30-6

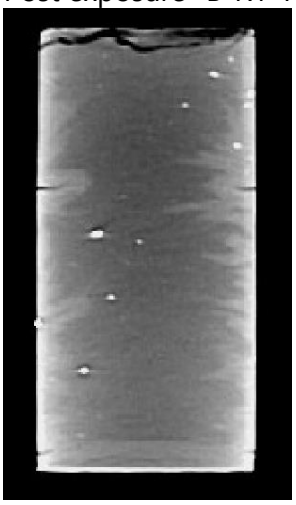

Post exposure- B-R1-T_{WCO2}S30-6

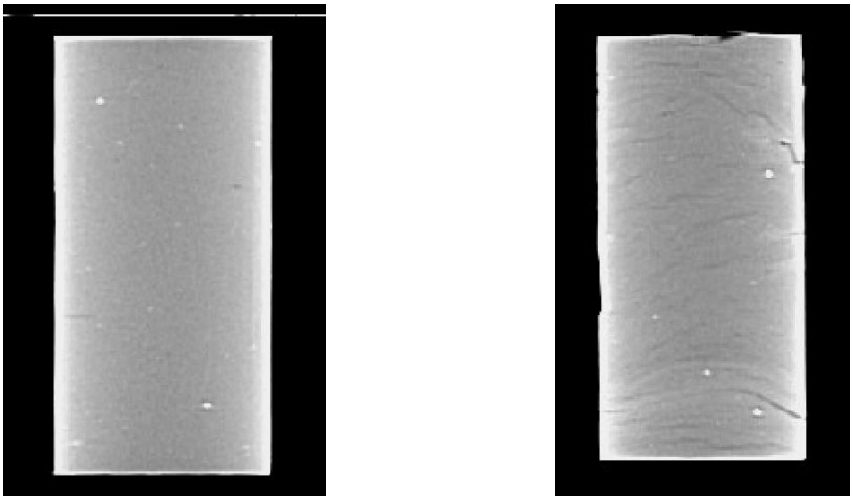

Before exposure- B-R1.5-T_{WCO2}S30-6 Post exposure- B-R1.5-T_{WCO2}S30-6

Figure 6.30 CT scans of pre-exposure (left column) and post-exposure (right column) of reconstituted samples exposed to wet $scCO_2$.

The effect of oil on specimens B-R1-T_{WCO2}S30-6 (second row) and B-R1.5-T_{WCO2}S30-6 (third row) is more prominent.

6.3.3 Effects of exposure to CO_2-saturated brine on reconstituted specimens of Clay B

Two reconstituted specimens B-R1-T_{BCO2}S30-6 and B-R1-T_{BCO2}S30-3 were exposed to CO_2-saturated brine for 30 days. For these specimens, metallic cage was modified to provide also axial containment by adding steel plates that hold the sample in place and plastic clamps for radial containment. After exposure, the metallic cage exploded, causing damage to the structure of the specimens. The specimens were not suitable for triaxial tests. Figure 6.31 shows the cage and pre-exposure specimen in (a) and post-exposure specimens which "exploded" in (b).

(a) (b)

Figure 6.31 Reconstituted samples and cages along with the samples of Clay B material exposed to CO_2-saturated brine (a) before exposure and (b) after exposure.

Effects on equivalent calcite content

ECC of specimen B-R1-T_{BCO2}S30-6 was determined along the height of the specimen. The values of ECC ranged between 37.2% to 37.7% as shown in Figure 6.32. The value of ECC before exposure was not recorded on this material but when compared to the sample exposed to wet $scCO_2$ (average value of 40.5% in Figure 6.27) low values of ECC are observed. The values of ECC along the height of the sample in the case of CO_2 saturated brine are less dispersed as compared to the sample exposed to wet $scCO_2$ (Figure 6.27).

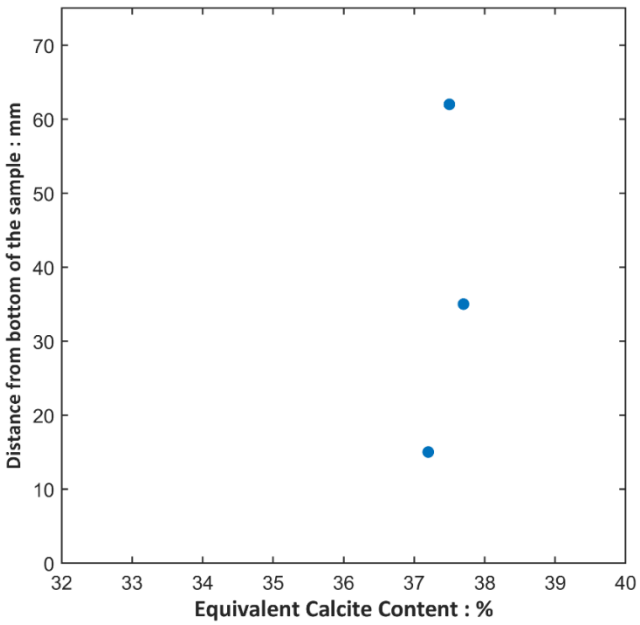

Figure 6.32 ECC of specimen B-R1-T_{BCO2}S30-6 along the height of the specimen.

Effects on mineralogy

The mineralogical analysis of the post exposure sample was not performed due to logistics and time constraints.

Effects on fabric and pore size density

SEM and MIP analysis are not relevant for this exposure condition as the cage exploded during the exposure and the fabric of the samples was disturbed. Therefore, the SEM and MIP analyses were not performed.

CT scans analysis

The CT scans of pre and post-exposure specimens are shown in Figure 6.33. The exposure of the specimen has caused physical damage to the sample which can be observed in the right column pictures.

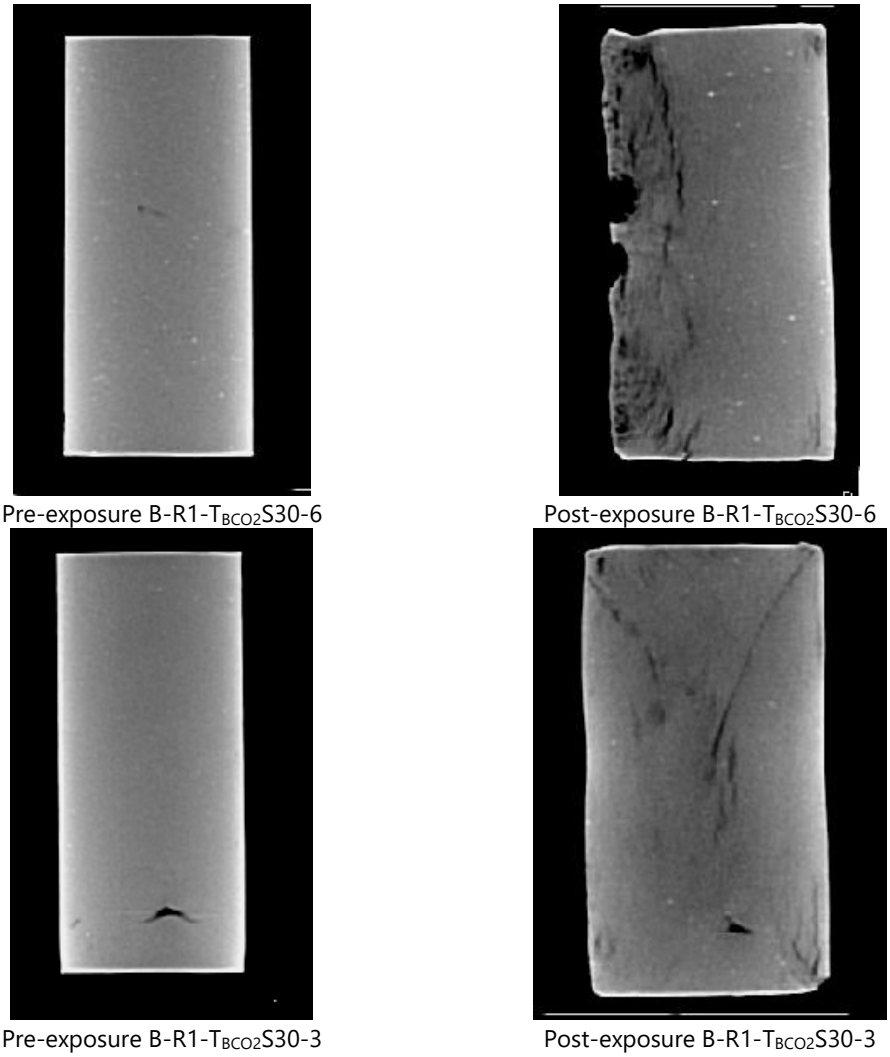

Pre-exposure B-R1-T_{BCO2}S30-6 Post-exposure B-R1-T_{BCO2}S30-6

Pre-exposure B-R1-T_{BCO2}S30-3 Post-exposure B-R1-T_{BCO2}S30-3

Figure 6.33 CT scans of pre-exposure (left column) and post-exposure (right exposure) reconstituted specimens exposed to CO_2-saturated brine.

6.3.4 Effects of exposure to wet $scCO_2$ on the powder of Clay B

As introduced earlier in this exposure case, a paste was prepared using the powder of Clay B material at its liquid limit (LL) and exposed to wet $scCO_2$ exposure. After 14 days, the powder was collected for ECC and XRD analyses. This 14-day exposed powder was then used to reconstitute samples for mechanical testing. The material underwent an additional exposure period, totaling 30 days. At the end of this 30-day exposure, ECC and XRD analyses were conducted again, along with mechanical tests on the reconstituted samples.

Effects on equivalent calcite content

The change in equivalent calcite content was insignificant after exposure. The powder had an ECC of 34.2% before exposure and increased slightly to 34.5% after 14 days of exposure. After 30 days of exposure, the ECC showed a more noticeable increase, reaching a value of 39.3%.

Effects on mineralogy

Initial mineralogical analysis before exposure is not available but a comparison between the mineralogy of 14 and 30 days of exposed powder is detailed in Table 6.15 and plotted in Figure 6.34.

Table 6.15 XRD analysis of exposed powder after 14 and 30 days of exposure.

Minerals	Mass Content (%)	
	14 days exposure	30 days exposure
Kaolinite	1.2	2.0
Chlorite	2.1	3.2
Illite Type*	17.6	17.8
Calcite	36.8	37.5
Dolomite/Ankerite	18.0	17.2
Quartz	17.8	17.2
Plagioclase	4.9	4.9
Others	1.6	0.2

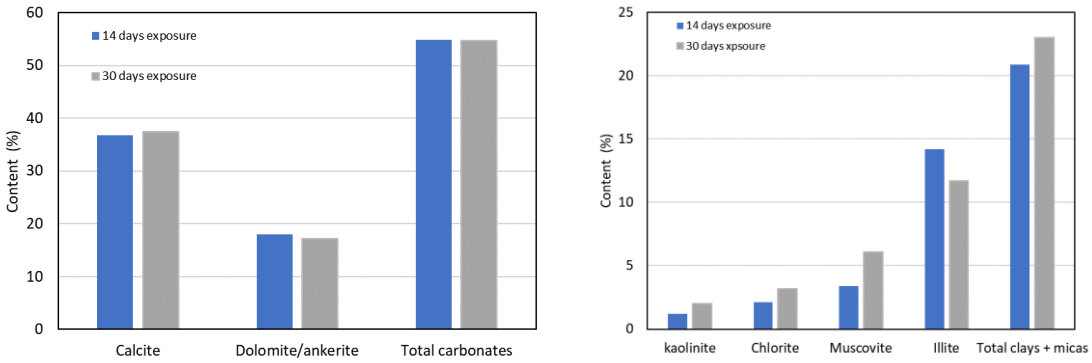

Figure 6.34 Mineralogy of exposed powder after 14 and 30 days of exposure to wet $scCO_2$.

Total carbonate content has not changed after 30 days of exposure whereas, an increase in total clay and mica content is observed. The total clay content increased from 20.9%

to 23%. All the clay minerals including kaolinite (1.2% to 2%), chlorite (2.1% to 3.2%) and illite type which is the combination of muscovite and illite (17.6% to 17.8%) increased after 30 days as compared to 14 days of exposure.

A minimal decrease in the quartz content was observed which decreased from 17.8% to 17.2%. The plagioclase content remained constant at 4.9%. Halite was another dominant mineral which reduced from 1.5% after 14 days to 0.1% after 30 days. The decrease in Halite can be attributed to the fact that the powder was used for triaxial testing where distilled water was used for flushing and saturation of the samples.

Effects on fabric and pore size density

In these exposure conditions, the powder was exposed to wet $scCO_2$, and the samples were prepared later in a consolidometer. It was then assumed that a minimal change in mineralogy would not change drastically the fabric and pore size density of the reconstituted specimen and would be similar to that of a specimen prepared with the original powder.

6.4 Conclusions

This Chapter was dedicated to the analysis of the effects of CO_2 exposure on the mineralogy and fabric of Clay A and Clay B samples. Exposure occurred through batch reaction tests, using dry $scCO_2$, wet $scCO_2$ and CO_2-saturated brine as a reaction fluid. Intact, reconstituted and slurry samples were introduced in the autoclave. Considerations are relevant also inasmuch the exposure procedure is concerned, as it was original for the laboratory where it was applied, and no standards are available in the international literature on the topic.

On the procedure of the exposure, it can be concluded that caging/containment of the sample is not necessary in case of dry and wet $scCO_2$ exposure. The caging is of paramount importance when exposing the sample to CO_2 saturated brine as it was shown that the sample disintegrated when not caged. Another aspect of caging is that a slight radial or axial swelling should be permitted which prevents the complete explosion of the caging. In one such case, the caging and the sample exploded when the caging was changed to an axially more rigid cage for which axial steel bars were used. It might be concluded with the present setup that the best caging system for these materials was given by a porous net around the side of the samples, two porous stones at the bottom and the top of the samples, and a system of clamps to hold all together both axially and radially. Possibly, to effectively reduce the swelling, the axial frame should be coupled with a stiffer holding of the samples in the radial direction.

On the study of microstructural and mineralogical analyses of different samples, it can be concluded that the effects of CO_2 were minimal for the material and the exposure times adopted in the study. In the case of exposure to dry $scCO_2$, it was found that dry $scCO_2$ desaturates the samples. The water content of the sample reduced substantially during the exposure period. In this case, the water lost by the specimens was collected at the bottom of the autoclave chamber. The joint effects of the geochemical reactions triggered by the CO_2 and water evaporation increased the carbonate content in the bottom half of the samples. Fabric effects were detected in terms of Pore Size Distribution, as the peak of the predominant pore size family decreased and shifted to slightly narrower pores. This result suggests that carbonate precipitation occurred predominantly in the larger pores, from which water evaporated.

In other cases of exposure to wet $scCO_2$ and CO_2 saturated brine, the water content of the sample was almost similar to the pre-exposure conditions. The geochemical analyses performed after exposure generally show very moderate mineralogical changes. The recurrent one was a slight increase in dolomite content, sometimes with a minor decrease in calcite.

SEM analysis conducted on 'original' intact and reconstituted samples of Clay B revealed the edge-to-face aggregations of clay particles. The SEM analysis of exposed intact samples of Clay B showed little to no changes in the fabric of material. The only possible effect of CO_2 was a very subtle alteration of the pyrite crystals surface. The salt in exposed samples almost completely disappeared.

CT scan analysis conducted on the reconstituted Clay A samples exposed to wet $scCO_2$ of Clay A showed no changes. The pre-exposure CT scans were not conducted but since the specimens were reconstituted it can be assumed that the density of the sample would be homogeneous. The specimen exposed to CO_2-saturated brine experienced some superficial layering on one end of a specimen with no effects on its physical structure.

As for the CT scans of intact samples of Clay B are concerned, some specimens showed microfractures after exposure to wet $scCO_2$. CT scans of these specimens were conducted only after exposure therefore the state before exposure was not known. These microfractures were found only on samples from same depth while another sample from a different depth showed no microfractures in post-exposure CT scans. These microfractures are most likely related to the depth of samples and not exposure procedure.

CT scans of reconstituted samples of Clay B exposed to wet $scCO_2$ showed a little wear and tear. This was due to the contamination of oil which leaked into the chamber

from the pump used for CO_2 injection. The CT scans of reconstituted sample exposed to CO_2 saturated brine showed the damage of cage explosion.

Chapter 7 Effects of CO_2 exposure on hydro-mechanical behavior

In the previous Chapter, the results of microstructural and mineralogical analyses on original (non-exposed) and exposed samples were presented. It was observed that when exposed to dry $scCO_2$, Clay A samples showed precipitation of carbonates. This precipitation resulted in the closure of large pores, as indicated by pore size distribution obtained through mercury intrusion porosimetry (MIP) analysis.

In other cases where intact samples from Clay B were exposed to wet $scCO_2$, minimal changes were observed in mineralogy and structure of the samples. The same was observed when reconstituted samples of Clay B were exposed to wet $scCO_2$. Similarly, the mineralogy of samples reconstituted from exposed powder was not affected substantially by the CO_2 treatment.

In this Chapter, the effects of CO_2 exposure on the mechanical behavior of the caprock samples are presented.

7.1 Description of different mechanical tests

Triaxial tests were carried out with the High Pressure Triaxial Apparatus (HPTA) and Medium Pressure Triaxial Apparatus (MPTA) described in Chapter 4. The investigation of the mechanical response was carried out through triaxial undrained tests consolidated at different stress levels on exposed and non-exposed samples. The following Section presents an introduction to the different mechanical tests carried out on exposed and non-exposed samples. The decision to conduct only consolidated undrained triaxial tests is based on time constraints. The low permeability of the samples requires a slow strain rate to prevent any buildup of pore pressure. Furthermore, previous results for Clay B intact sample (Ciancimino et al., 2024) indicate that the undrained scenario is the most critical for these materials.

7.1.1 Mechanical tests on Clay A

For the Clay A material, only reconstituted samples were tested. These samples were first

reconstituted in the consolidometer by applying two different effective vertical stresses (8.5 MPa and 15 MPa). They were then reloaded in the triaxial cell at the same effective vertical stress, along an anisotropic compression path (stress ratio K_0=0.50) believed to be the same developed by the material when reconstituted in oedometer conditions. This value is justified based on Jaky's (1948) equation which is widely adopted in practice for this purpose. In Jaky's equation for normally consolidated conditions (K_0=1-sin ϕ') when the friction angle ϕ' = 30° is inserted a value of K_0=0.50 is achieved.

As far as the consolidation at σ'_v=8.50 MPa (σ'_r=4.25 MPa) is concerned, only one non-exposed specimen was tested (A-R1-N-4.25). Whereas at the consolidation stress of σ'_v=15 MPa (σ'_r=7.50 MPa), four specimens were tested: two referring to the pre-exposure condition (A-R1-N-7.5 (1), A-R1-N-7.5 (2)), one referring to post-exposure to dry CO_2 (A-R1-T_{DCO2}S14-7.5) and another one to post-exposure to CO_2-saturated brine (A-R1-T_{BCO2}S14-7.5). Both the exposed specimens had twin specimens that underwent microstructural and geochemical investigations.

The tests conducted on Clay A reconstituted specimens are summarized in Table 7.1.

Table 7.1 List of triaxial tests conducted on Clay A reconstituted specimens.

Test ID	Caged/Uncaged	Notes
A-R1-N-4.25	-	Only specimen tested at this stress conditions
A-R1-N-7.5 (1)	-	
A-R1-N-7.5 (2)	-	
A-R1-T_{DCO2}S14-7.5	Caged	
A-R1-T_{BCO2}S14-7.5	Caged	
A-R1-T_{DCO2}S14	Uncaged	Dedicated to post-exposure microstructural and mineralogical analyses
A-R1-T_{BCO2}S14	Uncaged	Uncaged specimen-not recovered

7.1.2 Mechanical tests on Clay B

Both intact and reconstituted Clay B samples were tested. The in-situ stress state of Clay B discussed in Section 5.2.1 of Chapter 5, is assumed to be σ'_v =12.3 MPa and σ_r'=6 MPa therefore, K_0 for Clay B would be around 0.48.

Two intact specimens were tested before exposure at two different stress states. One specimen was consolidated to the in-situ stress and the other one was consolidated to twice the in-situ stress i.e., σ'_v = 24.6 MPa and σ_r'= 12 MPa.

As far as the post-exposure mechanical testing is concerned, four intact specimens were exposed to wet $scCO_2$ for 30 days and later tested in the MPTA. Three of these exposed specimens (B-I-T_{WCO2}S30-6, B-I_{MF}-T_{WCO2}S30-6 and B-I_{MF}-T_{WCO2}S30-6(1)) were consolidated at the in-situ stress ($\sigma_v' = 12.3$ MPa and $\sigma_r' = 6$ MPa) while one specimen (B-I_{MF}-T_{WCO2}S30-12) was consolidated at twice the in-situ stress of ($\sigma_v' = 24.6$ MPa and $\sigma_r' = 12$ MPa).

Two other intact specimens (B-I-N-Oed and B-I-T_{WCO2}S14-Oed) were tested in oedometer at high vertical stress. The non-exposed specimen was compressed up to a effective vertical stress of 25 MPa. The other specimen was tested after exposure to wet $scCO_2$ for 14 days at same vertical stress. The mechanical tests conducted on intact specimens of Clay B are summarized in Table 7.2.

Table 7.2 List of triaxial and oedometer tests conducted on Clay B intact specimens.

Test ID	Specimen Depth (m)	Caged/ Uncaged	Notes
B-I-N-6	1332.5-1332.6	-	
B-I-N-12	1299.6-1299.8	-	
B-I-T_{WCO2}S30-6	1331.0-1331.1	C	Intact specimen with no microfractures
B-I_{MF}-T_{WCO2}S30-6	1299.8-1300.0	U	Intact specimen with microfractures
B-I_{MF}-T_{WCO2}S30-6 (1)	1299.8-1300.0	C	Intact specimen with microfractures
B-I_{MF}-T_{WCO2}S30-12	1299.8-1300.0	U	Intact specimen with microfractures
B-I-T_{WCO2}S30	1299.8-1300.0	C	Used for microstructural and mineralogical analyses
B-I-N-Oed	1331.0-1331.1		Oedometer test-pre-exposure
B-I-T_{WCO2}S14-Oed	1299.37-1299.6		Oedometer test post-exposure

The effects of the exposure to wet $scCO_2$ on the mechanical behavior of reconstituted Clay B specimens were studied as well. Specifically, four reconstituted specimens (B-R1-N-3, B-R1-N-6, B-R1.5-N-6, and B-R3.0-N-6) were tested before exposure, while other three were used for exposure to wet $scCO_2$ (B-R1-T_{WCO2}S30-3, B-R1-T_{WCO2}S30-6, and B-R1.5-T_{WCO2}S30-6). These specimens were reconstituted at different stress levels and different Over Consolidation Ratios (OCR). The specimens used for pre-exposure mechanical tests included OCR 1.5 and 3.0 with respect to the in-situ stress and two specimens having OCR 1. The specimens with OCR 1 differed in the stress conditions,

one being at the in-situ stress conditions and the other at half of the in-situ stress ($\sigma_v' = 6.15$ MPa and $\sigma_r' = 3$ MPa). In case of post-exposure testing, three specimens, similar to the pre-exposure specimens were prepared and exposed to wet $scCO_2$ for 30 days. Only the specimen having OCR = 3 was not tested in post exposure condition.

Two other reconstituted specimens prepared at OCR 1 were exposed to CO_2 saturated brine for 30 days (B-R1-T_{BCO2}S30-3 and B-R1-T_{BCO2}S30-6). These specimens were damaged during the exposure period, with the cages exploding (as discussed in Section 5.3.3). These specimens are introduced here but were not tested mechanically as the structure of the specimens was damaged.

Tests conducted on reconstituted specimens are summarized in Table 7.3.

Table 7.3 List of triaxial tests conducted on reconstituted Clay B non-exposed specimens and specimens exposed to wet $scCO_2$.

Test ID	Caged/ Uncaged	Notes
B-R1-N-3		
B-R1-N-6		
B-R1.5-N-6		
B-R3.0-N-6		
B-R1-T_{WCO2}S30-3	C	
B-R1-T_{WCO2}S30-6	C	Triaxial tests were Initially planned but not conducted as the samples were contaminated with oil at the end of the exposure process.
B-R1.5-T_{WCO2}S30-6	C	
B-R1-T_{BCO2}S30-3	C	Tests were not conducted as the cage and samples were damaged during exposure.
B-R1-T_{BCO2}S30-6	C	

Lastly, another exposure condition where powder slurry was exposed to wet $scCO_2$ was also investigated. Two specimens were prepared from this exposed powder and were tested at OCR 1 and 1.5 after 14 and 30 days. Table 7.4 contains the list of these triaxial tests.

Table 7.4 List of triaxial tests conducted on reconstituted Clay B specimens exposed to CO_2 saturated brine and exposed powder.

Test ID	Notes
B-R1-T_{WCO2}P14-6	
B-R1.5-T_{WCO2}P14-6	
B-R1-T_{WCO2}P30-6	
B-R1.5-T_{WCO2}P30-6	

The results of these different triaxial and oedometer tests are discussed in the following sections.

Data on volumetric strains during saturation, Skempton's B parameter after saturation, and void ratios at the end of consolidation stage are documented in Appendix D for all the triaxial tests of Clay A and Clay B.

7.2 Results of triaxial tests for reconstituted specimens of Clay A

First, the mechanical response of the reconstituted exposed and non-exposed, normally consolidated specimens of Clay A is discussed. The non-exposed specimens included A-R1-N-4.25, A-R1-N-7.5(1) and A-R1-N-7.5(2) whereas the exposed ones included A-R1-T_{DCO2}S14-7.5 and A-R1-T_{BCO2}S14-7.5. The results of the triaxial tests are shown in Figure 7.1.

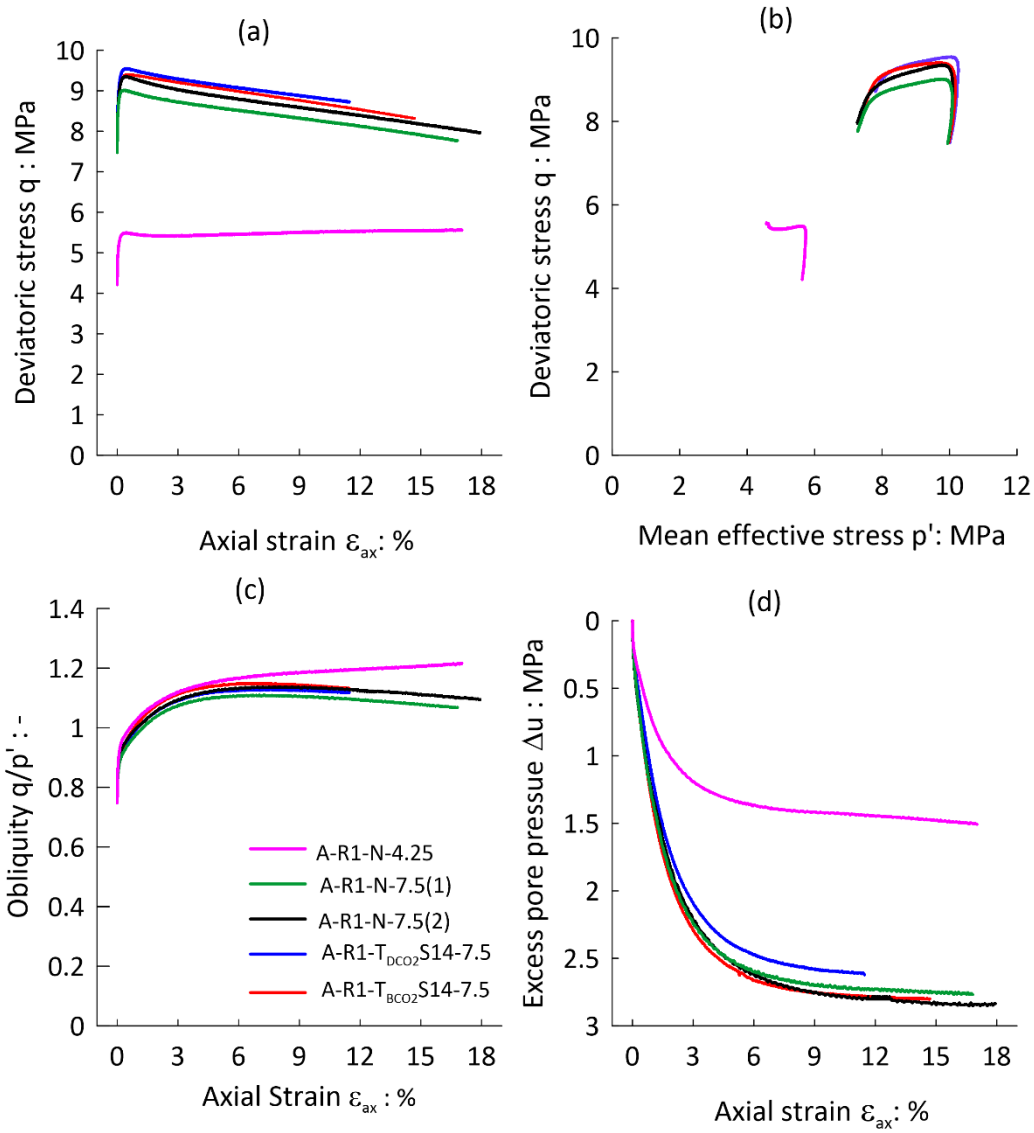

Figure 7.1 Comparison of triaxial test result for different Clay A reconstituted specimens (before and after exposure).

All the non-exposed samples showed a tendency to contract during shearing, reflected in the positive values of the pore pressure increase. The maximum deviatoric stress for the lower radial stress test (A-R1-N-4.25) was around 5.5 MPa and for the higher radial stress tests (A-R1-N-7.5(1) and A-R1-N-7.5(2)) was around 9.1 MPa.

The specimens A-R1-N-7.5 (1) and A-R1-N-7.5 (2) showed a limited softening behavior reaching the maximum strength. In terms of obliquity (q/p'), all the tests show a similar trend having a final value of around 1.1. The pore pressure initially increased and then remained about constant. The A-R1-N-4.25 specimen showed similar behavior. This specimen had slightly higher obliquity (1.2) at the end of shearing.

The exposed specimens (A-R1-T_{DCO2}S14-7.5 and A-R1-T_{BCO2}S14-7.5) also showed a contractive behavior similar to the non-exposed specimens. The behavior of exposed specimens is also comparable to that of non-exposed specimens both in terms of obliquity (q/p') and pore pressure.

Although the exposure of the samples to dry $scCO_2$ (A-R1-T_{DCO2}S14-7.5) showed a slight increase in the calcite content, (Figure 6.3 of Chapter 6) this did not impact significantly the mechanical behavior. The specimen A-R1-T_{DCO2}S14-7.5 (blue line in Figure 7.1) shows slightly higher q_{max} than the corresponding test of non-exposed samples, however, the peak obliquity q/p' was the same as the non-exposed specimens. The exposed specimen also showed slightly less contractive behavior as compared to the non-exposed ones (Figure 7.1 (d)). In the case of the specimen exposed to CO_2-saturated brine (A-R1-T_{BCO2}S14-7.5), the apparent layering observed in the CT scan shown in Figure 5.10 did not impact its mechanical behavior. As these results refer to reconstituted samples, where no bonding is expected, possible mechanical effects of CO_2 exposure are anticipated only as a consequence of mineralogy and porosity, and pore network changes. However, evidently, the petrophysical and mineralogical variations obtained in the previous chapter were not significant enough to affect the mechanical response.

7.3 Results of triaxial tests for intact specimens of Clay B

Consolidated undrained triaxial tests were conducted on intact specimens of Clay B after anisotropic consolidation to two stress levels: (a) in-situ stress state ($\sigma_v' = 12.3$ MPa and $\sigma_r' = 6$ MPa) and (b) twice the in-situ stress ($\sigma_v' = 24.6$ MPa and $\sigma_r' = 12$ MPa). These triaxial tests were conducted on specimens both non-exposed and exposed to wet $scCO_2$.

The results of tests conducted at in-situ stress state with radial effective stress of 6 MPa at the end of the consolidation phase are discussed first. These specimens include B-I-N-6, B-I-T_{WCO2}S30-6, B-I_{MF}-T_{WCO2}S30-6, and B-I_{MF}-T_{WCO2}S30(1). The comparison of these tests is shown in Figure 7.2. The non-exposed specimen is shown with a red line whereas the exposed specimens are shown with black lines. The non-exposed specimen (B-I-N-6, red line) showed a very brittle behavior with a marked drop in strength after an axial strain of about 1.5%, as it can be appreciated both in terms of deviatoric stress, q (Figure 7.2 (a)) and stress obliquity, q/p' (Figure 7.2 (c)). It showed a contractive behavior initially up to the maximum deviatoric stress as an increase in the over-pressure is noticed. Following the peak, overpressure decreased gradually as the sample deformed further (Figure 7.2 (d)). The decrease in pore pressure suggests a tendency to dilate.

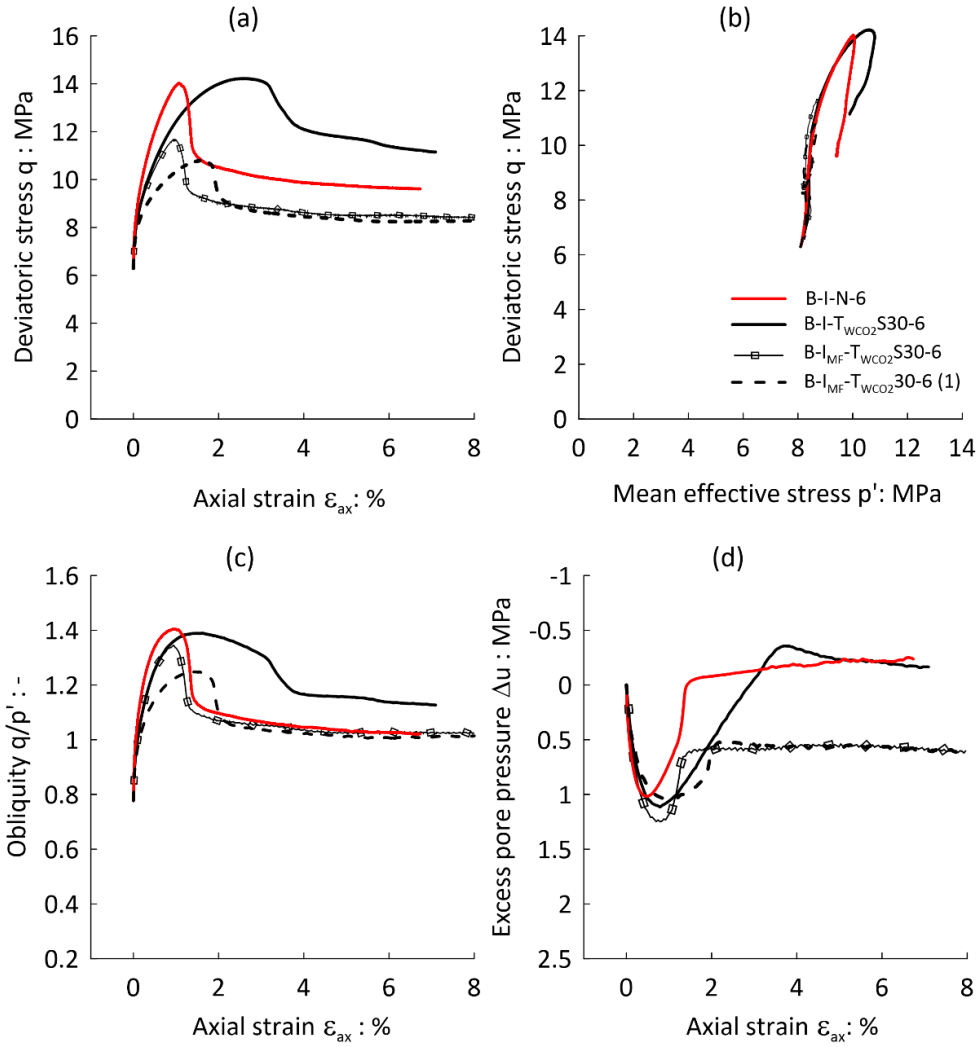

Figure 7.2 Triaxial tests conducted on intact Clay B specimens with radial stress of 6 MPa.

The maximum deviatoric stress (Figure 7.2 (a)) attained by the exposed specimen with no micro fissures (B-I-T_{WCO2}S30-6, continuous black line) is comparable to the non-exposed one (B-I-N-6), and so is the maximum obliquity. Initially, the pore pressure increased and then decreased, thus showing contraction first and a dilatant behavior afterwards. However, both softening and pore pressure decrease occurred less abruptly compared to the non-exposed specimen (Figure 7.2 (d)). As a consequence, the peak obliquity of the exposed specimen is the same as the non-exposed specimen, while the obliquity at the end of the test is higher. The exposed specimen in this case showed different post-peak behavior and higher residual strength in comparison to the non-exposed specimen.

Specimens, B-I_{MF}-T_{WCO2}S30-6 and B-I_{MF}-T_{WCO2}S30-6(1) both with micro fissures were also sheared after being consolidated at the in-situ stress conditions. Sample B-I_{MF}-

T_{WCO2}S30-6(1) (dotted black line) is the one for which CT scans were taken both before and after exposure (discussed and shown in Figure 5.24).

Compared to the non-exposed specimen, the exposed specimens with micro fissures also exhibited brittle behavior, but with a lower peak strength (Figure 7.2 (a)). Initially, these specimens showed a contractive behavior: as the peak deviatoric stress approached, a dilatant behavior developed testified by negative pore pressure. However, the dilatancy was less pronounced compared to B-I-N-6 (red line) and B-I-T_{WCO2}S30-6 (continuous black line). As for the non-exposed specimen, both exposed specimens with microfractures showed a marked strength loss after the peak. The obliquity at the end of the test was also pretty comparable to the one of the non-exposed specimen.

Two triaxial tests were conducted consolidating the specimen at twice the in-situ ones ($\sigma_v' = 24.6$ MPa and $\sigma_r' = 12$ MPa) i.e., B-I-N-12 (red line) and B-I_{MF}-T_{WCO2}S30-12 (black line). Figure 7.3 shows the comparison of these pre- and post-exposure tests. Compared to the lower stress state tests in Figure 7.2, these specimens were less brittle, which can be attributed to the higher confining stress. The post-exposure specimens have a lower maximum deviatoric stress (q_{max}) as compared to the non-exposed specimen. Post-peak softening is observed in the specimens and attained a constant value of obliquity q/p' at the end of the shearing phase.

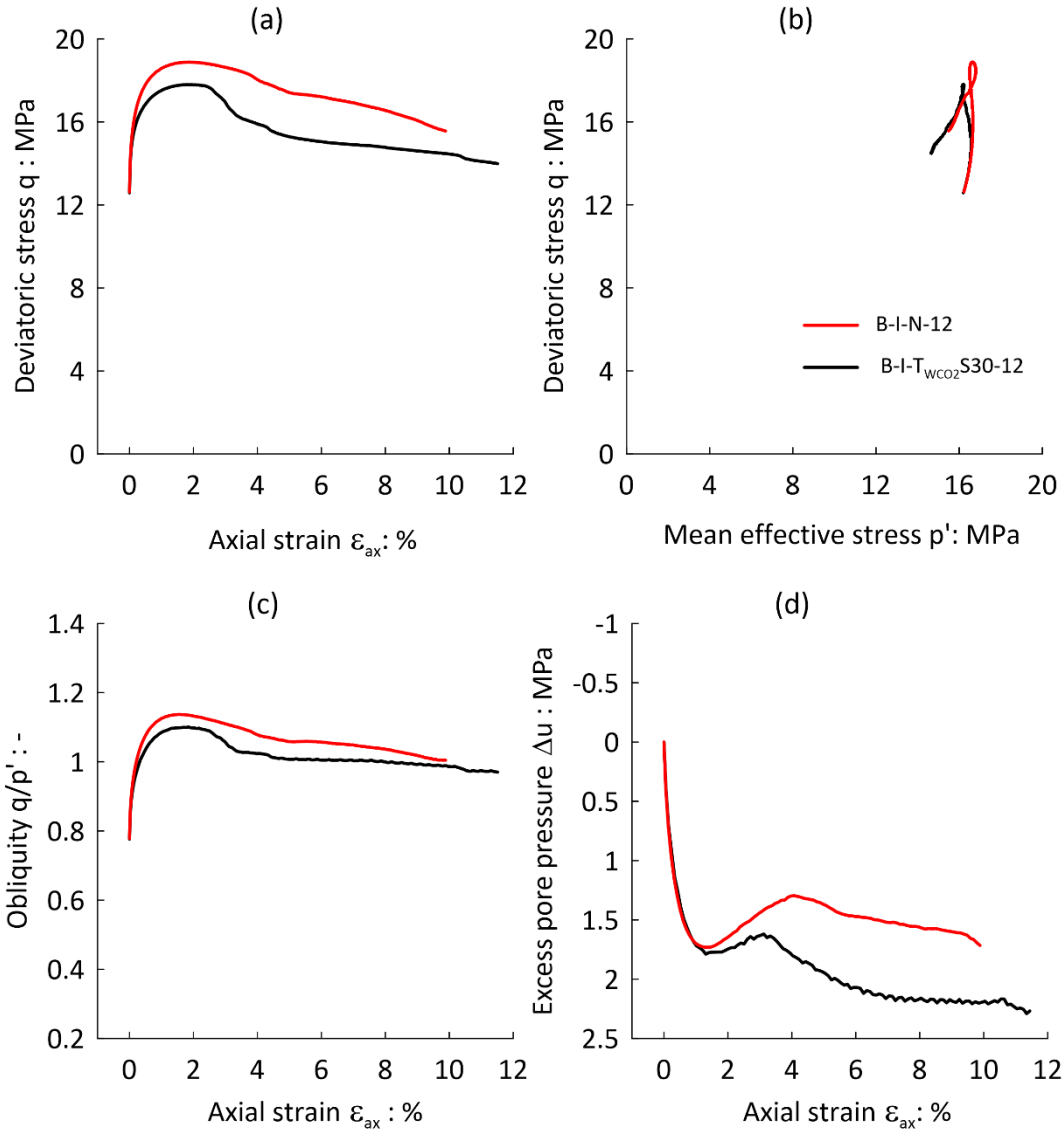

Figure 7.3 Triaxial test on intact Clay B specimens conducted with a radial stress of 12 MPa.

Initially, both the specimens exhibited contractive behavior, but after reaching peak deviatoric stress, the excess pore pressure began to decline, marking the onset of dilative behavior. After a temporary dilatancy, the specimens tended to contract (Figure 7.3 (d)). The exposed specimen has a lower maximum deviatoric stress (q_{max}) as compared to non-exposed one. Post-peak softening is observed for both samples, attaining similar q/p' obliquity values at the end of the shearing phase.

Figure 7.4 shows the peak and residual strengths of all intact Clay B specimens, for both exposed and non-exposed conditions. The red circles represent non-exposed samples, while the black circles indicate exposed samples.

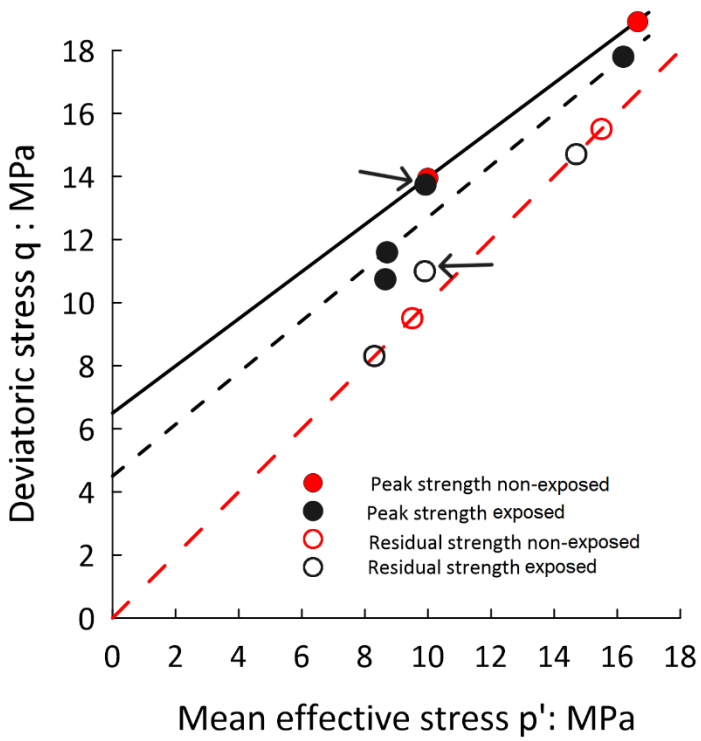

Figure 7.4 Peak and residual strength envelopes Clay B intact specimens exposed and non-exposed to wet CO_2.

Filled red and black circles denote the peak strength of non-exposed and exposed specimens, respectively. It can be observed that the peak strength of one exposed specimen (black filled circle shown with arrow) is very close to the one of the non-exposed specimens (black continuous line). This is the exposed specimen with no microfractures (B-I-T_{WCO2}S30-6) which had a similar q_{max} as the non-exposed specimen (B-I-N-6) in Figure 7.2 (a).

It can also be observed that the peak strength of the exposed specimens (black dashed line) rests below the peak strength of the non-exposed specimens (black continuous line). The specimens with lower peak strength envelopes are the exposed ones which had micro fissures i.e., B-I_{MF}-T_{WCO2}S30-6 and B-I_{MF}-T_{WCO2}S30-12.

The empty red and black circles denote the residual strength of non-exposed and exposed specimens, respectively. It can be observed that the strength of one exposed specimen (black empty circle shown with arrow) lies above the residual strength envelope (red dotted line). Such a result refers to the specimen B-I-T_{WCO2}S30-6, whose CT Scan showed no microfractures after exposure, having a different post-peak behavior and higher residual strength (continuous black line in Figure 7.2 (c)).

Adopting a linear Mohr Coulomb interpretation which linearizes the behavior over the stress range explored in the triaxial tests shows that the peak friction angle of non-exposed (B-I-N-6 and B-I-N-12) and exposed specimen with no microfracture (B-I-T_{WCO2}S30-6) is ϕ'_p=19°. The peak friction angle for exposed specimens with microfractures (B-I_{MF}-T_{WCO2}S30-6, B-I_{MF}-T_{WCO2}S30-12) is ϕ'_p=21°. The apparent cohesion for non-exposed and exposed specimens with no microfractures is c'_p=3.11 MPa. For exposed specimens with microfractures, the apparent cohesion is c'_p=2.55MPa. The residual friction angle of all specimens is ϕ'_r=25°, as summarized in Table 7.5.

Table 7.5 Values of angle of friction and apparent cohesion for intact specimens of Clay B.

	C′ (MPa)	ϕ′ (°)
Peak strength of non-exposed specimens and exposed specimens with no micro-fracture	3.11	19
Peak strength of exposed specimens with microfractures	2.55	21
Residual	0.00	25

As discussed earlier in Chapter 6, microfractures are generally linked to the depth of the specimen rather than the exposure procedure. However, it is difficult to determine definitively whether the reduced strength of this specimen is due to exposure or due to microfractures.

It is well known that the peak strength envelope of stiff clays is non-linear, while the residual strength envelope is linear. It is not surprising that the fitting peak friction angle is smaller than the residual one, as it proceeds from a linearization. The apparent cohesion has no physical meaning, but it is only an intercept of this linearization. A complete strength envelope would require tests at wider stress ranges including low stresses. The inclusion of such tests would impose a curved envelope as proposed by Ciancimino et al., (2024). In Figure 7.5 more tests are included at lower stress state. These tests were carried out at Eni laboratories, under stress-controlled conditions with stress rate $\dot{q}$ = 300 kPa/min on non-exposed samples.

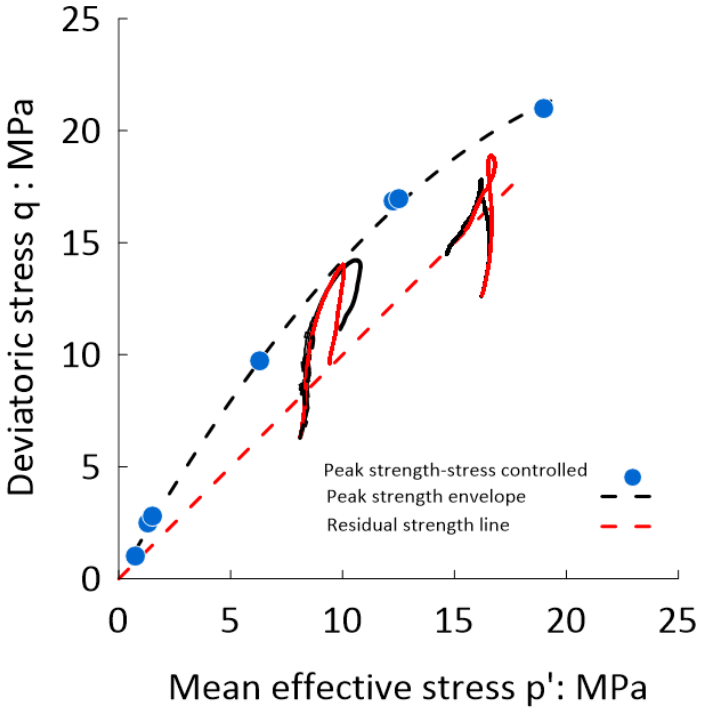

Figure 7.5 Curved strength envelope when tests at different stress state are included.

7.4 Results of the oedometer tests on intact specimen of Clay B

For the oedometer tests, the smaller diameter oedometer cell was used. High vertical loads reaching up to 25 MPa can be applied in this oedometer. One specimen (B-I-T_{WCO2}S14-Oed) was exposed to wet $scCO_2$ for 14 days before testing, and the other (S-I-N-Oed) was tested in its original condition.

Figure 7.6 shows the compression curves for both specimens.

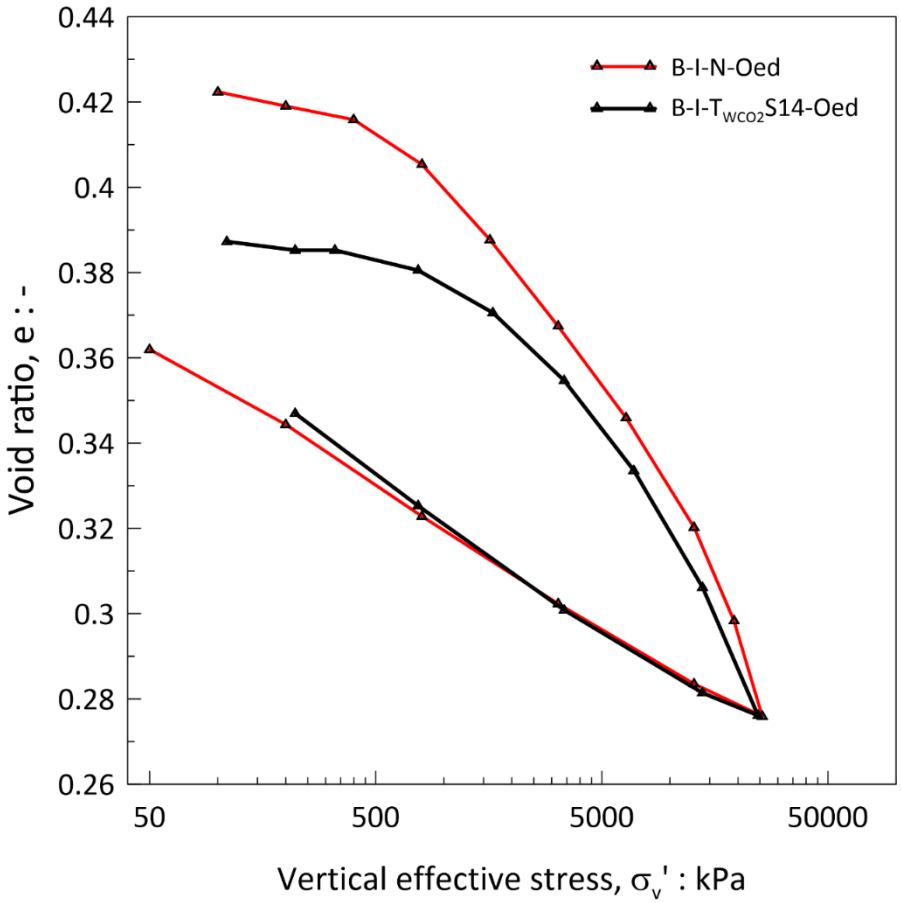

Figure 7.6 Oedometer test conducted on exposed and non-exposed intact specimens of Clay B material.

For the non-exposed specimen (B-I-N-Oed) the compression index (C_C) obtained from the (log-linear) part of the test is 0.085 whereas the swelling index (Cs) is 0.032 (obtained at the stress level between 13.9 MPa and 0.2 MPa). For the exposed specimen (B-I-T_{WCO2}S14-Oed) the Cc is 0.08 and Cs is 0.036. The exposed specimen has a comparatively lower void ratio at the start of the test and also has a lower Cc value, whereas the void ratios at the maximum vertical stress are almost the same.

The minimum and maximum pre-consolidation pressure was evaluated by drawing two tangent lines as shown in Figure 7.7 suggested by Casagrande (1936).

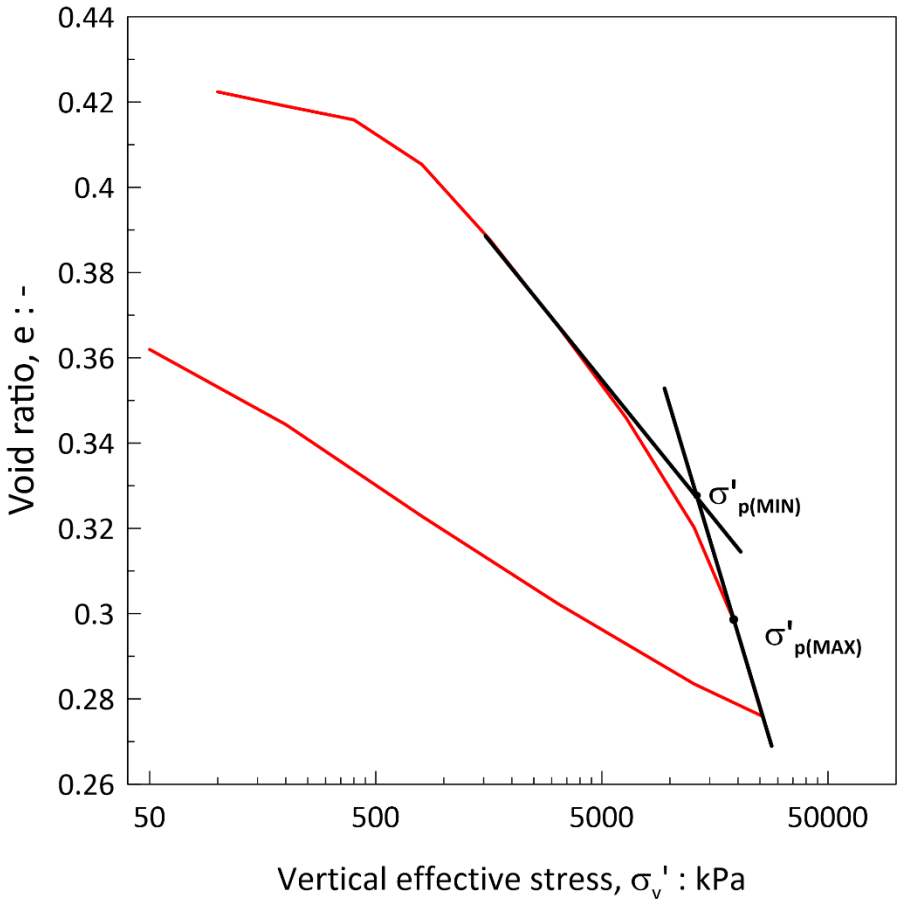

Figure 7.7 Maximum and minimum pre-consolidation stresses of intact specimens of Clay B.

Both exposed and non-exposed specimens have almost similar maximum and minimum pre-consolidation pressures. The maximum apparent pre-consolidation stress ($\sigma'_{P(MAX)}$) by the Casagrande method resulted to be around 19 MPa and the minimum apparent pre-consolidation stress ($\sigma'_{P(MIN)}$) is around 14 MPa. The pre-consolidation stress is between these two values and closer to $\sigma'_{P(MIN)}$ and by further following the Casagrande approach it is estimated to be around 16 MPa.

7.5 Results of triaxial tests for reconstituted specimens of Clay B exposed to wet $scCO_2$

Three reconstituted Clay B specimens—B-R1-T_{WCO2}S30-3, B-R1-T_{WCO2}S30-6, and B-R1.5-T_{WCO2}S30-6—were exposed to wet $scCO_2$, while four analogous samples—B-R1-N-3, B-R1-N-6, B-R1.5-N-6, and B-R3.0-N-6—were only reconstituted, maintaining the same loading history. Table 7.6 summarizes the number of tests conducted on different specimens.

Table 7.6 Different triaxial tests conducted on exposed and non-exposed specimens.

	Original state	**Exposed**	
	Specimen ID	**Specimen ID**	**Notes**
OCR=1 ($\sigma_r' = 3$ MPa)	B-R1-N-3	B-R1-T_{WCO2}S30-3	
OCR=1 ($\sigma_r' = 6$ MPa)	B-R1-N-6	B-R1-T_{WCO2}S30-6	Originally planned but not conducted as the specimens were contaminated by the pump oil during exposure.
OCR=1.5	B-R1.5-N-6	B-R1.5-T_{WCO2}S30-6	
OCR=3.0	B-R3.0-N-6		

Figure 7.8 shows the result of the triaxial test conducted on reconstituted specimens before exposure. The normally consolidated ones (B-R1-N-3 and B-R1-N-6) show a contractive behavior with an increase in overpressure. Deviatoric stress increases to a maximum value of around 1.5% of axial strain and then a slow decrease is observed.

In the case of the specimen with OCR 1.5 (B-R1.5-N-6) the maximum deviatoric stress is higher than the normally consolidated specimen (B-R1-N-6). In this case, the specimen initially exhibits dilatant behavior followed by contractive behavior.

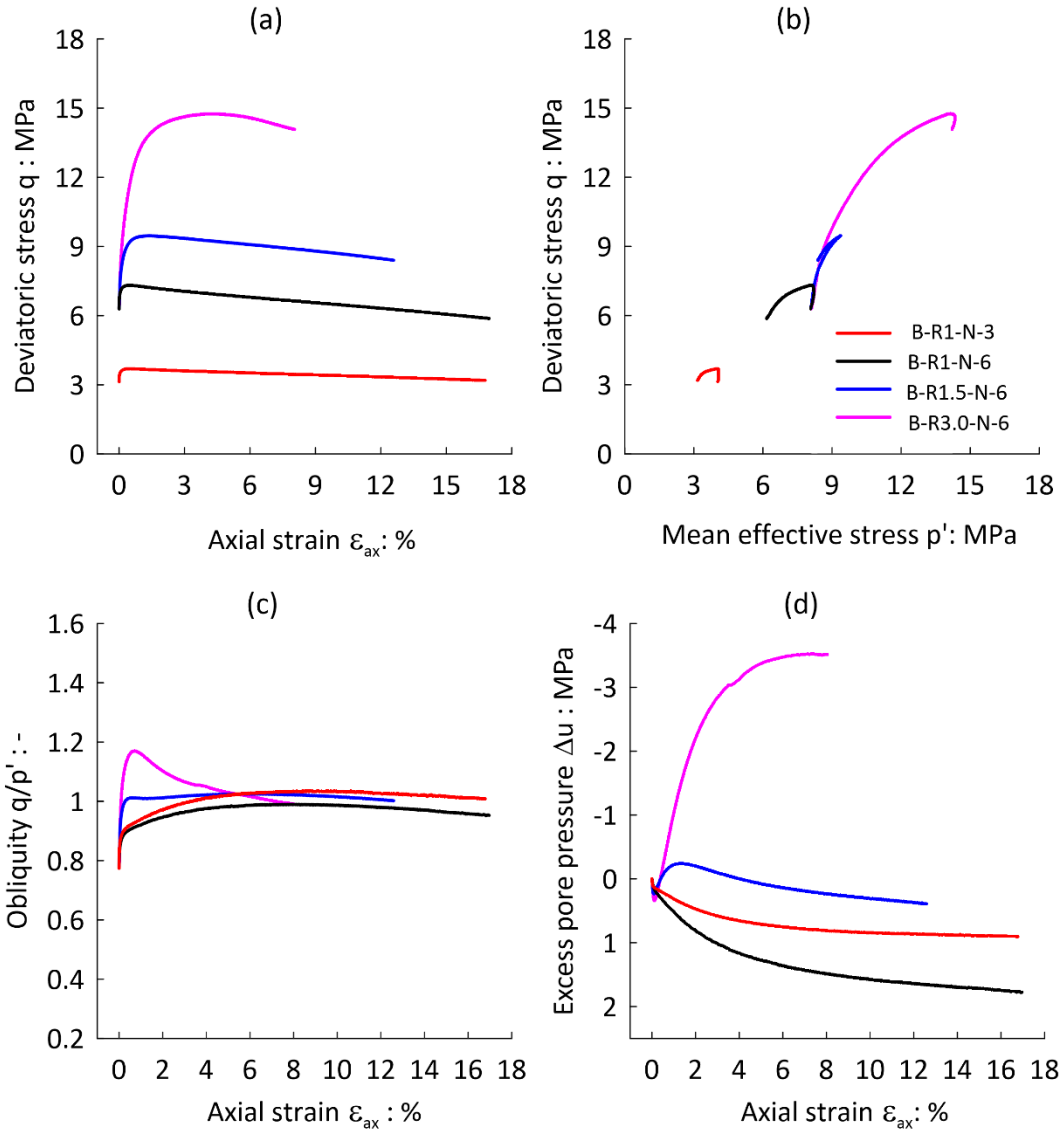

Figure 7.8 Effect of OCR on the mechanical response of non-exposed reconstituted Clay B specimens.

The specimen with OCR 3.0 (B-R3.0-N-6) exhibited a typical dilatant behavior. The deviatoric stress increased to values on the order of 14 MPa (Figure 7.8 (a)) for an axial strain ϵ_{ax}= 3% and then it reduced. Very dilative behavior can be appreciated, with an initial increase in pore pressure followed by a drastic decrease and final stabilization. The obliquity values at the end of the shearing phase were about q/p'=1 in all tests (Figure 7.8 (c)).

The only specimen which was triaxially tested after exposure was B-R1-T_{WCO2}S30-3 and the results are shown in Figure 7.9. The results of this exposed specimen are compared with the non-exposed specimen (B-R1-N-3).

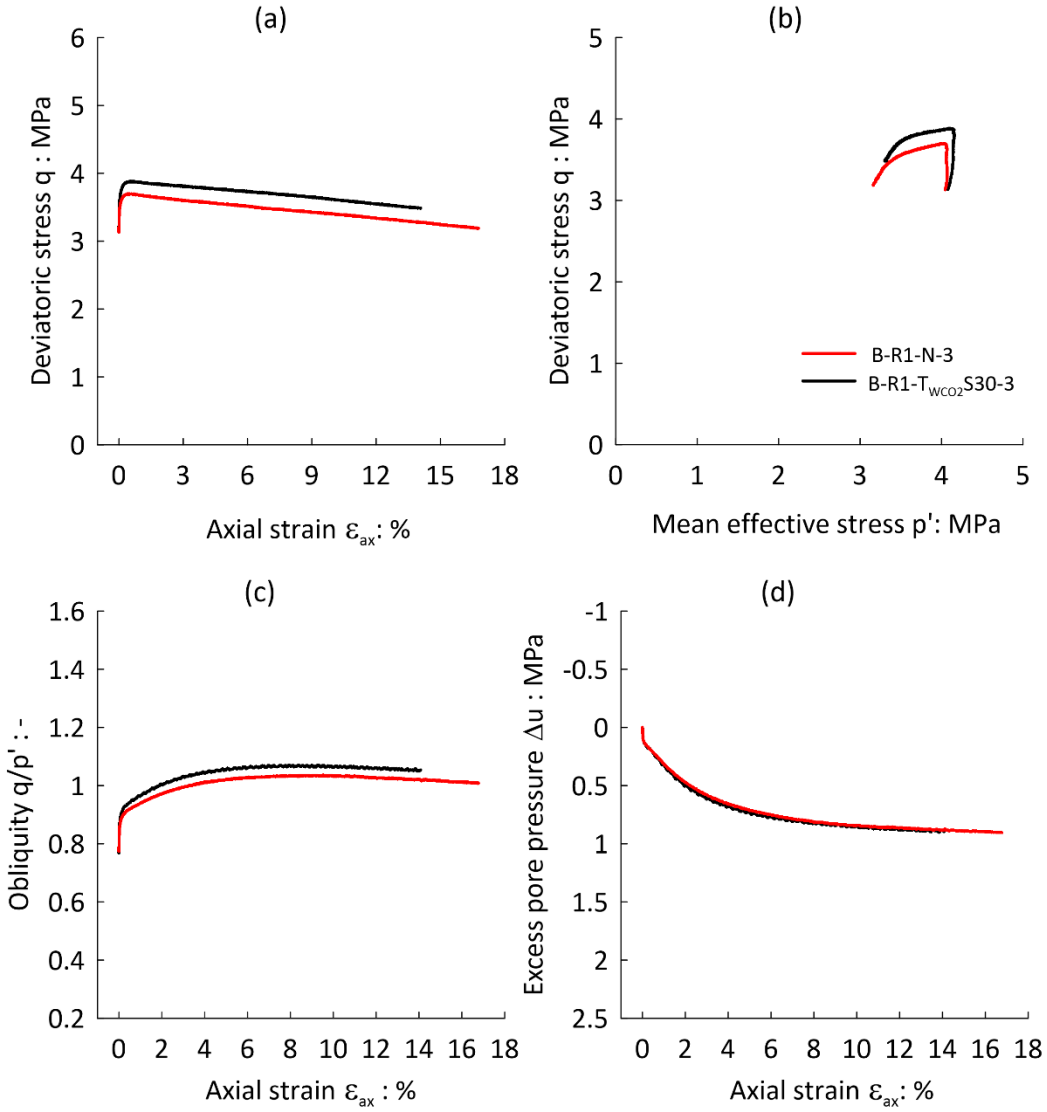

Figure 7.9 Results of undrained triaxial tests conducted on B-R1-T_{WCO2}S30-3 and B-R1-N-6.

Both specimens showed contractive behavior with an increase in pore pressure. The Maximum deviatoric stress was observed around 1.5% of the axial strain, then a slow decrease can be observed (Figure 7.9 (a)). The exposed specimen B-R1-T_{WCO2}S30-3 showed a slightly higher value of maximum deviatoric stress. The obliquity values at the end of the shearing phase were about q/p'=1.05 for B-R1-T_{WCO2}S30-3 and 1.01 for B-R1-N-3.

The other two exposed specimens were planned to be tested but they were polluted with oil during the exposure procedure. Therefore the tests were not performed on these specimens.

7.6 Results of triaxial tests of reconstituted specimens from exposed powder of Clay B

As discussed earlier in the chapter, slurry powder of Clay B was exposed to wet $scCO_2$ for 14 and 30 days. Two specimens were prepared from this exposed powder and were tested at OCR 1 and 1.5 after 14 and 30 days.

7.6.1 Results of tests on specimens reconstituted with 14 days of exposed powder

Two specimens, identified as B-R1-T_{WCO2}P14-6 and B-R1.5-T_{WCO2}P14-6, were tested under triaxial conditions after being prepared with powder exposed to wet $scCO_2$. The results of these tests are compared with the non-exposed reconstituted samples as shown in Figure 7.10. The red lines represent the non-exposed specimens, while the grey lines indicate the specimens prepared from the powder that was exposed for 14 days.

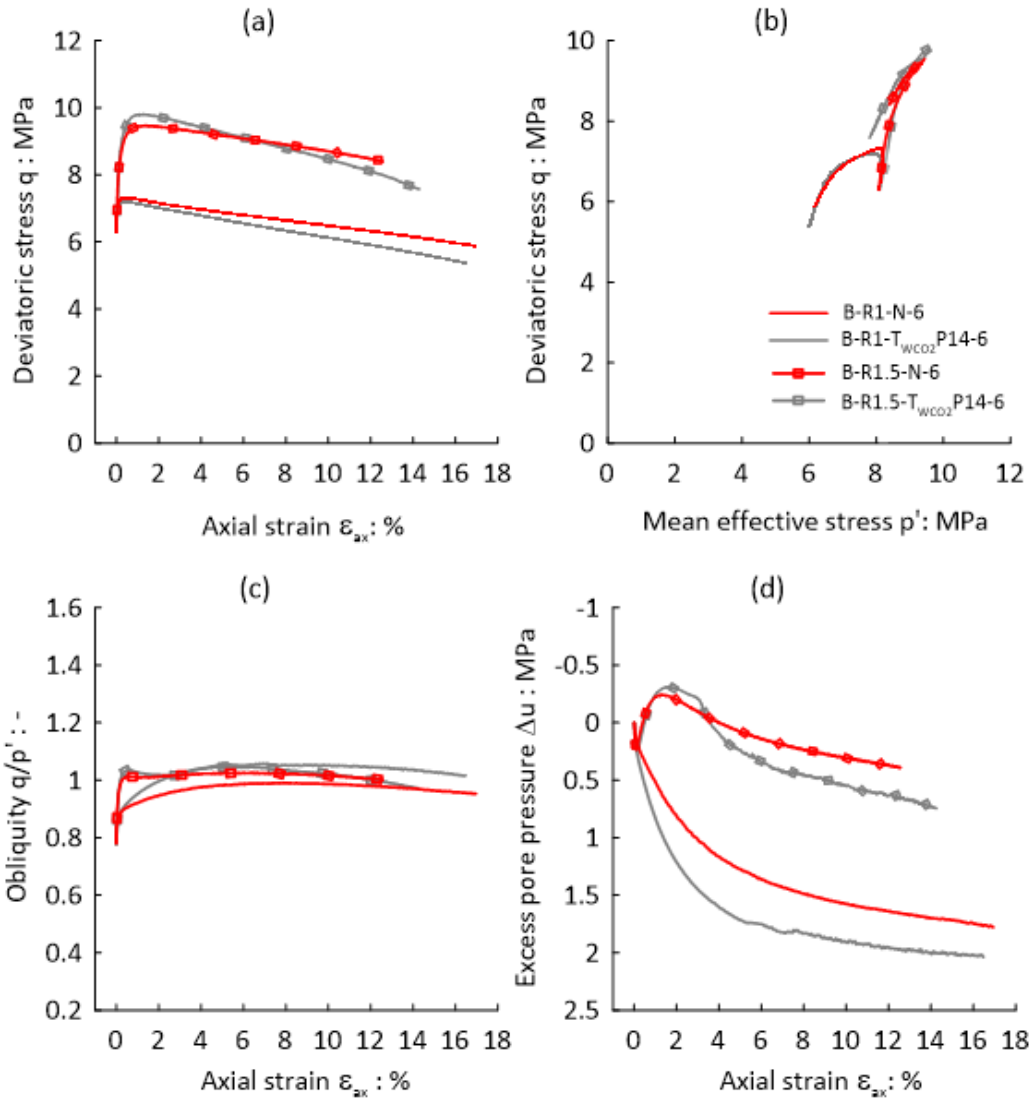

Figure 7.10 Results of undrained triaxial tests conducted on reconstituted specimens of Clay B, prepared both from non-exposed and 14 days exposed powder. The confining stress is 6 MPa with OCR=1 and OCR=1.5.

The specimens prepared with exposed powder have similar stress paths as non-exposed specimens. The specimens with OCR=1 (continuous black and red lines) have almost identical maximum deviatoric stress of 7.17 MPa at around axial strain of around 0.4%. After the peak, the deviatoric stress of both specimens gradually decreased.

The specimens showed a contractive behavior with an increase in the over-pressure (Figure 7.10 (d)). The specimen B-R1-T_{WCO2}P14-6 shows more contraction as compared to B-R1-N-6. In terms of q/p' both specimens show a gradual increase and eventually attain a constant value of around 1.

The specimen with OCR=1.5 (black and red lines with symbol) exhibits a dilatant behavior initially with a decrease in pore pressure and then a contractive behavior after around 2% of axial strains. For these specimens also the q/p', at the end of the test reaches a constant value of around 1 after an initial rapid increase.

It can then be concluded that the exposure of the soil powder to wet $scCO_2$ and the reconstitution of samples resulted in behavior that was completely similar to that of the samples prepared with the original powder.

7.6.2 Results of tests on specimens reconstituted with 30 days exposed powder

Two triaxial tests were carried out on specimens prepared from powder exposed to wet $scCO_2$ for 30 days. The specimen B-R1-T_{WCO2}P30-6, shown with continuous black line in Figure 7.11 exhibited a similar stress path as the non-exposed specimen (B-R1-N-6 in continuous red line). In the case of specimen B-R1.5-T_{WCO2}P30-6 (black line with symbol), the maximum deviatoric stress (Figure 7.11 (a)) has increased slightly as compared to non-exposed specimen B-R1.5-N-6 (red line with symbol). In terms of stress obliquity, all the specimen has similar values towards the end of the test (Figure 7.11 (a)). The specimens with OCR equal to around 1 show contractive behavior and the two specimens are identical, whereas the specimens with OCR 1.5 showed a moderately dilatant behavior. The specimen B-R1.5-T_{WCO2}P30-6 shows a gradual contraction after the dilation peak. This contraction after dilation is comparatively slow in the case of B-R1.5-T_{WCO2}P30-6 (Figure 7.11 (d)). The specimen B-R1-T_{WCO2}P14-6 showed more contraction as compared to the other two specimens.

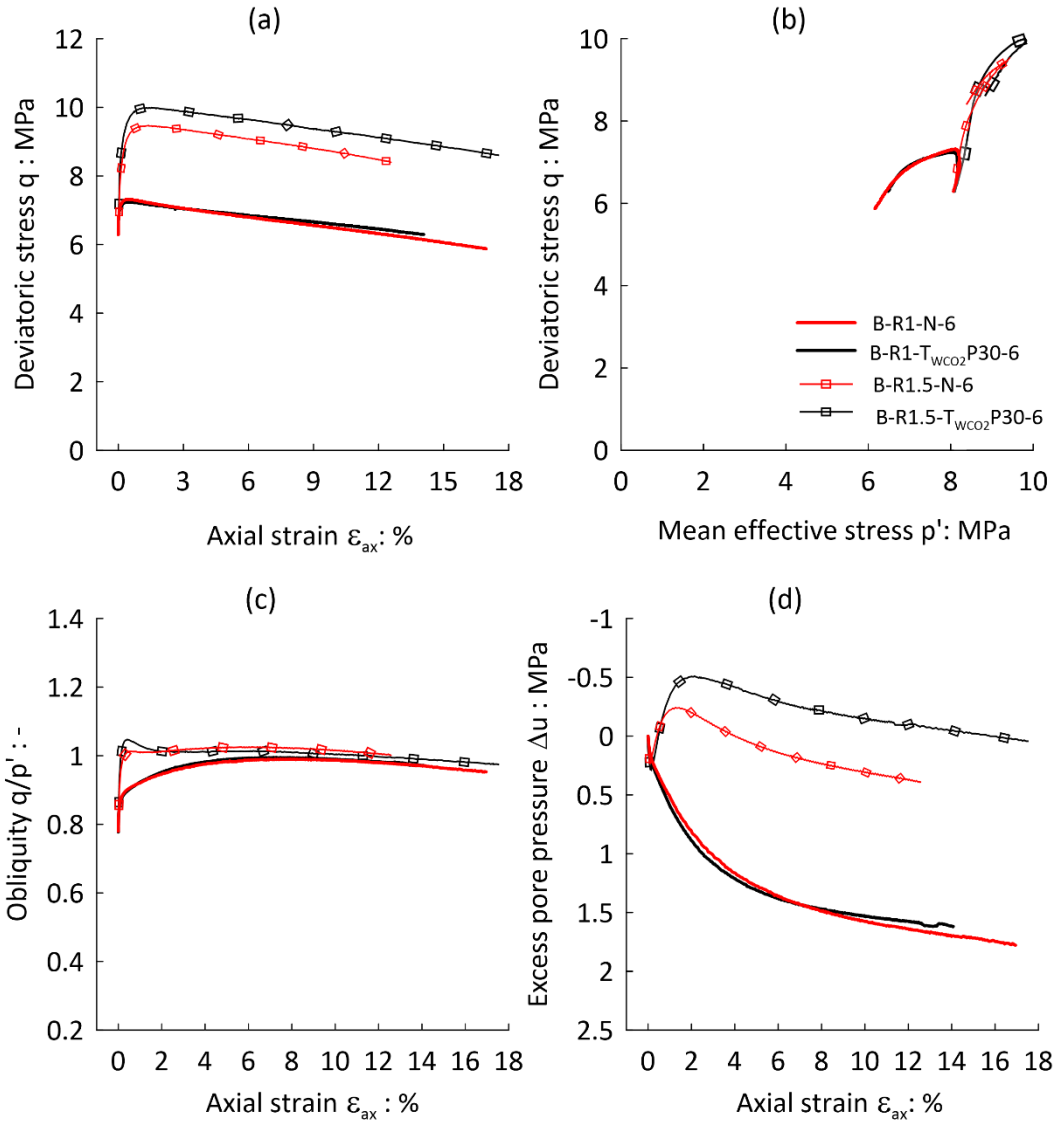

Figure 7.11 Results of triaxial tests on Clay B specimens reconstituted from non-exposed and 30 days exposed powder.

In Figure 7.12 the comparison of all the samples prepared with non-exposed powder and exposed powder is presented. Red lines are for the non-exposed samples, grey lines for 14 days exposed powder and black lines for 30 days exposed powder. The continuous lines are for OCR 1 specimens and the line with symbols are for OCR 1.5. Powder exposure induced a slight increase in the maximum deviatoric stress as observed especially in the case of OCR 1.5 (Figure 7.12 (a)). For OCR 1 no changes in terms of maximum deviatoric stress are noticed.

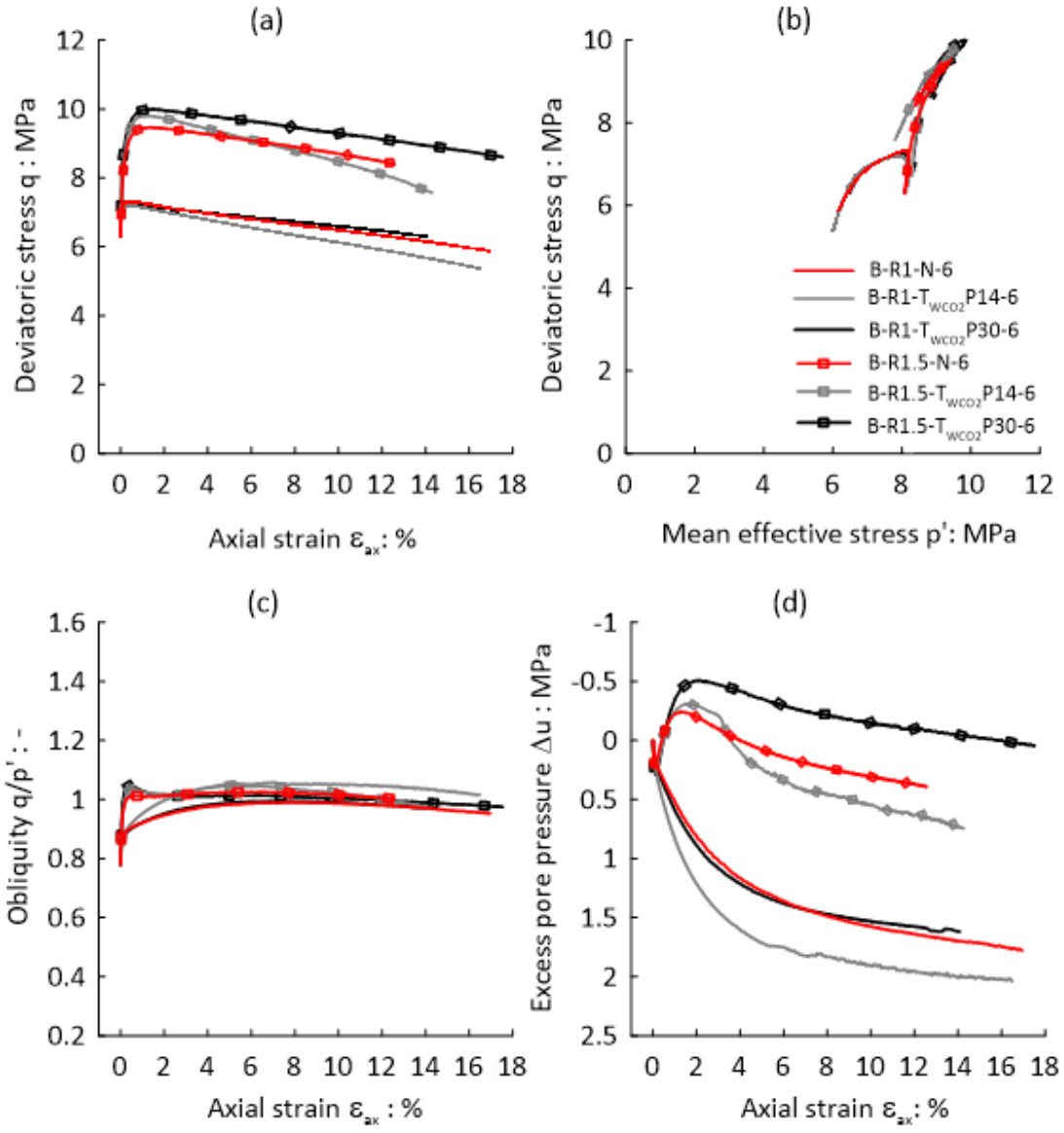

Figure 7.12 Results of triaxial tests conducted on Clay B specimens reconstituted from non-exposed, 14 days and 30 days exposed powder at radial stress of 6 MPa with OCR 1 and 1.5.

The specimens at OCR 1 (both exposed and non-exposed) show contractive behavior, slightly more evident for specimen B-R1-T_{WCO2}P14-6 (Figure 7.12 (d)).

The specimens with OCR 1.5 initially showed a dilatant behavior, followed by a contractant one. The contractant behavior of the specimen whose powder was exposed for 30 days, B-R1.5-T_{WCO2}P30-6 was less marked as compared to the specimen with shorter exposure period (B-R1.5-T_{WCO2}P-14-6) and non-exposed specimen (B-R1.5-N-6). In terms of stress obliquity (q/p'), the values range between 1.01 to 1.05 towards the end of the test.

7.7 Conclusions

The mechanical effects of the adopted exposure procedure were found to be null or, in a limited number of cases, very minor. The strength of Clay A normally consolidated specimens increased very slightly after 14 days of exposure to dry scCO_2 and, to an even smaller extent, after 14 days of exposure to CO_2 saturated brine. This specimen also showed negligibly less contraction during shearing as compared to the non-exposed and the specimens exposed to CO_2-saturated brine. The superficial wear and tear of the sample exposed to CO_2 saturated brine did not affect the mechanical behavior of the sample significantly.

The initial stiffness of Clay B intact samples exposed to wet CO_2 was found to be smaller as compared to one of the non-exposed samples. Some samples (the ones with micro fissures) showed a smaller peak strength which might be related to microfractures that were detected with post-exposure CT scans. In most cases CT scan was performed with not enough detail before exposure, however detailed CT scan analysis performed on one specimen suggests that the micro fractures were present before exposure so it likely depends on the in-situ state or on the coring conditions. The exposed specimen having no micro fractures showed a similar peak strength to the non-exposed sample but with less brittle failure. This sample also showed a post-peak softening with higher residual strength. This effect might be related to the exposure procedure; however, only one sample under these conditions is available to support these conclusions.

The oedometer tests conducted on exposed and non-exposed intact samples of Clay B also showed no significant change in the mechanical behavior. The exposed sample exhibited slightly lower void ratios at the beginning of the test. The exposure of the sample to wet scCO_2 did not affect its pre-consolidation pressure.

The non-exposed reconstituted specimens of Clay B demonstrated that specimens with an overconsolidation ratio (OCR) of 1 exhibited contractive behavior. The specimen with an OCR of 1.5 initially showed dilative behavior, followed by contractive one. In contrast, the sample with an OCR of 3 displayed dilative behavior when subjected to shearing. However, these samples recorded similar values of stress obliquity at the end of the test. When comparing the mechanical response of sole exposed specimen with the non-exposed sample conducted at half the in-situ stress state, a slight increase in peak strength can be observed; however, the overall behavior is similar.

No remarkable effects were detected in the case of reconstituted Clay B specimens prepared starting from exposing the soil in the slurry state to CO_2 for 14 and 30 days.

Chapter 8 Design and set up of an advanced oedometer for Multiphysics testing

In the early chapters, it is mentioned that the storage of CO_2 is a long-term process. The injection of CO_2 into saline aquifer acidifies the pore water and the geochemical reactions of minerals with the acidic water have slow kinetics. The time scale required for such projects typically spans hundreds to thousands of years (Benson & Cole, 2008). However, the duration available for laboratory testing is significantly shorter. Flowthrough experiments have been mostly conducted in literature to study the short-term effects of CO_2 injection and accelerate the process of CO_2 reaction with rock minerals (Rohmer et al., 2016). These experiments involve injecting CO_2 in various forms, such as supercritical dry, water-saturated, brine-saturated with CO_2 or in general acidic solutions. Generally, triaxial cells and oedometer cells are modified for flowthrough experiments. Among others, Le Guen et al., (2007) and Falcon-Suarez et al. (2017) carried out flowthrough experiments on geomaterials in modified triaxial cells.

In this study, flowthrough experiments to study the short-term effect of CO_2 injection were performed in an advanced oedometer specifically designed and built for this thesis. The oedometer is equipped with electrodes for Electrical Resistivity Tomography (ERT) and ultrasonic wave transducers. The ERT is utilized to monitor changes in the electrical conductivity of the specimen, which can be related to changes in the pore fluid composition, the degree of saturation and the fabric. The purpose of ultrasonic wave transducers is to track the evolution of ultrasonic wave velocities, which can be related to sample saturation, porosity and fabric changes.

This chapter describes the experimental setup and the calibration of its various components. It begins with an introduction to the electrical resistivity setup, detailing its operation and the measurement protocols. Next, it presents the inversion of electrical conductivity data obtained from a simulated flushing test, along with an open-source code that was used for this purpose. Finally, the chapter introduces the setup and calibration of ultrasonic wave transducers and discusses the interpretation of the signals they produce.

8.1 Advanced oedometer set-up

The conceptualization and development of the advanced oedometer was carried out at the DISEG department at Politecnico di Torino. This apparatus is an enhanced version of the EIT oedometer described in Comina et al. (2008). The advanced oedometer was built with a corrosion resistant INOX AISI 304, enabling it to withstand the harsh conditions of low pH solutions. The oedometer is equipped with 16 electrodes for Electrical Resistivity Tomography (ERT) and piezoelectric transducers for ultrasonic wave testing. The oedometer can host a sample having diameter of 50 mm and maximum height of 25 mm. The load is applied through a piston installed on the top cap (Figure 8.1)

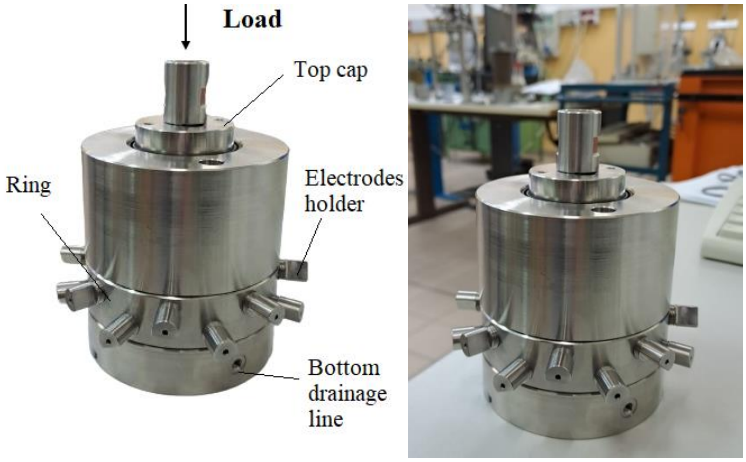

Figure 8.1 Setup of the advanced oedometer.

Drainage paths are provided at the bottom and top of the oedometer for the advection of fluids and pore pressure controls.

8.1.1 Electrodes for Electrical Resistivity Tomography

ERT is a tomography technique which aims at assessing the electrical conductivity distribution within a body, starting from electrical measurements taken from its periphery by means of electrodes. ERT can be used to image subsurface soil and rock properties, such as porosity, water content, and clay content. It also has vast applications in environmental geotechnics, hydrology, and other soil sciences such as agriculture. Cosentini et al. (2012) have listed some of the geotechnical engineering applications at laboratory scale, where besides allowing imaging of the sample, ERT can be used to track evolutions of the sample degree of saturation (Cosentini et al., 2012) or changes in the pore fluid composition (e.g. Comina et al., 2011). Falcon-Suarez et al., (2018) in their brine-CO_2 flowthrough tests simulated CO_2 injection and withdrawal on Sleipner core sample. The authors conducted controlled inflation and depletion cycles on the core sample to assess how CO_2-brine interactions affect the rock's properties while measuring

ultrasonic waves together with electrical resistivity.

In the advanced oedometer, 16 electrodes for ERT are placed on the specimen side, evenly distributed in two levels, with 8 electrodes in each level. The two levels of electrodes are at elevations 8 mm and 17 mm from the bottom of the sample. The top and bottom electrodes are offset by 22.5° so that they do not fall on the top of each other, their position is shown in Figure 8.2. Figure 8.2 (a) is a drawing section that shows their position at the bottom layer, whereas Figure 8.2 (b) shows the position of the electrodes of both layers. Figure 8.2 (c) is a picture of the central and bottom body of the oedometer with the electrode holders inserted. The electrodes are made of 0.8 mm stainless steel wires and insulated with plastic insulators (green colour insulators in Figure 8.2 (d). These insulators are heated on the electrodes for better adhesion. The electrodes are inserted into the specimen and are held in place with the help of O-ring, plastic holder and screws. After tightening the screws, the plastic holder applies a pressure on the O-ring which prevents the electrodes from moving back and also constraints the fluid within the oedometer. The electrode, O-ring, plastic holder and the screws are shown in Figure 8.2 (d).

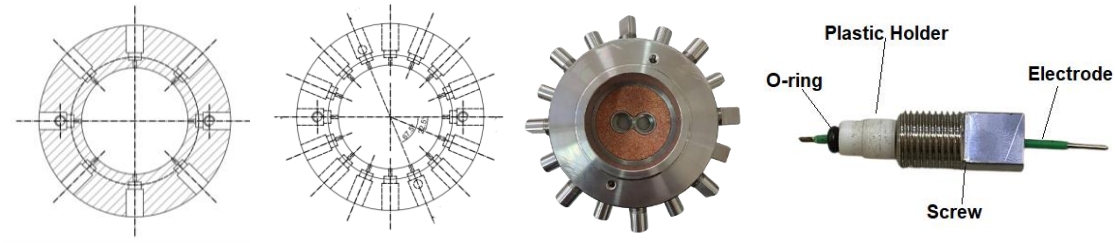

(a) (b) (c) (d)

Figure 8.2 Distribution of electrodes around the periphery of the oedometer ring and the electrode fixing mechanism.

The stainless steel used to build the oedometer and the ring is electrically conductive, however, for ERT purposes the electrical current must be confined within the specimen. This required insulation of the inner part of the ring. An insulating paint from PIT colour S.A.S (serie 6000 rivestimento isolante epossidico) was used for this purpose initially. After some initial trial tests, the paint peeled off due to lack of adhesion. The issue of adhesion was solved by substituting the paint with a 3D printed, 0.5-mm-thick plastic ring. The plastic ring was adhered to the main ring using epoxy resin. The original diameter of the oedometer ring was 51 mm and the application of the 0.5-mm insulation reduced the effective diameter to 50 mm, which was the desired size. The positions of the electrode holes in the plastic ring (illustrated in Figure 8.3 with blue colour plastic) were carefully aligned with those on the main ring.

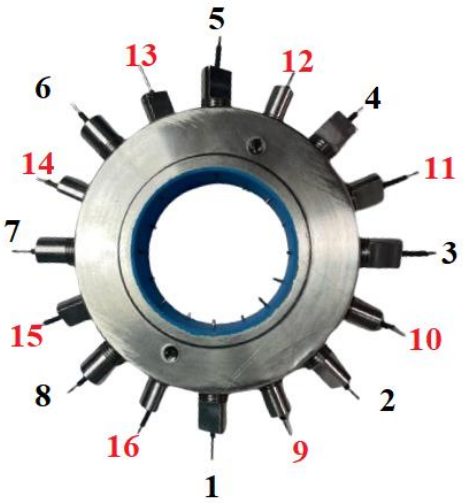

Figure 8.3 Oedometer ring with 3D plastic insulation and electrodes. Black numbers refer to top level electrodes, and red numbers refer to bottom level electrodes.

The material of the plastic ring was also investigated for its resistance to the adverse effects of acidic solutions. For this purpose, plastic ring was immersed in hydrochloric acid (HCl) with a pH=1 for more than 30 days. The same procedure was repeated also using an HCl solution with pH=0. The weight of the plastic ring was measured before and after immersion to assess any changes in mass, which were found to be practically null.

Two different schemes were tested for the insertion of the electrodes. According to the first one, electrodes are stainless steel rods pushed into the specimen (Figure 8.3). The advantage of this scheme is that it ensures adequate contact between specimen and electrodes. However, as electrodes are inserted into the specimen, they might affect the free movement of the soil specimen when a large vertical displacement occurs. Although this is a local perturbation which might have negligible consequences on the mechanical response, another ring with flat shaped electrodes was also designed. The 'head' of the electrodes was in this case a square silver plate with 2 mm side, welded to the silver rods and positioned in recesses specially made in the plastic ring, as shown in Figure 8.4, where the 3D printed plastic ring is in white.

Figure 8.4 Oedometer ring with flat-shaped electrodes.

The Complex Impedance Tomograph (CIT) (introduced in Chapter 4) was used to inject electrical current from two electrodes and acquire the electrical potential from two others.

Electrical conductivity of the porous stones

To ensure that the electrical current injected during the tests propagates exclusively within the specimen, the porous stones used at the top and base of the oedometer must be electrically resistive as compared to the soil and the liquid used for the flowthrough experiments. The actual value of their electrical conductivity when saturated with water solution with a relatively high concentration (1 M NaCl solution, electrical conductivity of about 80 mS/cm) was determined using a multimeter (Hewlett Packard-34401A). Two steel disks of 8 mm radius were connected to the electrodes of a multimeter for better contact between porous stone and electrodes as shown in Figure 8.5.

A resistance value of around 40 kOhm was obtained for the saturated porous stone. The experiment was then numerically reproduced using the Finite Element (FE) software *COMSOL Multiphysics*®, where the electrical conductivity was changed by trial-and-error method until obtaining the resistance measured in the experiments.

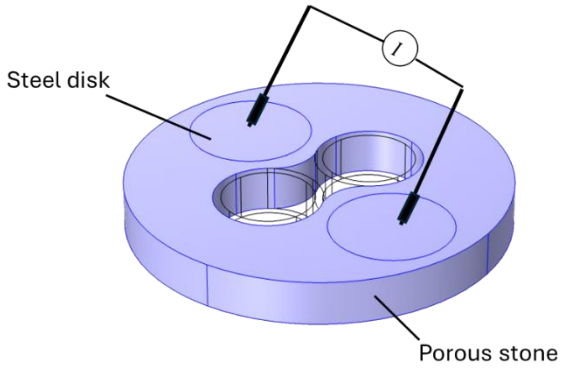

Figure 8.5 Scheme of the porous stone resistance measurement.

In *COMSOL* the "Electric Currents (ec)" physics was used for this purpose. The measured resistance value of 40 kOhm was well reproduced by adopting an electrical conductivity of 0.008 S/m for the saturated porous stone. As such electrical conductivity is very small compared to the expected one of the tested soils, the porous stones were considered not to affect the electrical measurements. Such a conclusion is also confirmed by the good agreement between experimental electrical measurements taken filling the oedometer ring with saline solutions, in touch with the saturated porous stones, and the results of numerical simulations where the stones were considered fully resistive, presented in Section 8.2.5.

8.1.2 Ultrasonic waves transducers

The device used in the oedometer utilizes non-interfering piezoelectric elements specialized for the detection of P-waves and S-waves. Flat-shaped piezoelectric elements with a square cross-section, produced by CTS/Noliac, have been employed—one for compression (P) waves and the other for shear (S) waves. The multilayer piezoceramic elements were encapsulated in a custom-made metal mould and then coated with special epoxy resins. The ultrasonic wave transducers allow to investigate the changes in the elastic properties of the geomaterial at small strains as the injecting fluid reacts with the geomaterial over time, therefore altering its structure or affecting the degree of saturation, or as the effective stress evolves. These transducers for P and S waves are placed at the base and top cap of the oedometer. The porous stones at the bottom and top base were cut accordingly to accommodate the two transducers, as shown in Figure 8.6.

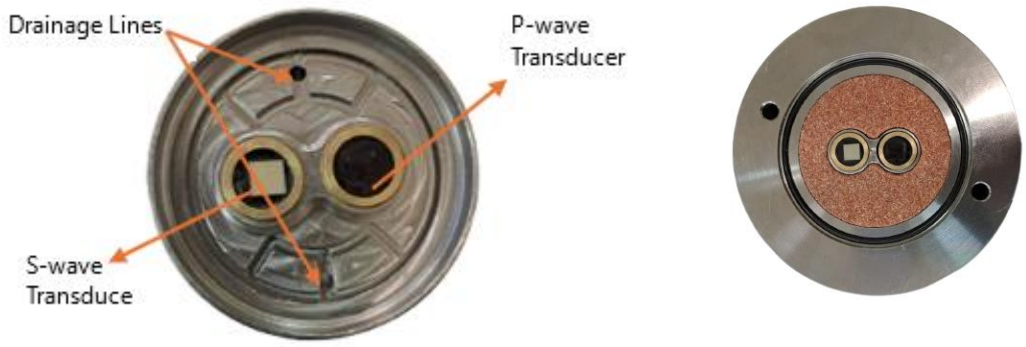

(a) (b)

Figure 8.6 Top and bottom base of the advanced oedometer with ultrasonic wave transducers. (a) drainage lines and grooves for spreading the fluid are evident. (b) These lines and grooves are covered by porous stones for testing in image.

8.1.3 Hydraulic loads and drainage paths

In flowthrough experiments fluids are injected through the sample by imposing a pressure difference across the sample. The oedometer has drainage lines at the base and top which are shown in Figure 8.6 (a). The injected fluid must be distributed as equally as possible over the specimen. To this aim lateral grooves were provided making it easy for fluids to spread before entering the porous stones, and eventually, the sample, as shown in Figure 8.6 (a). The bottom drainage lines are used to inject the fluid and are connected to a GDS pump. Porous stones were then placed over the drainage grooves (Figure 8.6 (b)). During the tests, filter paper sheets were placed between the specimens and the porous stones to prevent the material from clogging the porous stone and drainage lines, and the effluent was collected from the top drainage lines in a vessel or beaker. The fluid pressure/flow rate imposed in the tests was controlled by a corrosion-resistant pump manufactured by GDS instruments (HPDPC-H) (introduced in Chapter 4).

The definition and calibration of the protocol for ERT and ultrasonic measurements are described in the following sections.

8.2 Working and calibration of electrical resistivity setup

Before running tests, the electrical setup was calibrated to minimize errors that could impact subsequent ERT inversions. A key objective was to ensure that no electrical bridges formed between the specimen within the oedometer ring and the surrounding stainless-steel components, which could severely distort the resistivity measurements.

This was done with an analysis of geometrical factors, *i.e*. the ratio between the apparent resistance detected by two electrodes used to measure the electrical potential drop and the resistivity of the body onto which they are applied, supposed as homogeneous. The experimental geometrical factors were determined by filling the oedometer ring with salt solutions with known electrical conductivity: those were then compared with the results of simulations run with the FE code *COMSOL Multiphysics*®. Once the existence of electrical bridges was excluded, experimental and numerical data were also used to define a protocol for the electrical measurements. This protocol was then adopted for resistivity inversions made with the *ResIPy* software, as described in the following section.

8.2.1 Quadripoles for electrical resistivity measurement and geometrical factors

Electrical resistivity ρ, or its inverse electrical conductivity σ, is a basic parameter in electromagnetism and represents the capacity of a given material to resist the flow of electric current when an electric field is applied. As far as soils are concerned, the resistivity ρ is primarily dependent on the resistivity of the pore fluid ρ_f, the structure of the pores, the mineralogy of the solid grains, and more specifically the diffuse double layer for clayey soils, water content, saturation, temperature, etc. (see e.g. Klein and Santamarina 2003). Empirical correlations between ρ and different soil and fluid parameters have been established (e.g., Archie 1942; Keller and Frischknecht 1966; Gupta and Hanks 1972).

The electrical measurements which were used to feed the ERT were based on a traditional four-electrode measuring scheme, in which the electric current (I) is injected through a pair of electrodes (in the following A and B) and the potential difference (ΔV) is measured by another pair of electrodes (in the following M and N), as discussed in Section 4.14 of Chapter 4.

Assuming that the investigated body is homogeneous, the (apparent) resistance R read by a given quadripole is

$$R = \frac{\Delta V}{I} \tag{8.1}$$

This resistance is linearly related to the resistivity of the medium through the expression:

$$R = \rho\kappa \tag{8.2}$$

where κ (Length^{-1}) is a geometrical factor which only depends on the problem geometry (distance between the electrodes, their mutual position, size and shape of the

specimen). In the following, κ will also be called cell constant, as it will be used to link specific resistance measurements to the equivalent homogeneous resistivity of the specimen.

A comparison between geometrical factors obtained experimentally and obtained through numerical simulations was performed, to check both the proper functioning of the experimental apparatus and to determine which quadripoles might provide significant measurements to be used in ERT reconstructions.

8.2.2 Protocol of measurements for 3D inversion

For the reconstruction and inversion of electrical resistivity data, it is important to identify the protocol of measurements. For the reconstruction of electrical conductivity maps of a heterogenous specimen many measurements are required. The number of measurements is limited by time and resources required for the data acquisition and inversion. On the other hand, few measurements will result in an inversion of lower resolution. In this study, three different sequences of measurements were studied to identify which electrical measurements could provide a good reconstruction of electrical maps. The significant measurements from each sequence were merged into the protocol adopted for ERT 3D reconstructions.

In the first sequence, the current-injecting and the potential-measurement electrodes are on the same level. In the following, the sequence is described referring to the top level of electrodes (electrodes 1-8). Different combinations of electrodes were used. For instance, having electrodes 1 and 2 where current is injected (A-B=1-2) and electrodes 3 and 8 where the potential drop is measured (M-N=3-8), as shown in Figure 8.7. The A and B remain fixed while the potential measuring electrodes change to 3-7, 3-6 and 3-5 etc. Then the current injecting electrodes were changed to 1,3 (A-B=1-3) and the potential measuring electrodes were changed among the other possible pairs in the plane. In this sequence, electrode 1 was fixed as ‘A’ electrode.

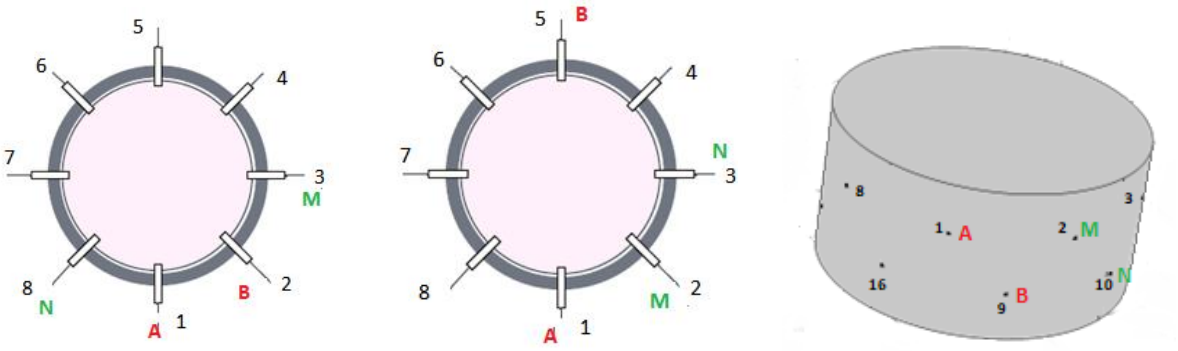

(a) (b) (c)

Figure 8.7 Examples of quadripoles for the three different sequences of measurements used in this study.

This collection of measurements requires 105 quadripoles, per level as shown in Table 8.1. By applying the same scheme also for the bottom level of electrodes, 210 quadripoles are adopted by the first sequence.

Table 8.1 Quadripoles of electrodes for sequence 1, top level.

Current injection electrodes (A-B)	Voltage measurements electrodes (M-N)
1-2	3-8, 3-7, 3-6, 3-5, 3-4 4-8, 4-7, 4-6, 4-5 5-8, 5-7, 5-6 6-8, 6-7 7-8
1-3	2-8, 2-7, 2-6, 2,5, 2-4 4-8, 4-7, 4-6, 4-5 5-8, 5-7, 5-6 6-8, 6-7 7-8
1-4	2-8, 2-7, 2-6, 2-5, 2-3 3-8, 3-7, 3-6, 3-5 5-8, 5-7, 5-6 6-8, 6-7 7-8
1-5	2-8, 2-7, 2-6, 2-4, 2-3 3-8, 3-7, 3-6, 3-4 4-8, 4-7, 4-6 6-8, 6-7 7-8

1-6	2-8, 2-7, 2-5, 2-4, 2-3 3-8, 3-7, 3-5, 3-4 4-8, 4-7, 4-5 5-8, 5-7 7-8
1-7	2-8, 2-6, 2-5, 2-4, 2-3 3-8, 3-6, 3-5, 3-4 4-8, 4-6, 4-5 5-8, 5-6 6-8
1-8	2-7, 2-6, 2-5, 2-4, 2-3 3-7, 3-6, 3-5, 3-4 4-7, 4-6, 4-5 5-7, 5-6 6-7

In sequence 2 the four electrodes involved in the measurements also lay on the same level. The injecting electrodes (A-B) are opposite to each other, as shown in Figure 8.7 (b). The potential measuring electrodes (M-N) are on either side of A-B. For example, if current is injected in A-B=1-5, then M-N= 2-3, 2-4, 3-4 and 6-8, 6-7, 7,8. The quadripoles of the electrodes for sequence 2 are shown in Table 8.2. It resulted in 24 measurements for one level (48 in total).

Table 8.2 Quadripoles of electrodes for sequence 2, top level

Current injection electrodes (A-B)	Voltage measurements electrodes (M-N)
1-5	2-3, 2-4, 3-4 6-8, 6-7, 7-8
2,6	3-4, 3-5, 4-5 1-7, 1-8, 7,8
3-7	4-5, 4-6, 5-6 2-1, 2-8, 1-8
4,8	5-6, 5-7, 6-7 1-2, 1-3, 2-3

Quadripoles of sequence 3 involve electrodes from both levels, as shown in Figure 8.7 (c). One electrode from each level is used to inject the current, and the other two electrodes from each level are used to measure the electrical potential, as summarized in Table 8.3. This sequence consists of a total number of 56 quadripoles.

Table 8.3 Quadripoles of electrodes for sequence 3

Current injection electrodes (A-B)	Voltage measurements electrodes (M-N)
1-9	2-10, 3-11, 4-12, 5-13, 6-14, 7-15, 8-16
2-10	1-9, 3-11, 4-12, 5-13, 6-14, 7-15, 8-16
3-11	1-9, 2-10, 4-12, 5-13, 6-14, 7-15, 8-16
4-12	1-9, 2-10, 4-12, 5-13, 6-14, 7-15, 8-16
5-13	1-9, 2-10, 3-11, 4-12, 6-14, 7-15, 8-16
6-14	1-9, 2-10, 3-11, 4-12, 5-13, 7-15, 8-16
7-15	1-9, 2-10, 3-11, 4-12, 5-13, 6-14, 8-16
8-16	1-9, 2-10, 3-11, 4-12, 5-13, 6-14, 7-15

8.2.3 Determination of experimental geometrical factors

The experimental geometrical factors were determined for two different configurations, one with the porous stones and the other one without the porous stones. Sodium chloride (NaCl) solutions were used in both calibrations.

The first configuration was obtained by gluing the bottom of the central part of the oedometer cell (ring + structure of the cell), without porous stones, to a plastic sheet, which is electrically non-conductive. The oedometer ring was filled with NaCl saline solutions with molarities ranging from 0.2 M to 1 M. The selected concentrations used in the calibration fall within the range of the material's electrical conductivity expected to occur in the flowthrough experiments. The three measuring sequences were performed for each solution molarity.

The electrical conductivity σ of each molar solution was measured with a conductivity-meter (Mettler Toledo SevenMulti – introduced in Chapter 4). It was then converted to resistivity as $\rho = 1/\sigma$. The electrical resistivity of the solution used was plotted against the measured resistance for each quadripole. The slope of the regression line providing the linear trend between these points is indeed the geometrical factor of the quadripole. Figure 8.8 shows the regression lines for 6 quadripoles from sequence 1.

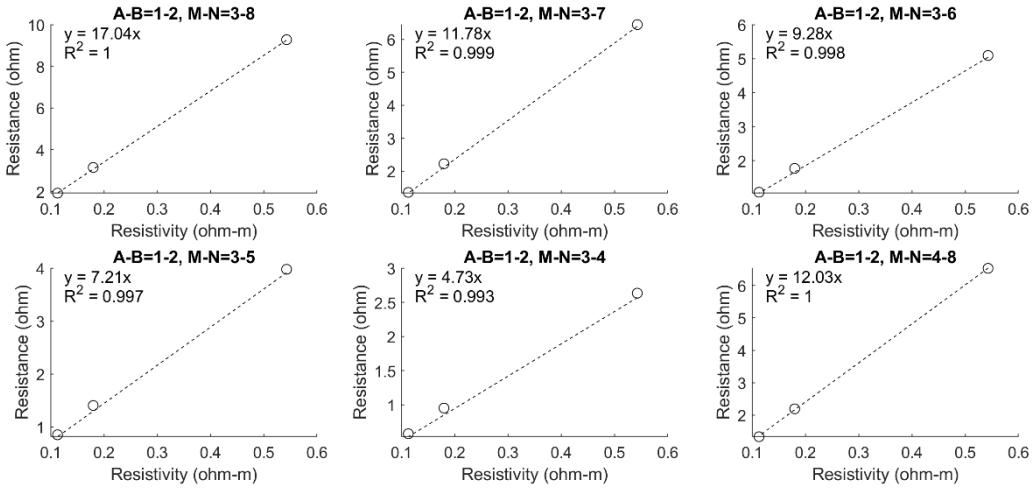

Figure 8.8 Experimental geometrical factors determined using three salt solutions with different molarities for first sequence.

The second configuration was obtained with the oedometer in its full working assembly. This involved the porous stones at its bottom and its top. In this configuration, only the 0.5 M NaCl solution was poured into the oedometer ring and used as a calibration specimen, which further allowed determining the role of the porous stones in the electrical measurements that can be acquired during the tests. The three sequences described earlier were imposed and the geometrical factor for each quadripole was obtained as the ratio between the apparent resistance and the solution resistivity.

8.2.4 Determination of numerical geometrical factors

The geometrical factors of an ideal, perfectly insulated cell were determined numerically through the FE software *COMSOL Multiphysics®* assuming stationary condition and validity of Ohm's law. In *COMSOL* the physics "electric current (ec)" was utilized for this purpose. The electrical charge balance equation:

$$\nabla \cdot (\sigma \nabla V) = 0 \qquad 8.3$$

where V is the electrical potential, was solved to this extent.

A cylindrical sample of the same size as the ones used in the experiments (diameter D = 50 mm and height H = 25 mm) was discretised. The inserted electrodes were simulated as points, as shown in Figure 8.9.

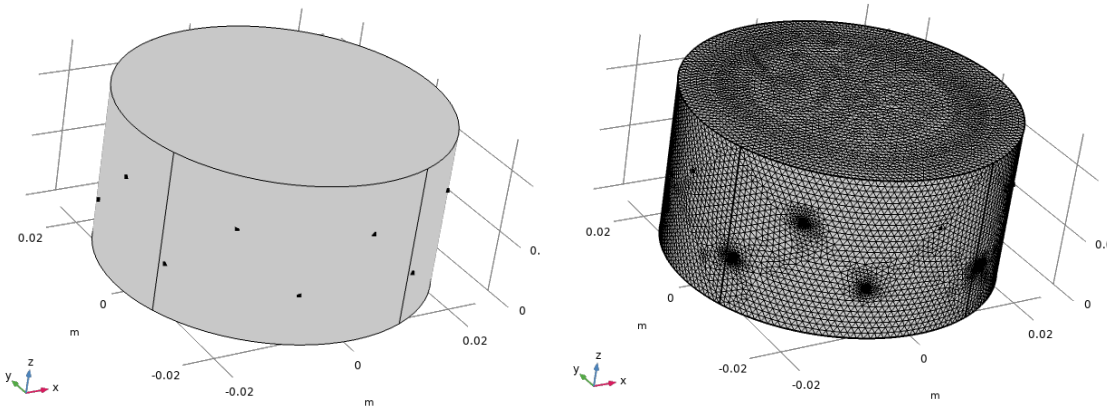

(a) (b)

Figure 8.9 Sample discretization in *COMSOL Multiphysics*. (a) sample prepared with cylinder along with electrodes (b) discretized sample into triangular mesh.

As it was done for the experimental case, two different geometries were used in the numerical simulations. The first one is restricted to the sample only, whose boundaries are considered electrically non-conductive: in other words, no electrical current is considered to travel through the porous stones. The second one explicitly takes into account the presence of the porous stones, shaped for the placement of the ultrasonic wave transducers. The electrical conductivity assigned to the porous stone was σ = 0.008 S/m, consistent with what was reported in the previous section.

A homogeneous electrical conductivity σ =1 S/m (resistivity ρ = 1 Ohm·m) was assigned to the sample. The measuring sequences discussed above were simulated. No electrical flux was allowed to take place at the boundaries, except for the A and B electrodes, through which the injection of 1A electrical current was simulated. The potential drop ΔV between the electrodes M and N was the outcome of the simulation.

As an example, Figure 8.10 shows the equipotential lines obtained when current is injected from electrodes 1 and 2. Figure 8.10 (a) shows the equipotential lines for the case where only the sample was considered and Figure 8.10 (b) shows the case where the porous stones and the ultrasonic wave transducers were also simulated.

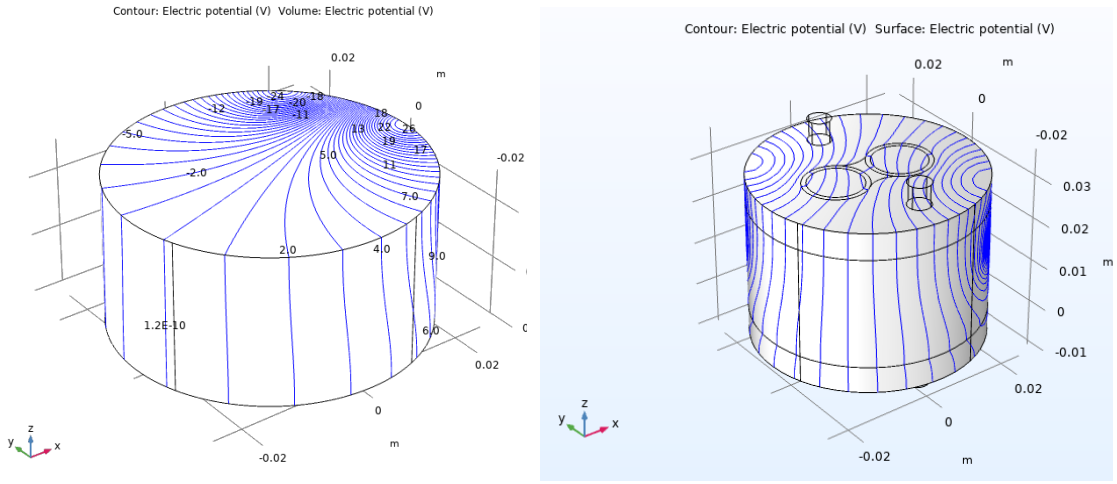

(a) (b)

Figure 8.10 Electrical potential through the sample obtained from *COMSOL* when the electrical current is injected through electrodes 1 and 2. (a) neglecting the electrical conductivity of the porous stones (the top and bottom of the sample are non-conductive boundaries), (b) modeling the porous stones as conductive objects.

Adopting unit values for the resistivity and the electrical current allows easy determination of the geometrical factor. As $\Delta V = RI = \rho\kappa I$, then $\kappa = \Delta V/\rho I$, the potential difference in the simulation is equal to the geometrical factor expressed in terms of m^{-1}.

8.2.5 Comparison between experimental and numerical geometrical factors and adopted experimental protocol

The experimental and numerical geometrical factors of the considered quadripoles are presented in Table 8.4 (complete table is presented in Appendix A). By comparing the results for the case with and without porous stones, it can be appreciated that results were not affected by the presence of the porous stones, neither in the experiments nor in the numerical simulations.

Table 8.4 Comparison of experimental and numerical geometrical factors.

A	B	M	N	Experimental geometrical factors obtained through regression line (1/m)	Experimental geometrical factors obtained with top and base (1/m)	Numerical geometrical factors- sample only (1/m)	Numerical geometrical factors- top and base (1/m)
1	2	8	3	17.04	16.97	17.21	17.04
1	2	8	4	11.78	12.03	12.10	11.95
1	2	8	5	9.28	9.60	9.63	9.51
1	2	8	6	7.21	7.54	7.58	7.50
1	2	8	7	4.73	5.15	5.10	5.06

Furthermore, there was generally a good correlation between the experimental and numerical geometric factors. These results suggest satisfactory electrical insulation so that no electrical bridges occurred between the sample and the metal of the oedometer.

The complete comparison of the experimental and numerical geometrical factors for the three sequences is presented in Figure 8.11. Results from both simulations where only the sample and the sample with both top and base porous stones are included. Figure 8.11 (a) shows the comparison for sequences 1 and 3 with emphasis on geometrical factors ranging below 3 m^{-1} whereas Figure 8.11 (b) shows all the geometrical factors for the three sequences.

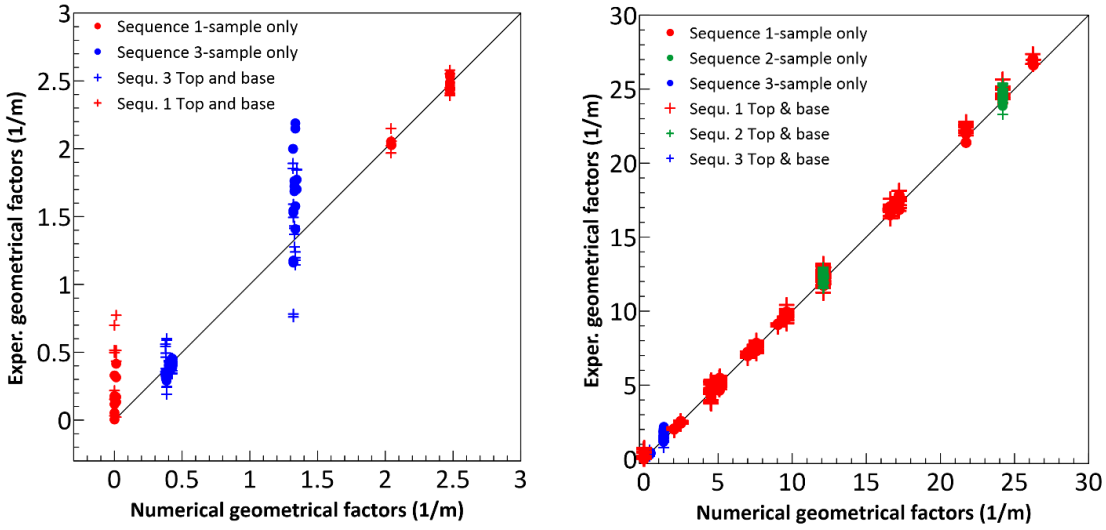

Figure 8.11 Comparison of numerical and experimental geometrical factors with and without top and base. (a) comparison of sequences 1 and 3 with emphasis on geometrical factors from 0-3 m^{-1} (b) comparison of the three sequences.

The comparison of the numerical and experimental geometrical factors allowed finalizing a protocol of measurement. This was accomplished by removing the quadripoles whose relative error between numerical and experimental geometrical factors was higher than 10%, *i.e.* 5% of measurements from sequence 1, none from sequence 2 and 46% from sequence 3. The threshold error of 10% was considered very likely to be a consequence of non-controllable factors such as small imperfections in the physical position of the electrodes (either in terms of coordinates of the holes through which they were inserted or because pushed too deeply in the sample) or to some gas production because of electrode reactions. Larger differences were mostly related to the relative position of the electrodes AB and MN.

The numerical evaluation of the potential drop between electrodes M and N for some quadripoles numerical from sequence 1 was about zero (consequently, the corresponding geometrical factor was also about zero). An example is as follows: when the current is injected in 1-5 (Table 8.1 and Figure 8.7.a) electrodes 3-7 fall on very close equipotential lines, as shown in Figure 8.12, so that the potential drop between them is nearly zero. As a consequence in light of equations 8.1 and 8.2, this quadripole cannot provide any significant information about the sample resistivity. In sequence 1, ten such quadripoles resulted in a null geometrical factor (Figure 8.11(a)), and these were excluded from the final protocol of measurement.

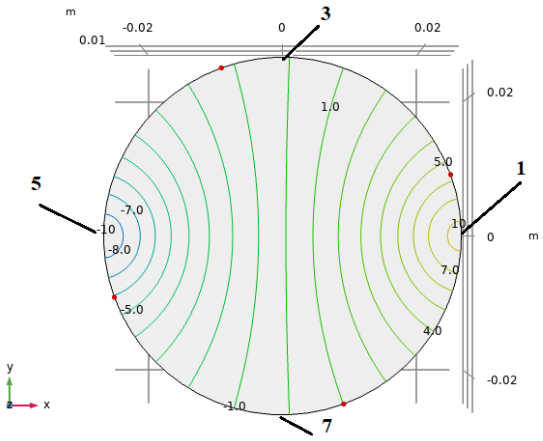

Figure 8.12 Quadripole with zero potential drop between M and N in sequence 1.

For sequence 3, there were a large number of quadripoles for which the relative error between the numerical and experimental geometrical factor was above 10%. It was observed that most of such quadripoles had the AB and MN pairs in close vicinity. For example, when the current is injected in electrodes 1-9 large errors were found when M-N was equal to 2-10, 3-11, 7-15 and 8-16. Although this did not occur in all similar configurations, only the quadripoles where the injecting and measuring pairs are 'far' from each other were included in the definitive protocol used in the tests. For example, with A-B=1-9 only the M-N couples 4-12, 5-13 and 6-14 were considered.

The protocol adopted for 3D ERT reconstructions included 200 measurements from sequence 1, 48 measurements from sequence 2 and 24 measurements from sequence 3, for a total of 272 quadripoles.

8.3 Electrical Resistivity Tomography and its implementation in the study

Electrical Resistivity Tomography (ERT) is a geophysical technique used to image the subsurface resistivity distribution by injecting electrical current into the ground and measuring the resulting potential differences (e.g., van Schoor, 2002, Chambers et al., 2006, Cardarelli et al., 2008). These measurements are used to infer the resistivity (or conductivity) of the subsurface, which can provide insights into the geological, hydrological, or structural properties of the Earth. ERT is now extensively used in a wide range of environmental and geotechnical studies e.g., monitoring landslides and imagining landfill sites. In the context of laboratory applications, it can be used to track local changes in the pore fluid or in the fabric occurring during tests involving transient phenomena.

ERT is based on an inversion process which solves for the true resistivity distribution in the subsurface/soil sample from the measured apparent resistivities. The inversion problem solves the governing PDE $(\nabla \cdot (\sigma \nabla V) = 0)$ to calculate the expected potential given a resistivity model (forward model). Then the objective function is solved by minimizing the difference between observed and predicted data while imposing regularization such as (e.g. Cardarelli & De Donno, (2019)).

$$\phi = ||\mathrm{W}_d(\mathrm{d}_{\mathrm{obs}} - \mathrm{d}_{\mathrm{calc}})||^2 + \lambda^2||\,\mathrm{W}_{\mathrm{m}}\mathrm{m}\,||^2 \qquad 8.4$$

where:

$\mathrm{d}_{\mathrm{obs}}$: observed data (apparent resistivities);

$\mathrm{d}_{\mathrm{cal}}$: calculated data from the forward model;

W_d: data weighting matrix;

m: model resistivity parameters;

W_m: regularization matrix (smoothness constraints);

λ: regularization parameter controlling the trade-off between data fit and model smoothness.

These methods aim to find the best distribution of geoelectrical parameters consistent with observed measurements. This involves minimizing the misfit between the set of four electrode measurements and the predicted response from a geoelectrical model. Because of the non-linear nature of the problem, the inversion proceeds iteratively until the misfit between the predicted response and the measurements is within a given tolerance.

8.3.1 Introduction to *ResIPy*

For this study, the inversion was performed in an open-source software *ResIPy* (Blanchy et al., 2020). Its easy-to-use Graphical User Interface (GUI) and the ability to work with different types of tomography (field tests) and shapes (laboratory tests) make it a useful tool.

For the 3D inversion in *ResIPY*, the problem is discretized in tetrahedral or triangular prism mesh. The number of nodes is 4 (tetrahedron) or 6 (triangular prism). The triangular prism mesh may be convenient for simple geometry (such as laboratory tests) and computationally efficient. Tetrahedral elements can adapt to irregular boundaries, complex subsurface features, and uneven surfaces (field cases). The position of the electrodes can be specified within the mesh as node points. It is possible to control the mesh refinement by specifying a characteristic length associated with each electrode node. Smaller characteristic lengths will result in a finer mesh. It is also possible to specify a growth factor that controls the increase in element size where less resolution is required

(e.g. away from the electrodes and, in field cases where the electrodes are on the surface, with depth).

Figure 8.13 shows an example of a discretized sample such as the ones used in this work, with a triangular prism mesh with finer elements near the electrodes. The location of the electrodes was provided in terms of X, Y and Z coordinates, reflecting their position in the advanced oedometer cell.

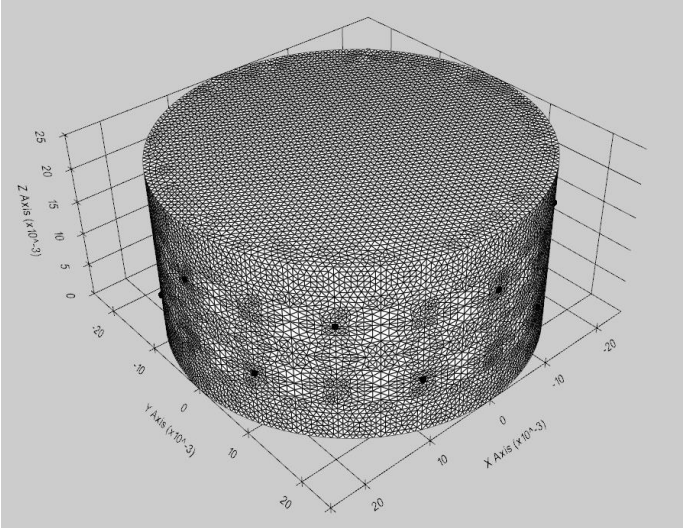

Figure 8.13 An example of triangular prism mesh for the tested samples. Mesh refinement is performed close to the electrodes.

The *ResIPy*'s GUI (Graphical User Interface) facilitates data importing, data filtering, mesh generation, data inversion and plotting of inverse models. The *ResIPy* GUI has a series of tabs, as shown in Figure 8.14, that allow to navigate through the necessary stages of importing and filtering data, generating a mesh and inverting data. The code also allows to work with time-lapse survey data to observe any changes with time concerning the initial stage (reference measurements).

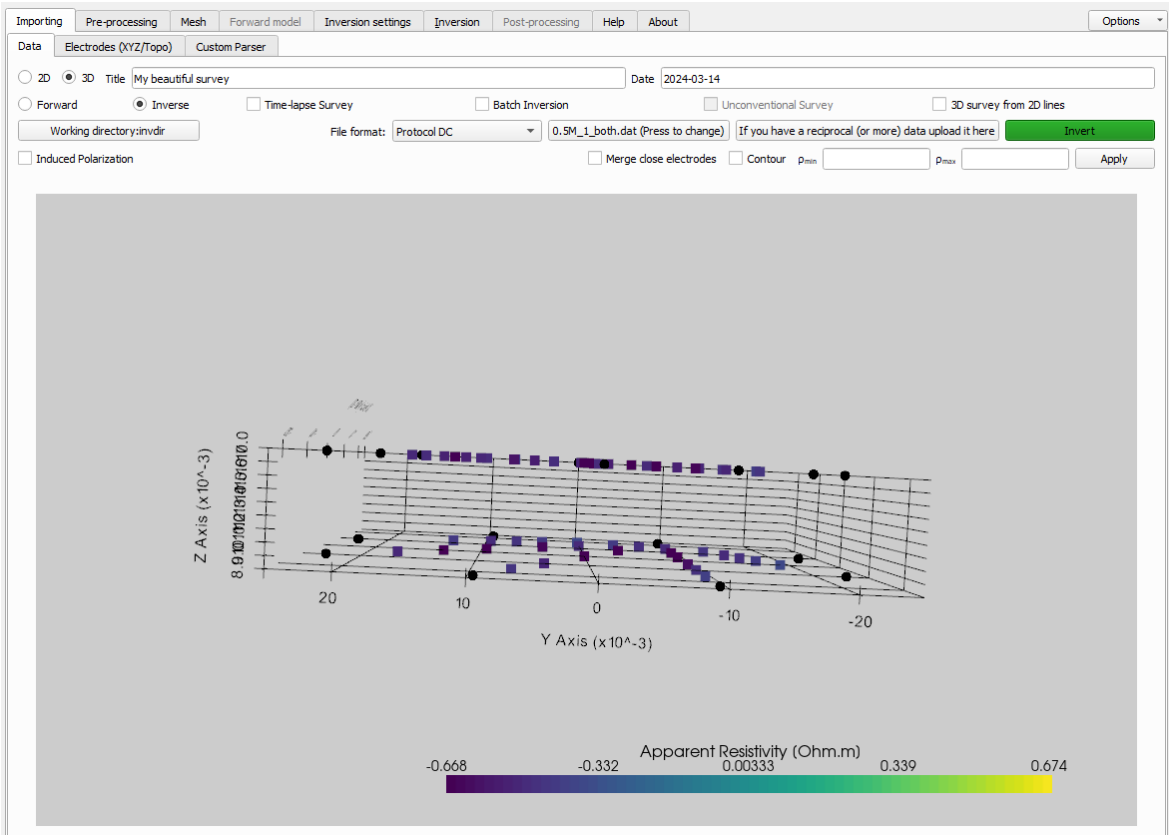

Figure 8.14 The graphical user interface of *ResIPy* showing tabs for data importing, data filtering, mesh generation and inversion.

8.3.2 Inversion process in *ResIPy*

ResIPy adopts an inversion algorithm with the minimization of an objective function, similar to the one introduced in Equation 8.4. In the following, the terminologies and terms used in the *ResIPy* environment are introduced. The inversion in *ResIPy* is an iterative process, and it solves:

$$\left(J^T W_d^T W_d J + \alpha R\right) \Delta m = J^T W_d^T \left(d - f(m_i)\right) - \alpha R m \quad 8.5$$

$$m_{i+1} = m_i + \Delta m \quad 8.6$$

where:

J is the Jacobian, such that $J_{i,j} = \partial d_i / \partial m_j$;

d is the data vector;

m_i is the parameter vector at iteration i;

W_d is the data weight matrix, assumed to be diagonal, with diagonal values $W_{i,i} = 1/\epsilon_i$ and ϵ_i is the standard deviation of measurement i;

α is the regularization (or smoothing) parameter;

R is the roughness matrix, which describes the connectivity of parameter blocks;

$f(m)$ is the forward model for parameters m.

Equations 8.5 and 8.6 are solved repeatedly until satisfactory convergence is achieved. In *ResIPy* this is defined by the data misfit reaching a required tolerance. The data misfit is expressed as a root mean square error, i.e.

$$RMS = \sqrt{\frac{1}{N}\sum\left(\frac{d_i - f_i(m)}{\epsilon_i}\right)^2} \quad 8.7$$

where *N* is the number of measurements. The target tolerance should be 1. Equations 8.5 and 8.6 result from the minimisation of an objective function composed of a data misfit and a model misfit. The data misfit describes the mismatch between the observations (*d*) and the forward model (*f(m)*) as:

$$\Psi_{\mathrm{d}} = (d - f(m))^T W_d^T \, W_d\big(d - f(m)\big) \quad 8.8$$

where modal misfit can be expressed as

$$\Psi_m = m^T R m \quad 8.9$$

The smoothing factor, alpha (α) is a factor that affects the distribution of the electrical conductivity in the inversion aiming at providing the smoothest distribution of resistivity which is consistent with the observed data. The adopted smoothness can be different in the vertical and horizontal direction leading to reconstructions which emphasize the heterogeneity in one or the other direction. This is made by introducing anisotropy in the smoothing factor, i.e., through an alpha_aniso (a_ai) parameter. The default value of a_ai=1 adopts the same smoothing in the horizontal and vertical directions. Values of a_ai greater than 1 lead to reconstructions where the heterogeneity is increased in the vertical directions. Values of a_ai smaller than 1 lead to reconstructions where the heterogeneity is increased in the horizontal directions. The impact of a_ai on the heterogeneity of the reconstructed maps of electrical conductivity was investigated together with the overall potentialities of the *ResIPy* using 'synthetic' data for a flushing test generated in *COMSOL*.

8.4 Inversion of a synthetic flushing test

Before running laboratory experiments, the potentialities of *ResIPy* in reconstructing trustable maps of electrical conductivity for samples with heterogenous pore fluid

composition, similar to those expected to occur during real tests, were checked on synthetic data.

A synthetic flushing test thought to take place in the advanced oedometer was simulated with *COMSOL Multiphysics*®. In the numerical model a saline sample was virtually placed into the oedometer and flushed with distilled water injected from its bottom. The soil sample was assigned an initial salt concentration and a corresponding electrical conductivity according to Archie's law. Under diffusion and advection of distilled water the salt concentration decrease in the sample over time was simulated. This also leads to a heterogeneous distribution of electrical conductivity in the sample. The electrical resistivity data over time and the related measurements that would be obtained with the protocol and procedure described in Section 8.2 were generated based on *COMSOL*, thus simulating the physical electrical measurements that would be acquired in the test. The obtained resistance (data) vector was then inserted in *ResIPy* for inversion. The synthetic (*COMSOL*) and reconstructed (*ResIPy*) electrical conductivity were then compared.

8.4.1 Description of the synthetic model and test

The synthetic test simulated in *COMSOL* is based on a model which is the replica of the advanced oedometer. It consists of a specimen of 25 mm height and 50 mm diameter with electrodes on the two levels, according to the scheme of Section 8.1. The specimen was created by a cylinder with electrodes introduced as points. Porous stones at the top and bottom were also included, accounting for their actual shape as shown in Figure 8.5 and Figure 8.6 (b). The drainage lines were also modelled by cylinders with 2.5 mm diameter over the porous stones to inject the fluid (Figure 8.15).

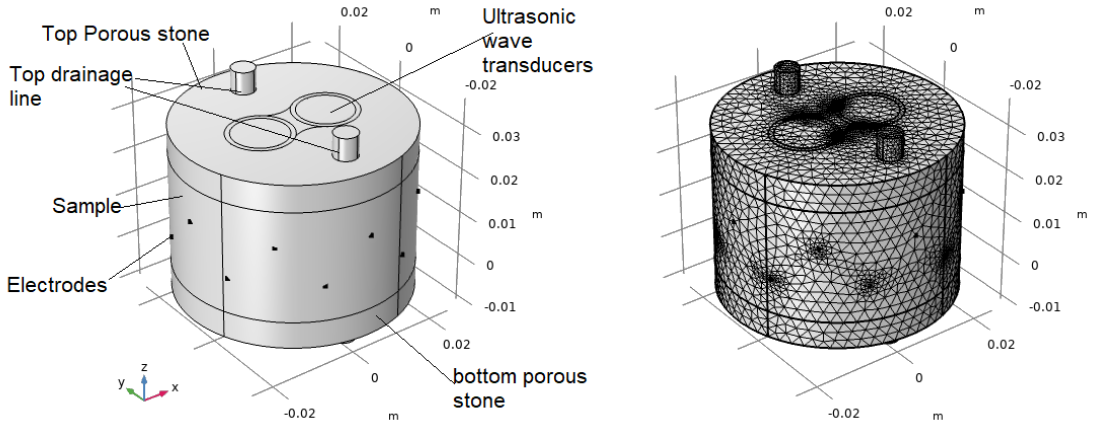

Figure 8.15 *COMSOL* model of the advanced oedometer along with porous stones and drainages.

The model was discretized into a fine mesh with smaller elements near the electrodes. A

triangular mesh was used with a maximum element size of 0.002 m and a minimum element size of 7.5e-5 m. The meshed model is shown in Figure 8.15. The specimen was assigned a pore pressure p=0 kPa and a NaCl concentration of 180 mol/m^3, equal to the one of the pore fluid in the reconstituted clayey samples used for the test in the advanced oedometer. The initial salt concentration in the porous stones was set equal to 0 (distilled water). A pressure of 400 kPa was applied at the bottom drainage line, whereas the pressure applied at the top drainage was kept equal to 0 kPa (Figure 8.16). This induced the flow of distilled water from bottom to top. The total simulation time was 20 hours.

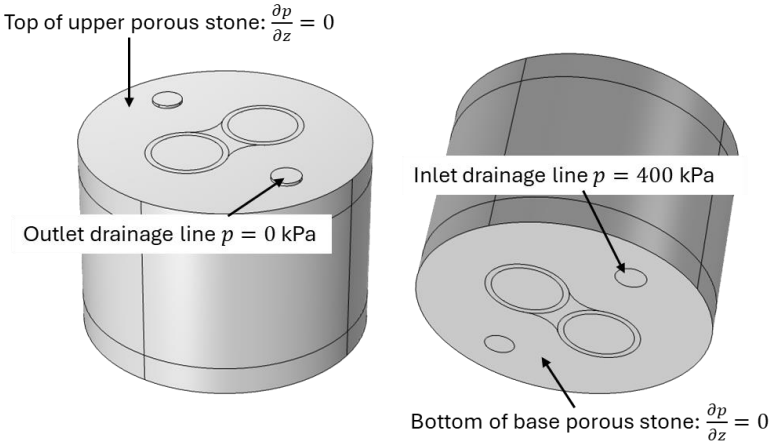

Figure 8.16 Boundary conditions at top and bottom drainage lines and porous stones.

The mass balance equations of the liquid phase and of the dissolved salt were solved. The local salt concentration at different times was converted into electrical conductivity of the soil, which was used to determine the electrical potential drops measured through the defined protocol. Details concerning the procedure are provided in the following.

Mass balance of water

The mass balance equation of water was modelled as:

$$\frac{\partial \phi \rho_w}{\partial t} + \nabla \cdot (\rho_w \boldsymbol{u}) = 0 \qquad 8.10$$

where ϕ is the porosity of the porous medium and ρ_w is the water mass density. The vector $\boldsymbol{u}$ is the seepage velocity, which is related to the pressure gradient through Darcy's law:

$$\boldsymbol{u} = -\frac{K}{\rho_w g} \nabla(p + \rho_w g z) \qquad 8.11$$

where p is pressure and K is the hydraulic conductivity of the medium.

The porosity and hydraulic conductivity of the specimen were assigned based on typical values for a clayey specimen ϕ=0.25 and $K = 1 \cdot 10^{-10}\, m/s$. The porous stones were assigned a porosity of 0.44 and a hydraulic conductivity of $K = 1 \cdot 10^{-4}\, m/s$.

Mass balance of salt

The rate at which a chemical constituent moves through the soil is determined by several transport mechanisms. These mechanisms often act simultaneously on the chemical species and may include advection, diffusion and dispersion. In this study only advection and diffusion were considered for simplicity, also considering that other transport mechanisms were expected to play a negligible role during the physical tests.

Neglecting adsorption, the advection-diffusion equation for the transport of a species is (e.g., Bear and Chang, 2010)

$$\frac{\partial \phi c}{\partial t} + \nabla \cdot (\boldsymbol{J} + \boldsymbol{u}c) = 0 \qquad 8.12$$

$$\boldsymbol{J} = -D_e \nabla c \qquad 8.13$$

where c is the concentration of the species and D_e is the effective diffusion coefficient of the species in the porous medium. The seepage velocity was obtained from Equation 8.11 through Darcy's law. The coefficients of diffusion (D) for the porous stones and the specimen were set to $10 \cdot 10^{-10}\, m^2/s$. The effective coefficients of diffusion were obtained by employing Millington & Quirk, (1961) model. The model accounts for the effects of tortuosity of the sample and porous stone by $D_e = \phi/\tau\ D$. The tortuosity factor accounts for the reduced diffusivity since the solid grains of the sample or porous stone hinder the motion of the fluid. The Millington and Quirk model takes into account the relationship between porosity and tortuosity as $\tau = \phi^{-1/3}$.

No flux boundary condition which is a second type boundary, was assigned to the boundary of the sample. At the inlet of the specimen, a prescribed flux boundary condition was assigned.

Balance of electrical charge

The "Electric Currents (ec)" physics of *COMSOL* was employed to numerically estimate the potential drops that would be acquired applying the measurement protocol at different times. This required defining the local electrical conductivity of the specimen, which was obtained in two steps.

Firstly, the electrical conductivity of the liquid in the pores σ_L was obtained starting from the local contaminant concentration as found solving the transport problem (Eq.

8.12 and 8.13). To this extent, the relationship between concentration and electrical conductivity of sodium chloride solutions in Hervas et al. (2006) (Eq. 8.14) was used:

$$\sigma_L(S/m) \;=\; 0.0080959 \cdot c\ (mol/m^3\ ) \qquad 8.14$$

The local electrical conductivity of the soil σ_S was then related to the corresponding pore fluid electrical electrical conductivity through Archie's law (Eq. 8.15):

$$\sigma_S = S_r^n \phi^m \sigma_L \qquad 8.15$$

where *Sr* is the degree of saturation and *n* and *m* are model parameters. As the specimen was assumed saturated the parameter *n* was not defined. Whereas, based on the experimental measurements provided in Appendix A, it was assumed *m=1.5*.

The porous stone was assigned an electrical conductivity of 0.008 S/m as discussed in Section 8.1.1.

8.4.2 Simulation results

The flushing of distilled water resulted in a decrease in salt concentration at different times of analysis. Figure 8.18 shows a map of salt concentration along a vertical plane passing through the centre of the specimen at the start (Figure 8.18 (a)), after 5 hours (Figure 8.18 (b)), after 10 hours (Figure 8.18 (c)) and after 20 hours (Figure 8.18 (d)) of the flushing test. In Figure 8.17 the plane of analysis is shown with dotted black line which was used for concentrations and electrical conductivity data visualization. Vertically and horizontally heterogeneous distribution of concentration can be observed. The vertical heterogeneity is due to a decrease in the concentration of salt along the height whereas the horizontal heterogeneity is due to the presence of ultrasonic wave transducers hindering the free movement of salts around it as discussed in later sections.

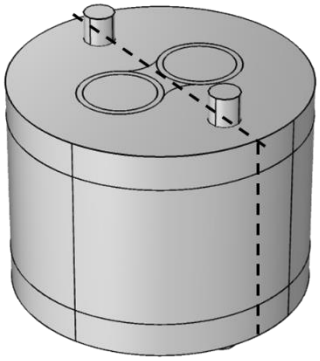

Figure 8.17 Model with plane of analysis shown with dashed line.

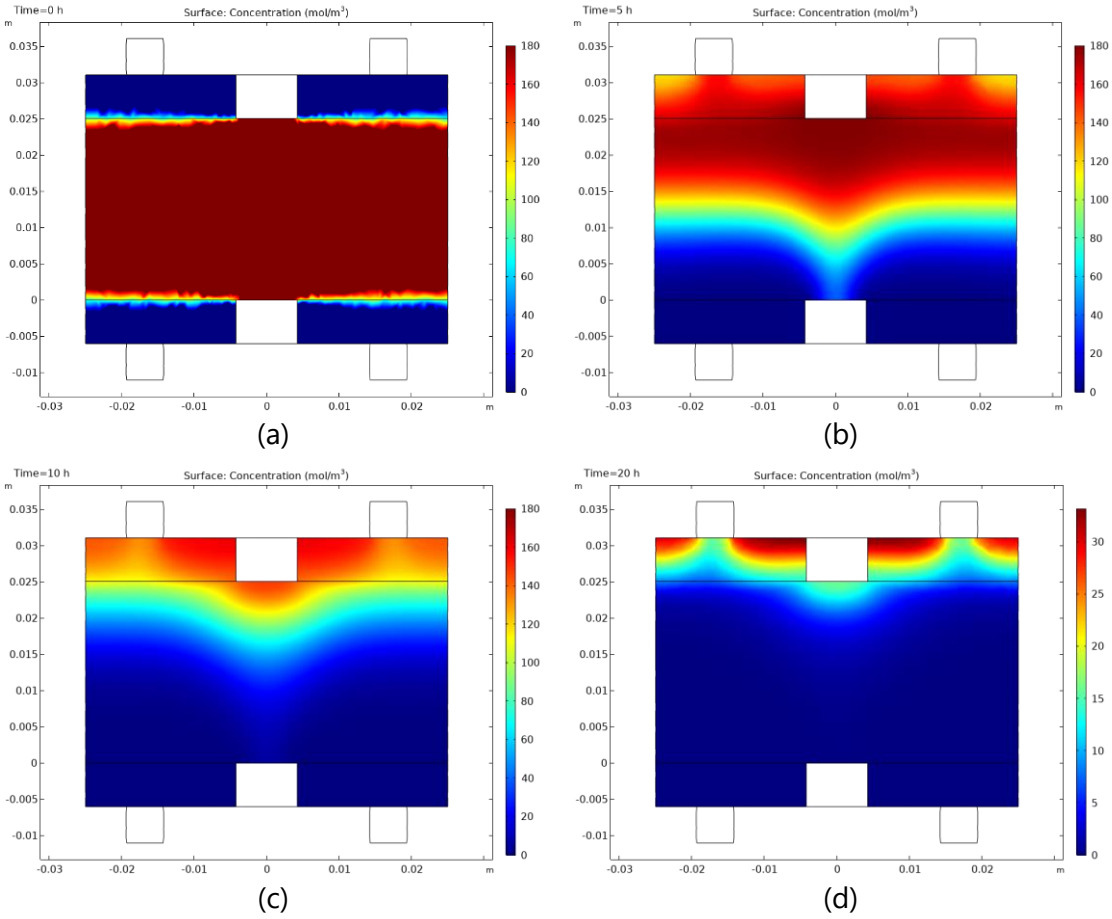

Figure 8.18 Maps of salt concentration along the vertical plane passing through the center of the specimen (a) start of flushing (b) after 5 hours of flushing (c) after 10 hours and (d) after 20 hours of flushing distilled water.

Figure 8.19 shows the distribution of the soil electrical conductivity in the specimen at different time of flushing test, obtained using Equations 8.14 and 8.15.

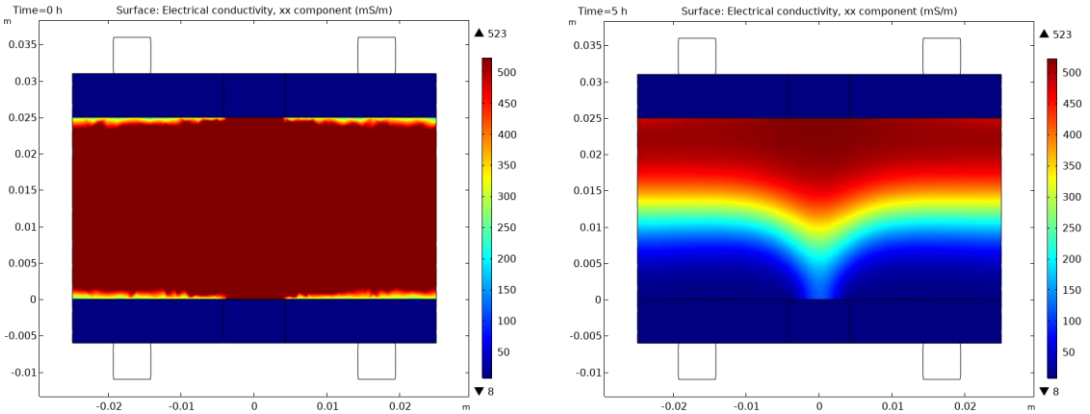

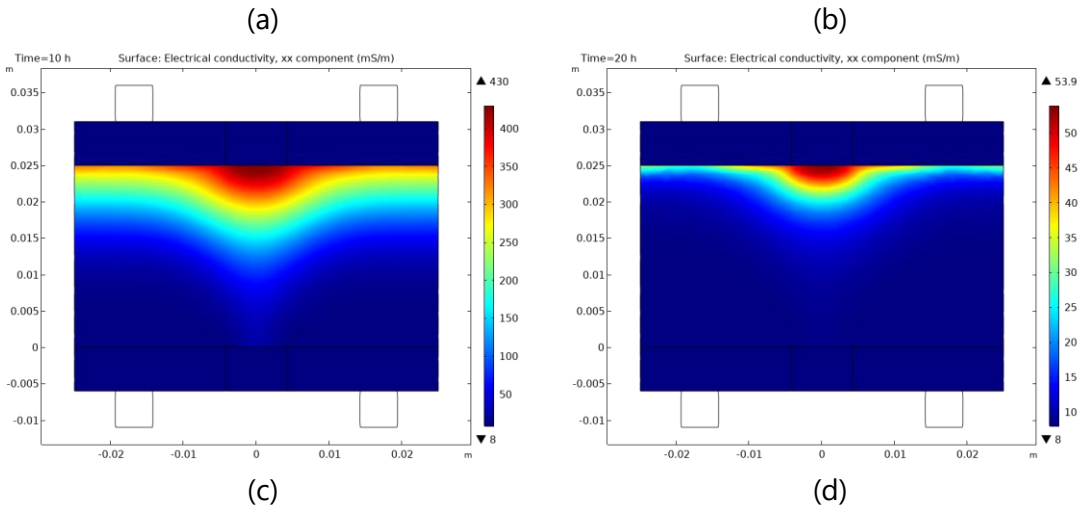

Figure 8.19 Maps of electrical conductivity of the sample obtained through Equations 8.14 and 8.15 (a) at the start of synthetic flushing test (b) after 5 hours (c) after 10 hours and (d) after 20 hours of flushing distilled water.

It shall be noticed that, as the distilled water is introduced in the model through the drainage lines, the NaCl concentration, and then also the electrical conductivity, is not homogeneous in any horizontal section of the samples. As an example, Figure 8.20 shows the distribution of electrical conductivity after 5 hours at different heights of the specimen. Five different sections were selected, i.e., at the bottom (0 mm), at the level of bottom electrodes (8 mm), at the middle of the specimen (12.5 mm), at the level of top electrodes (17 mm) and at the top of the specimen (25 mm). The role of the space occupied by the ultrasonic wave transducers in the bottom and top caps can be appreciated in these figures.

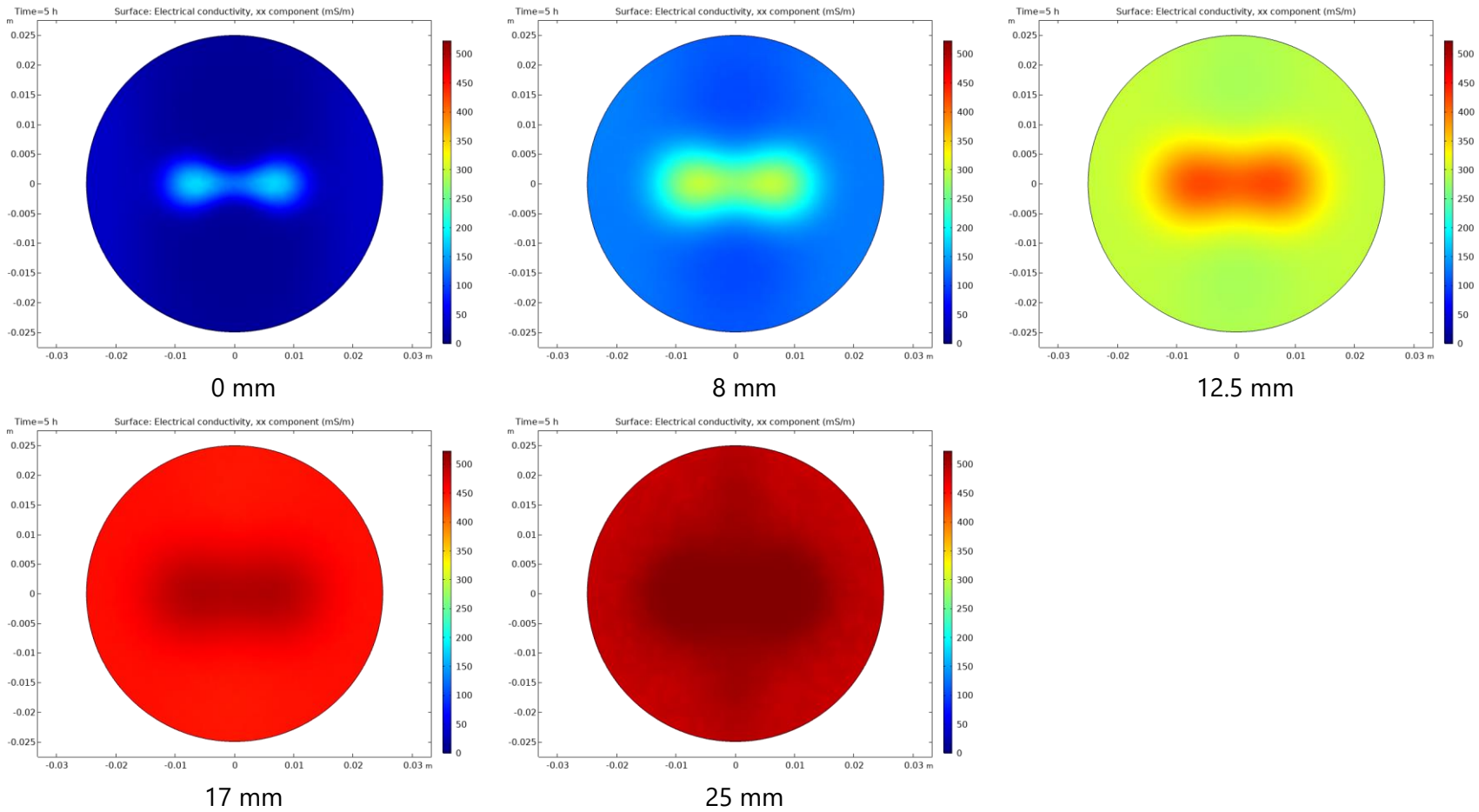

Figure 8.20 Distribution of electrical conductivity at different heights after 5 hours of flushing.

8.4.3 Set up of ERT reconstructions

Synthetic measurements referring to different times were obtained with the *COMSOL* "electric currents (ec)" physics. The electrical charge balance equation (equation 8.3) was solved using the electrical conductivity maps determined as above, following the protocol of measurements identified in Section 8.2.

The synthetic data of the electrical resistance obtained this way was imported to *ResIPy* in .dat format. This file contains information on the four electrodes and the resistance value for each quadripole. The *ResIPy* sample was then discretized in triangular mesh. The minimum size of the element was set to 0.0015 m (1.5 mm). The role of the smoothness factor (α) and its anisotropy index (a_ai), which controls the electrical conductivity heterogeneity in the model, was also explored through a sensitivity analysis. As the *COMSOL* simulation presents heterogeneity of σ mainly in the vertical direction, values of a_ai greater than 1 were explored.

The reconstructed electrical conductivity distribution maps from *ResIPy* were compared to the synthetic data of *COMSOL*. The comparison was conducted in terms of electrical conductivity distribution at different heights of 0, 8, 12.5, 17, and 25-mm. For each section the electrical conductivity distribution was interpreted as a line histogram. These results are presented in the next paragraphs.

ERT reconstruction results for t=0 (initial condition)

Figure 8.21 shows the comparison between the *COMSOL* values and reconstructed values of *ResIPy* for different alpha anisotropy (a_ai) at the beginning of the synthetic tests. The theoretical values of electrical conductivity in *COMSOL* are shown in black lines in Figure 8.21. They are equal to 523 mS/m (which in light of equations 8.14 and 8.15 corresponds to the initial concentration c= 180 mol/m^3 imposed in the model) for all the sections except the ones at the sample bottom and top (H=0 mm and H=25 mm), where the effects of the distilled water diffusion from the porous stones are observed since the beginning of the simulation.

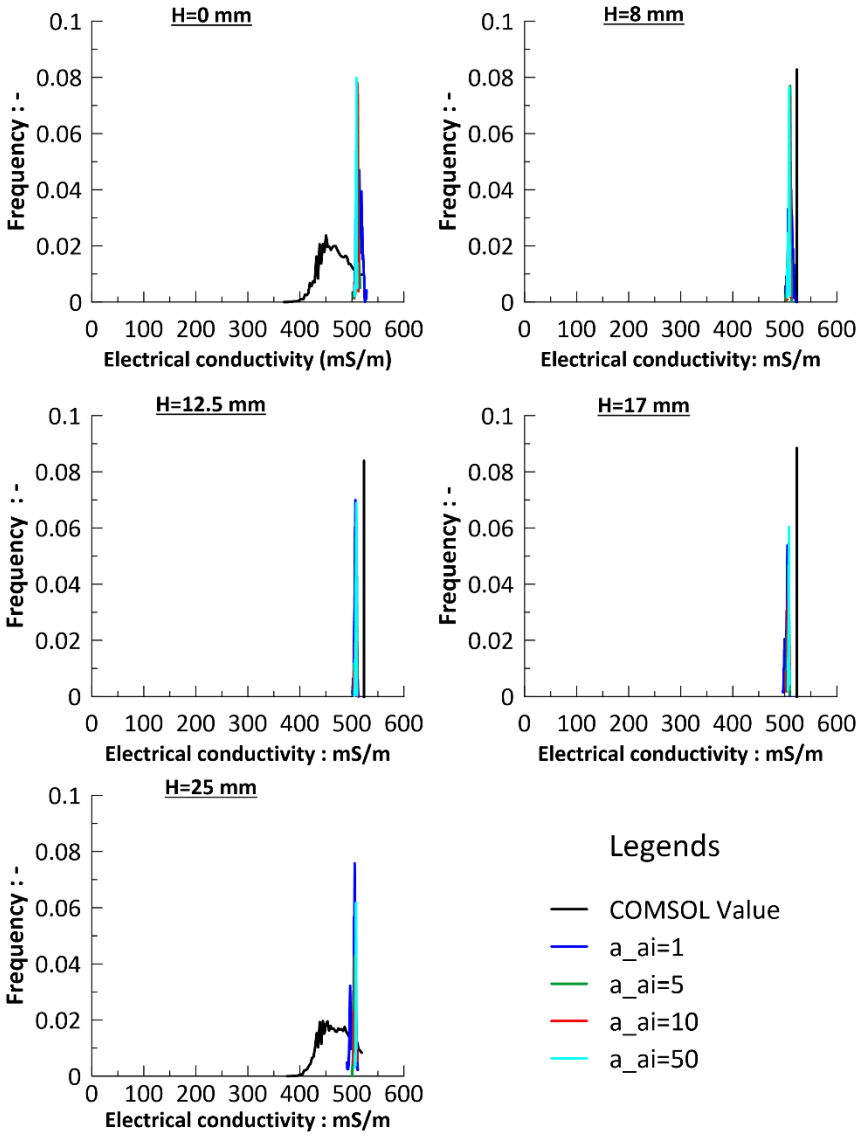

Figure 8.21 Comparison of *COMSOL* and *ResIPy* electrical conductivity histograms at the beginning of the simulation.

The values of conductivity of *COMSOL* and *ResIPy* are comparable in the central sections. Larger discrepancies between the *COMSOL* data and the inversion results are found at the sample's top and bottom, possibly because of limitations in the *ResIPy* algorithm in the presence of strong gradients such as those occurring in these sections. The reconstructed values of electrical conductivity for a_ai=1 have a comparatively wider distribution than others, as shown by the blue line in Figure 8.21. By increasing the anisotropy of the smoothness factor value (a_ai) the dispersion of electrical conductivity decreases. No significant changes are appreciated when a_ai≥ 5.

To allow the reader to appreciate the role of the anisotropy parameter, the image referring to H=8mm and H=17 mm is replotted in Figure 8.22 by enlarging the x-axis.

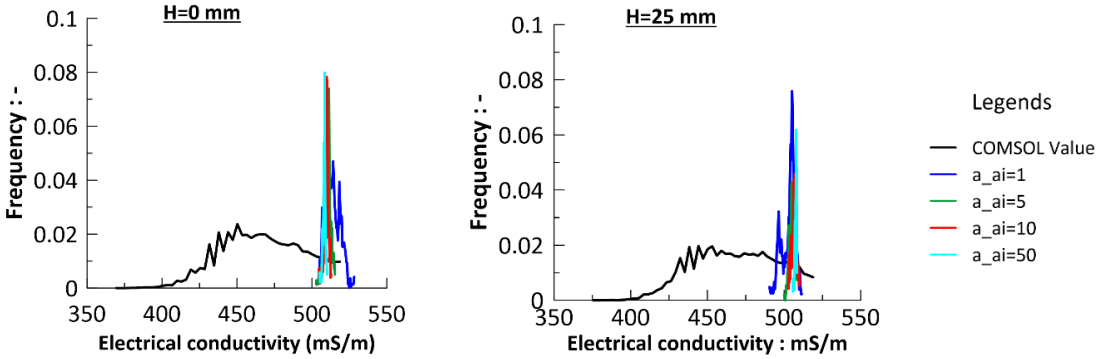

Figure 8.22 Comparison of *COMSOL* and *ResIPy* electrical conductivity histograms at the beginning of the simulation at H=8 and H=17 mm height with enlarged x-axis.

ERT reconstruction results for t=5 hours

As anticipated in Figure 8.19 (b), the electrical conductivity referred to a *COMSOL* simulation time of 5h is largely heterogeneous in the vertical direction, and it is around 20 mS/m at the bottom of the specimen and around 507 mS/m at its top.

The comparison between simulated and reconstructed electrical conductivity, organized in histograms at different heights, is presented in Figure 8.23.

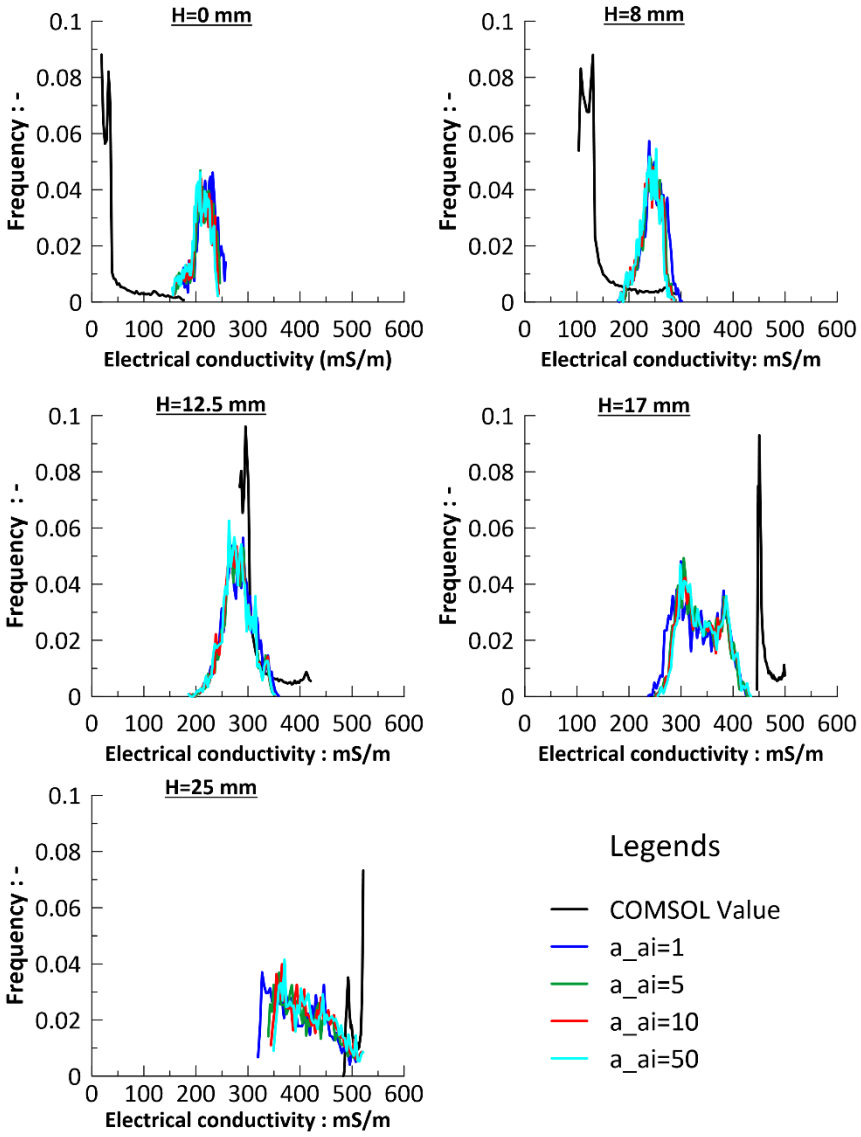

Figure 8.23 Comparison of *COMSOL* and *ResIPy* electrical conductivity histograms for t=5 hours.

At H=0 mm it is observed that the reconstructed values of electrical conductivity in *ResIPy* are overestimated as compared to *COMSOL* values: the *COMSOL* values range between 10 and 50 mS/m, whereas the range of *ResIPy* values is between 150 and 250 mS/m. In the case of *COMSOL* value, at H=0 mm, some parts of the section had higher σ up to 180 mS/m referred as 'tail'. This is the part of the specimen where the ultrasonic wave transducers are present as shown in Figure 8.20.

At the height of 8 mm the difference between the *COMSOL* and reconstructed electrical conductivity is smaller compared to 0 mm height, *COMSOL* values ranging between 100 and 150 mS/m and *ResIPy* values ranging from 180 to 300 mS/m. Also, at this height, the 'tail' has values up to 300 mS/m in the case of *COMSOL* values.

The closest agreement between *COMSOL* and *ResIPy* is found at the center of the specimen (H=12.5mm). At this height, the *COMSOL* values had a lower tail where higher levels of conductivity were observed as compared to the other two heights (0 and 8 mm). In this case, the tail is small because the flushing of salt concentration is not significant. For heights of 17 mm and 25 mm the *ResIPy* electrical conductivity is underestimated compared to *COMSOL* and the distribution is more heterogeneous, especially for H=25 mm.

Changes in a_ai did not affect the distribution of electrical conductivity significantly. Overall, with higher values of a_ai a narrower range of values and a more homogenous distribution can be observed for H=25 mm section.

ERT reconstruction results for t = 10 hours

The electrical conductivity of the specimen decreased significantly in the bottom half of the samples after a simulation time of 10 hours. The related histograms of electrical conductivity along the height of the specimen are shown in Figure 8.24.

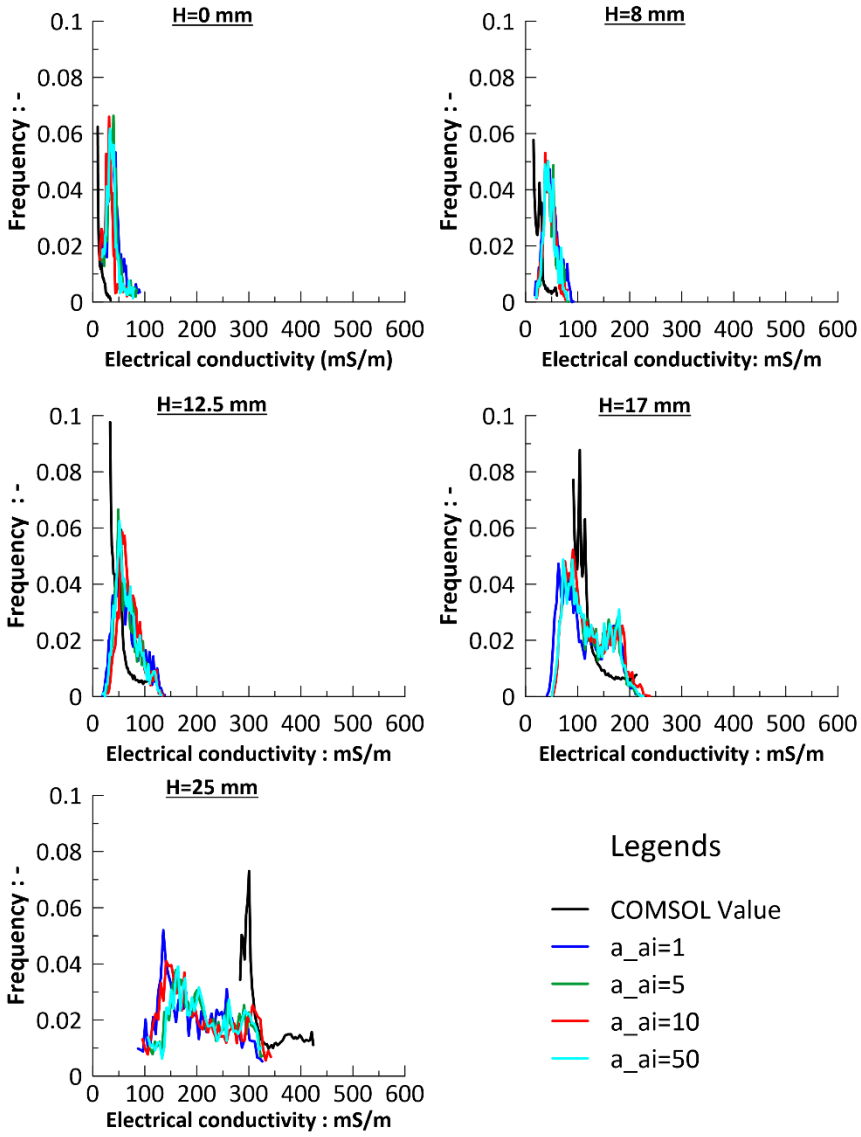

Figure 8.24 Comparison of *COMSOL* and *ResIPy* electrical conductivity histograms for t=10 hours.

As compared to the histograms for t=5 hours the difference between *COMSOL* and *ResIPy* values is smaller in the bottom half of the sample. *ResIPy* reconstructed σ values are slightly overestimated for H=0 mm, H=8 mm and H=12.5 mm, but the difference with *COMSOL* is not significant.

For H=17 mm reconstructed data are very close to *COMSOL* ones but are more heterogenous. The reconstructed values of conductivity range between 50 and 250 mS/m. The *COMSOL* values are between 80-120 mS/m with a 'tail' reaching up to 200 mS/m. In case of H=25 mm the reconstructed values provided by *ResIPy* largely underestimate the electrical conductivity of the *COMSOL* model with extreme heterogeneity. The range of reconstructed values is 90 to 350 mS/m. A large part of the

COMSOL values is between 280-340 mS/m with some parts of the section ranging up to 420 mS/m. This part, as stated earlier, is a portion of the sample near the ultrasonic wave transducers which might hinder the movement of fluid across it.

ERT reconstruction results for t = 20 hours

Towards the end of flushing test simulation, the electrical conductivity of the specimen has reduced significantly. The related distribution of electrical conductivity along the height of the specimen is shown in Figure 8.25.

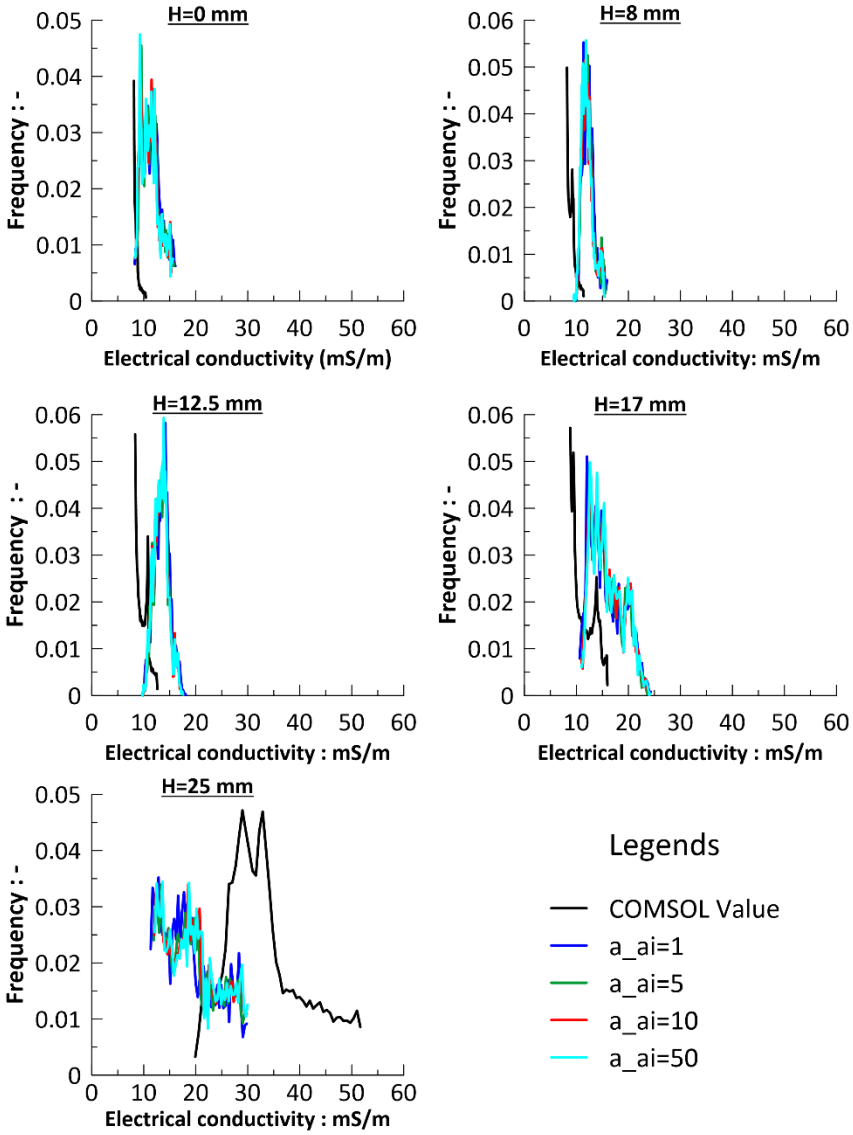

Figure 8.25 Comparison of *COMSOL* and *ResIPy* electrical conductivity histograms for t= 20 hours.

For the large section of the specimen, the *COMSOL* and reconstructed values of electrical conductivity are well coordinated with an insignificant overestimation. At the height of

25 mm, the reconstruction underestimates the values of electrical conductivity as compared to the *COMSOL* values. The *COMSOL* values range between 20 to 50 mS/m and the reconstructed values range between 10 to 30 mS/m.

When comparing the average values of electrical conductivity in the whole specimen at different times of analysis, the electrical conductivities obtained from both the reconstruction and *COMSOL* are very similar. At the beginning of the flushing process and after 20 hours, the two electrical conductivity values are nearly identical. However, at the 5-hour mark, there is the largest discrepancy, with the reconstructed values from *ResIPy* overestimating the average electrical conductivity. In contrast, at the 10-hour mark, the reconstructed values were slightly underestimated. The comparison is provided in Table 8.5.

Table 8.5 Comparison of average electrical conductivity values obtained from *ResIPy* and *COMSOL*.

	Average values of electrical conductivity	
Time (h)	Reconstructed σ	*COMSOL* σ
0	507.3	508.4
5	296.7	276.1
10	93.5	102.7
20	14.5	14.2

8.4.4 Considerations on the reconstruction results provided by *ResIPy* for the synthetic test

Through the analysis of the results presented above, it can be concluded that the potential of *ResIPy* is notable when the gradient of electrical conductivity is relatively small (case of t=0 and t=20 hours). When electrical conductivity changes over a small length are large (small gradients) *ResIPy* reconstructions are poorer. This is the case of the reconstruction at t=5 hours, where *ResIPy* overestimated quite largely the electrical conductivity in the bottom third of the specimen. The reconstruction was always good in the middle of the specimen. The reconstruction with *ResIPy* was not completely able to obtain the horizontal heterogeneity induced by the presence of ultrasonic wave transducers in the top and bottom caps. The reconstructed values showed more heterogeneity at 17- and 25-mm height, in the case of 5 and 10 hours.

As expected, a_ai values did not significantly impact the average value of reconstructed electrical conductivity, but rather in its statistical distribution, whose variability on the horizontal plane decreases as a_ai increases. For t=0 hour the

comparison of the electrical conductivity distribution among a_ai shows imposing a_ai≥5 has a minor effect on the statistical distribution. For other times of analysis (t=5,10 and 20), a_ai seems not to impact the distribution of the electrical conductivity.

8.5 Ultrasonic waves transducers

In the advanced oedometer cell, piezoelectric elements were used for ultrasonic wave transducers. A piezoelectric element generates an electric charge when mechanically stressed, and it deforms when an electric voltage is applied. For this reason, these elements are commonly used as transducers to evaluate the elastic properties of materials at low levels of deformation. The piezoelectric material can be polarized either normally or tangentially to its surface, respectively allowing for the generation of compression (P) waves and shear (S) waves. The ultrasonic wave transducers used in the advanced oedometer were manufactured by Megaris s.r.l. Further details about the piezoelectric transducers and the preliminary calibration tests will be provided in the following paragraphs.

8.5.1 Piezoelectric elements used in advanced oedometer

The devices used in the advanced oedometer are non-interfering piezoelectric square flat-shaped elements produced by CTS/Noliac, one specialized for P-waves and one for S-waves. Both transducers are composed of multilayer piezoceramic elements that achieve maximum performance with low operating voltages.

NAC2003 planar component was used for compression wave transducer. The NAC2003 plate actuator has dimensions of 5 mm x 5 mm x 2 mm and provides a free displacement of 3 µm. The maximum force that it can withstand is 1050 N. The unloaded and unencapsulated resonant frequency is higher than 486 kHz.

NAC2402-H2.3 shear component was utilized for shear wave transducers. The Noliac NAC2402-H2.3 shear stack has shear motion only along one predefined direction on the plane tangent to the piezoelectric. The component has dimensions of 5 mm x 5 mm x 2.3 mm and provides a free displacement of 3 µm. The unloaded and unencapsulated resonant frequency is higher than 700 kHz.

The transducers are encapsulated in a custom-made metal mold and then coated with special epoxy resins (Figure 8.26). The casing/mold (made of brass) has double grooves for O-ring insertion and specific cavities for the installation of piezoelectric elements and their wiring.

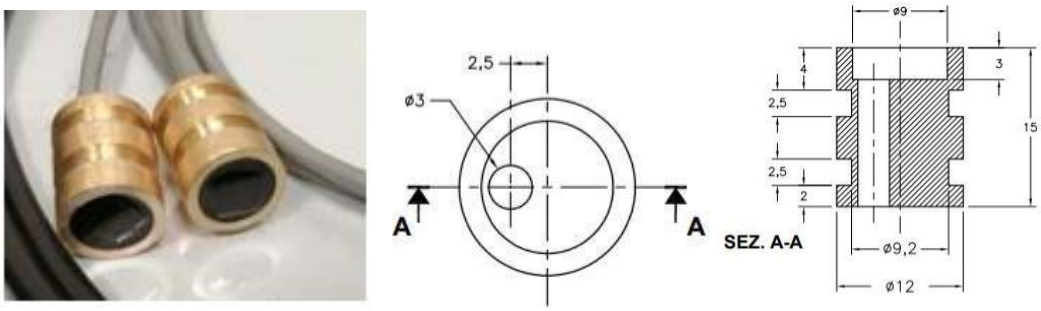

Figure 8.26 Ultrasonic wave transducers in the advanced oedometer along with top view and cross-section of the mold.

The operating frequencies under unloaded conditions for both transducers, after encapsulation in metal supports, are close to 300 kHz.

The transducers are handed in through a hardware-software system developed by Megaris s.r.l. (Figure 8.27). The hardware components consist of a signal acquisition and generation board, along with an input and output signal amplification and conditioning board. The Red Pitaya STEMlab is a commercial board capable of generating or receiving data at rates of up to 125 MS/s, with a full scale of in reception and $\pm 1\ V$ in generation. The signals generated and received by the Red Pitaya are further amplified using the amplification and conditioning board, which can amplify the voltage and current of the generated signals while providing a variable gain for the received signals from transducers.

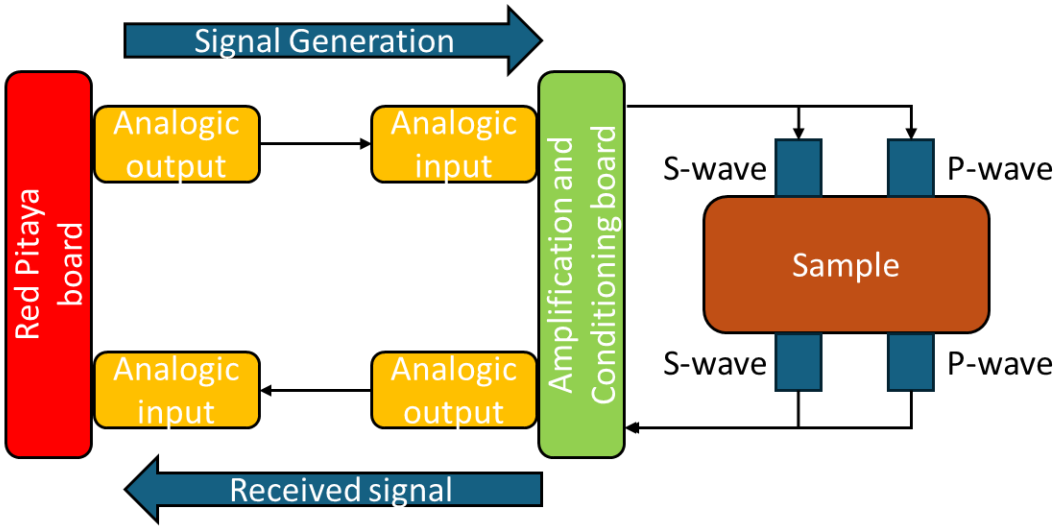

Figure 8.27 Functional diagram of the amplification and conditioning board together with connections to and from Red Pitaya board.

The hardware system is controlled by software developed by Megaris. This software enables the definition, acquisition and visualization of wave signals (Figure 8.28). The main user interface for measuring wave velocities consists of 5 sections: a window for

visualizing the waves (Figure 8.28 - 1); a table (Figure 8.28 - 2) displaying sample details including diameter, height and mass); a measurement specifications setup section (Figure 8.28 - 3) where users can select parameters such as time window duration, single sine frequency, generation amplitude, input gain, signal inversion and the choice of P/S transducers; a series of buttons (Figure 8.28 - 4) for initiating new measurements, computing and displaying the first arrival time of waves, and loading previous measurements; a section (Figure 8.28 - 5) for manually measuring wave arrival times using the start-to-start and peak-to-peak methods (two cursors can be moved along the timeline by the user for this purpose). This adjustment of the cursor allows to obtain an initial estimate of P and S waves within the software. The software employs both time-domain and frequency-domain approaches to evaluate the arrival time of the waves, including Start-to-Start and Peak-to-Peak methods, Cross-Correlation, and unwrapped Phase Angle methods.

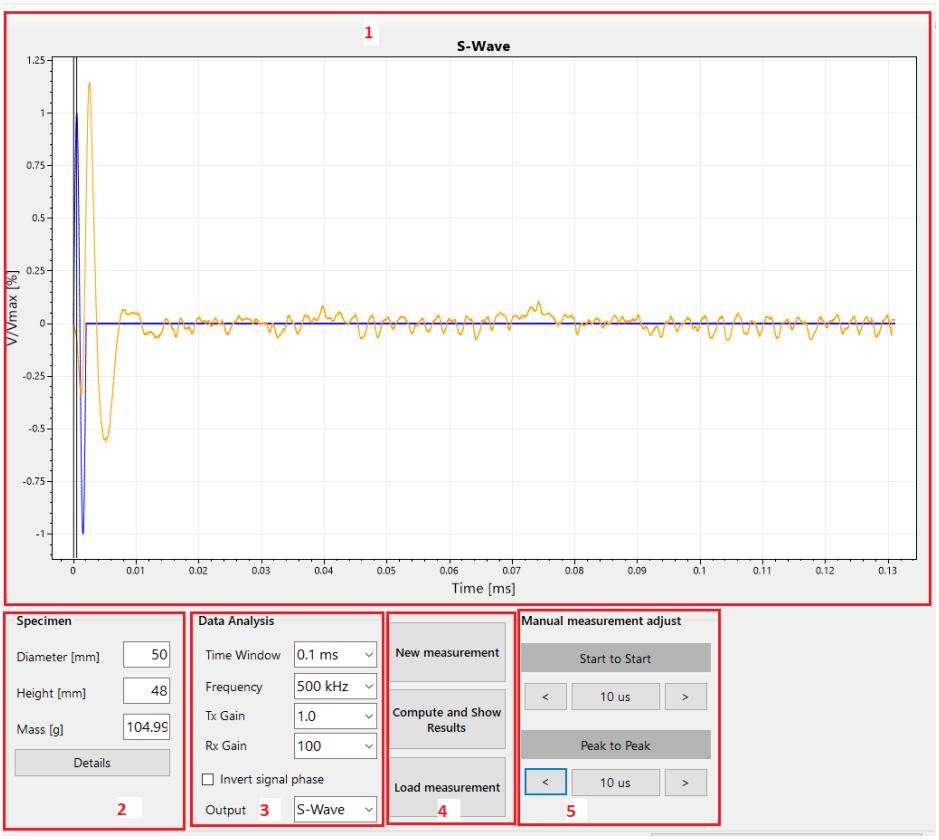

Figure 8.28 The user interface of the software to record and visualize the ultrasonic waves.

The software can record and save data in .txt and .csv formats, enabling users to export the recorded data for further analysis and processing with their preferred methods or tools.

8.5.2 Calibration of ultrasonic wave transducer

The P and S wave transducers were initially calibrated using dry and saturated sand samples. The dry sand sample was prepared through the dry pluviation technique which ensures acceptable degree of homogeneity of the sample. In this technique dry sand was poured into the oedometer ring through a plexiglass cylinder of 50 mm diameter. The cylinder has a predetermined height which insures an initial void ratio between 0.55 and 0.60 as detailed in Ciancimino's PhD dissertation (Ciancimino, 2021). Perth sand was used for calibration purposes because of its physical properties which make it stable during the preparation and installation of oedometer cell.

To prevent the occlusion of the porous stones and ensure effective coupling between the transducers and the sample, a filter paper sheet was cut and placed between the samples and the porous stones (Figure 8.29).

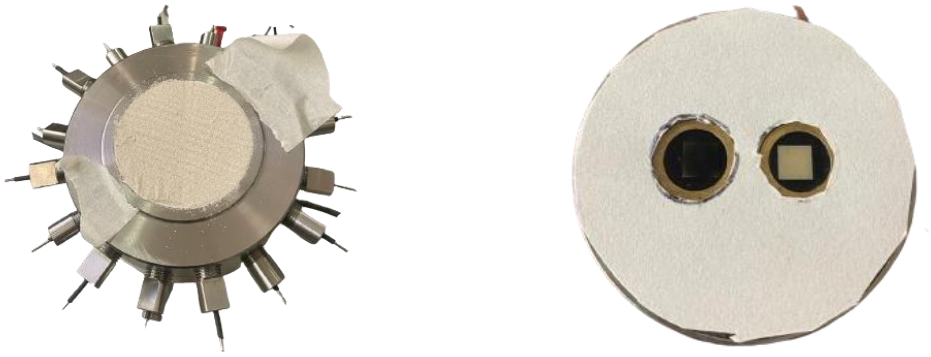

(a) (b)

Figure 8.29 Oedometer ring filled with Perth sand (a) detail of the filter paper assembly with space for piezometric elements (b).

To enhance the contact between the sample and the transducers, grease was applied on the top of the ultrasonic wave transducers. The sample was subjected to a maximum pressure of 6 MPa, and ultrasonic waves were recorded at various stress levels. The S-wave transducer exhibited suboptimal coupling at very low stress levels, which resulted in the absence of measurements for S-wave velocity below 1500 kPa.

Test on dry Perth sand

The ultrasonic wave signals obtained for a sample of dry Perth sand are discussed first. The sand was loaded in the oedometer, and signals were recorded at different stress levels and frequencies. The system enables the recording of signals across a frequency range of 20 Hz to 800 kHz. The instrument's ability to vary the input signal frequency allows for the identification of the frequency range that optimizes the output signal

quality for each transducer. Figure 8.30 displays the P and S wave signals at a stress level of 3500 kPa, for frequencies ranging from 60 kHz to 800 kHz. The input signals are shown in blue whereas the output signals are shown in orange colour.

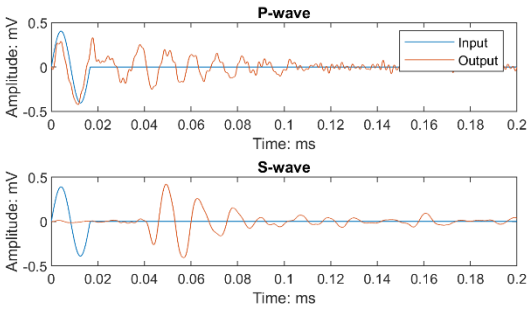

60 kHz

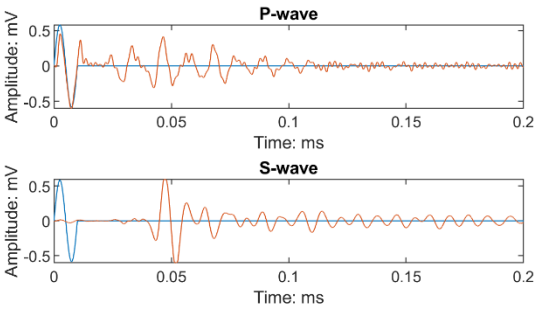

100 kHz

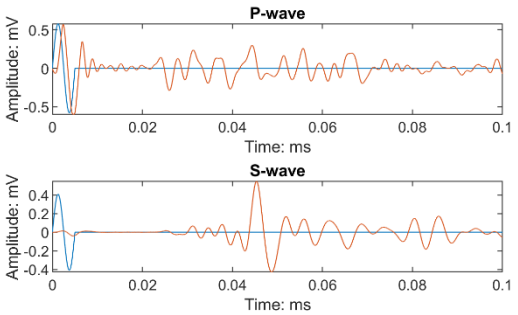

200 kHz

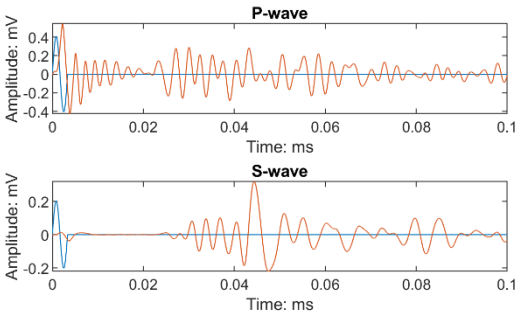

300 kHz

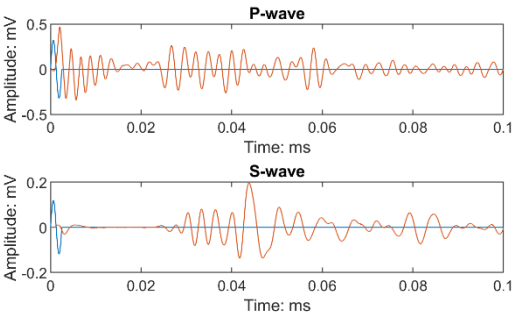

400 kHz

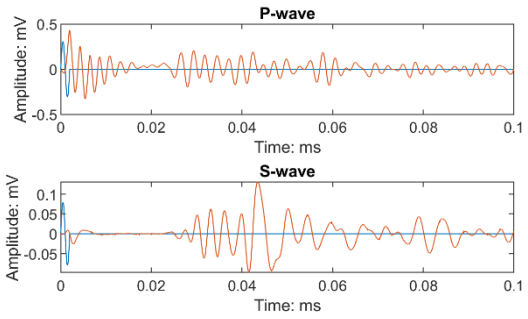

500 kHz

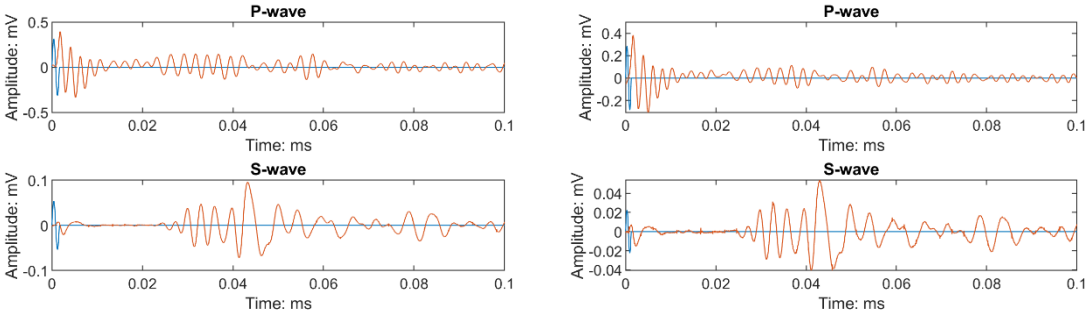

Figure 8.30 P and S wave signals at $\sigma_v' = 3500\ kPa$ at different frequencies.

The figure serves as an example to demonstrate that the instrument can record signals at different frequencies and for evaluation of waves user can select the optimal one. For instance, in the case of dry sand, frequencies of 300 kHz and 400 kHz produced a clearer output signal for the P-wave transducer, enabling a manual estimation of the arrival time at approximately 0.02416 ms (Figure 8.31). In the case of the S-wave transducer, the frequencies of 60 kHz and 100 kHz yielded a good output signal, with a nearly clear wave arrival time that can be manually estimated at around 0.0401 ms (Figure 8.32).

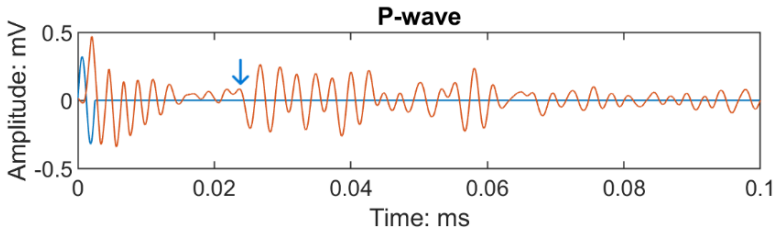

Figure 8.31- P wave signal of Perth dry sand at vertical stress of 3500 kPa at 400 kHz.

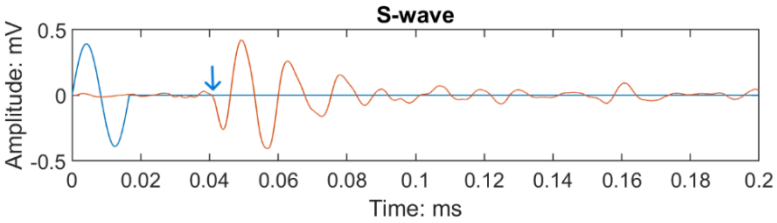

Figure 8.32 S wave signal of Perth dry sand at vertical stress of 3500 kPa at 60 kHz.

With arrival times of 0.02416 ms and 0.0401 ms, the P-wave and S-wave velocities were measured as 983 m/s and 592 m/s, respectively, under an effective vertical stress of 3500 kPa. These values are comparable to those of ultrasonic waves observed in Perth sand, as discussed by Ciancimino, (2021). The author performed resonant column tests on Perth sand at different vertical stresses to obtain a correlation between confining stress and small strain shear modulus (G). For a similar stress state and void ratio (0.534), they obtained a value of Vs=600 m/s. Poisson's ratio for the sample was between 0.22-0.27.

P waves signals are affected by cross-talk as shown in Figure 8.30. Although the S wave signals in this case are not affected by cross talk but in other cases (when clays were tested discussed in Chapter 9) the signals were affected by cross-talk. Also, at low stresses the stress the waves signal is not detected. This can be related to coupling between the sample and transducer. In case of weak coupling the energy is not transmitted through the sample and probably the signal is lost in noise.

Test on saturated Perth sand

The dry sand sample was loaded to 6100 kPa and saturated with distilled water for the wave measurements in saturated conditions. The advanced oedometer was connected to a tank of distilled water through drainage lines. The tank was placed at a slightly higher height than the oedometer so to apply a water pressure of about 5 kPa. The arrivals of P and S waves were analyzed at 3500 kPa along the unloading path and are presented in Figure 8.33. In the signal of S-wave, the first arrival of the P wave can also be appreciated because of cross-talk of compression waves (orange arrow).

The saturated sand had a P wave value of 1513 m/s with arrival time of around 0.01555. In the signal of S-wave the arrival of 0.041792 ms resulted in a value of 565 m/s.

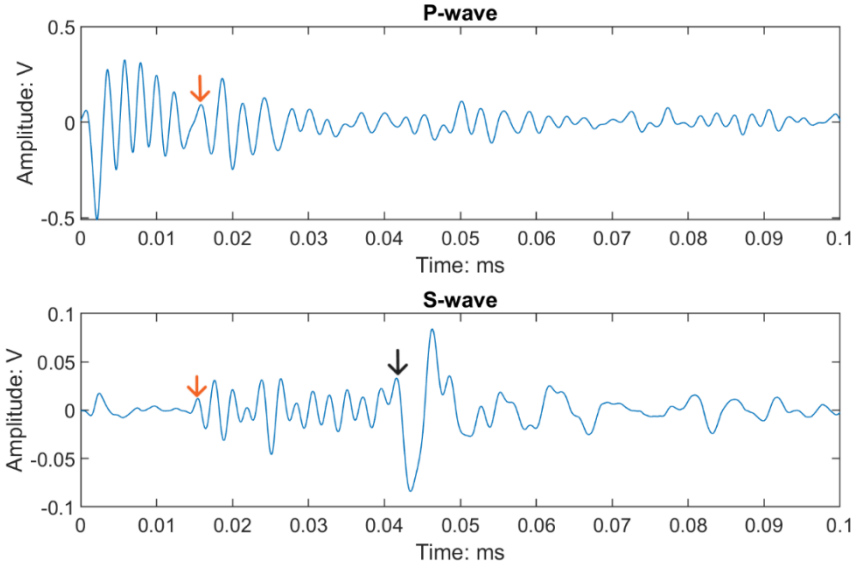

Figure 8.33 The first arrival of P and S waves for saturated sand, recorded at 600 kHz.

8.5.3 Interpretation of signals

The purpose of interpretations of ultrasonic measurements is to determine the propagation velocities of compression and shear waves within the sample ($V_{P,S}= H/t_{P,S}$).

This determination requires measurement of the current height of the sample H at the time of ultrasonic measurements.

Determining the arrival time of waves through visual analysis of the recorded signal in the time domain is the most commonly used method. However, this approach relies on having high-quality signal recording with a high signal-to-noise ratio.

Thus, the determination of wave arrival times according to this mode is done by manual detection of characteristic points of the signal, such as: first signal deflection (t_F) from zero (first arrival), point of maximum (t_{Max}) or minimum(t_{Min}), the first point corresponding to a threshold (t_T, usually 10 %), the first zero point of the sine wave (t_C) (Figure 8.34).

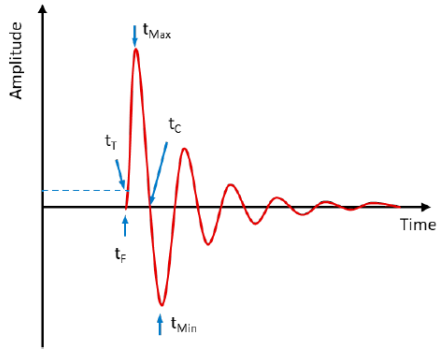

Figure 8.34 Criteria for identifying wave transit time identifying characteristic points (Kaczmarek, 2001).

Recorded signals, especially those related to shear waves, are affected by several phenomena that affect their quality, including near-field effects, geometry effects (distance/wavelength ratio), edge effects, geometry and size of the sample under test, and cross-talk (Sanchez-Salinero et al. 1986; Arroyo et al. 2003, Lee & Santamaria 2005, Brignoli et al. 1996, Arulnathan et al. 1998, Rio et al. 2003, Arroyo et al. 2006).

Several alternative approaches can be used for determining arrival times, either by analysis of signals in the time domain or in the frequency domain. For example, it is possible to estimate arrival times based on the detection of reflected waves, if the recording of the signal at the receiver is of good quality, and, above all, there is a clear distinction between the multi-reflections of the wave. In such a case, estimation can be done either by the identification of wave characteristic points (Figure 8.34) or by the application of the cross-correlation function (Arulnathan et al. 1998, Lee & Santamarina 2005).

In recent years, methods based on time-frequency analysis of signals have been proposed as suitable approaches for determining arrival times. Kumar & Shinde (2019) proposed a method based on the Sliding Fourier Transform of the signal recorded at the

receiver, which allows the π-point identification approach to be applied without the need to generate a continuous sinusoidal input signal with variable frequency. Good results have been obtained through the use of the wavelet transform of signals (Arroyo 2007, Bonal et al. 2012, Capilla 2006, Fernàndez Lavin & Ovando Shelley, 2002).

As part of approaches based on time-frequency analysis of signals, the wavelet transformation method enables the determination of the time of arrival of waves by analyzing only the signals recorded at the receivers, thus without the need to know the input signals. The wavelet transformation method of signal interpretation does not require manual picking of any signal; each signal is analyzed individually without being related to others as done in the case of the cross-correlation method.

Wavelet transformation method

A wavelet is a mathematical function of finite length and fast oscillation. Wavelet transformation decomposes a signal into scaled and translated versions of a wavelet function, which is a localized oscillatory function with finite energy. This decomposition provides a time-frequency representation of the signal, enabling the analysis of changes in frequency content over time. Unlike traditional Fourier-based methods, wavelet transformation allows for simultaneous localization in time and frequency, making it particularly suited for detecting transient phenomena like wave arrivals. Several types of wavelets can be defined by elementary functions such as the Haar wavelet or more complex from a mathematical point of view e.g., Morlet, Meyer, Mexican Hat etc. as shown in Figure 8.35.

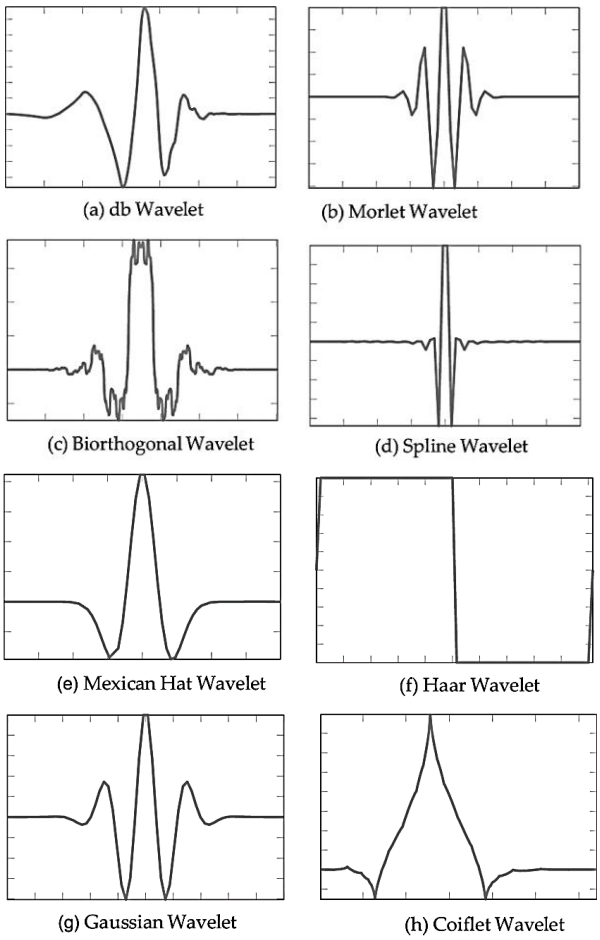

Figure 8.35 Different types of wavelets (Misiti et al. 2019).

In the wavelet transformation, the signal is decomposed using a family of wavelet functions (called daughter wavelets), obtained by scaling (i.e., compressing or dilating), by means of a scaling factor (s), and translating along the time axis, through a translation factor (b), an original wavelet function ($\psi(t)$), called the mother wavelet:

$$\psi_{s,b}(t) = \frac{1}{\sqrt{s}}\,\psi\left(\frac{t-b}{s}\right) \qquad 8.16$$

A good combination of the scale and shape coefficients makes it possible to obtain a frequency-scale relationship, such that the wavelet transformation allows for good frequency resolution at low frequencies, but, simultaneously, good temporal localization at high frequencies.

Like the Fourier transform, a continuous wavelet transformation (CWT) or discrete wavelet transformation (DWT) of an *x(t)* signal can be operated in wavelet transformation. In practical applications where waveforms acquired at receivers are recorded as discrete signals in the time domain, the discrete wavelet transformation is of greater interest.

The DWT consists of considering the discretization of the scale (s), and translation parameters (b), in the following way:

$$s = 2^{-j}$$
$$b = k2^{-j} \quad 8.17$$

Therefore, the wavelet representation takes the following form:

$$\psi_{j,k}(t) = \frac{1}{2^{-j/2}}\,\psi(2^j t - k) \quad 8.18$$

Where *k* represents the position in time, and j is the scale index or transformation level. The discrete wavelet transformation of a signal *x(t)*, which in discrete form can be expressed as *x(k),* can then be written as:

$$d_{j,k} \approx 2^{\frac{j}{2}} \sum_n x(n)\psi\left(2^j n - k\right) \quad 8.19$$

The algorithm for the numerical implementation of the discrete wavelet transformation of a discrete signal in the time domain was proposed by Mallat in 1989. It follows a multi-resolution scheme based on a double filtering approach. In a signal, the low-frequency content represents the most important part, which gives the signal its identity, while the less important high-frequency content defines only small nuances of it (Misiti et al. 2019). Based on this observation, the analysis of signals, using the wavelet transformation, can be limited to the definition of pairs of coefficients: 'approximate coefficients' or 'scale coefficients' (A), which contain the information on the low frequencies of the signal, and 'detail coefficients' or 'wavelet coefficients' (D), which contain the information of the high frequencies of the signal. These coefficients are determined by applying low-pass and high-pass filters to the signal of interest. Since the signal resulting from the application of the low-pass filter may still contain important details, a subsequent step can be carried out in which both filters are further applied. The process can be iterated until satisfactory level splitting is achieved, thus defining a wavelet decomposition tree for the signal (Figure 8.36). The filtering process is always combined with an undersampling process in the analysis of digital signals.

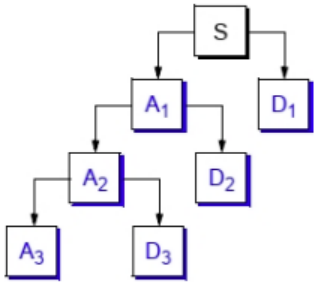

Figure 8.36 Multilevel decomposition tree by signal wavelet transform (Misiti et al., 2019).

The original signal can then be reconstructed from the coefficients A and D, according to the following relationship:

$$x(t) = A(J,t) + \sum_j D(j,t) = \sum_k a_{J,k}\, 2^{\frac{H}{2}}\, \varphi(2^H t - k) + \sum_j \sum_k d_{j,k}\, 2^{\frac{j}{2}} \psi(2^j t - k) \qquad 8.20$$

Where J is the maximum decomposition level of the signal, $\psi(t)$ is the adopted mother wavelet, $a_{J,k}$ are the approximate coefficients obtained for the H level, $d_{j,k}$ are the wavelet detail coefficients, and *φ(t)* is defined as the scaling function, related to the mother wavelet.

This function can also be scaled and translated to form a family of scaling functions, which in the discrete domain takes the form:

$$\varphi_{j,k}(t) = \frac{1}{2^{-j/2}}\, \varphi(2^j t - k) \qquad 8.21$$

The simplest wavelet function that can be used in the transformation is the 'Haar wavelet' which was adopted in this study.

$$\psi(t) = \begin{cases} 1 & 0 \le t < 0.5 \\ -1 & 0.5 \le t < 1 \\ 0 & others \end{cases} \qquad 8.22$$

In such a case, the evaluation of the approximate coefficients or scaling coefficients (A) and the detail coefficients or wavelet coefficients (*D*), at the j+1 level of signal decomposition can be evaluated from the *x(j)* signal at the *j-th* level, following the equations:

$$\begin{aligned} A(j+1,i) &= \frac{1}{\sqrt{2}}[x(j,2i-1) + A(j,2i)] \\ D(j+1,i) &= \frac{1}{\sqrt{2}}\,[x(j,2i-1) - A(j,2i)] \end{aligned} \qquad 8.23$$

Where i represents the position in time (i=0- $2^{(J-j)}{}_{+}1$), j is the transformation level, the range of which is 0-(J-1). The maximum number of transformation levels (*J*) can be defined by the length (*N*) signal analyzed as ($J = Log_2(N)$).

Each level of wavelet decomposition is associated with an energy content that can be evaluated as the sum of the square of the coefficient *D(j,i):*

$$E(j) = \sum_i [D(j,i)]^2 \qquad 8.24$$

The function *E(j)* is also called the variance or wavelet spectrum. The quantity $[D\ (jj,i\ )]^2$ represents the energy associated with the coefficient *D(j,i)*.

Energy preservation is a feature of wavelet transformation, so we have that the total energy of the *x(t)* signal must be equal to that of the transformed signal:

$$E_{tot} = \sum_{t=0}^{N} [x(t)]^2 = \sum_j \sum_i [D(j,i)]^2 \qquad 8.25$$

Analysis of the variance of the wavelet *E(j)* in the time domain turns out to be a useful tool for identifying a time variation associated with a specific event, such as the arrival of a wave. The time of arrival of a wave can thus be identified by identifying the instant at which there is a first deviation of the energy value from its mean value. Then, if the ratio of the square of the wavelet coefficients to the average energy change is reported in the time domain:

$$e_j = \frac{[D(j,i)]^2}{\frac{1}{2^{J-j}} \sum_i [D(j,i)]^2} \qquad 8.26$$

The identification of the time at which the first peak of the relationship is observed, Eqn. 8.26, (Figure 8.37), determines the arrival time of the wave. This criterion has been used for the identification of microseismic events (Capilla 2006) and for determining the arrival time of shear waves (Fernàndez Lavin & Ovando Shelley, 2020).

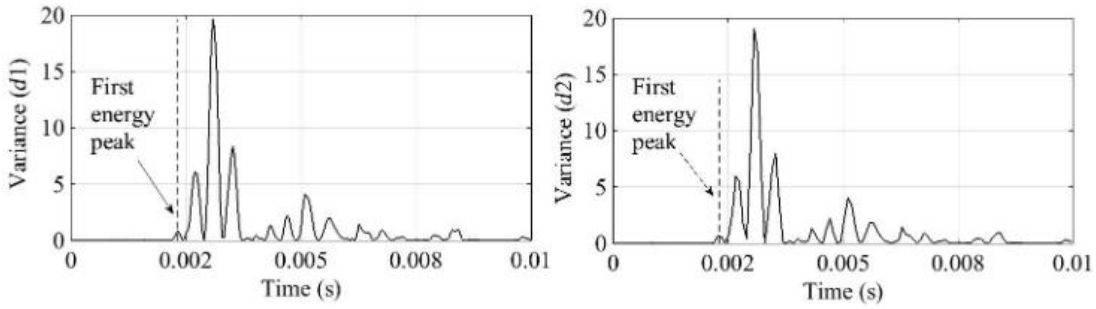

Figure 8.37 Location of energy peaks (Eq. 8.26), for the first two levels of signal decomposition by wavelet transformation (Fernàndez Lavin & Ovando Shelley, 2020).

In this study, the signal interpretation method based on the wavelet transformation was applied for both P-wave and S-wave arrival estimation. A *MATLAB* code was written for the algorithm of Haar wavelet transformation, and the results were interpreted.

Cross-correlation method

Apart from wavelet transformation, cross-correlation method was also employed for the first arrival interpretation of waves. It was used as a complementary tool for the waves arrival elaborations.

The cross-correlation function represents a measure of the correlation of two signals *x(t)* and *y(t)* in the time domain. The correlation function is expressed by the following relationship:

$$RR_{x-y}(\tau) = \lim_{\tau \to \infty} \frac{1}{T} \int_T x(t) \cdot y(t+\tau) dt \qquad 8.27$$

where T is the time duration of the signals and τ represents the time difference between the signals. The function defined in this way has a maximum (or minimum depending on the phase concordance or discordance of the two signals) at the value τ, which can then be considered precisely the travel time of the wave.

The signal processing methodology for cross-correlation in determining the first arrival of elastic waves is based on the application of cross-correlation function between a reference signal and other signals. The reference signal is acquired at a loading step where the signal is clear and all other signals recorded at other test instants. The determination of wave arrival time using such a function assumes that both signals are of the same nature (Santamarina and Fam 1997). Such a signal interpretation protocol makes it possible to free oneself from recording input signals, and from having to analyze each signal individually recorded at the receiver transducers in the time domain.

The procedure is applied according to the following three steps:

1) One output signal is taken as a reference one which is analyzed in the time domain for determination, by manual picking, of the time of first arrival (t_0).
2) All other signals recorded at subsequent loading phases are analyzed by applying the cross-correlation function Eq. 8.27, which will provide the time lag (τ_i) between the signal taken as the reference and all others.
3) The time of first arrival of the recorded wave at the i-th signal will then be obtained from:

$$t_i = t_0 \pm \tau_i \qquad 8.28$$

The procedure is done through a MATLAB code and it allows signals analyzed at different loading of test to be realigned with the one taken as the reference. This makes it possible to possibly observe variations in the signals in terms of waveforms and amplitudes resulting from the progression of degradation processes in the samples recorded during the test.

The signal interpretations of different tests conducted in advanced oedometer are presented in Chapter 9.

8.6 Conclusions

The setup and calibration of the advanced oedometer were established. The advanced oedometer can be utilized for both electrical resistivity tomography and ultrasonic wave measurements. These measurements serve to monitor changes in the properties of pore fluid compositions and alterations in the fabric of samples, respectively.

For electrical resistivity tomography, a measurement protocol was established which was designed for recording data on electrical conductivity. The protocol strikes a balance between acquisition time and the level of detail gathered during the reconstruction of electrical conductivity distribution within the samples. It includes specific sequences of electrodes that capture detailed readings of electrical conductivity across the sample. This protocol was ultimately employed in the tests conducted with the advanced oedometer.

The inversion process was performed in an open-source code, *ResIPy*. The simulation of the flushing test in *COMSOL* allowed to obtain electrical conductivity data which was for inversion. The potentialities of *ResIPy* to invert the electrical conductivity data obtained from the simulated flushing were investigated. The average values of reconstructed and *COMSOL* electrical conductivity showed that *ResIPy*'s potential is significant. The inverted values of electrical conductivity were similar to that of the *COMSOL* data in cases when less heterogeneity of electrical conductivity was observed. Comparing the two electrical conductivity data at different heights of the sample revealed that the *ResIPy* can reconstruct the heterogeneity of the sample for most of the cases when the electrical conductivity gradient was relatively small. The effect of anisotropy of the smoothness factor in *ResIPy* showed that its effect is minimal especially when the range of electrical conductivity was large.

The calibration of ultrasonic wave transducers demonstrated its potential and working. An introduction to wavelet transformation and cross-correlation was provided which will be used for interpretation of the P and S-wave signals.

Chapter 9 Effects of acid exposure on caprock material

As stated in Chapter 8 an experimental campaign was designed to investigate the short-term effects of the interaction of caprock materials with an acid solution, such as the one that might develop because of CO_2 dissolution. Clay B and Clay C were used in this study of acid exposure through diffusion and flowthrough experiments run under oedometer conditions. A 0.01 M HCl (pH=2) solution was employed to force chemical interactions between the acid and the soil. As discussed in the literature review (Chapter 3) the pH achieved by CO_2 dissolution into the brine in reservoir conditions is about 3.3 (Grgic, 2011; Sterpenich et al., 2009). However, a lower pH was adopted in the tests as an attempt to further force the reactions between the carbonate minerals and the solids (decalcifications) which are the main ones expected for geochemical reactions. This strategy is aimed at attempting to increase the dissolution of carbonates, which impact the mechanical behavior of the caprock, and that in field conditions might be enhanced by transport phenomena occurring for very long times, which largely exceed those of laboratory experiments.

The material was exposed to acid under diffusion and advection conditions (flowthrough experiments). In the diffusion tests, standard oedometer cell basins were filled with the pH 2 acid solution at a defined vertical stress. Flowthrough experiments were conducted using the advanced oedometer cell, where the acid solution was injected from the base of the sample. The aim of the investigation was to study the effects of carbonate dissolution in reconstituted and intact samples and its effect on the pre-consolidation pressure and compressibility. Notice that, at present, the loading frame adopted in the experiments run in the advanced oedometer does not allow imposing the vertical stresses relevant for the in-situ conditions. However, the purpose of the experiments was addressing preliminary changes in response that would occur as a consequence of acid migration and possible carbonate dissolution.

This chapter presents the outcomes of these experiments. The chapter starts with an introduction to the tests conducted, accounting for the mechanical, hydraulic and chemical histories imposed during the tests. The results of these tests are then discussed.

For the advection tests conducted in the advanced oedometer, additional data from Electrical Resistivity Tomography (ERT) and ultrasonic wave analysis are also presented.

9.1 Test plan

Three oedometer tests were carried out on reconstituted specimens of Clay B. One reconstituted specimen was used to determine the reference mechanical behavior (without chemical interactions). The specimen was loaded and unloaded by stepwise changes of the applied axial load and always kept in contact with distilled water. A second reconstituted specimen was loaded and then exposed to acid through diffusion, while a third specimen was loaded and then exposed to acid through advection in the advanced oedometer (flowthrough experiment).

Other three oedometer tests were carried out on intact specimens of Clay C. One specimen served as a reference for the mechanical behavior: it was loaded and unloaded by stepwise changes of the applied axial load and always kept in contact with distilled water. The other specimen was loaded and then exposed to acid through diffusion. The third specimen was tested in the advanced oedometer where the specimen was exposed to acid under advection conditions.

The ID of the tests follow the same guidelines as discussed in Chapter 6. The ID starts with the Clay type i.e., B' or 'C' followed by the state of the sample i.e., intact (I) or reconstituted (R) sample. The ID then provides information on the exposure and non-exposure of the sample. 'N' is used for non-exposed and 'T' is used in the case where the test is performed in acidic environment. The term T, in the subscript, also provides information on the state of acid exposure, i.e., diffusion (Diff) or advection (Adv). The last two terms of the ID represent that it is an oedometer test and the effective vertical stress at which the exposure of the sample was performed.

9.2 Sample preparation

9.2.1 Clay B specimens

The Clay B dry powder was mixed with distilled water at a water content of about w = 50 % (1.16 LL). Using this slurry a sample was consolidated by stepwise increase of the axial load up to 1 MPa. After that, the consolidated specimen was unloaded, dismantled and cut into three specimens for testing. Two specimens were tested in conventional oedometers: their initial height was 20 mm. Another specimen was used for flowthrough experiment in the advanced oedometer and had an initial height of 25 mm. In oedometer, these specimens were loaded to a maximum vertical stress of 6 MPa.

9.2.2 Clay C specimens

Intact specimens had an original diameter of 50 mm and height of 25 mm. Apart from the specimens used for advection test, the samples were trimmed to obtain specimens for the small diameter oedometer (diameter of 25.2 mm and height of 20 mm). Such specimens were tested up to vertical stress of 28 MPa. Distilled water was added under a vertical effective stress of 12.5 kPa to saturate the specimen. The specimen showed swelling when water was added which was prevented by increasing the vertical stress until the swelling stopped at 109 kPa and was left for 24 hours. The specimen used for advection was used without trimming as it had the exact dimensions of the advanced oedometer.

9.3 Chemo-Hydro-Mechanical loading histories

9.3.1 Reconstituted specimens

Test B-R-N-Oed-1 was performed to determine the reference mechanical behavior of the reconstituted soil without interaction with the acid solution. The adopted loading-unloading sequence in terms of axial stress (MPa) was: 0.054, 0.107, 0.243, 0.486, 1, 2, 4, 6, 2.89, 1.05, 0.27, 0.135.

All the loads were kept constant between 24 to 56 hours, except for the ones at 1 MPa and 4 MPa, which were kept constant for one week as summarized in Table 9.1.

Table 9.1 Details of each load and the time of application for B-R-N-Oed-1.

Vertical stress σ'_V - (MPa)	Time of loading – (hours)	Remarks
0.054	24	
0.107	26	
0.243	32	
0.486	26	
1	171	Creep
2	28	
4	174	Creep
6	56	
2.89	27.8	
1.05	25	
0.27	28.5	
0.135	42	

Test B-R-T_{Diff}-Oed-1 was aimed at investigating the chemo-hydro-mechanical response upon exposure to acid solution through diffusion, both in terms of transient behavior

during diffusion and impact on the compression behavior. The applied loading sequence in terms of vertical stress (MPa) was: 0.049, 0.098, 0.196, 0.392, 0.784, 1, 1.54, 3, 6.1, 3, 1.54, 0.19.

All the loads were kept constant between 24 to 96 hours, except for the one of 1 MPa, which was kept constant for around 37 days as summarized in Table 9.2. Almost immediately after applying such load (after about 10 minutes), the distilled water in the oedometer cell basin was removed and replaced by a 0.01 M HCl solution (pH=2), allowing for diffusion of H^+ and Cl^- ions from the basin towards the sample, while other ions (Ca^{2+}, Na^+, Mg^{2+}, CO_3^{2-}…) diffused from the sample towards the basin. The pH of the acid in the cell was recorded over time and the solution in the cell basin was replaced by a new pH 2 solution after the pH increased. The pH was measured once every day initially and the acid solution was replaced when the pH increased above 3.

Table 9.2 Details of each load and the time of application for B-R-T_{Diff}-Oed-1.

Vertical stress (σ'_V) - (MPa)	**Time of loading – (hours)**	**Remarks**
0.049	24	
0.098	24	
0.196	28	
0.392	24	
0.784	96	
1	889 (~37 days)	Diffusion of 0.01M HCl
1.54	45	
3	28	
6.1	40	
3	30	
1.54	24	
0.19	36	

Test B-R-N-Oed-1 aimed at determining the creep parameter and behavior for normally consolidated sample. Although running the creep at the same stress of test B-R-T_{Diff}-Oed-1 would have allowed for a direct comparison between the two tests, it is believed that that viscoplastic modeling with the VNM, for these normally consolidated materials, allows a very good forecast of the response also at different stresses and different creep times. By repeating the creep stage twice (1 MPa and 4 MPa), test B-R-N-Oed-1 allowed clearly appreciating the increase in preconsolidation stress associated with the creep and a more insightful view of the effects of the long-term stress application on mechanical behavior. Notice that a model would have been in any case required to allow appreciating

the geochemo-mechanical effects of exposure to acid for the B-R-T_{Adv}-Oed-1 test, as in the latter case the pore pressure distribution is not homogeneous within the sample.

Test B-R-T_{Adv}-Oed-1 was performed to investigate the chemo-hydro-mechanical response upon exposure by forced advection, both in terms of transient behavior during the advection stage and impact on the compression behavior. The applied loading sequence in terms of vertical stress (MPa) was: 0.054, 0.108, 0.216,0.432, 0.863, 1, 1.5, 2, 2.9, 6.15, 3, 1.3, 0.27, 0.108.

All the loads were kept constant between 24 to 96 hours, except for the one of 1 MPa, which was kept constant for ~35 days, during which a 0.01 M HCl solution was injected into the specimen through forced advection as shown in Table 9.3. The acid was injected into the specimen using a pressure/volume controller by GDS instruments ((HPDPC-H pump) applying a pressure of 0.5 MPa from the bottom of the sample while leaving the drainage at the top of the sample open. The effluent was collected, and pH was measured over time. The ERT and ultrasonic wave measurements were recorded over the course of the test. After exposure to acid, the specimens of both the diffusion and advection tests were loaded to 6 MPa and then unloaded.

Table 9.3 Details of each load and the time of application for B-R-T_{Adv}-Oed-1.

Average effective vertical stress (σ'_V) - (MPa)	**Time of loading – (hours)**	**Remarks**
0.054	24	
0.108	25	
0.216	30	
0.432	28	
0.863	96	
1	839 (~35 days)	Advection of 0.01M HCl
1.5	32	
2	28	
2.9	32	
6.15	30	
3	25	
1.3	24	
0.27	25	
0.108	46	

Figure 9.1 shows the complete setup of the advanced oedometer during the advection test (B-R-T_{Adv}-Oed-1). On the top right is the acid tank connected to the GDS corrosion-resistant pump. On the top left is the Complex Impedance Tomograph (CIT) used for

injecting currents and acquiring potentials. It is connected to the advanced oedometer through electrodes in green colour. The effluent is collected in a beaker connected through top drainage to the advanced oedometer.

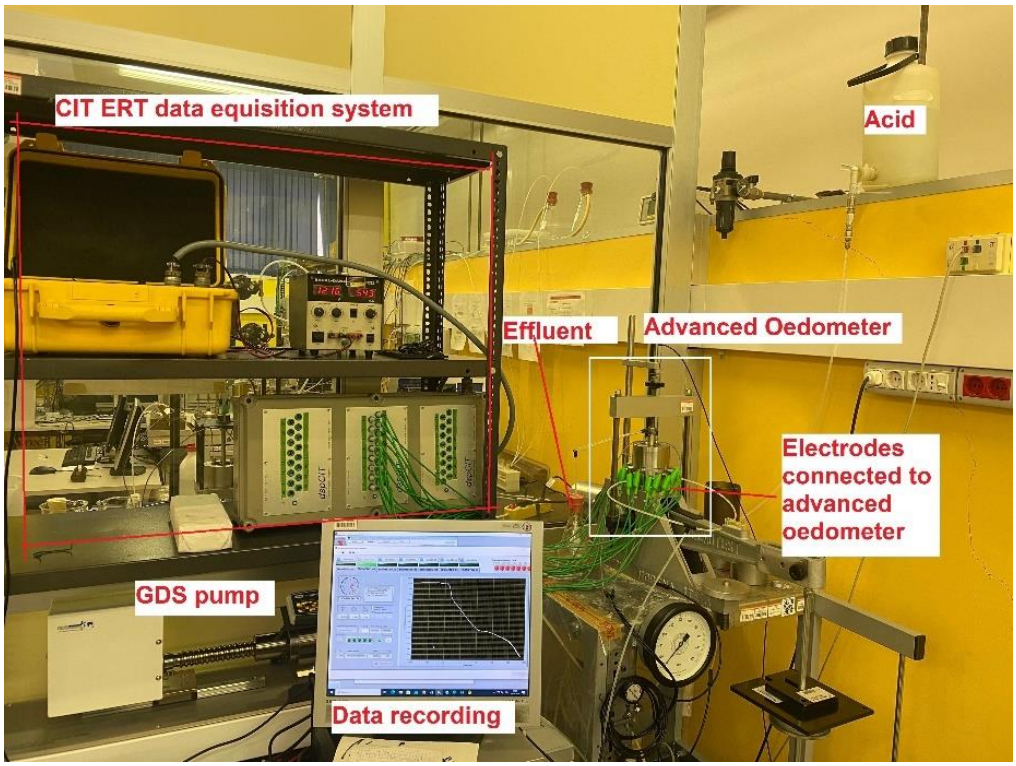

Figure 9.1 Setup of advanced oedometer including acid tank, GDS pump and CIT data recording system.

The diffusion (B-R-T_{Diff}-Oed-1) and the advection (B-R-T_{Adv}-Oed-1) stages took place on normally consolidated (NC) samples, under the same average effective stress of 1 MPa. However, the effective stress state imposed in the B-R-T_{Diff}-Oed-1 test was homogeneous, whereas it was heterogeneous in the B-R-T_{Adv}-Oed-1 test, because of the pressure difference between the sample bottom and top. Under steady-state conditions, the fluid pressure in the centre of the sample was 0.25 MPa. The vertical total stress applied was then 1.25 MPa, so to ensure a vertical effective stress in the centre of the sample of 1 MPa (see Table 9.4).

Table 9.4 Stress state of reconstituted specimens at the stage of exposure to acid.

	B-R-T_{Diff}-Oed-1	**B-R-T_{Adv}-Oed-1**
Total stress $\boldsymbol{\sigma_V}$ (MPa)	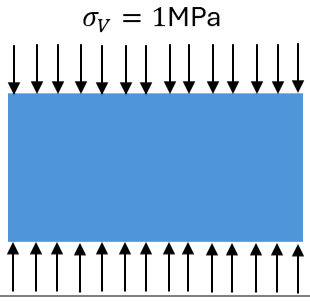	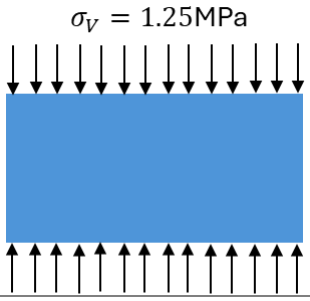
Fluid Pressure $\boldsymbol{u}$ (MPa)	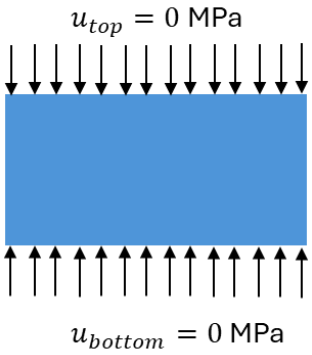	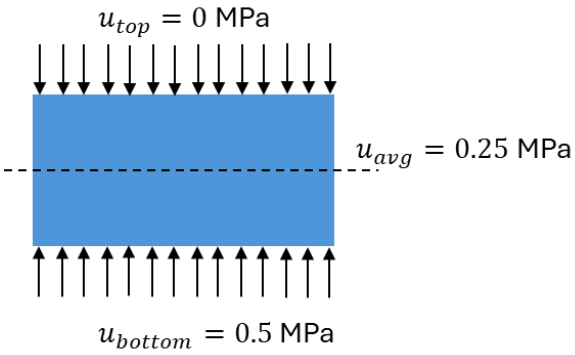
Effective Stress $\boldsymbol{\sigma'_V}$ (MPa)	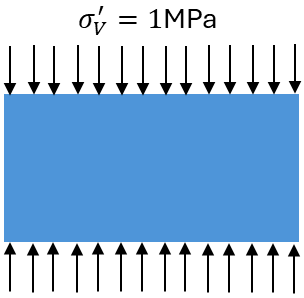	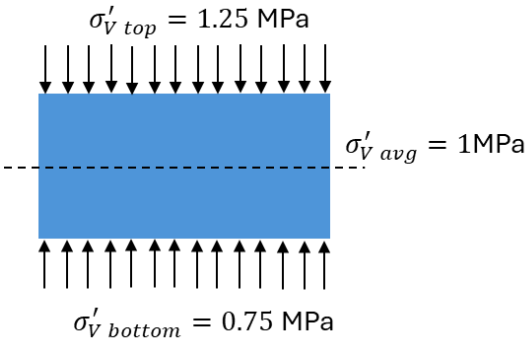

9.3.2 Intact specimens

Intact specimens were tested in a small diameter oedometer (diameter 25.2 mm), which makes it possible to apply high vertical stress of 28 MPa. One specimen was tested in standard conditions (distilled water as fluid in the cell basin, test C-I-N-Oed). The applied loading sequence in terms of vertical stress (MPa) was: 1.5, 3.198, 7, 14, 21.1, 28.14, 14.07, 3.52.

Test C-I-T_{Diff}-Oed-13 was performed to investigate the chemo-hydro-mechanical response of the intact specimen upon exposure to acid by diffusion, both in terms of

transient behavior during the diffusion stage and impact on the compression behavior. The applied loading sequence in terms of vertical stress (MPa) was: 0.109, 0.220, 0.440, 0.879, 2.6, 6.15, 13, 20, 28.14, 13, 2.6.

The diffusion step occurred under a vertical effective stress of 13 MPa and it lasted 30 days. The pH of the acid in the cell was recorded over time and the solution in the cell basin was replaced by a pH 2 solution after the pH increased. The pH was monitored around every two or three days and the acid in the basin was replaced by a fresh solution when the pH increased above 2.5.

Test C-I-T_{Adv}-Oed-1.5 was performed in advanced oedometer where acid was injected at vertical effective stress of 1.5MPa. The acid injection pressure was 0.5 MPa at the bottom of the sample. The stress state of the two tests is shown in Table 9.5.

Table 9.5 Stress state of intact specimens of Clay C at the stage of exposure to acid.

	C-I-T_{Diff}-Oed-13	**C-I-T_{Adv}-Oed-1.5**
Total stress $\boldsymbol{\sigma_V}$ (MPa)	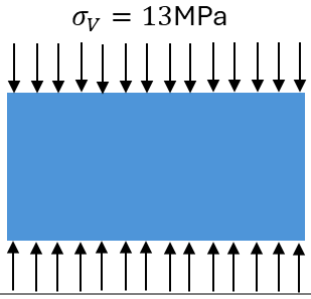	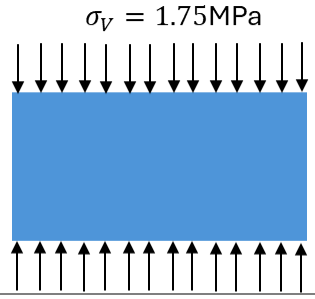
Fluid Pressure $\boldsymbol{u}$ (MPa)	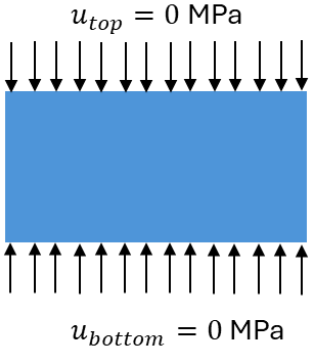	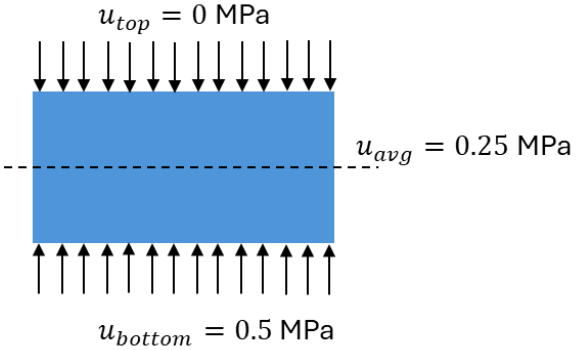
Effective Stress $\boldsymbol{\sigma'_V}$ (MPa)	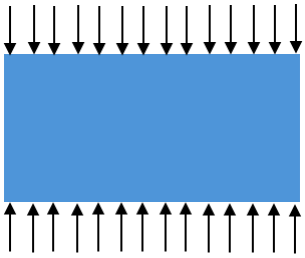	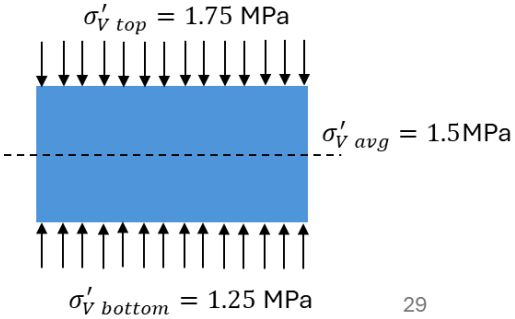

29

Table 9.6 summarizes all the tests done on Clay B and Clay C with number of days of exposure.

Table 9.6 Summary of all the tests.

Test	Max axial stress (MPa)	Creep (Y/N)	Diffusion (Y/N)	Advection (Y/N)
B-R-N-Oed-1	6	Y (1 week at 1 MPa 1 week 4 MPa)	N	N
B-R-T_{Diff}-Oed-1	6	N	Y (37 days)	N
B-R-T_{Adv}-Oed-1	6	N	N	Y (35 days)
C-I-N-Oed	28	N	N	N
C-I-T_{Diff}-Oed-13	28	N	Y (30 days)	N
C-I-T_{Adv}-Oed-1.5	6.7	N	N	Y (43 days)

9.4 Experimental results of tests on Clay B specimens

The results of the tests performed on the Clay B reconstituted specimens are presented in this section by comparing the compression curves of the three tests. This section also contains the results on the time evolution of strains during the exposure stages of diffusion and advection tests. For the advection test the time evolution of electrical conductivity and ultrasonic waves are also presented.

9.4.1 Compression curves

The comparison of the compression curves of the three tests carried out on reconstituted specimens is presented in Figure 9.2. The blue line shows the compression curve of the test on non-exposed sample (B-R-N-Oed-1) for which the creep behavior was studied at 1 and 4 MPa for 1 week. The red lines show the compression curves of exposed specimens where the acid was introduced in the specimen at 1 MPa under diffusion or advection.

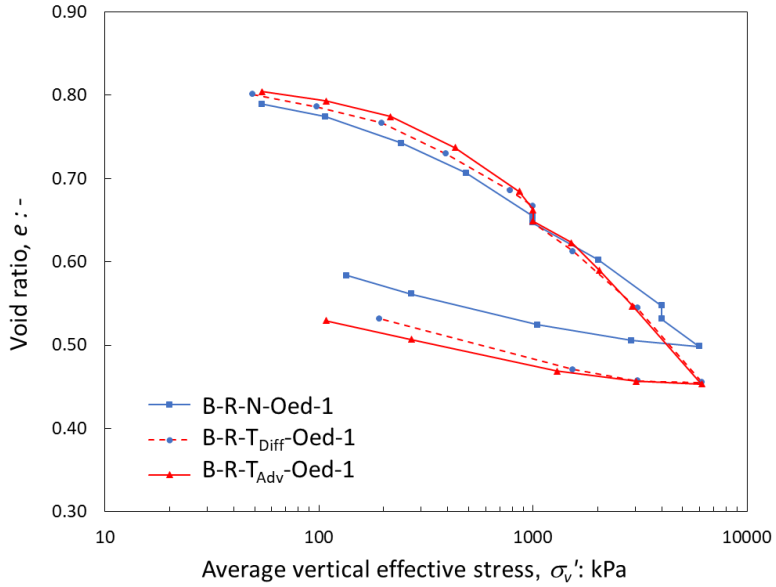

Figure 9.2 Compression lines of reconstituted specimens with water, acid diffusion and acid advection.

The deformations occurring during the exposure stage of about one month, induced either by diffusion (test B-R-T_{Diff}-Oed-1) or by advection (test B-R-T_{Adv}-Oed-1), appear to be slightly larger than those related to one week of creep (test B-R-N-Oed-1). However, the following compression behavior appears to be significantly influenced by acid exposure. Upon the first load imparted after exposure, the compression curve of the B-R-T_{Adv}-Oed-1 appears to overlap almost perfectly with the one of B-R-N-Oed-1, while the compression curve of the B-R-T_{Diff}-Oed-1 moves to a slightly lower void ratio. At higher loads (σ' > 2 MPa) both exposed specimens appear to be more compressible than the non-exposed specimen and at the highest stress of 6 MPa, both exposed specimens have the same void ratio (e = 0.454), noticeably smaller than the non-exposed specimen (e = 0.498). Therefore, although the impact of the carbonate dissolution appears to be modest in terms of strains accumulated during the exposure stage, it seems to affect the compressibility of the soil, which is appreciably increased. The change in slope of the compression curve of the B-R-T_{Adv}-Oed-1 at σ_v = 2 MPa might also indicate a small collapse of bonds, which cannot withstand larger stresses. The compression indexes of the reconstituted samples are presented in Table 9.7.

Table 9.7 Compression indices for reconstituted specimens of Clay B.

	B-R-N-Oed-1	**B-R-T_{Diff}-Oed-1**	**B-R-T_{Adv}-Oed-1**
C_r (-) *	0.072	0.063	0.063
C_c (-) **	0.220	0.261	0.286
C_s (-) ***	0.059	0.062	0.050

(*) evaluated in the stress range 98 kPa – 196 kPa

(**) evaluated in the stress range 1540 kPa – 6160 kPa

(***) evaluated in the stress range 3000 kPa – 135 kPa

9.4.2 Time evolution of strains during the exposure stages

The exposure of the reconstituted specimens to acid was carried out at 1MPa. Flowthrough experiments were carried out for around one month, the recorded strains are expected to be the sum of creep effects and geochemical effects. The Vermeer & Neher (1999) creep model (Appendix C for a short description of the model and its use) was used for model fitting to differentiate between the effects related to geochemical reactions (e.g. carbonate dissolution) and creep. Therefore, purely geochemical strains can be evaluated as the difference between total strains and model ones. Figure 9.3 shows the experimental results and the model fitting for the creep stage of test B-R-N-Oed-1. The parameters were obtained for the reconstituted sample that was not exposed to acid. The parameters used in the model fitting are the recompression index, $C_r = 0.072$, compression index, $C_C = 0.179$, secondary compression index, $C_\alpha = 0.004$ and coefficient of consolidation, $C_V = 1.4 \cdot 10^{-7} m^2/s$. For the model fitting a lower value of Cc is used as compared to that stated in Table 9.7. The smaller values of Cc adopted in the test modelling can be explained considering that the values of Table 9.7 were evaluated at a stress level between 1500-6160 kPa which is higher than 1 MPa at which the creep was analyzed. In contrast, the stiffness of the specimen under the creep load is slightly higher than the one at higher stresses.

In the model simulation, the sample was discretized in three layers, and the time evolution of the effective stress in the middle of each of them was modelled according to the Terzaghi consolidation equation, with perfect drainage at both ends of the sample.

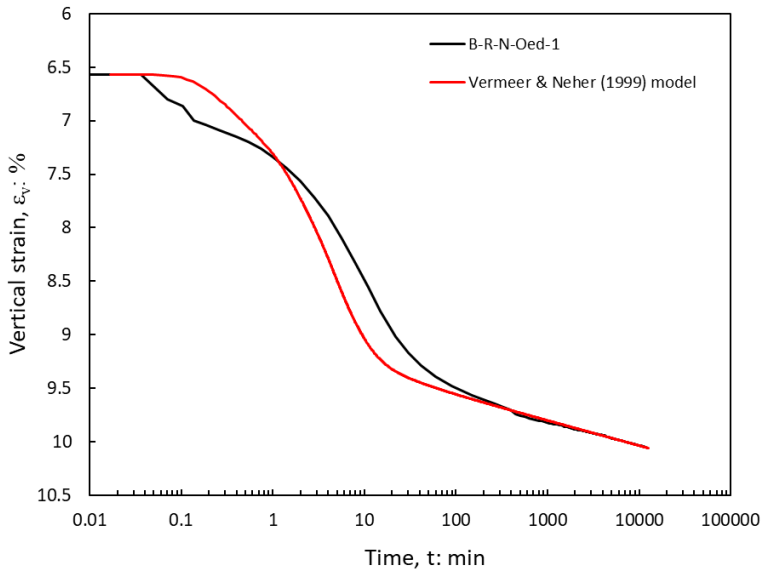

Figure 9.3 Time evolution of vertical strain during the consolidation and creep stage of test B-R-N-Oed-1.

The time evolution of the vertical strain during the diffusion stage of test B-R-T_{Diff}-Oed-1 and the predictions of the Vermeer & Neher (1999) model (VNM), accounting only for the expected consolidation and creep strains, are shown in Figure 9.4. It can be appreciated that the strains predicted by the model do not follow the classical 'S' shape of consolidation + creep stages. This aspect can be explained, and reproduced by the VNM, accounting for the effects of creep on the prensolidation stress (see e.g. Bjerrum, 1967). To this extent, it is convenient considering the role of the loading sequence applied, particularly the previous load step where an axial stress of 0.784 MPa was applied. Such stress was kept constant, instead of one day as in conventional tests, for four days. During this time, the preconsolidation stress increased above the applied stress value. According to the predictions of the VNM, the value of the preconsolidation stress achieved this way was about 0.84 MPa. After four days, the stress was increased to 1 MPa (i.e. the stress increment was equal to about only one-fourth of the previously applied stress), i.e. to a stress only slightly greater than the developed preconsolidation stress. This procedure contrasts with the one of traditional testing, where for normally consolidated samples the applied stress doubles the preconsolidation one, and explains the shape both of the experimental curve before exposure to acid and of the predictions of the VNM model.

The implications of the loading duration on the preconsolidation stress and of the preconsolidation stress on the creep strains according to the VNM are briefly discussed in Appendix B. The adopted parameters of the VNM model and of the Terzaghi's 1D consolidation were $C_r = 0.072$, $C_c = 0.179$, $C_\alpha = 0.0046$ and $C_V = 1.4 \cdot 10^{-7} m^2/s$.

The acid solution was poured into the oedometer cell basin about 10 minutes after applying the load. Comparison with the VNM predictions suggests that a small increase in the vertical strain, due to the geochemical reactions, occurred afterwards.

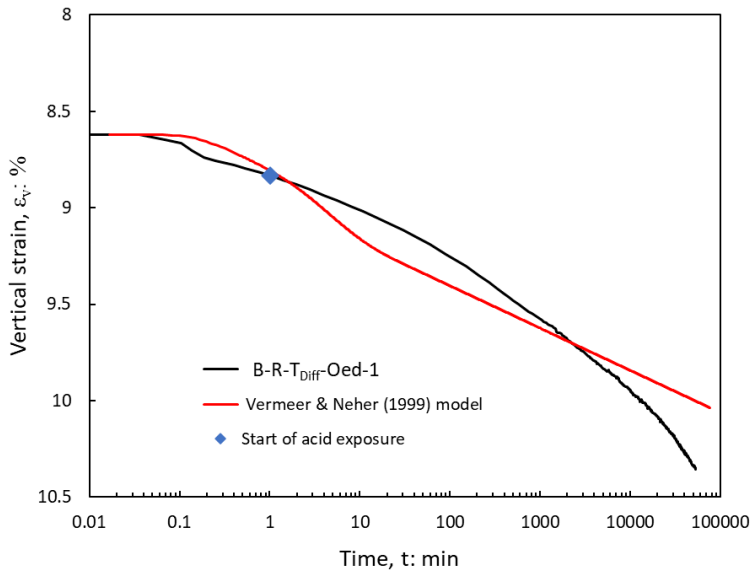

Figure 9.4 Time evolution of vertical strain during the diffusion stage of test B-R-T_{Diff}-Oed-1.

The experimental line shows higher strain in comparison to the model after around 6 days which might be reasonable time for diffusion of acid from the cation towards the specimen and following decalcification reaction.

Figure 9.5 shows the experimental curve for the advection stage of test B-R-T_{Adv}-Oed-1, along with model fitting. The simulations were carried out considering the imposed hydraulic history, which accounts for the effect of consolidation imparted by the increase of vertical stress and the transient hydraulic history which took place as the fluid pressure was increased at the bottom of the specimen.

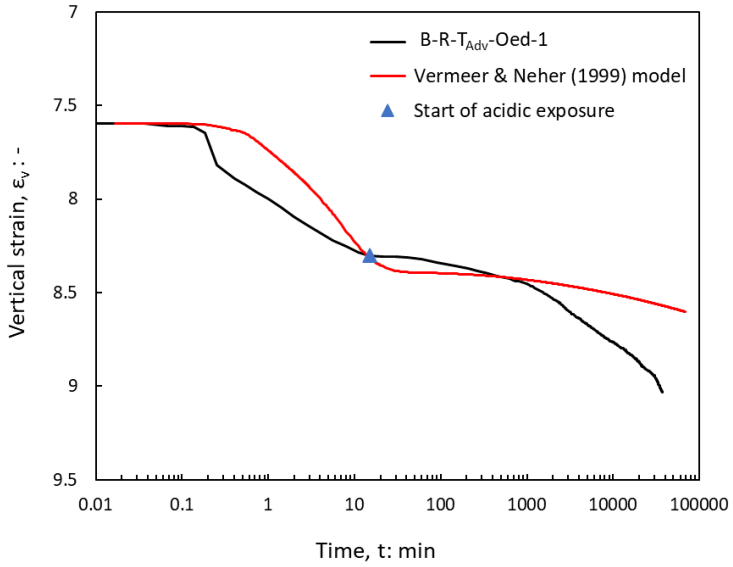

Figure 9.5 Time evolution of vertical strain during the advection stage of test B-R-T$_{Adv}$-Oed-1.

Figure 9.6 shows the vertical strains due to geochemical reactions both in advection and diffusion tests. It is the difference between the experimental vertical strain, which is the combined effect of geochemical and mechanical stress, and the vertical strain of the Vermeer and Neher model, which is due to mechanical stress only. The advection test has induced an additional strain of 0.58% and the diffusion test has induced an additional strain of 0.48% because of acid exposure after around 35 days. The difference between the two tests is not very significant and the compressibility when comparing B-R-T$_{Diff}$-Oed-1 and B-R-T$_{Adv}$-Oed-1, post-exposure is almost similar as shown in Figure 9.2.

According to the loading history imparted in the diffusion tests, the pure viscoplastic strain would increase from about 8.6% to 10.4%. The strain in the advection test would instead pass from about 7.6% to 9.1% because the stress path here includes: (a) loading with consolidation ; (b) partial unloading of the sample due to application of pressure at the inlet of the sample, which reduces the stress state.

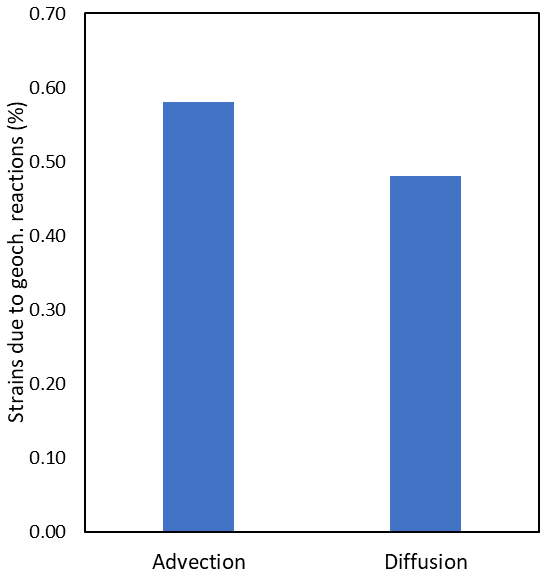

Figure 9.6 strains induced by geochemical reactions when exposed to acid in advection and diffusion conditions.

9.4.3 Time evolution of pH and acid volumes used

In the diffusion test, the cell of the oedometer was filled with 450 ml of 0.01M HCl solution. The pH of the acid solution was monitored over time at least once every working day and the solution of the cell basin was removed and replaced with a fresh 0.01M HCl solution after the pH increased above 3. The cumulated volume of acid over the time of exposure and measured pH in the cell basin are shown in Figure 9.7. In total, around 4 litres of acid were used during the exposure period. The pH showed a rapid increase at the start of the exposure period. The blue squares in Figure 9.7 show the fluid replacement of cell basin with a pH 2 acid. The first replacement of the cell was made after around 24 hours during which the pH increased from 2 to 5.8. Afterwards, it took around 3 days for the pH to increase from 2 to 6.78. After around 14 days the change in pH was much slower as the pH replaced after day 14 took 4 days to increase from 2 to 3.28. The initial rapid increase in pH might be related to the full buffering capacity of the sample due to carbonate dissolution and cell oxidation due to acid.

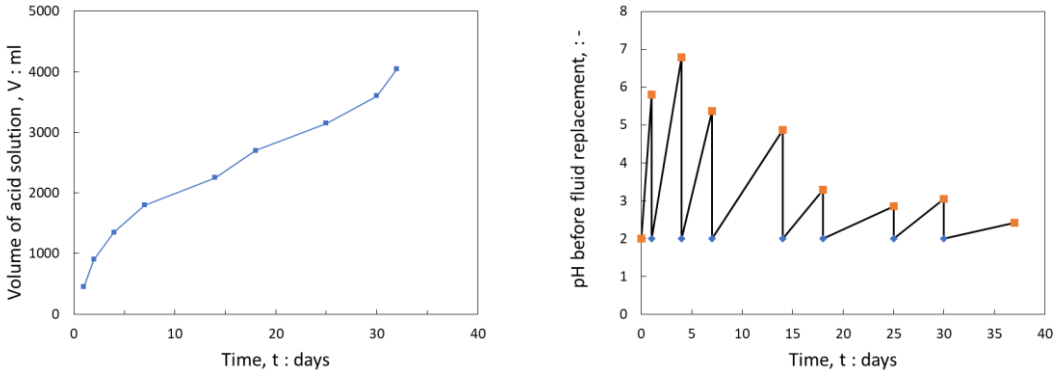

(a) (b)

Figure 9.7 Diffusion stage of test B-R-T_{Diff} -Oed-1. Time histories of (a) volume of acid solution used (b) pH in the cell basin.

The volume of acid solution injected during the advection stage of test B-R-T_{Adv}-Oed-1 is presented in Figure 9.8 (a). In total a volume of 600 ml of acid was injected into the specimen accounting for 35 pore volumes (the ratio between the volume of injected solution and total volume of the sample). The flow rate appears to be constant with time, which indicates that the permeability remained about constant. Figure 9.8 (b) shows the pH of effluent over time. A decrease in pH can be observed, due to the consumption of the carbonates over time, which reduced the buffering capacity of the specimen.

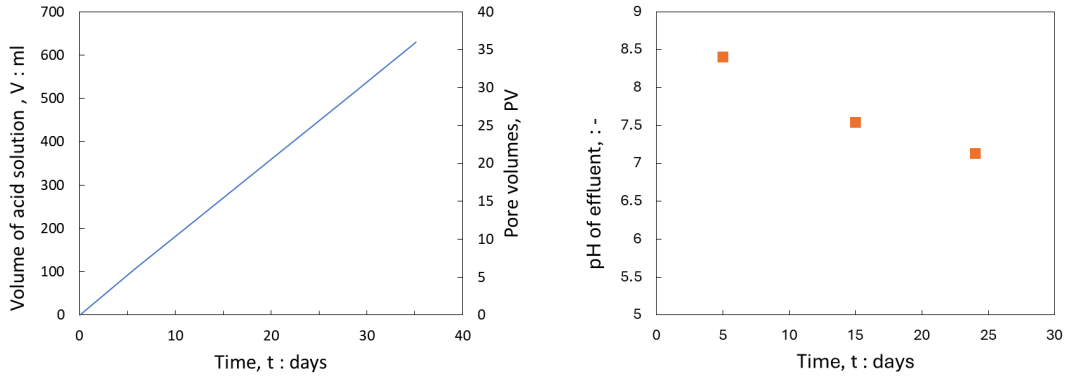

(a) (b)

Figure 9.8 (a) Volume of injected acid solution along pore volume in time and (b) pH of effluent for advection stage of test B-R-T_{Adv}-Oed-1.

9.4.4 Equivalent Calcite Content at test end

Equivalent Calcite Content (ECC) was determined along the height of the specimen after sample dismantling. The results for the three tests on the reconstituted specimens are shown in Figure 9.9. The non-exposed specimen (B-R-N-Oed-1) showed a homogeneous ECC value of 37.8% (dotted line). The ECC of the specimen exposed to acid diffusion (test B-R-T_{Diff}-Oed-1, blue points) was smaller both at the top (36.1%) and bottom (36%) part

of the specimen as compared to the middle part of the specimen, where the ECC was comparable to the one of the non-exposed specimen (37.4%). The higher decrease at the top and bottom part of the specimen is related to the proximity of these sections to the cell basin, from which diffusion takes place. The center of the specimen might not have been exposed to the carbonate dissolution reactions because of the reaction kinetics, longer diffusion times and of the buffering of the pore fluid due to the reactions with carbonate in the sections closer to the boundaries of the specimen.

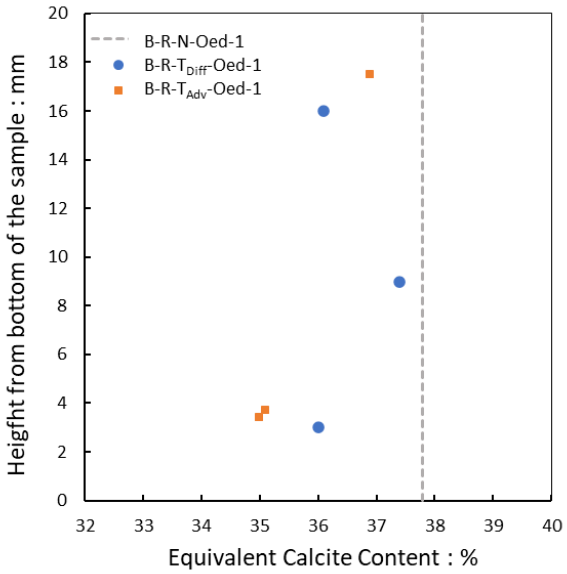

Figure 9.9 Equivalent calcite content determined after dismantling of the reconstituted specimens.

The ECC of the B-R-T$_{Adv}$-Oed-1 specimen, represented by orange squares, was found to increase from the specimen bottom (elevation 4 mm, ECC = 35 %) to the specimen top (elevation 17.5 mm, ECC=36.9 %). This trend is consistent with the flow of the acid solution taking place in the upward direction, which promotes reactions to take place mainly at the specimen base. As carbonate dissolution reactions cause the consumption of H+ ions, the pH also increases after that the fluid reacts in the bottom part of the specimen, as evidenced also by the higher pH of the effluent. Higher pHs do not allow for reactions to take place.

9.4.5 Time evolution of ultrasonic wave velocities during the advection test

Test B-R-T$_{Adv}$-Oed-1 was carried out in the advanced oedometer cell introduced in Chapter 8 which is equipped with ultrasonic wave transducers and electrodes for ERT. Compression (P) and shear (S) waves were recorded during the loading and unloading of the oedometer and the advection stage of the acid injection.

As an example, Figure 9.10 shows the P-wave signal and its energy obtained through wavelet transformation along with the first arrival time for vertical effective stress of 1500 kPa. It can be observed that the first arrival time can be detected on an energy spike in the energy graph. The arrival is when the energy spike starts to increase. The P waves were recorded at different frequencies ranging between 100- 800 kHz. The signal of 500 kHz showed a better quality in terms of arrival time selection.

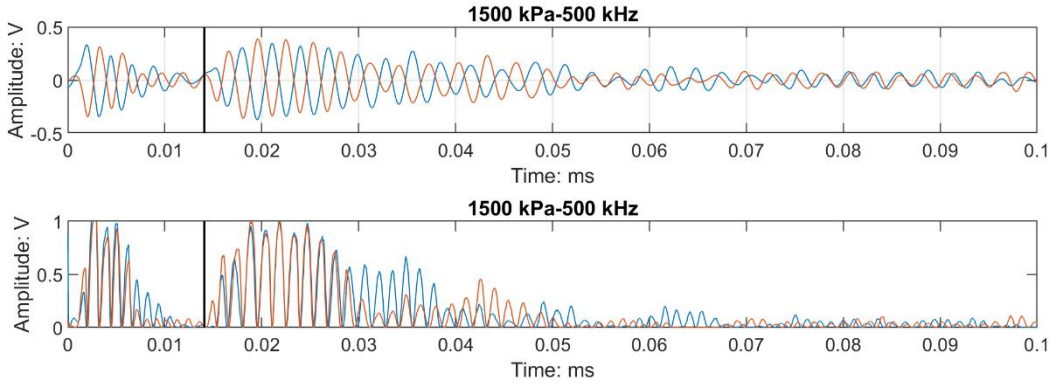

Figure 9.10 P wave signal and energy graph at 1500 kPa vertical stress along with the time of arrival shown in black line.

Determination of S wave arrivals was based on a combination of wavelet transformation and visual inspection. The S-wave signals were not detectable easily for the vertical stresses below 1 MPa. S wave signals were better almost after 1 MPa of effective vertical stress. Figure 9.11 shows S wave signals at different vertical stresses along with the first arrival times of the signals. The signal at 1000 KPa vertical stress refers to the 35 days of advection.

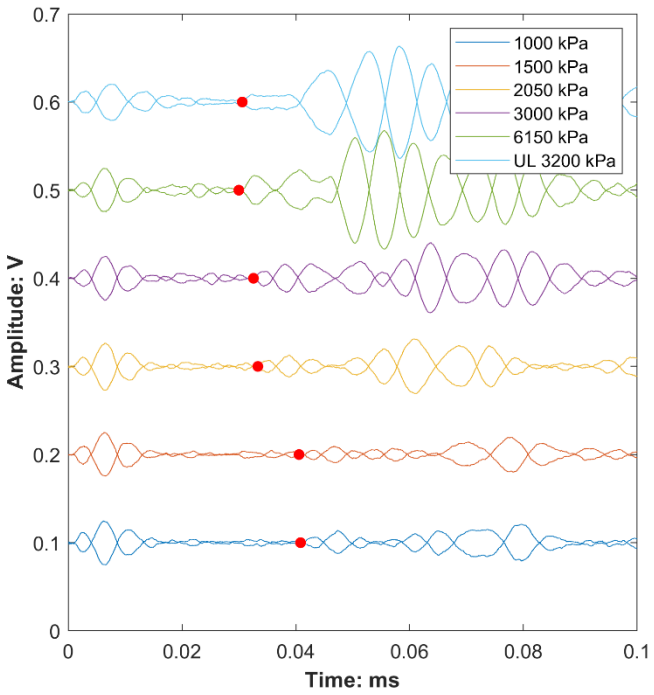

Figure 9.11 S wave signals recorded at 100 kHz for different vertical stresses along with first arrival times in red dots.

Figure 9.12 shows the P and S wave velocities during the loading and unloading. The values of the P and S waves were recorded at the end of every oedometer step. The reported value of P wave velocity at 1000 kPa was recorded after 1.5 hours from the start of the advection.

The S wave signals were not detectable at the initial stages of the loading and better signals were obtained when the contact between the transducer and specimen was improved at higher loads (above 1 MPa). As a consequence, the velocities are provided only for vertical stresses above 1 MPa.

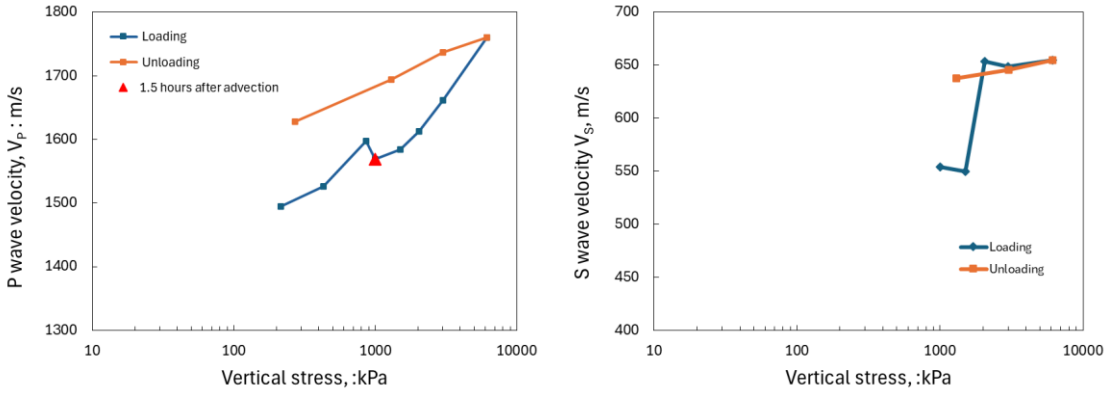

(a) (b)

Figure 9.12 P and S wave velocities during loading and unloading of test B-R-T_{Adv}-Oed-1.

The P-wave velocity decreased during the advection stage, as shown in Figure 9.13 (a). The P wave velocity before the advection stage is 1597 m/s, whereas during the advection stage, it decreases to around 1534 kPa. The S-wave velocity during the advection stage is about constant and it ranges between 539 and 555 m/s (Figure 9.13 (b)).

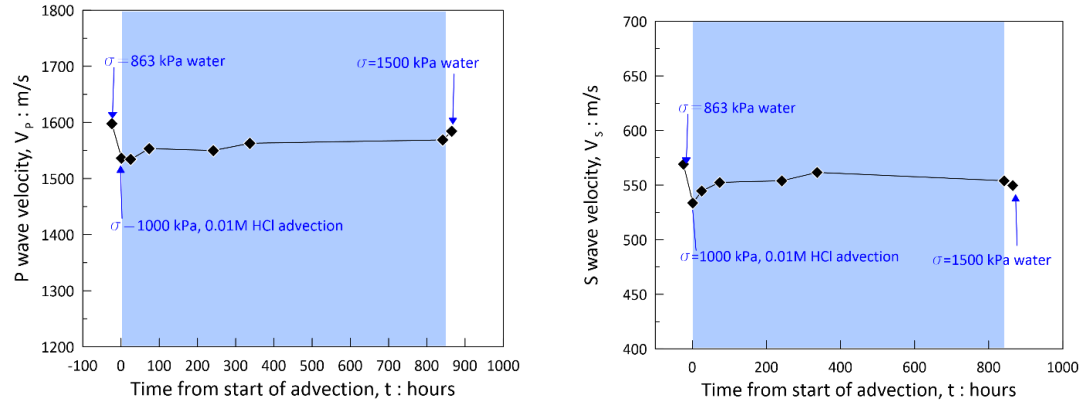

(a) (b)

Figure 9.13 P and S wave velocities during advection stage of test B-R-T_{Adv}-Oed-1

The decrease in the P wave velocity (V_p) might be due to a slight desaturation, related to the gaseous CO_2 generation when acid reacts with carbonates present in the specimen. Although the decrease is not pronounced. It shall be noticed that according to Biot's theory for the low-frequency range (Biot, 1956), the velocity of the compressional wave in a saturated (or almost saturated) soil with incompressible grains is:

$$V_P = \sqrt{\frac{E_{oed} + \frac{K_f}{\phi}}{\rho}} \qquad 9.1$$

where E_{oed} is the (drained) oedometer modulus, K_f is the effective bulk modulus of the fluid in the pores and $\rho=\rho_s\,(1-\phi) + \rho_f\,\phi$ is the soil mass density, ρ_s being the mass density of the grains and the ρ_f being the mass density of the fluid and ϕ being the porosity.

When the pores are filled with water, the degree of water saturation is S_w=1 and the bulk stiffness of the fluid is equal to the water's (K_f = K_w =2.1 GPa). The following correction (e.g. Makvo et al., 1998) can be applied when a small fraction of the porosity is occupied by another fluid, for instance, gas having a degree of saturation $S_g = 1 - S_w$.

$$\frac{1}{K_f} = \frac{S_w}{K_w} + \frac{S_g}{K_g} \qquad 9.2$$

where K_W and K_g are the stiffness of water and gas respectively.

By assuming that the gas behaves as a perfect one, its stiffness can be assumed as equal to its pressure- *i.e.,* the one of the water in the pores (between 500 kPa and 0 kPa). Thus, a very small degree of gas saturation largely impacts on the K_f value and then on the velocity V_P.

There is a strong dependency of the V_p (and bulk undrained modulus) on Sr, because V_p depends on the bulk modulus of all the phases, and particularly the fluid phases weighted in respect of their degree of saturation. Therefore, provided the large difference in the bulk moduli of gas and water, a decrease in V_p is observed even for small values of gas saturation. On the other hand, V_S does not depend on the fluid in the porous space, whereas it depends on the effective stress and load history (e.g. normally consolidated vs overconsolidated). Gu et al., (2021) also observed that P-waves decrease considerably when the saturation decreased negligibly. On the other hand, S-waves were not affected by the initial change in degree of saturation. Therefore, the possible effects of desaturation on V_S would descend from an increase in the effective stress due to suction. It should be observed that the developed gas is anticipated to be still in bubble form – and not a continuous one – so that no suction is still acting in the sample. Indeed, suction effects would lead to an increase in the V_S with suction whereas V_S remains practically constant during the advection, suggesting that no relevant suction was developing in the sample. A possible explanation of the experimental outcomes is then that gas developed in form of bubbles – not as a continuous phase – which allows for a decrease in V_P and a practically constant value of V_S.

9.4.6 Time evolution of electrical conductivity during advection

Electrical measurements were carried out during the whole test in the advanced oedometer, adopting the protocol described in Chapter 8. The resistance data were inverted using ResIPy, while ParaView was used to present the resulting maps of electrical conductivity.

Figure 9.14 shows maps of the electrical conductivity at elevations of 8, 12.5 and 17 mm of the specimen during the loading and unloading of the oedometer test. The resistance data were recorded at the end of every loading step. A slight decrease in

electrical conductivity was observed during the first loading steps, which might be explained through Archie's law (Equation 7.14) considering the decrease in porosity associated with compression. The electrical conductivity decreased drastically after 1000 kPa, following the advection of the acid, as shown in Figure 9.14.

σ'_v (kPa)	Electrical conductivity (mS/m)
215	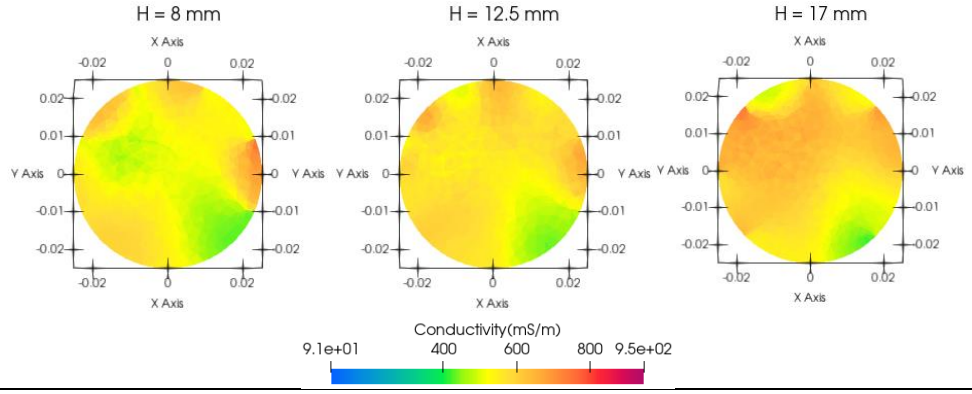
432	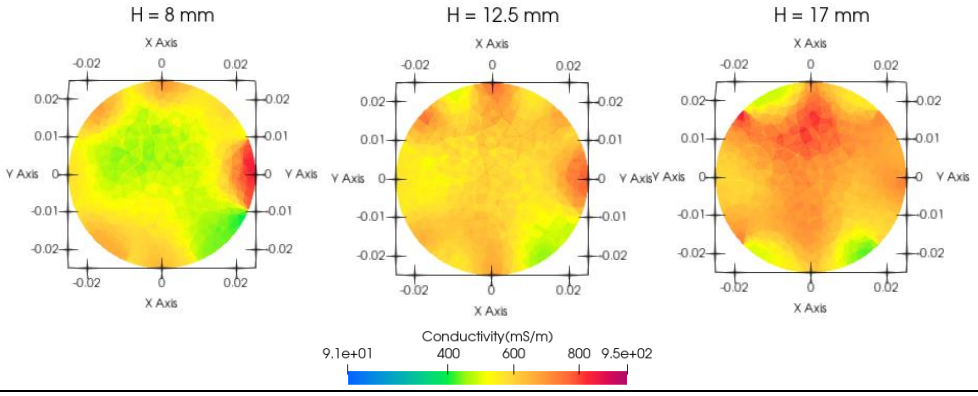
863	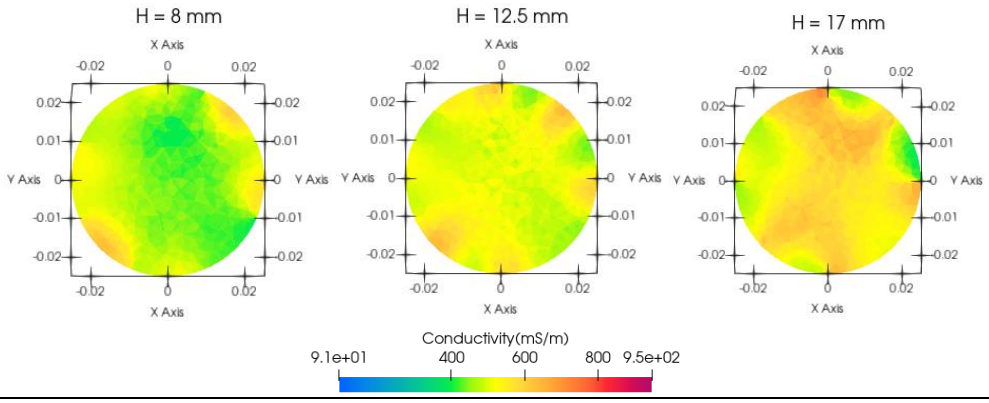

1000
After 2 hours of advection

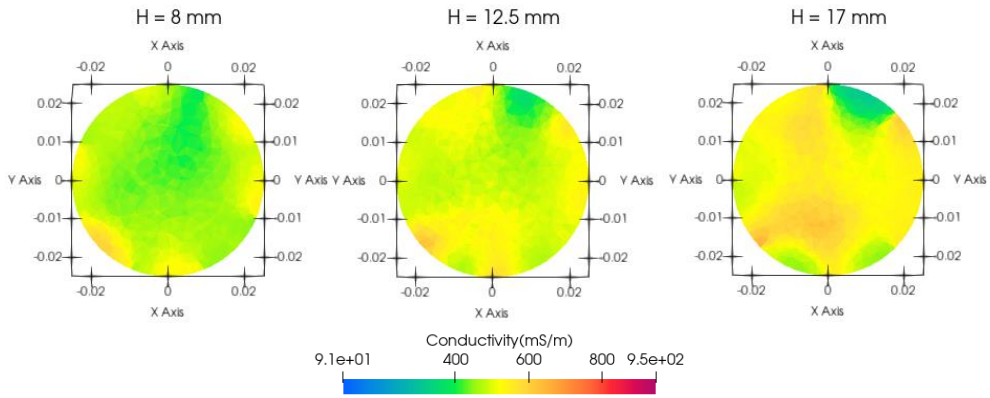

1000
After 17 hours of advection

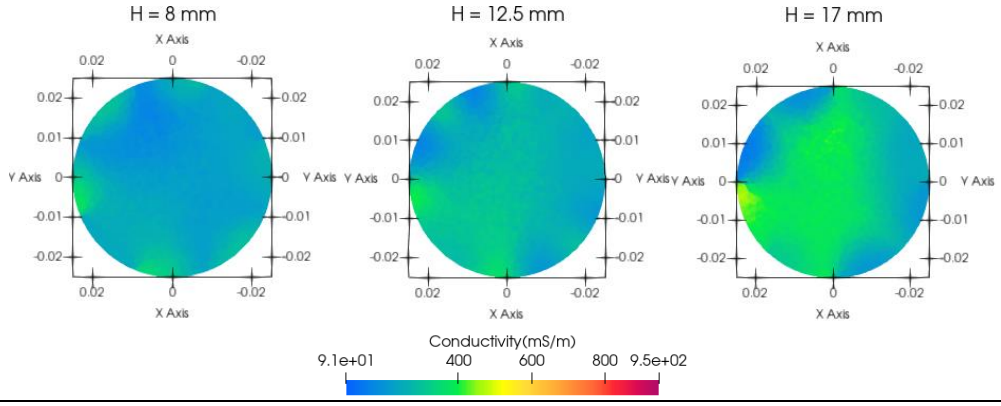

1511

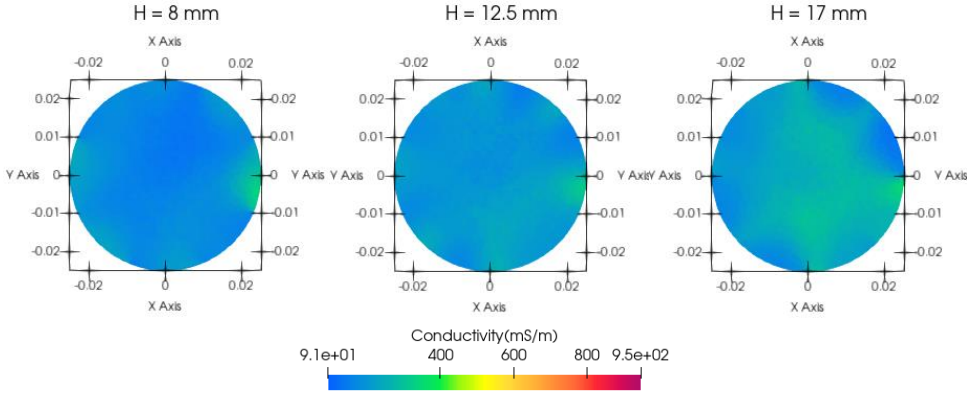

2050	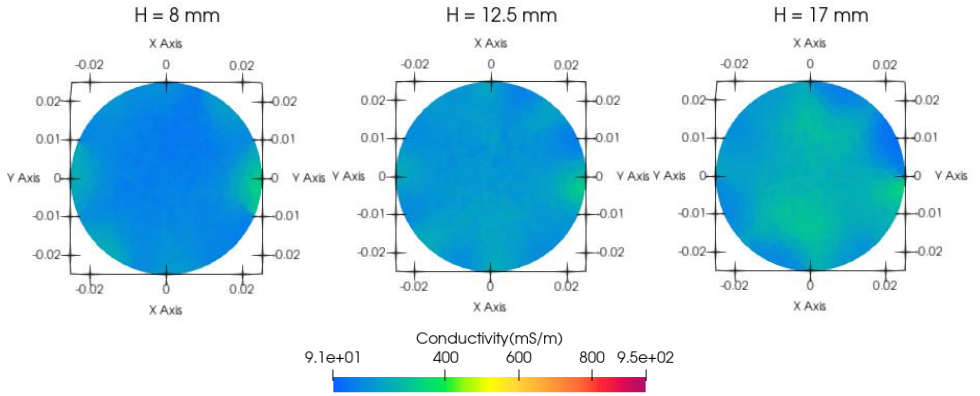
2914	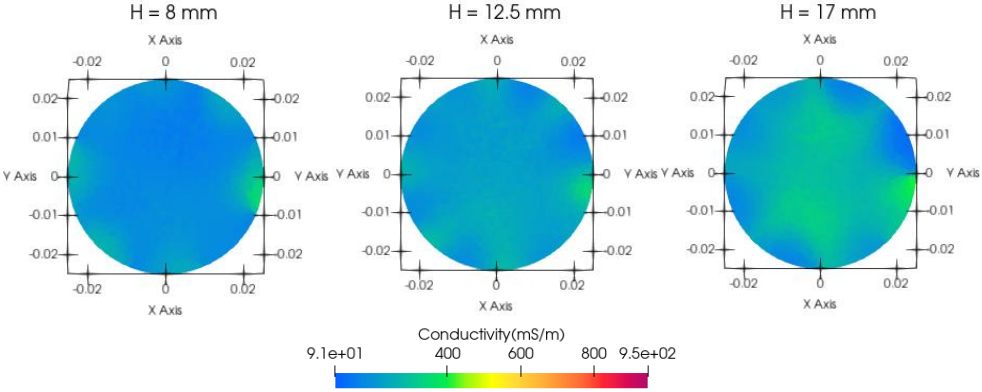
6150	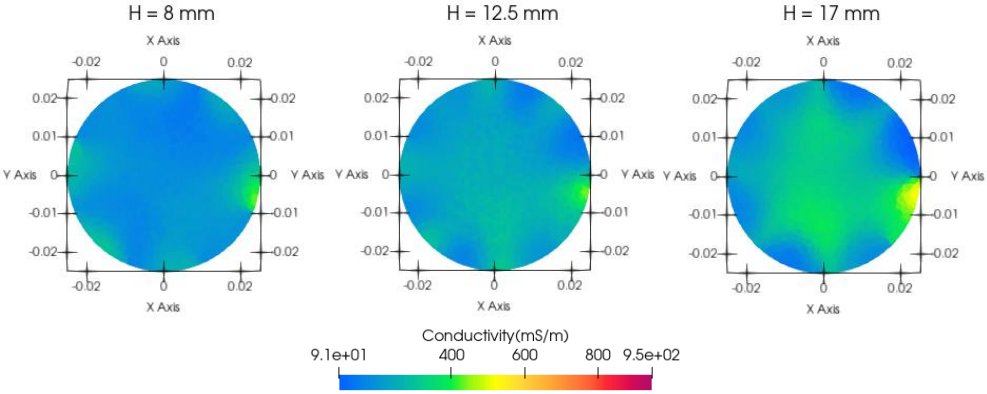

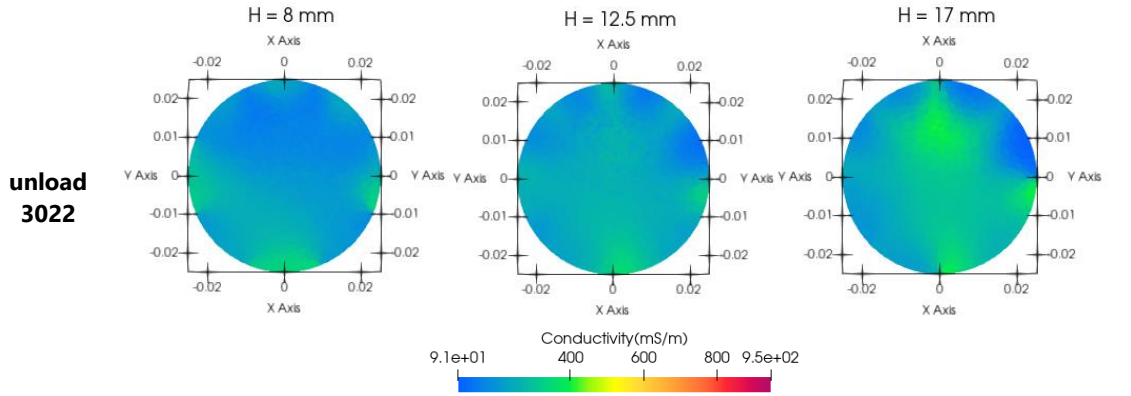

Figure 9.14 Electrical conductivity at different heights of the sample during the loading and unloading of test B-R-T_{Adv}-Oed-1

Figure 9.15 shows the frequency density distribution of the electrical conductivity of the FE elements of the ERT reconstruction obtained for the different stages of the test. As for the advection stage, the image refers to 2 hours and 17 hours from the start of the advection. The continuous line refers to the loading steps and to measurements taken 2 and 17 hours after the start of advection. The dotted lines show the loading steps after advection, and the lines with symbols represent the unloading step.

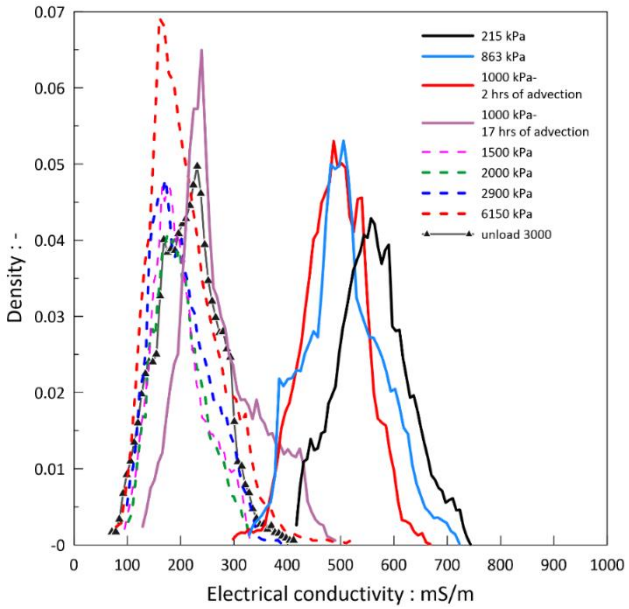

Figure 9.15 Statistical distribution of reconstructed electrical conductivity for the FE elements of the ERT inversion during loading stages of test B-R-T_{Adv}-Oed-1.

It is evident that electrical conductivity decreased significantly after the advection of the acid. The average value of the electrical conductivity before the advection was around 500 mS/m, whereas it decreased to around 180 mS/m after advection.

Figure 9.16 shows the time evolution of electrical conductivity during the advection stage at elevations 8, 12.5 and 17 mm from the bottom of the specimen.

Time	Electrical conductivity (mS/m)
2 hrs	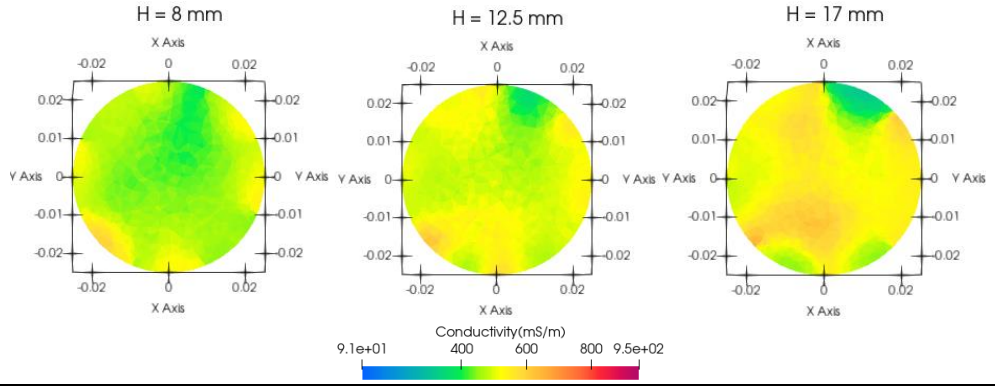
17 hours	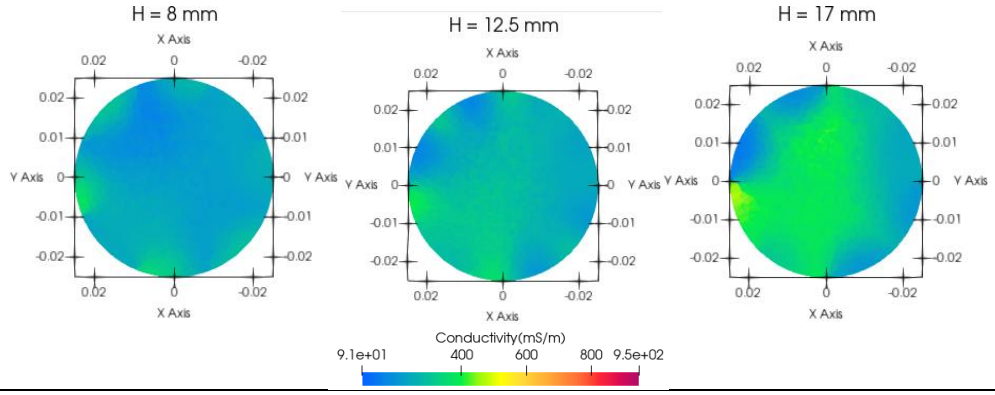
5 days	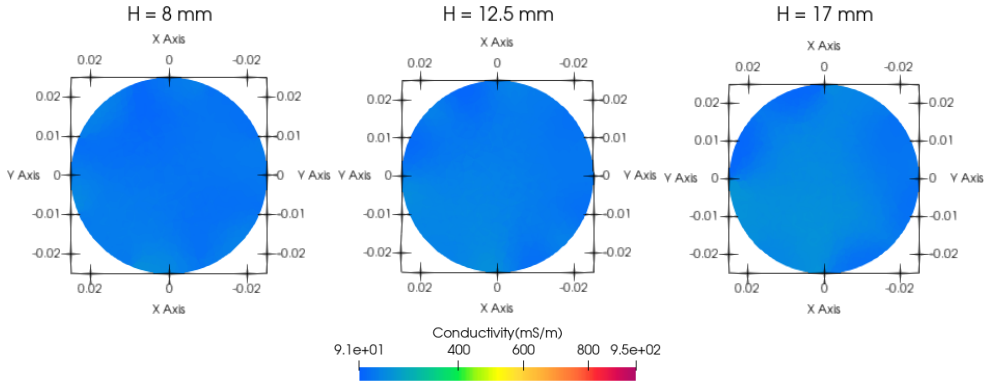

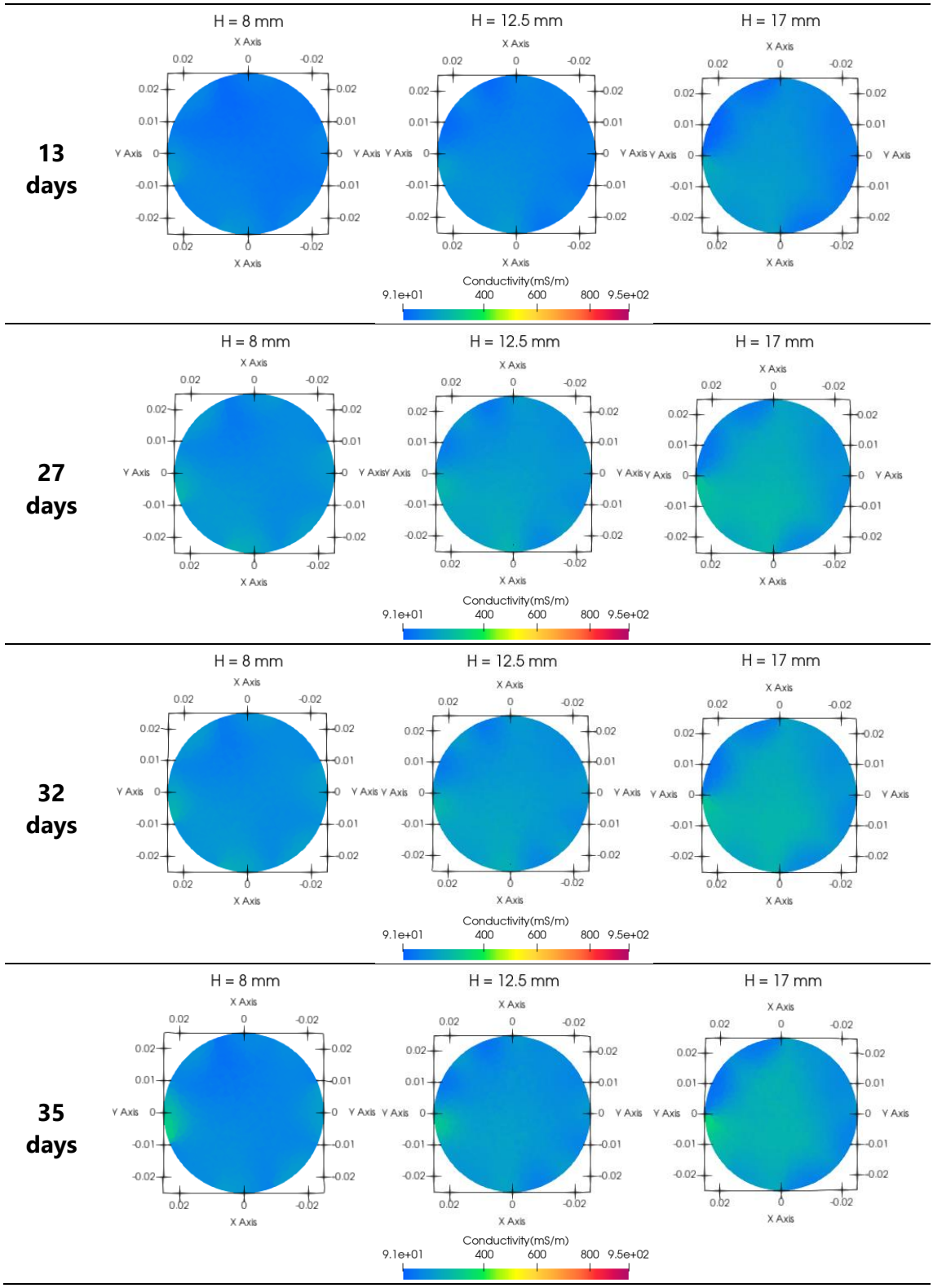

Figure 9.16 Electrical conductivity during the advection phase at different heights of the specimen.

Figure 9.17 shows the density distribution of the electrical conductivity of the specimen during the advection stage. The blue line shows the density distribution of electrical conductivity at vertical load of 863 kPa which is one step before the start of advection. It can be observed that during the first two hours of advection the changes in electrical conductivity are not significant. However, the decrease in electrical conductivity is very evident during the following days. In the figure, the black and grey lines show the electrical conductivity after 2 hours, 17 hours and 5 days. At these times the average electrical conductivity decreases from 500 mS/m (2 hours) to 250 mS/m (17 hours) and then 110 mS/m (5 days). The lowest value of average electrical conductivity was actually found after 5 days, then an increase was observed up to 180 mS/m (27 days).

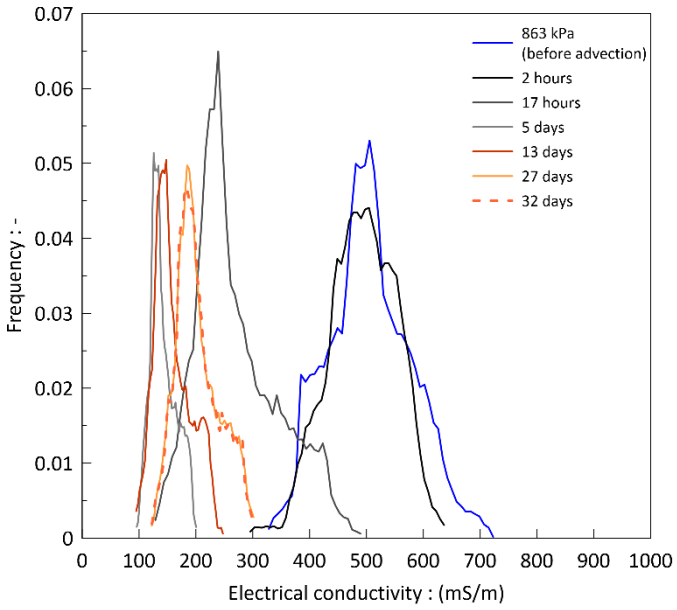

Figure 9.17 Statistical distribution of reconstructed electrical conductivity for the FE elements of the ERT inversion during the advection stage of test B-R-T_{Adv}-Oed-1.

Figure 9.18 shows the time evolution of the average electrical conductivity reconstructed at different elevations of the specimen. In Figure 9.18 (a) it can be seen that after 17 hours the electrical conductivity value is almost halved with respect to the start of the advection. At all given times, the reconstructed electrical conductivity increases with elevation, although the difference in values is modest.

Plotting the time evolution of electrical conductivity in terms of pore volumes of injected fluid, *i.e.* of the ratio between the injected volume of solution at any given time and the volume of the pores of the specimen (equal to ϕ V, where ϕ = 0.407 is the porosity during the advection stage and V = 44.61ml is the volume of the specimen), might help in understanding the causes of such a decrease. Such a plot is presented in Figure 9.18(b): the electrical conductivity decreases to half the initial value after 1 pore volume has flown

through the specimen. At this time the ions present in the native (pre-advection) pore fluid are expected to be completely expelled through advection. Further decrease, and later final increase, in the electrical conductivity has to be related mainly to the geochemical reaction processes (carbonate dissolution and consumption of H^+ ions), which might also imply a slight desaturation due to the release of CO_2 in gaseous form. Notice that the dotted line in Figure 9.18 (b) provides the expected value of the soil electrical conductivity when it is fully saturated by the 0.01 M HCl solution, which was obtained by introducing the electrical conductivity of the acid σ_f= 9.12 mS/cm in Archie's law (equation 7.14) where the value of parameter m is 1.5.

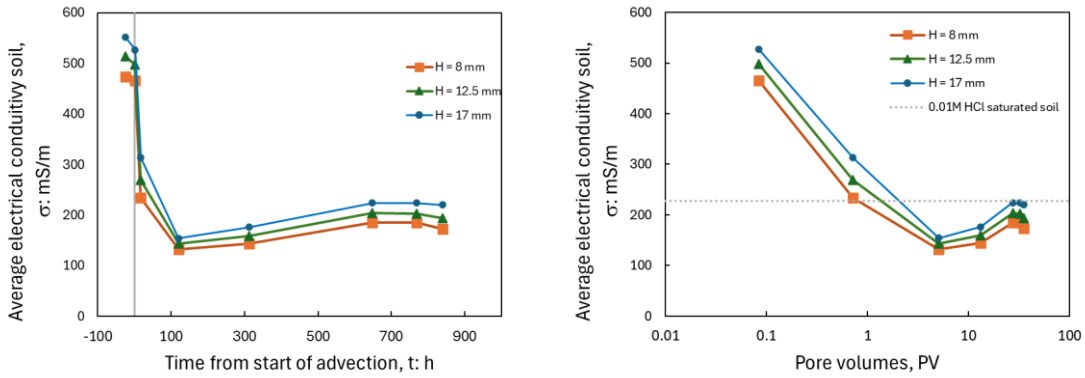

(a) (b)

Figure 9.18 (a) Average electrical conductivity along the height of the sample during the advection stage over time (b) average electrical conductivity along the height of the sample during advection stage in terms of pore volume.

9.5 Experimental results of tests on Clay C specimens

The results of the tests performed on the intact specimens of Clay C are presented in this section by comparing the compression curves of the three tests. This section also contains the results on the time evolution of strains during the exposure stages of diffusion and advection tests. For the advection test the time evolution of electrical conductivity and ultrasonic waves are also presented.

9.5.1 Compression curves

Two intact specimens were tested in the small diameter oedometer, which allows imposing vertical stress up to 28 MPa. One specimen was tested by keeping distilled water (C-I-N-Oed) in the cell basin during the whole test duration, while the other one was exposed to diffusion of 0.01M HCl solution for 30 days under a constant vertical load of 13 MPa (C-I-T_{Diff}-Oed-13). The third specimen was tested in advanced oedometer under advection condition (C-I-T_{Adv}-Oed-1.5) for around 42 days. The compression

curves of the three specimens are compared in Figure 9.19.

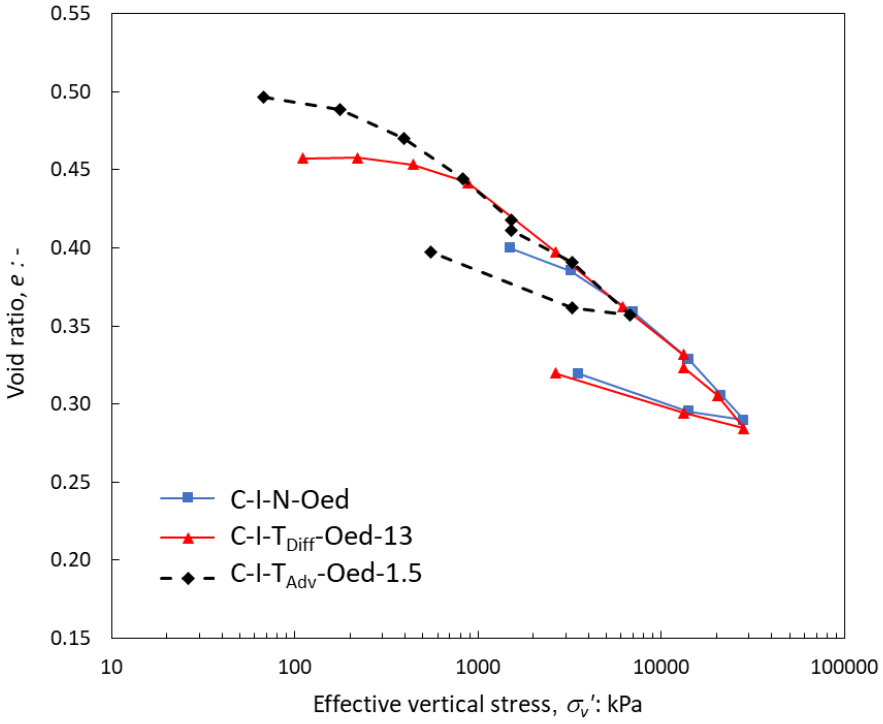

Figure 9.19 Compression curves for the three intact specimens.

A small reduction of void ratio occurred during the diffusion stage run under a vertical stress of 13 MPa ($\Delta e \cong$ - 0.015), because of the combined effect of creep and geochemical reactions. As for the advection test, advection was imposed at a vertical stress of σ_v' = 1.5MPa and it leads to a practically no void ratio change.

As the specimens proceed from a depth of 2758 m, the pre-consolidation stress is expected to exceed 28 MPa and it cannot be detected by the loading with the oedometer used. Thus, it cannot be associated with the bend of the experimental curve of specimens B-I-T_{Diff}-Oed-13 and B-I-T_{Adv}-Oed-1.5 occurring around σ'_v= 1 MPa. The compressibility of the specimens was then expressed in terms of reloading index C_r (determined between 20 and 28 MPa for tests C-I-N-Oed and C-I-T_{Diff}-Oed-13 whereas between 3.2 and 6.7 MPa for C-I-T_{Adv}-Oed-1.5) and swelling index C_s (determined during unloading between 13 and 2.6 MPa for tests C-I-N-Oed and C-I-T_{Diff}-Oed-13 whereas between 6.7 MPa and 0.5MPa for C-I-T_{Adv}-Oed-1.5). The specimen exposed to acid diffusion showed only a negligible change in the reloading index, although immediately after the diffusion stage (13 MPa < σ'_v < 20 MPa) it seemed to be slightly stiffer than the non-exposed specimen. The post-advection behavior of test C-I-TAdv-Oed-1.5 was not altered. The secondary compression index (C_α) are determined from figures 9.22 and 9.23. These values correspond to the values without chemical reaction, i.e., the slope of blue line. Table 9.8

summarizes the compression indices of the three specimens. It is worth mentioning that secondary compression indices are two vertical stresses: C-I-TDiff-Oed-13 is at 13 MPa and C-I-TAdv-Oed-1.5 is at 1.5 MPa.

Table 9.8 Compressibility for intact specimen of Clay C.

	C-I-N-Oed	C-I-T_{Diff}-Oed-13	C-I-T_{Adv}-Oed-1.5
C_r (-)	0.126	0.147	0.106
C_s (-)	0.033	0.036	0.037
C_α (-)	-	0.0017	0.0018

9.5.2 Time evolution of pH and acid volumes used

In the diffusion stage of test C-I-T_{Diff}-Oed-13, the acid was added to the cell basin after the end of primary consolidation at 13 MPa. The distilled water was replaced by around 150ml of 0.01M HCl solution. The acid solution was replaced by fresh 0.01M HCl solution when the pH of the acid in the cell basin increased above 2.5. Figure 9.20 (a) shows the cumulative volume of acid used for the exposure of the intact specimen. Figure 9.20 (b) shows the pH of the acid solution in the cell before it was replaced by the 0.01M solution (pH 2 solution). The slower geochemical processes, related to the acid penetration, are also confirmed by the slower change in pH as compared to the reconstituted specimen. A plausible reason for this might be the lower diffusion coefficient of the intact specimen, whose fabric is tighter due to the smaller size of its pores and the bonding provided by the carbonate grains.

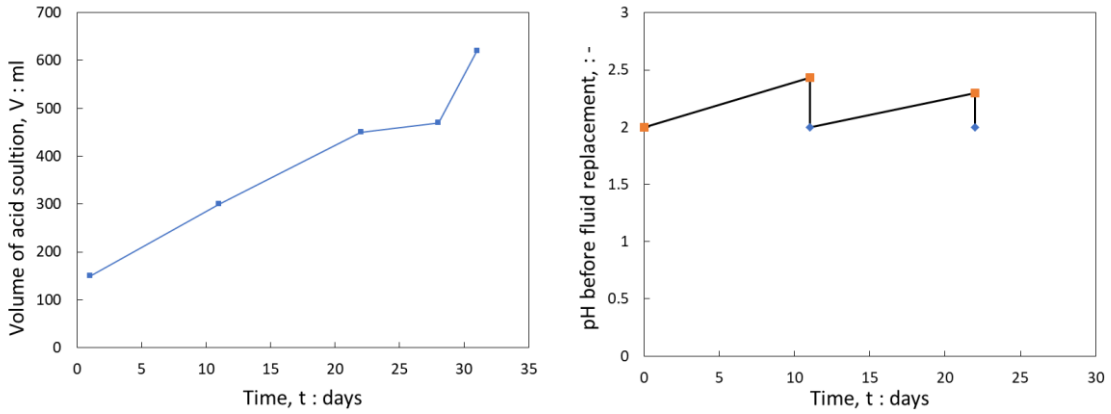

(a) (b)

Figure 9.20 Volume of acid solution used during the exposure (a) and pH of acid solution before replacing it with a pH 2 solution.

The volume of acid solution injected during the advection stage of test C-I-T_{Adv}-Oed-1.5 is presented in Figure 9.21 (a). In total a volume of around 60 ml of acid was injected into

the specimen accounting for around 4.5 pore volumes (the ratio between the volume of injected solution and total volume of the specimen). The flow rate gets constant after around 5 days. Figure 9.21 (b) shows the pH of effluent over time.

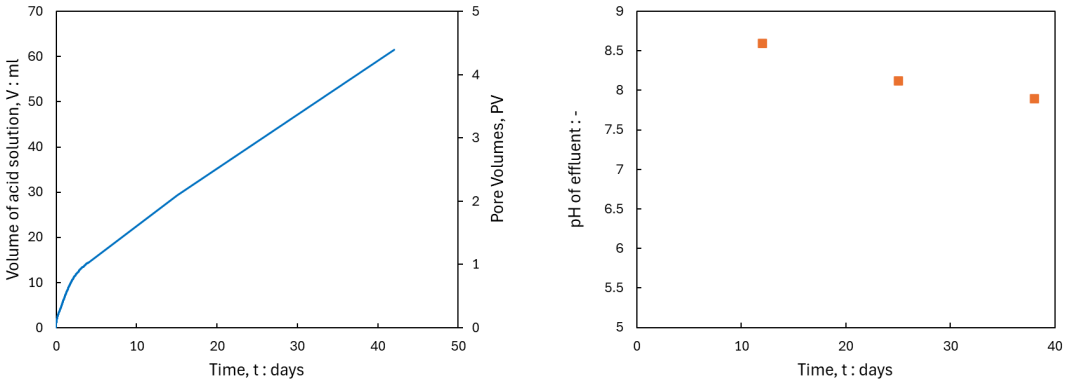

(a) (b)

Figure 9.21 Volume of injected acid solution along pore volume in time and (b) pH of effluent for advection stage of test C-I-T_{Adv}-Oed-1.5.

9.5.3 Time evolution of void ratio during the exposure stage

The time evolution of void ratio for the intact specimen exposed to acid at 13 MPa (C-I-T_{Diff}-Oed-13) during the exposure phase is shown in Figure 9.22. In Figure 9.22 (a) the orange line shows the recorded experimental line. A deviation from the expected creep line, which represents the strains occurring without geochemical reactions and is here depicted in blue by simply extending the secondary compression line, can be seen only after 10000 minutes (around 7 days). Figure 9.22 (b) shows the differential void ratio caused by the acid reaction, obtained as the difference between the void ratio of the 'creep line' and the experimental ones. The increase in differential void ratio, albeit very small, starts to be more appreciable after 30000 minutes. This time is larger than what was observed in the tests on reconstituted specimens, indicating that the overall geochemical process (transport and reactions between acid and soil) is slower in the intact material compared to the reconstituted one.

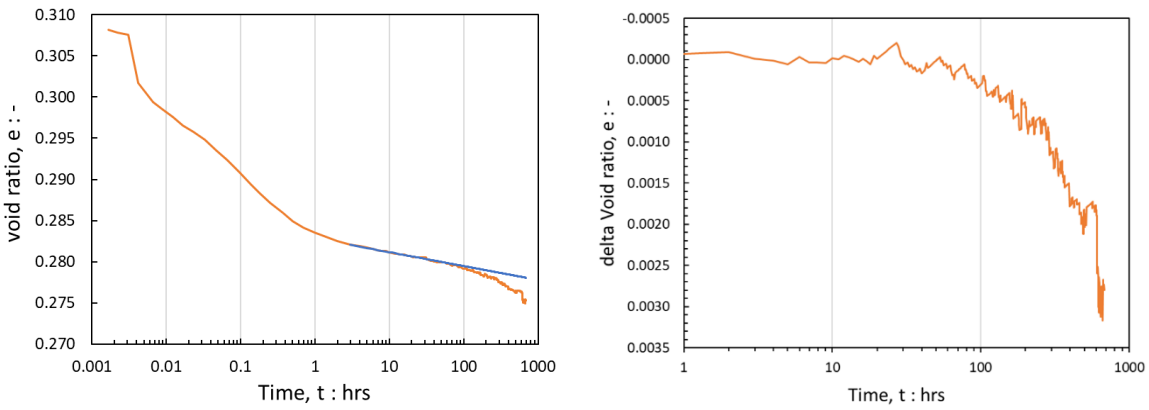

(a) (b)

Figure 9.22 Time evolution of void ratio and differential void ratio during exposure stage.

The time evolution of void ratio during the exposure stage of specimen C-I-T_{Adv}-Oed-1.5 is shown in Figure 9.23. The acid injection was introduced after the end of primary consolidation. The acid injection has hardly produced any significant changes in the specimen after 42 days of exposure. The change in void ratio is negligible as shown by the comparison of orange (test curve) and blue line (creep line).

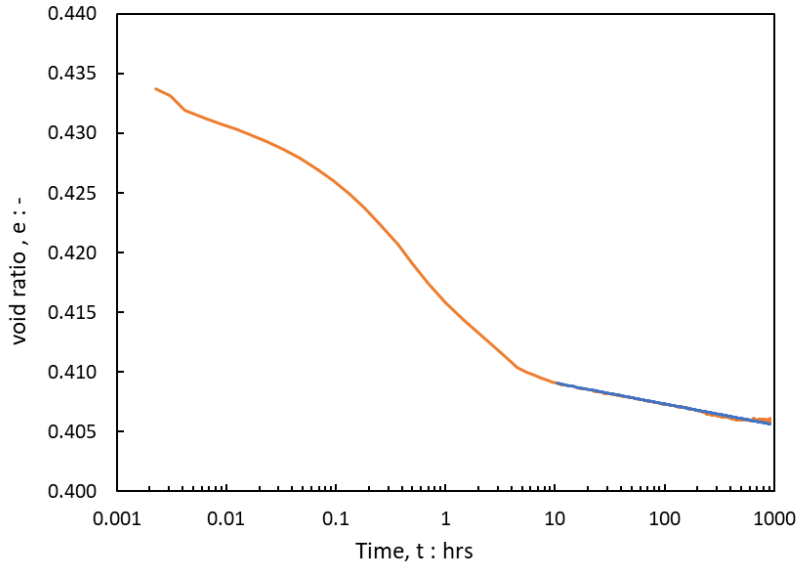

Figure 9.23 Time evolution of void ratio during exposure stage of C-I-T_{Adv}-Oed-1.5

The lack of acid effects might be related to the amount of acid injection. The pressure of acid injection was 500 kPa which for the intact specimen, whose permeability is low as compared to the reconstituted specimen was less. The acid volume injected shows that much less volume of acid was injected as compared to the reconstituted test (B-R-T_{Adv}-Oed-1).

9.5.4 Equivalent calcite content at test end

Equivalent Calcite Content (ECC) of the specimens were determined before and after the test. The ECC for before exposure was performed on the material which was obtained from trimming of the specimen exposed in diffusion condition (C-I-T_{Diff}-Oed-13) during the preparation of the specimen for small diameter oedometer. After the exposure to acid in the oedometer test the specimen C-I-T_{Diff}-Oed-13 was divided along the height and ECC was obtained at the top and bottom part of the specimen. The non-exposed material resulted in an ECC of 35%. Post-exposure analysis showed that the top part of the specimen had an ECC of 34.8% whereas the bottom part of the specimen had an ECC of 36% as shown in Figure 9.24. The figure also shows the ECC of the specimen exposed to acid in advection condition (C-I-T_{Adv}-Oed-1.5) in orange symbols. The height of specimen in this case was 25 mm so the determination at the top of the specimen lies above that of C-I-T_{Diff}-Oed-13.

The change in the ECC, for both the specimens is almost negligible at the top of the specimens. Whereas at the bottom of the specimens a little increase of 1% was observed compared to the non-exposed material.

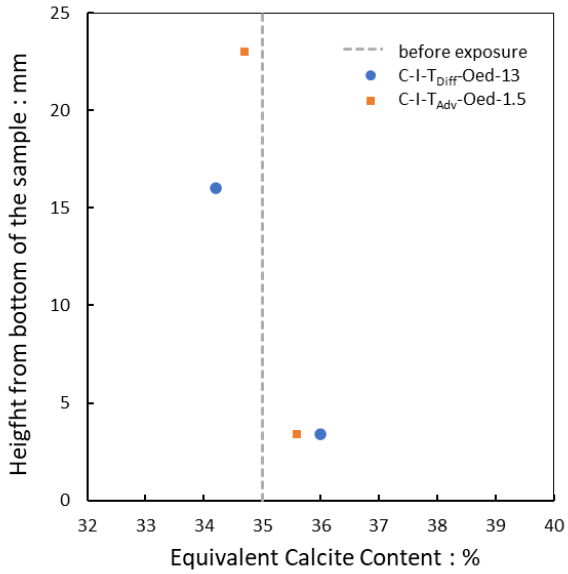

Figure 9.24 Equivalent calcite content determined before and after the exposure for C-I-T_{Diff}-Oed-13 and C-I-T_{Adv}-Oed-1.5.

9.5.5 Time evolution of ultrasonic wave velocities during the advection test

The ultrasonic waves were analysed based on wavelet transformation and cross-correlation. Figure 9.25 shows a signal along with its energy and time of arrival for P wave

at 3251 kPa vertical stress. The energy graphs are obtained through wavelet transformation discussed in Chapter 8.

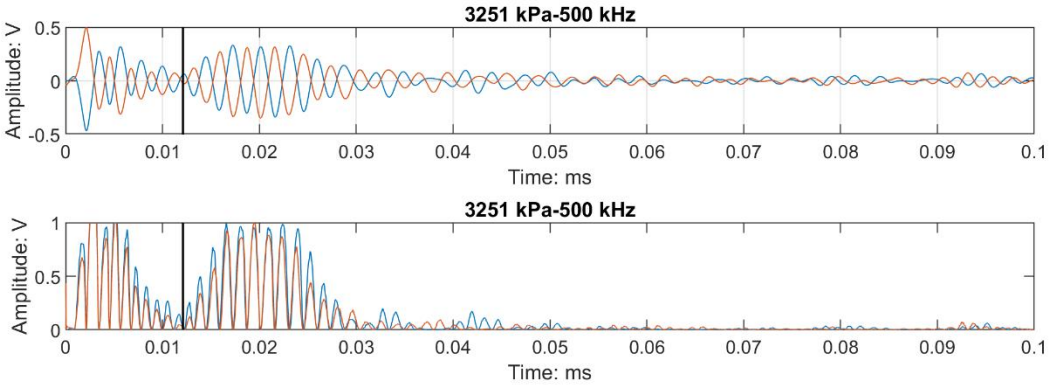

Figure 9.25 P wave signal and corresponding energy graph at vertical stress of 823 kPa for C-I-T_{Adv}-Oed-1.5.

Figure 9.26 shows two signals analysed during cross-correlation analysis. The reference signal is the one recorded at 823 kPa. The cross-correlation was applied taking into account the first arrival of this signal. The figure also shows in dotted lines the 'window' for which the arrival time was analysed. The arrival times were consistent for both wavelet and cross-correlation methods.

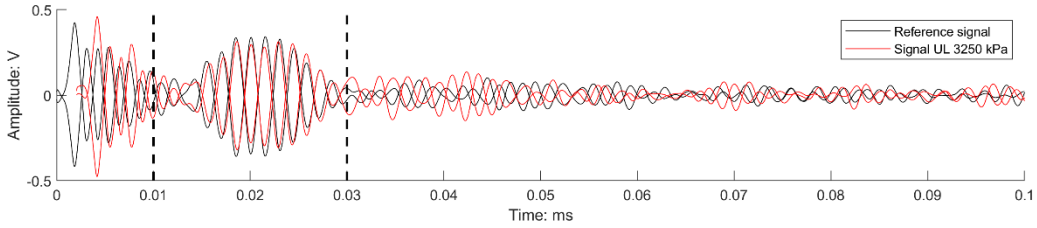

Figure 9.26 Alignment of signal at unloading step of 3250 with reference signal recorded at 823 kPa by cross-correlation.

Figure 9.27 shows signals for S-wave signals and energy graphs during the loading (6700 kPa) and unloading (3250 kPa) steps at 80 kHz.

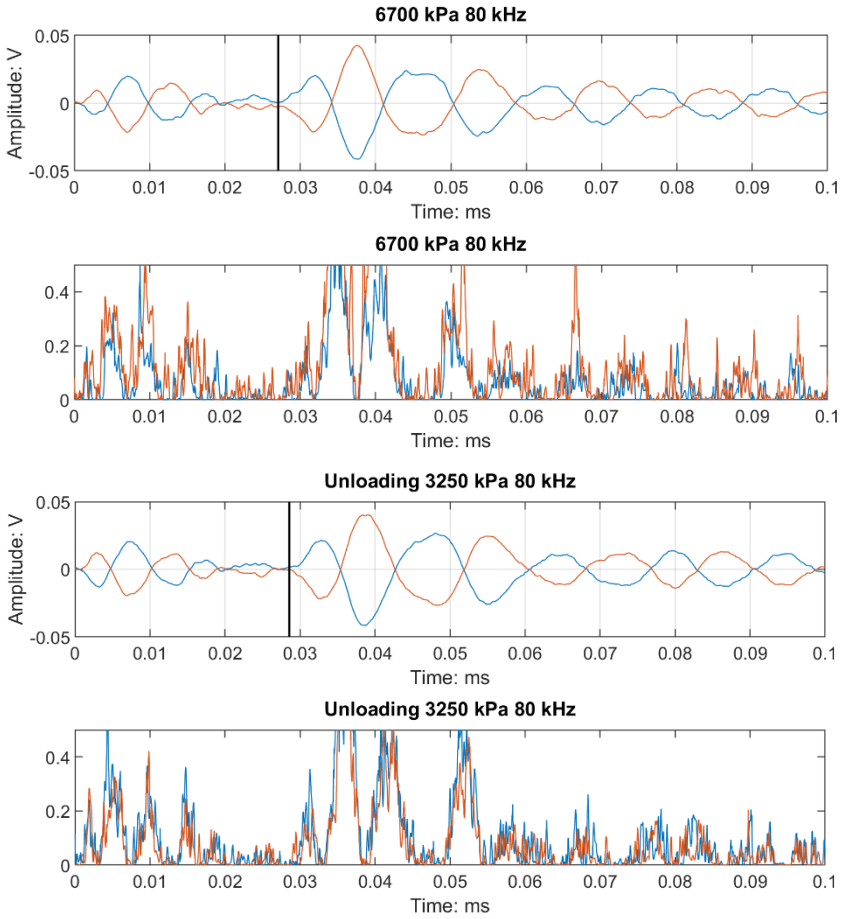

Figure 9.27 S wave signal and corresponding energy graph at vertical stress of 6700 kPa and 3250 kPa for C-I-T_{Adv}-Oed-1.5.

The P and S wave values during the test are shown in Figure 9.28. P-wave values are higher compared to the reconstituted specimen. S-wave signals were not noticeable until after around 30 days of advection therefore no signals were analysed before that. With sustained loading the increase in contact between the specimen and transducer resulted in better signals with time.

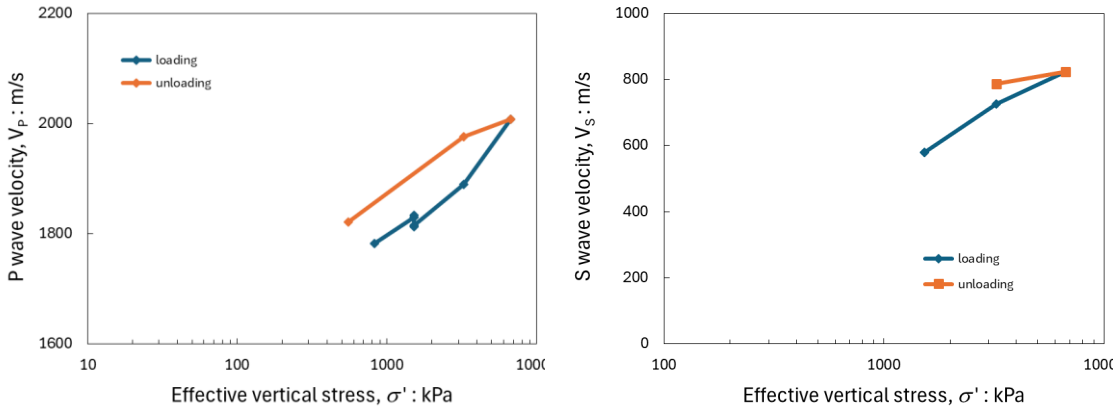

(a) (b)

Figure 9.28 P and S wave velocities during loading and unloading of test C-I-T_{Adv}-Oed-1.5

The change in P-waves with time during advection is shown in Figure 9.29. The first value of P-waves is before the advection. After the start of advection, the first determination was carried out after 1 day of advection. A slight increase can be observed as compared to the 823 kPa step. This might be due to the effect of loading. In contrast to the reconstituted specimen, a decrease in P-wave was not observed. The reason for this might be related to the slow effect of acid on intact sample and also considering that, because of the smaller permeability of the intact sample less acid was introduced compared to the test on reconstituted sample. The P-wave remains constant with a negligible decrease towards the end of advection.

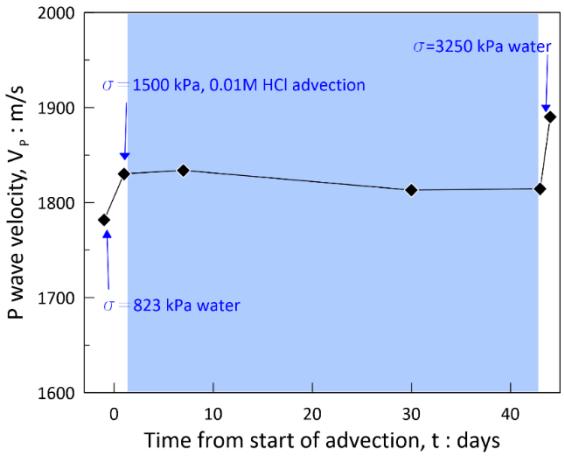

Figure 9.29 Change in P-wave during advection of acid for C-I-T_{Adv}-Oed-1.5.

Figure 9.30 shows S wave signals with selected first arrival times. The first arrivals of the signals of the advection stage (bottom two signals) are comparatively less detectable. For the higher stresses the arrival time can be detected with wavelet transformation as shown by energy graphs in Figure 9.27.

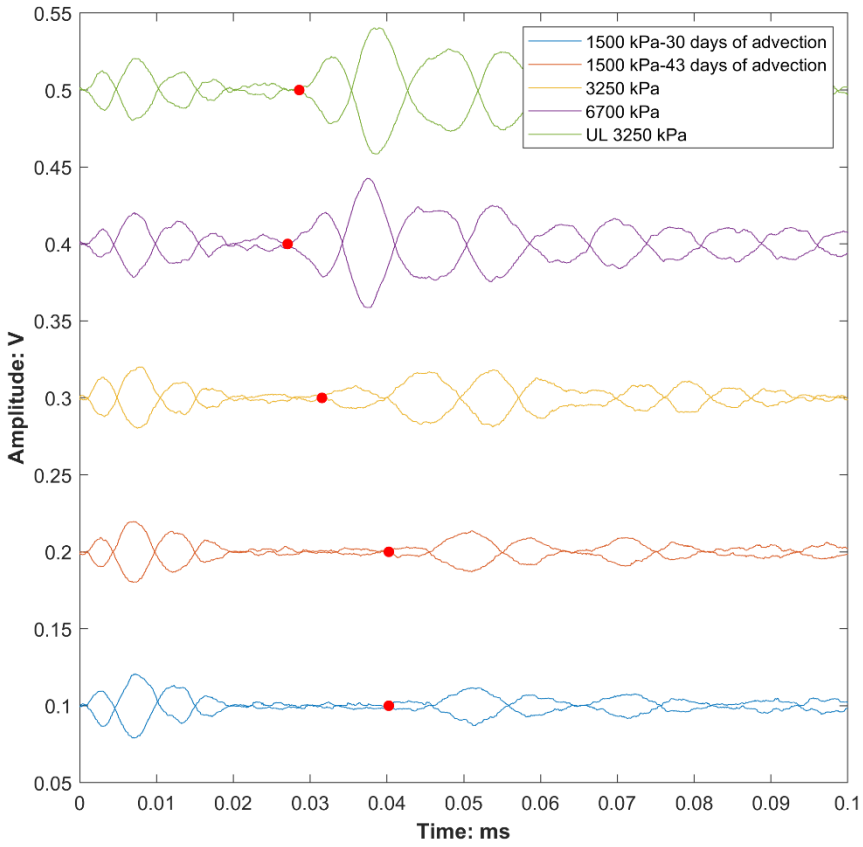

Figure 9.30 S wave signals recorded for different vertical stresses along with first arrival times in red dots. The 'UL 3250 kPa' is for the unloading step at 3250 kPa.

9.5.6 Time evolution of electrical conductivity during advection

Electrical measurements were performed throughout the advection stage following the protocol described in Chapter 8. The resistance data were then inverted using ResIPy and ParaView was used to present the resulting maps of electrical conductivity.

Figure 9.31 shows maps of the electrical conductivity of specimen C-I-T_{Adv}-Oed-1.5 at the heights of 8, 12.5 and 17 mm of the specimen during the loading and advection phase of the oedometer test.

σ'_v (kPa)	Electrical conductivity (mS/m)
Start of the test (~10 kPa)	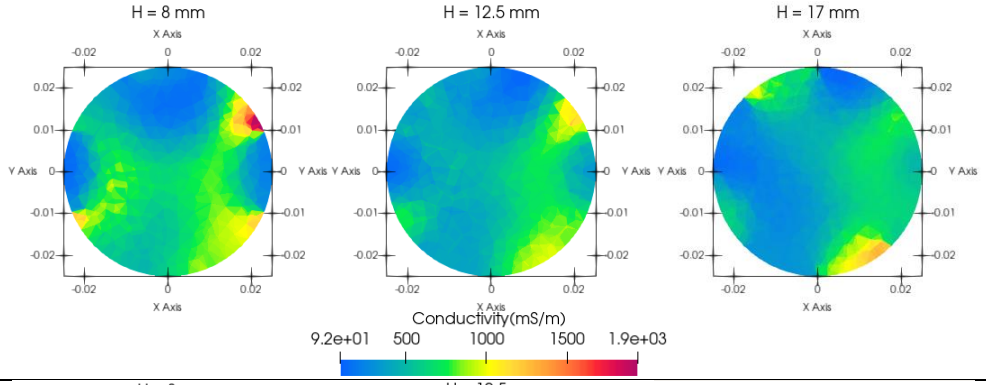
823 kPa	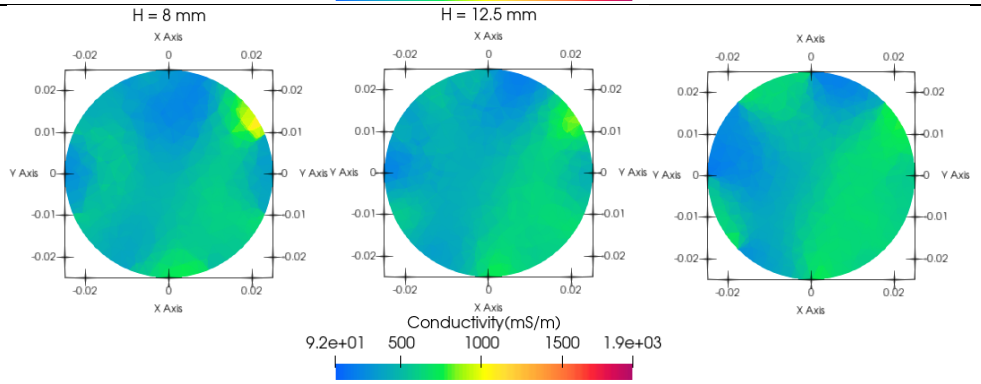
1500 kPa/ 1 hr of advection	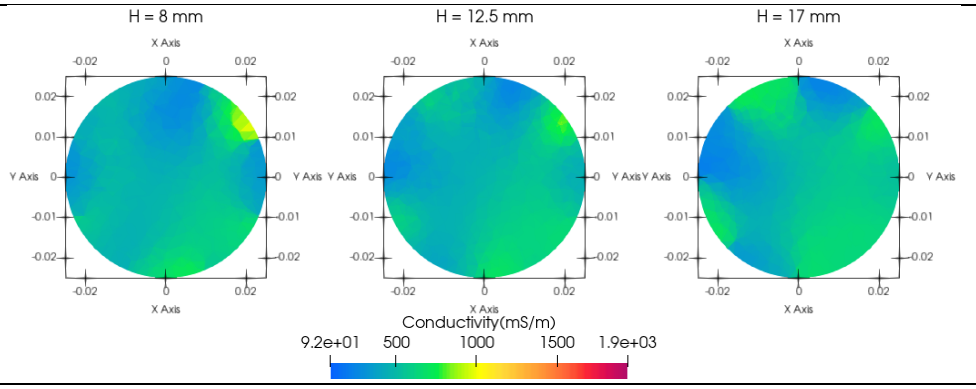
1500 kPa/ 7 hrs of advection	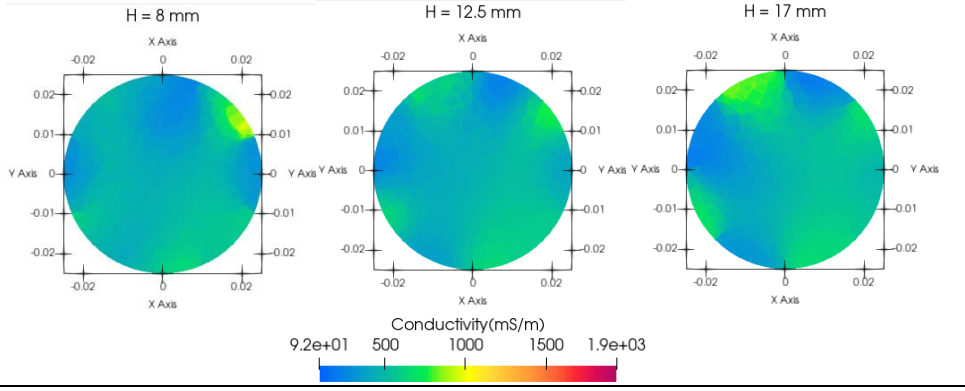

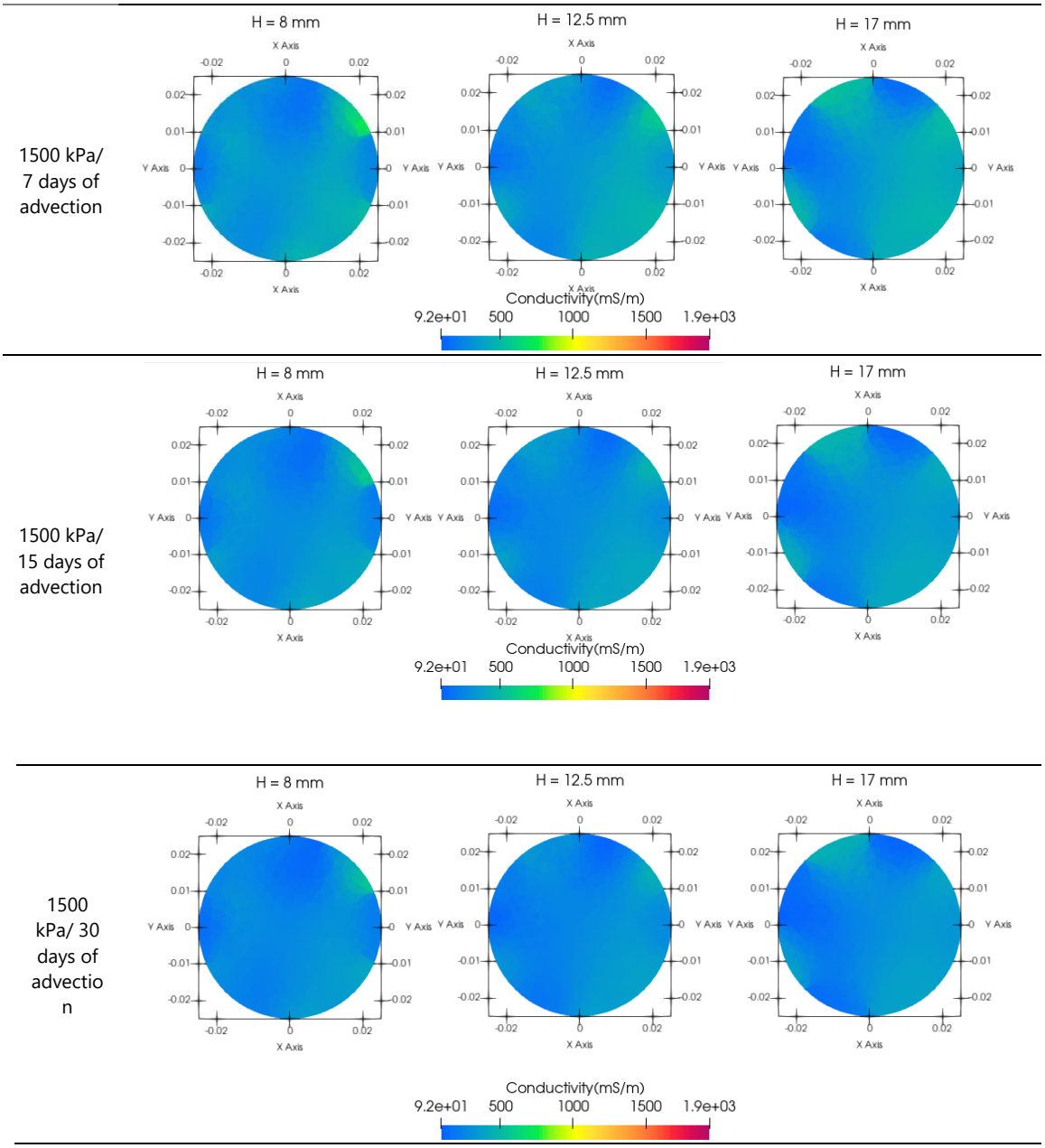

Figure 9.31 Electrical conductivity at different heights of the sample during the loading of test C-I-T_{Adv}-Oed-1.5.

The change in the electrical conductivity during the advection process is also shown in Figure 9.31. A minimal change in electrical conductivity can be observed at the start of acid injection.

Figure 9.32 shows the statistical distribution of electrical conductivity during the test. At the start of the test, there are some parts with higher electrical conductivity although the mean values of electrical conductivity are almost similar to the one of 823 kPa (Figure

9.32 (a)). The average value of electrical conductivity at the start of the test is 525 mS/m. At the end of 823 kPa and after 1 hour of the advection phase the average value of electrical conductivity is 495 mS/m and 496 mS/m respectively.

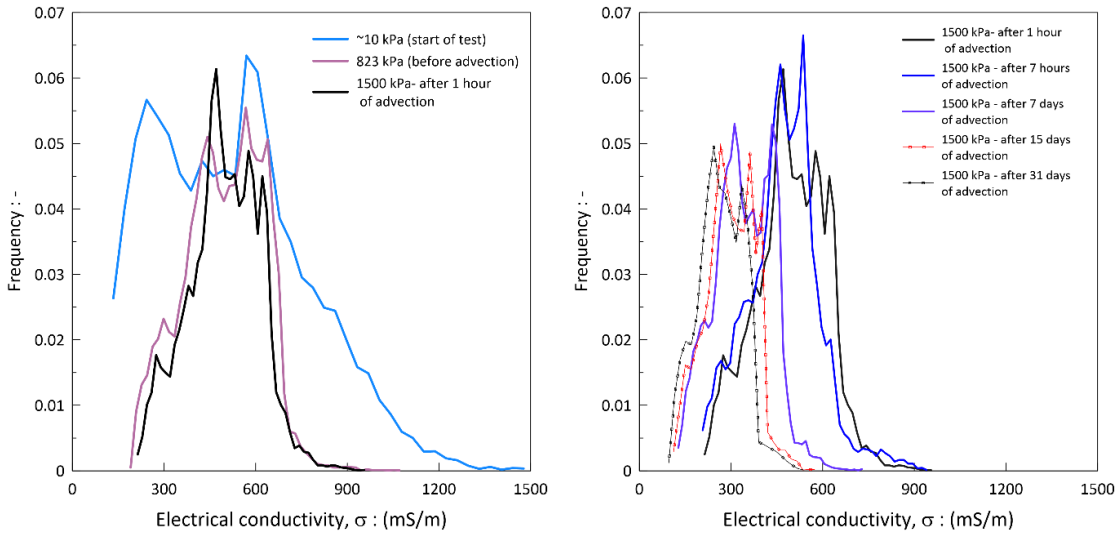

(a) (b)

Figure 9.32 Statistical distribution of electrical conductivity during the loading phase before and during the advection phase.

The values of electrical conductivity remain similar at the start of the advection. A change in the electrical conductivity is observed after 7 days with the mean value of electrical of 341 mS/m as shown by the blue line in Figure 9.32 (b). The average values of electrical conductivity after 15 and 31 days were 296 mS/m and 267 mS/m respectively. In this case, the value of electrical conductivity reduced to half of its starting value after almost 31 days, contrary to the case of the reconstituted specimen (B-R-T_{Adv}-Oed-1) where the value reduced to its half value after just 17 hours. The effect of changes in electrical conductivity on P and S waves was not observed.

No further data during the test was obtained as the CIT system, which records the resistance data had a technical failure which was beyond repair in the test duration.

Figure 9.33 shows the time evolution of the average electrical conductivity reconstructed at different heights of the specimen. Figure 9.33 (a) shows that the decrease in electrical conductivity is slow as compared to the reconstituted specimen. It can be seen that at all given times, the reconstructed electrical conductivity is slightly higher for H = 17 mm although the difference is negligible.

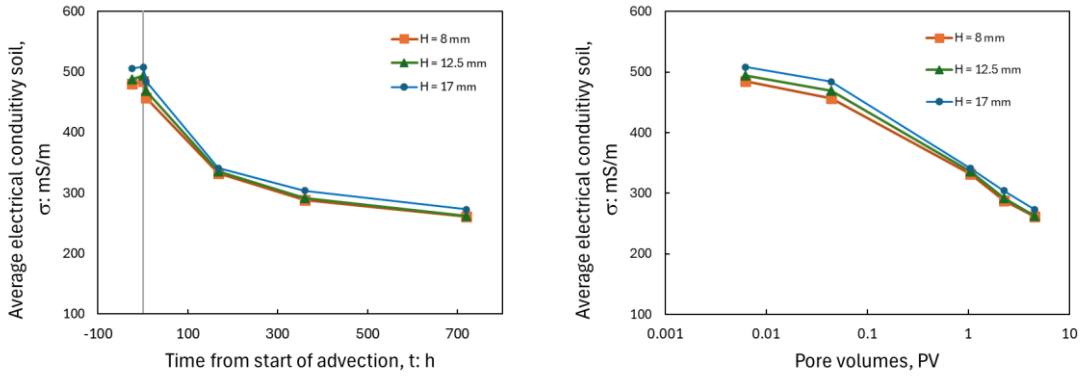

(a) (b)

Figure 9.33 (a) Average electrical conductivity along the height of the specimen during the advection stage over time (b) average electrical conductivity along the height of the specimen during advection stage in terms of pore volume for C-I-T_{Adv}-1.5.

Figure 9.33 (b) shows the plot of time evolution of electrical conductivity in terms of pore volumes of injected fluid. As introduced earlier, the pore volume is the ratio between the injected volume of solution at any given time and the volume of the pores of the specimen. The volume of specimen during the advection stage was 46 ml with average porosity of $\phi = 0.293$. It can be observed that after 4.5 pore volumes the value of electrical conductivity has decreased to half of its original value.

9.6 Conclusions

In the literature, the short-term effects of CO_2 storage are studied employing flowthrough experiments in which different forms of CO_2 are injected into samples. For this purpose, an advanced oedometer cell was designed and developed. The oedometer is equipped with electrodes for Electrical Resistivity Tomography (ERT) and ultrasonic wave transducers.

This chapter presented the results of oedometer tests carried out to investigate the effect of the interaction between acid and the soil minerals on the compressibility of the clayey samples, similar to those expected to arise as short-term effects of CO_2 storage. Three oedometer tests were carried out each on reconstituted specimens from Clay B and intact specimens of Clay C. These experiments were designed to investigate the mechanical and chemical responses of both the reconstituted and intact specimens under varying conditions of acid exposure.

One reconstituted specimen of Clay B was used as a control to establish the baseline mechanical behavior (without chemical interaction). This specimen was subjected to step loading and unloading cycles with axial load changes while continuously saturated with distilled water. The second reconstituted specimen was loaded and then exposed to acid

by diffusion for about one month. It was then further loaded again and finally unloaded. The third specimen was loaded and then exposed to acid by advection in the advanced oedometer (flowthrough experiment, around one month also in this case). It was then further loaded up to 6 MPa and unloaded. Both reconstituted specimens showed an increase in compressibility after acid exposure, which can be related to the dissolution of calcite. Strains that would have occurred during the exposure stage because of creep were evaluated through the model of Vermeer and Neher (1999): this interpretation suggests that the vertical strains due to the exposure stage are about 0.58% and 0.48% in the advection and diffusion tests respectively after around 35 days.

The advection test (flowthrough test) was run in the advanced oedometer and electrical resistance and ultrasonic wave data were obtained during the test. The resistance data was recorded following the protocol of measurement. The data was then inverted in *ResIPy* after removing a few measurements affected by systematic errors.

In the case of reconstituted test tested under advection conditions, ERT reconstructions showed a decrease in the average value of electrical conductivity. A sharp decrease was observed during the first 17 hours of acid flow, with average electrical conductivity dropping to about half of its initial value. The electrical conductivity decrease is consistent with the 'expulsion' of ions from the sample, induced by the advection imposed by the acid flux. The lowest value of average electrical conductivity was observed after 5 days, and then a slight increase was observed. Eventually, the electrical conductivity approached the value predicted by Archie's formula for saturation with a 10^{-2} M HCl solution, even though the effluent pH was still above 6 after one month of advection.

During the advection stage, a decrease in the P wave velocities was noticed, while the S wave velocity remained about constant. These changes might be consistent with a (very small) decrease in the saturation degree of the specimen, due to the release of CO_2 as the product of calcite dissociation reactions. After advection, upon loading of the sample, an increase in the P and S wave was observed.

Three similar tests were performed on intact specimens of Clay C. One specimen provided the reference (no chemical interaction) mechanical behavior. The second specimen was loaded, exposed to acid by diffusion, and further loaded. The third specimen was tested in the advanced oedometer subjected to acid injection. The specimen was loaded and exposed to acid for around 42 days by advection conditions. At the end of the advection, the specimen was further loaded and unloaded.

A rather insignificant reduction in the void ratio was observed in the exposed specimens of Clay C as a result of the combined effects of creep and geochemical reactions both in diffusion and advection conditions.

In case of diffusion test, the dissolution of the carbonate if any, was very small compared to the one shown by the reconstituted specimen tested in analogous conditions: this aspect was appreciated both in terms of pH measured at the specimen boundaries and in terms of void ratio, which started showing some slightly appreciable changes after 21 days. Such large reaction times appear to point out the role played by the tight fabric of the intact specimens, which is likely to reduce the effective diffusivity of the specimen besides ensuring a stiffer behavior.

In case of advection test, the effects during the advection were insignificant. The effects on the compressibility were also negligible.

The change in electrical conductivity of the specimen was not as immediate as in the case of reconstituted specimen. The value of electrical conductivity reduced to half of its starting value after almost 30 days. The slow reduction was due to the low permeability of the specimen resulting in the lower amount of acid injection in comparison to the reconstituted specimen. In total around 60 ml of acid was injected, accounting for around 4.5 pore volume.

The P wave value showed almost constant values during the advection phase. The value increased minimally after loading later maintaining a constant trend. The initial increase might be the effect of loading as the acid injection and its effects are slow at the start of the advection.

In terms of the effect of acid exposure on clayey materials, it can be concluded that it changes the compressibility of the samples both under diffusion and advection as was observed in the case of reconstituted specimens. In case of intact specimens, the fabric of the specimen is more structured and tight, making it difficult for the acid to percolate and react with carbonates of samples. With this delay in calcite dissolution, longer testing times might be advisable for intact caprock specimens under higher pressure of acid injection.

Chapter 10 Conclusions and recommendations

For successful storage of CO_2 in a CCS project, the integrity of the sealing i.e., caprock is of predominant importance, since it provides the structural trapping required for the early stages of storage and prevents the injected CO_2 from leaking back into the atmosphere.

The sealing capacity of caprocks depends on aspects such as the threshold capillary pressure, low permeability, high sorption capacity, high ion exchange capacity, and high swelling ability (Bildstein et al., 2009; Ilgen et al., 2018). The injected CO_2 reacts with the host formation, the pore fluid, and also the caprock through different hydrological mechanisms, which include the dissolution of CO_2 in formation fluid and its diffusion in dissolved form through the caprock. The extent of transport and reaction processes depends on the composition of the pore fluid and the rocks, as well as on the in-situ pressure and temperature (Benson & Cole, 2008; Oelkers & Cole, 2008). However, reactions such as dissolution/precipitation might change the porosity, permeability and mineralogy of the rock formations, ultimately affecting their mechanical properties.

The effects of possible reactions between CO_2 – or acid solutions - and saturated caprock on the hydro-mechanical properties of three Italian carbonatic clayey caprocks were studied. Clay A samples, having a carbonate content of about 51%, were cored from a depth of around 3520 meters from a field in the onshore Romagna area of Eastern Italy. Clay B samples, hhaving a carbonate content of about 39%, were cored from a depth of around 1300 m from a field in the Po Valley. Clay C samples, with a carbonate content of about 48 %, were cored from a depth of about 2760 m from a Central Adriatic field. The study was carried out in two phases. In the first scheme of experiments, reconstituted samples from Clay A and intact samples from Clay B were exposed to dry $scCO_2$, wet $scCO_2$ and CO_2-saturated brine in a batch reactor. After exposure to CO_2 the samples were tested mechanically in high pressure and medium pressure

triaxial cells. The results were compared to the mechanical tests carried out on non-exposed samples. To complement the mechanical tests microstructural analyses were also carried out on exposed and non-exposed samples. These included the determination of water content, equivalent calcite content, mineralogy, pore size distribution and fabric structure.

In the second scheme of experiments, to study the short-term effects of CO_2 injection, reconstituted and intact samples were exposed to a low pH HCl solution. The low pH solutions were used to expedite the chemical reactions involved in the CO_2-brine-rock system. The samples were exposed to diffusion and advection conditions (flowthrough experiments). The latter were carried out in an advanced oedometer, developed for this study, capable of carrying out electrical resistivity tomography and ultrasonic wave velocity measurements.

The key findings of the study are presented and discussed below, together with some recommendations for future research.

10.1 Conclusions

10.1.1 Exposure procedure to CO_2

The reconstituted and intact samples were exposed to dry $scCO_2$, wet CO_2 and CO_2-saturated brine. The temperature and pressure conditions were 60° C and 15 MPa, similar to those anticipated for a depth of about 1500 m. The exposure time of the samples was 14 and 30 days. Reconstituted samples of Clay A were exposed to dry $scCO_2$ and CO_2-saturated brine for 14 days. Intact and reconstituted samples of Clay B were exposed to wet $scCO_2$ for 30 days, Clay B slurry was exposed to wet $scCO_2$ for 14 and 30 days. Some of the exposed specimens were caged/contained by a mesh to ensure their structural integrity of the sample with the help of plastic clamps around it.

Caging was found to be of paramount importance when exposing to CO_2 saturated brine, where uncaged specimens were not able to sustain on their own. It had little to no importance in the case when exposing to dry and wet $scCO_2$, where uncaged specimens were able to sustain on their own. Flexible (slightly deformable) cages were found to be a better option than more rigid ones, as the latter failed because of the swelling pressure developed by the specimens, which were then lost. It can be concluded with the present setup that the best caging system for these materials was given by a

mesh around the side of the samples, two porous stones at the top and bottom of the samples, and a system of clamps to integrate them both axially and radially. In the literature, no standard for exposure procedures is available, and such a caging system is an original outcome of this research. In case the rigid frame of steel bars is used, the axial frame should be coupled with a stiffer and more resistant radial containment than the adopted one.

10.1.2 Effect of CO_2 exposure on microstructure

Microstructural analyses were carried out on samples before and after exposure to CO_2. It involved the investigation of water content, Equivalent Calcite Content (ECC), mineralogy (XRD analysis), Pore Size Density (MIP analysis), homogeneity (CT scans) and fabric structure (SEM analysis) of the samples.

The combined effects of geochemical reactions from CO_2 and water evaporation increased the carbonate content in the lower half of the samples. Changes in mineralogical composition were coupled with fabric effects observed through Pore Size Distribution, as the peak of the predominant pore size family decreased and shifted toward slightly narrower pores. A conclusion from this can be inferred that the carbonate precipitation occurred predominantly in the larger pores, from which water evaporated. The precipitation of minerals when exposed to dry $scCO_2$ was also observed by other researchers (e.g., Nooraiepour et al., 2018). The precipitation of such minerals might result in improved caprock integrity and on the other hand also affect the injectivity of CO_2.

Exposure to wet $scCO_2$ and CO_2 saturated brine did not cause appreciable changes in the specimens' water content. The geochemical analyses performed after exposure generally showed very moderate mineralogical changes. In most cases, a slight increase in dolomite content was observed along with a minimal decrease in calcite.

SEM analysis conducted on ‘original’ intact and reconstituted Clay B specimens revealed edge-to-face aggregations of clay particles. The SEM analysis of exposed Clay B intact specimens showed little to no changes in the fabric of the material. The only possible effect of CO_2 was a very subtle change in the pyrite crystals' surface and the disappearance of salt minerals.

CT scans were carried out to investigate possible changes in density due to exposure. As for reconstituted Clay A specimens, no changes were observed upon exposure to wet $scCO_2$, whereas exposure to CO_2-saturated brine lead to a limited ‘layering’ on one end of the specimen, which however was not found to affect the mechanical response.

The post-exposure CT scans of intact Clay B specimens cored from about the same depth showed microfractures after exposure to wet $scCO_2$. Only one of those specimens was also CT scanned before exposure, and microfractures were also found in this initial condition. On the other hand, another intact Clay B specimen, cored from a different depth, showed no microfractures in post-exposure CT scans. Despite the scarcity of pre-exposure analysis, CT scans seem to suggest that the detected microfractures are most likely related to the in situ – or coring- procedure of the samples and not to the exposure procedure.

10.1.3 Effects of CO_2 exposure on hydro-mechanical behavior

High pressure consolidated-undrained triaxial tests were carried out on both pre and post-exposure samples. The mechanical effects of the adopted exposure procedure were found to be null or, in a limited number of cases, very modest. The strength of Clay A normally consolidated specimens increased very slightly after 14 days of exposure to dry $scCO_2$ and, to an even smaller extent, after 14 days of exposure to CO_2 saturated brine. The specimen exposed to dry $scCO_2$ also showed slightly less contraction during shearing as compared to the non-exposed and to the specimens exposed to CO_2-saturated brine. In literature, some authors have registered an increase in the strength of the caprock material when exposed to dry $scCO_2$ (e.g., Dewhurst et al., 2020; Choi et al., 2021) but mostly a decrease was observed when exposed to CO_2-saturated brine (e.g., Choi et al., 2021).

In the case of Clay B intact, reconstituted, and samples prepared with exposed powder were studied. Two oedometer tests were also conducted on exposed and non-exposed specimens with vertical stress up to 25 MPa.

The initial stiffness of intact Clay B specimens exposed to wet CO_2 was found to be smaller compared to the one of non-exposed specimens. Some specimens exhibited a reduced peak strength that may be attributed to microfractures detected through post-exposure CT scans. The exposed specimen that did not have microfractures displayed a peak strength similar to that of the non-exposed specimen, although its failure was not that brittle, and its residual strength was higher compared to non-exposed specimen. This might be related to the exposure procedure and effects of CO_2, however, only one specimen was available under these conditions to support such conclusions.

The oedometer tests conducted on exposed and non-exposed intact samples of Clay B did not show any significant change in the mechanical behavior. The pre-consolidation pressure analysis showed no effects of wet sCO_2 exposure.

The non-exposed reconstituted specimens of Clay B demonstrated that specimens with an OCR = 1 exhibited contractive behavior. The specimen with OCR = 1.5, showed initial dilatant behavior, followed by contractive one. On the other hand, the sample with OCR = 3 displayed dilation during shearing. However, these specimens had similar stress obliquity at the end of the test. Upon comparing the mechanical response of the exposed specimen to the non-exposed sample tested at half the in-situ stress level, a slight increase in peak strength was noted; however, the overall behavior remained similar.

No significant effects were detected in the case of reconstituted Clay B specimens prepared with exposed powder in the slurry state to CO_2 for 14 and 30 days.

The decision to expose the samples for 14 and 30 days was based on the experience of industry experts and initial numerical simulations. The time of numerical simulation was based on adopting only the diffusion of CO_2 in the sample without considering the chemical reactions. Also, in literature the time of exposure to CO_2 is quite diverse. (Vespo et al., 2025) studied this aspect in their numerical simulation study, which involved the chemical reactions. They found that higher times of reactions were required therefore implying higher exposure times. Batch reaction tests with higher exposure times, temperature and pressure might result in more significant changes in hydro-mechanical behavior. This might be more prominent in the case of intact samples. To reproduce in the laboratory the long-term effects that might arise in the field, it might be required to impose harsher conditions, which might speed up reaction times. The exposure procedure could also be changed to one where sample is exposed to brine, followed by dry $scCO_2$ and finally to wet $scCO_2$ mimicking the in-situ conditions during exposure.

Future batch reaction tests can be designed and carried out with higher temperature and pressure conditions which might result in more significant changes in chemo-hydro-mechanical behavior as found by some research in the literature. Batch reaction experiments conducted with different forms of CO_2 can be used to reproduce the in-situ conditions.

10.1.4 Effects of acid exposure on hydro-mechanical behavior

Acid exposure of reconstituted and intact samples was carried out in oedometer. These experiments were carried out to investigate the mechanical and chemical responses of both the reconstituted and intact specimens under varying conditions of acid exposure. Three oedometer tests were carried out on reconstituted specimens of Clay B and intact specimens of Clay C.

The response of specimens of both clays after exposure, either induced by diffusion or by flowthrough, was compared to the one of control specimens of the same clays, where only mechanical load histories, with some creep stage, were imparted.

As for Clay B reconstituted specimens, both diffusion and flowthrough were carried out for one month, under an effective vertical stress of 1 MPa. As for the intact Clay C specimens, diffusion was carried out under a vertical effective stress of 13 MPa for around one month, whereas flowthrough was carried out under a vertical effective stress of 1.5 MPa for 42 days.

Flowthrough tests were carried out in an advanced oedometer allowing for monitoring changes in the electrical conductivity and P and S wave velocity of the specimens.

Exposure to acid caused an increase in compressibility of Clay B specimens, which can be attributed to the dissolution of carbonates. To distinguish between the chemical strain from the strains that would have occurred during the exposure stage because of creep, the model of Vermeer and Neher (1999) was employed. The interpretation suggested that the vertical strains due to the chemical reaction were about 0.58% and 0.48% in the advection and diffusion tests, respectively.

In the case of reconstituted sample tested under advection condition, ERT reconstructions showed a decrease in the average value of electrical conductivity during the acid injection. A prominent decrease was recorded after 17 hours of injection (≈ 0.7 pore volume). The average value of electrical conductivity after 17 hours decreased to about half of its initial value. The lowest value of electrical conductivity was observed after 5 days (5 pore volumes of injected acid) followed by a slight increase and eventually becoming constant. During the advection stage, a decrease in the P wave velocities was noticed, while the S wave velocity remained about constant.

Acid exposure, both through diffusion and flowthrough, caused a rather insignificant reduction in the void ratio of intact clay C specimens. The dissolution of carbonates was rather modest compared to one of the reconstituted specimens tested in similar conditions, which can be attributed to the structured and tight fabric of the intact specimens which retards transport of dissolved species. The structured fabric not only ensured stiffer behavior but might also affect the effective diffusivity of the sample.

In the flowthrough test conducted on the intact sample of Clay C the change in electrical conductivity was slower with respect to the one of the Clay B reconstituted specimen both with respect to time and pore volumes. The value of electrical conductivity reduced to half of its initial value after almost 30 days (4.5 pore volumes). The slower reduction in comparison to the reconstituted specimen can be attributed to the low

permeability of the intact specimen resulting in a lower amount of acid injection. In total around 60 ml of acid was injected accounting for around 4.5 pore volumes which was around 35 PV in the case of reconstituted specimen. The measurement of P waves showed an initial increase followed by a constant trend during the advection. The recorded initial increase might be related to loading imparted together with the acid flow, as the effects of acid injection on the electrical conductivity (and then on pore fluid composition) were much slower.

10.1.5 Design and setup of advanced oedometer

An advanced oedometer was designed and set up for this study. It can be employed for electrical resistivity tomography and ultrasonic wave measurements. ERT measurements are useful to monitor changes in the properties of pore fluid composition, fabric and degree of saturation, whereas ultrasonic wave velocity measurements are used to monitor the changes in the fabric of samples and degree of saturation.

The setup and calibration of the advanced oedometer were established. For electrical resistivity tomography, a measurement protocol was determined which was used for recording data on electrical conductivity with a number of readings balancing the acquisition time and the desired accuracy of the reconstruction.

The inversion of electrical conductivity data was carried out in the FE code *ResIPy*. Initially, the potentialities of ResIPy were investigated with data from simulated flushing tests in COMSOL. The average values of reconstructed and *COMSOL* electrical conductivity showed that *ResIPy* has significant potential. Comparing the electrical conductivity data of *ResIPy* and COMSOL at different heights of the sample revealed that *ResIPy* can reconstruct the electrical conductivity distribution when the electrical conductivity gradient was relatively small.

Insights for advanced oedometer

The advanced oedometer is an effective device to study the effects of different fluids interacting on the hydro-chemo-mechanical behavior of geomaterials with its ERT and ultrasonic waves setup. There are some limitations and areas of improvement in its use including the data interpretation and elaboration of ERT and ultrasonic waves. Some insights and recommendations in this regard are listed below.

- During the data acquisition process of ERT, systematic measurement errors can arise owing to the electrode positioning, and possible polarization effects. The smaller size of the instrument as compared to the in-situ tests might also have boundary interference. The errors may occur due to poor contact between the

sample and the electrodes, especially during the early stages of loading of the oedometer test. Additionally, after repeated data acquisition, the electrodes may oxidize and degrade, leading to further errors toward the end of the test. It is essential to remove the sequences of data affected by these errors before performing the inversion.

- P and S wave signals can be recorded at different frequencies making it easy to elaborate the first arrival time. The signal recording is subject to intact contact between the transducer and sample, especially in the case of S wave transducer. It was observed that after around 200 kPa detectable P wave signals were obtained whereas in the case of S waves, this was obtained after 1-1.5 MPa.
- Wavelet transformation has proven to be particularly useful for analyzing P and S waves. In some cases of P wave analysis, where visual inspection alone was insufficient, wavelet transformation was employed to determine the first arrival. The arrival of S waves is more impacted by crosstalk, making it challenging to detect their first arrival time. For signals recorded under higher vertical stress, the arrival time was identified using both wavelet transformation and cross-correlation. However, this process becomes more difficult at small vertical loads.
- The vertical stress limit of 6-7 MPa is another practical limitation especially when studying the intact samples that were extracted from higher depths those of interest in geological storage of CO_2.
-

10.2 Recommendations for future research

The exposure procedure adopted for CO_2-rock interaction in this study showed minimal effects on the microstructural and hydro-mechanical behavior of samples. The cage/containment adopted in this study with porous stone is effective. For future tests, when the axial containment with steel bars is adopted a more rigid radial containment should be adopted to prevent any swelling.

Future batch reaction tests can be designed and carried out with higher reaction times, temperature and pressure conditions which might result in more significant changes in chemo-hydro-mechanical behavior as found by some research in the literature. Batch reaction experiments conducted with different forms of CO_2 can be used to reproduce the in-situ conditions. At the in-situ state the caprock near the wellbore, before the injection of CO_2, will be saturated with brine. After injection of CO_2 the brine is displaced, leaving the caprock exposed to wet CO_2 and eventually to dry scCO_2. With the passage of time the CO_2 might dissolve in brine and the dry conditions might change again to wet CO_2 and eventually CO_2-saturated brine conditions. Similar exposure

conditions can be adopted in future laboratory experiments where the samples are exposed successively to brine, wet $scCO_2$, and dry $scCO_2$, mirroring exactly the in-situ conditions of the near wellbore zone. It is important to use intact clay samples as it has structured fabric and the effects on hydro-mechanical properties after such exposure can be well explored.

In the case of flowthrough experiments, the advanced oedometer can be improved where a wide range of fluids will be employed. Control over temperature and pressure, not only in the advanced oedometer but the circuits carrying the fluids will be essential in this case. With such control, it will be possible to use CO_2 in different forms and better mimic the in-situ conditions involving the advection of fluids.

Finally, the geochemical aspects and their effects on the mechanical properties of caprock can be well understood by a coupled numerical reactive transport model. Such model can be useful in understanding the intrinsic reactions of different minerals coupled with hydro-mechanical properties of the material. Such CHM numerical models should be validated against experimental exposure tests and can be used to simulate the geochemo-mechanical behavior of caprocks.

Appendix A

This appendix lists all the geometrical factors determined for advanced oedometer calibration. The table lists the geometrical factors determined experimentally and numerically with top and base.

Table A.1 Comparison of experimental and numerical geometrical factors.

A	B	M	N	Experimental geometrical factors obtained through regression line (1/m)	Experimental geometrical factors obtained with top and base (1/m)	Numerical geometrical factors- sample only (1/m)	Numerical geometrical factors- top and base (1/m)
1	2	8	3	17.04	16.97	17.21	17.04
1	2	8	4	11.78	12.03	12.10	11.95
1	2	8	5	9.28	9.60	9.63	9.51
1	2	8	6	7.21	7.54	7.58	7.50
1	2	8	7	4.73	5.15	5.10	5.06
1	2	7	3	12.19	11.97	12.10	11.97
1	2	7	4	7.03	6.89	7.00	6.89
1	2	7	5	4.53	4.39	4.52	4.44
1	2	7	6	2.49	2.41	2.48	2.44
1	2	6	3	9.72	9.40	9.62	9.53
1	2	6	4	4.58	4.40	4.52	4.45
1	2	6	5	2.05	1.97	2.04	2.00
1	2	5	3	7.65	7.39	7.58	7.53
1	2	5	4	2.49	2.43	2.48	2.44
1	2	4	3	5.13	4.95	5.10	5.09
1	3	8	2	12.21	11.25	12.10	11.97
1	3	8	4	24.62	24.31	24.21	23.92
1	3	8	5	16.91	16.26	16.62	16.39
1	3	8	6	12.35	11.75	12.10	11.95
1	3	8	7	7.83	7.28	7.58	7.50
1	3	7	2	4.27	3.97	4.52	4.47

1	3	7	4	16.89	16.91	16.62	16.42
1	3	7	5	9.14	8.96	9.04	8.89
1	3	7	6	4.55	4.48	4.52	4.45
1	3	6	4	12.36	12.46	12.10	11.97
1	3	6	5	4.60	4.50	4.52	4.44
1	3	5	2	4.99	5.12	4.52	4.42
1	3	5	4	7.74	7.99	7.58	7.53
1	3	4	2	12.75	13.20	12.10	11.95
1	4	8	2	4.51	3.76	4.52	4.45
1	4	8	3	22.31	21.87	21.73	21.48
1	4	8	5	26.98	26.70	26.25	25.90
1	4	8	6	16.98	16.44	16.62	16.39
1	4	8	7	9.93	9.35	9.63	9.51
1	4	7	2	5.49	5.62	5.10	5.06
1	4	7	3	12.33	12.48	12.10	11.97
1	4	7	5	16.93	17.17	16.62	16.39
1	4	7	6	7.06	7.09	7.00	6.88
1	4	6	2	12.58	12.67	12.10	11.95
1	4	6	3	5.18	5.46	5.10	5.09
1	4	6	5	9.88	10.09	9.62	9.51
1	4	5	2	22.49	22.79	21.73	21.45
1	4	5	3	4.67	4.66	4.52	4.42
1	4	3	2	17.82	18.14	17.21	17.03
1	5	8	3	12.50	11.78	12.10	11.95
1	5	8	4	24.81	24.63	24.21	23.90
1	5	8	6	24.86	25.10	24.21	23.90
1	5	8	7	12.48	11.97	12.10	11.95
1	5	7	2	12.56	12.68	12.10	11.95
1	5	7	4	12.31	12.57	12.10	11.95
1	5	7	6	12.19	12.99	12.10	11.95
1	5	6	2	24.84	25.66	24.21	23.89
1	5	6	3	12.28	13.21	12.10	11.94
1	5	4	2	24.84	25.19	24.21	23.89
1	5	4	3	12.25	12.71	12.10	11.95
1	5	3	2	12.48	12.40	12.10	11.95
1	6	8	2	4.64	4.81	4.52	4.44

1	6	8	3	5.32	4.96	5.10	5.06
1	6	8	4	12.43	12.05	12.10	11.95
1	6	8	5	22.23	22.62	21.73	21.45
1	6	8	7	17.71	17.41	17.21	17.04
1	6	7	2	22.39	22.42	21.73	21.48
1	6	7	3	12.45	12.56	12.10	11.97
1	6	7	4	5.35	5.45	5.10	5.09
1	6	7	5	4.42	5.02	4.52	4.42
1	6	5	2	26.83	27.38	26.25	25.89
1	6	5	3	16.87	17.58	16.62	16.39
1	6	5	4	9.74	10.42	9.62	9.50
1	6	4	2	16.98	16.92	16.62	16.39
1	6	4	3	7.05	7.05	7.00	6.88
1	6	3	2	9.93	9.79	9.63	9.51
1	7	8	2	12.34	12.46	12.10	11.97
1	7	8	3	4.42	4.68	4.52	4.47
1	7	8	5	4.76	4.52	4.52	4.42
1	7	8	6	12.47	12.48	12.10	11.95
1	7	6	2	24.80	24.96	24.21	23.92
1	7	6	3	16.89	17.20	16.62	16.42
1	7	6	4	12.21	12.61	12.10	11.97
1	7	6	5	7.66	7.95	7.58	7.53
1	7	5	2	16.88	17.03	16.62	16.39
1	7	5	3	9.10	9.18	9.04	8.89
1	7	5	4	4.57	4.66	4.52	4.44
1	7	4	2	12.36	12.26	12.10	11.95
1	7	4	3	4.55	4.52	4.52	4.45
1	7	3	2	7.81	7.73	7.58	7.50
1	8	7	2	17.35	17.60	17.21	17.03
1	8	7	3	12.11	12.31	12.10	11.97
1	8	7	4	9.60	9.91	9.63	9.53
1	8	7	5	7.55	7.77	7.58	7.53
1	8	7	6	5.07	5.17	5.10	5.08
1	8	6	2	12.21	12.83	12.10	11.95
1	8	6	3	6.99	7.28	7.00	6.88
1	8	6	4	4.53	4.73	4.52	4.44

1	8	6	5	2.49	2.58	2.48	2.44
1	8	5	2	9.76	10.14	9.63	9.50
1	8	5	3	4.51	4.70	4.52	4.44
1	8	5	4	2.04	2.15	2.04	2.00
1	8	4	2	7.70	8.01	7.58	7.50
1	8	4	3	2.44	2.55	2.48	2.44
1	8	3	2	5.19	5.46	5.10	5.06
9	10	16	11	17.40	16.97	17.22	17.12
9	10	16	12	12.19	12.03	12.11	11.99
9	10	16	13	9.68	9.60	9.63	9.54
9	10	16	14	7.64	7.54	7.59	7.53
9	10	16	15	5.08	5.15	5.11	5.08
9	10	15	11	12.23	11.80	12.11	12.03
9	10	15	12	7.01	6.90	7.00	6.90
9	10	15	13	4.59	4.44	4.52	4.46
9	10	15	14	2.55	2.39	2.48	2.44
9	10	14	11	9.69	9.40	9.63	9.59
9	10	14	12	4.45	4.51	4.52	4.46
9	10	14	13	2.03	2.05	2.05	2.01
9	10	13	11	7.58	7.35	7.59	7.57
9	10	13	12	2.43	2.45	2.48	2.44
9	10	12	11	5.15	4.90	5.11	5.13
9	11	16	10	12.08	11.87	12.12	12.08
9	11	16	12	24.07	24.69	24.21	23.89
9	11	16	13	16.63	16.80	16.63	16.41
9	11	16	14	12.14	12.12	12.11	11.96
9	11	16	15	7.49	7.68	7.59	7.52
9	11	15	10	4.59	3.97	4.53	4.56
9	11	15	12	16.49	16.93	16.62	16.38
9	11	15	13	9.11	9.14	9.04	8.89
9	11	15	14	4.63	4.45	4.52	4.44
9	11	14	12	11.79	12.51	12.10	11.93
9	11	14	13	4.47	4.70	4.52	4.45
9	11	13	10	4.59	5.23	4.51	4.33
9	11	13	12	7.33	7.82	7.58	7.48
9	11	12	10	11.88	13.09	12.09	11.82

9	12	16	10	4.25	4.40	4.53	4.50
9	12	16	11	21.41	22.22	21.73	21.45
9	12	16	13	26.62	27.00	26.26	25.95
9	12	16	14	16.77	16.70	16.63	16.42
9	12	16	15	9.53	9.77	9.63	9.53
9	12	15	10	5.39	5.41	5.10	5.03
9	12	15	11	11.97	12.35	12.10	11.92
9	12	15	13	16.94	17.04	16.63	16.42
9	12	15	14	7.23	6.94	7.00	6.89
9	12	14	10	12.69	12.35	12.10	11.91
9	12	14	11	4.64	5.52	5.10	5.03
9	12	14	13	9.73	10.13	9.63	9.53
9	12	13	10	22.49	22.57	21.73	21.44
9	12	13	11	5.10	4.77	4.53	4.50
9	12	11	10	17.30	17.72	17.20	16.95
9	13	16	11	12.01	12.44	12.11	11.97
9	13	16	12	24.53	25.09	24.22	23.96
9	13	16	14	24.39	24.45	24.21	23.91
9	13	16	15	11.89	12.31	12.11	11.97
9	13	15	10	12.41	12.47	12.10	11.90
9	13	15	12	12.51	12.54	12.11	11.99
9	13	15	14	12.51	12.08	12.10	11.94
9	13	14	10	25.10	24.60	24.19	23.84
9	13	14	11	12.67	12.21	12.10	11.94
9	13	12	10	24.96	24.96	24.21	23.89
9	13	12	11	12.46	12.49	12.11	11.98
9	13	11	10	12.35	12.35	12.10	11.91
9	14	16	10	5.02	4.48	4.51	4.39
9	14	16	11	4.87	5.31	5.11	5.08
9	14	16	12	12.07	12.42	12.11	11.98
9	14	16	13	21.99	22.20	21.73	21.47
9	14	16	15	16.85	17.44	17.22	17.08
9	14	15	10	22.00	22.04	21.73	21.46
9	14	15	11	12.01	12.21	12.11	11.99
9	14	15	12	4.81	5.11	5.11	5.09
9	14	15	13	5.05	4.68	4.51	4.39

9	14	13	10	27.04	26.70	26.24	25.86
9	14	13	11	17.03	16.79	16.62	16.39
9	14	13	12	9.80	9.72	9.62	9.49
9	14	12	10	17.05	16.82	16.62	16.37
9	14	12	11	7.19	7.07	7.00	6.90
9	14	11	10	9.88	9.75	9.62	9.47
9	15	16	10	12.76	11.56	12.09	11.89
9	15	16	11	4.91	3.81	4.51	4.41
9	15	16	13	4.19	5.35	4.53	4.47
9	15	16	14	11.73	12.95	12.12	12.02
9	15	14	10	24.52	24.46	24.21	23.91
9	15	14	11	16.78	16.75	16.63	16.44
9	15	14	12	12.08	12.19	12.11	11.98
9	15	14	13	7.60	7.56	7.59	7.55
9	15	13	10	16.82	16.78	16.62	16.36
9	15	13	11	9.11	9.10	9.04	8.89
9	15	13	12	4.53	4.56	4.52	4.43
9	15	12	10	12.33	12.22	12.10	11.93
9	15	12	11	4.62	4.54	4.52	4.46
9	15	11	10	7.70	7.68	7.58	7.47
9	16	15	10	17.71	16.78	17.20	16.97
9	16	15	11	12.48	11.62	12.10	11.93
9	16	15	12	9.86	9.17	9.62	9.49
9	16	15	13	7.81	7.16	7.58	7.50
9	16	15	14	5.30	4.72	5.10	5.06
9	16	14	10	12.27	12.04	12.10	11.91
9	16	14	11	7.05	6.84	7.00	6.88
9	16	14	12	4.50	4.41	4.52	4.43
9	16	14	13	2.47	2.40	2.48	2.44
9	16	13	10	9.73	9.58	9.62	9.47
9	16	13	11	4.57	4.45	4.52	4.44
9	16	13	12	2.03	2.02	2.04	1.99
9	16	12	10	7.76	7.59	7.58	7.48
9	16	12	11	2.53	2.44	2.48	2.44
9	16	11	10	5.21	5.14	5.10	5.04
1	5	2	3	12.30	12.54	12.10	11.68

1	5	2	4	24.58	25.39	24.21	23.37
1	5	3	4	12.33	12.72	12.10	11.69
1	5	6	7	12.34	12.65	12.10	11.68
1	5	6	8	24.44	24.53	24.21	23.37
1	5	7	8	12.07	11.85	12.10	11.69
2	6	3	4	12.15	11.93	12.10	11.68
2	6	3	5	24.17	24.94	24.21	23.36
2	6	4	5	11.96	12.95	12.10	11.68
2	6	7	8	12.02	12.37	12.10	11.68
2	6	7	1	24.27	25.21	24.21	23.36
2	6	8	1	12.28	12.78	12.10	11.68
3	7	4	5	11.88	12.77	12.10	11.68
3	7	4	6	24.05	25.31	24.21	23.36
3	7	5	6	12.19	12.50	12.10	11.68
3	7	8	1	12.19	12.53	12.10	11.68
3	7	8	2	24.34	24.09	24.21	23.36
3	7	1	2	12.17	11.52	12.10	11.68
4	8	1	2	12.12	11.52	12.10	11.68
4	8	1	3	24.28	24.27	24.20	23.36
4	8	2	3	12.08	12.83	12.10	11.68
4	8	5	6	12.41	12.86	12.10	11.68
4	8	5	7	24.57	25.05	24.20	23.36
4	8	6	7	12.25	12.05	12.10	11.68
9	13	10	11	12.18	12.32	12.10	11.63
9	13	10	12	24.56	24.82	24.20	23.36
9	13	11	12	12.33	12.39	12.11	11.72
9	13	14	15	12.25	12.21	12.10	11.67
9	13	14	16	23.67	24.65	24.21	23.38
9	13	15	16	11.45	12.35	12.11	11.71
10	14	11	12	12.28	11.94	12.11	11.73
10	14	11	13	24.32	24.32	24.20	23.38
10	14	12	13	12.11	12.33	12.10	11.65
10	14	15	16	11.56	12.32	12.11	11.69
10	14	15	9	24.85	24.46	24.21	23.33
10	14	16	9	13.36	12.07	12.10	11.64
11	15	12	13	11.83	12.47	12.10	11.64

11	15	12	14	23.73	24.71	24.20	23.34
11	15	13	14	11.95	12.22	12.11	11.70
11	15	16	9	13.26	11.66	12.10	11.65
11	15	16	10	25.39	23.27	24.21	23.39
11	15	9	10	12.26	11.56	12.11	11.73
12	16	9	10	11.59	11.87	12.11	11.73
12	16	9	11	23.47	24.50	24.21	23.36
12	16	10	11	11.80	12.53	12.10	11.63
12	16	13	14	12.22	12.50	12.11	11.71
12	16	13	15	24.56	24.37	24.21	23.38
12	16	14	15	12.36	11.78	12.10	11.67
1	9	4	12	0.40	0.42	0.43	0.45
1	9	5	13	0.37	0.38	0.41	0.41
1	9	6	14	0.41	0.44	0.43	0.46
2	10	5	13	0.39	0.40	0.43	0.44
2	10	6	14	0.41	0.39	0.40	0.42
2	10	7	15	0.39	0.36	0.43	0.42
3	11	6	14	0.46	0.48	0.43	0.43
3	11	7	15	0.40	0.42	0.41	0.42
3	11	8	16	0.44	0.48	0.43	0.44
4	12	1	9	0.41	0.41	0.43	0.39
4	12	7	15	0.38	0.40	0.42	0.44
4	12	8	16	0.40	0.42	0.40	0.43
5	13	1	9	0.39	0.43	0.41	0.44
5	13	2	10	0.40	0.43	0.43	0.46
5	13	8	16	0.42	0.39	0.43	0.40
6	14	1	9	0.42	0.39	0.43	0.46
6	14	2	10	0.40	0.39	0.40	0.43
6	14	3	11	0.45	0.44	0.43	0.40
7	15	2	10	0.39	0.40	0.43	0.43
7	15	3	11	0.41	0.42	0.41	0.42
7	15	4	12	0.39	0.41	0.42	0.46
8	16	3	11	0.44	0.42	0.43	0.45
8	16	4	12	0.41	0.38	0.40	0.42
8	16	5	13	0.44	0.46	0.43	0.45

Appendix B

This appendix summerizes the process of Archi'e law parameters on Clay B material. The local electrical conductivity of the soil σ_S is related to the corresponding pore fluid electrical electrical conductivity through Archie's law (Equation $B.1$):

$$\sigma_S = S_r^n \phi^m \sigma_L \qquad (B.1)$$

where S_r is the degree of saturation and *n* and *m* are model parameters. The parameter *m* was determined after determining the electrical conductivity of the liquid (σ_L) and of the sample (σ_S) as discussed in the following paragraphs.

First, the electrical conductivity of the liquid was determined from the electrolyte squeezed out of paste. The paste was made by mixing pulverized Clay B powder with distilled water at a water content of 50% (1.16 LL). It was left to sit for 24 hours to allow the water to dissolve the salts present in the clay.

After this period, the electrolyte was extracted from the paste under pressure. To achieve this, the soil paste was placed in a ring with a diameter and height of 50 mm. This ring was then positioned in a cell allowing undrained conditions at the bottom and drained conditions at the top. Filter paper sheet was placed on top of the sample to prevent clogging of the drainage line. The cell was then pressurized under press machine, which forced the electrolyte out of the sample. The electrical conductivity of the resulting electrolyte (water) was measured to be 1.457 S/m measured using a conductivity-meter (Mettler Toledo SevenMulti).

Additionally, the electrical conductivity of the paste (σ_s) was determined using a 1D electrical conductivity measurement. For this purpose, a four-electrode scheme was employed, as shown in Figure B.1, where electrodes A and B were used to inject current, while electrodes M and N measured the potential drop. The electrical conductivity of the paste was found to be $\sigma_s = 0.51$ S/m.

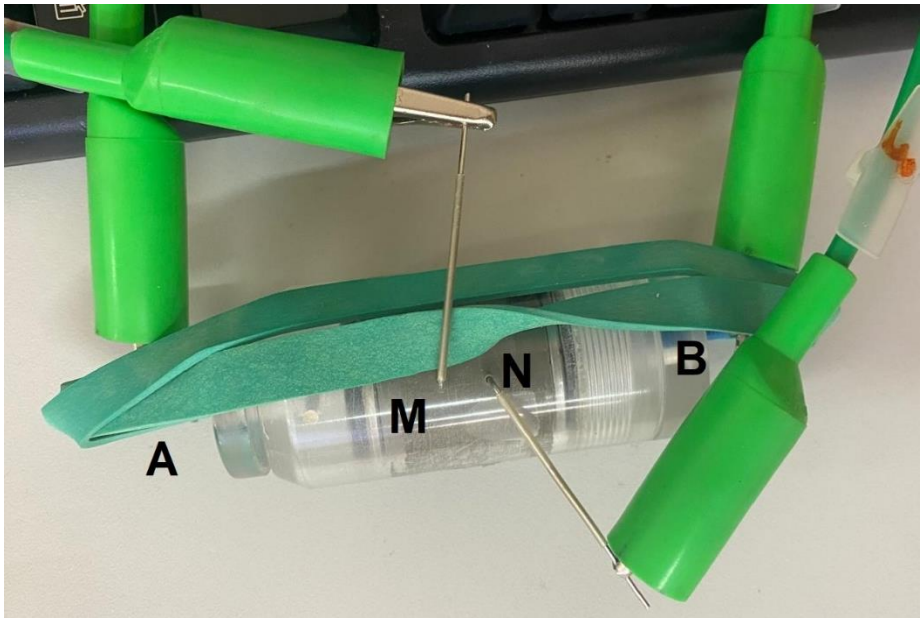

Figure B.1 1D electrical conductivity measurement with 4 electrodes scheme.

The parameter m was then determined assuming a fully saturated sample resulted in a value around 1.5 from Equation $B.1$.

Appendix C

This appendix summarizes the implementation of the Vermeer Neher model for the prediction of creep strains

Vermeer & Neher (1999) presented the soft soil model addressing the long-term deformation (secondary compression) often observed in near-normally consolidated clays, silts, and peat. The authors developed a creep model based on a differential form of the logarithmic creep law. The strain at the end of the consolidation (ϵ_c) can be described by an equation in the form.

$$\epsilon_c = \epsilon_c^e + \epsilon_c^c = A \ln \frac{\sigma'}{\sigma_0'} + B \ln \frac{\sigma_{pc}}{\sigma_{p0}} + C \ln \frac{\tau_c + t'}{\tau_c} \qquad (C.1)$$

where ϵ_c is the total strain sum of an elastic ϵ_c^e and a plastic component ϵ_c^c. In the model, the creep strains are considered as irreversible and then merged with the plastic ones. For step-to-step loading of oedometer test, σ_0' represents the initial effective pressure before loading and σ' is the final effective loading pressure. The values σ_{p0} and σ_{pc} represents the pre-consolidation pressure corresponding to before-loading and end-of-consolidation states respectively. τ_c is the time to the end of primary consolidation and t' is the creep time (starting from the end of primary consolidation).

In Equation $C.1$ the constants A, B and C are related to the recompression index (C_r), compression index (C_c) and secondary compression index (C_α) as

$$A = \frac{Cr}{(1 + e_0) \cdot \ln 10}$$

$$B = \frac{Cc - Cr}{(1 + e_0) \cdot \ln 10}$$

$$C = \frac{C_\alpha}{(1 + e_0) \cdot \ln 10}$$

For non-failure situations as met in oedometer loading conditions, an instantaneous plastic strain component is not assumed, as used in traditional elastoplastic modelling. In addition to this concept, the authors adopted Bjerrum's (1967) idea that the

preconsolidation stress depends entirely on the amount of creep strain being accumulated over time and the following equation is considered.

$$\epsilon = \epsilon^e + \epsilon^C = A \ln \frac{\sigma'}{\sigma_0} + B \ln \frac{\sigma_p}{\sigma_{p0}} \rightarrow \sigma_p = \sigma_{p0} \exp\left(\frac{\epsilon^C}{B}\right) \qquad (C.2)$$

The longer a soil sample is left to creep the larger the preconsolidation pressure (σ_p) grows. The time-dependency of the preconsolidation pressure (σ_p) is then obtained by combining Equations $C.1$ and $C.2$.

$$\epsilon^C - \epsilon_C^C = B \ln \frac{\sigma_p}{\sigma_{pc}} = C \ln \frac{\tau_C + t'}{\tau_C} \qquad (C.3)$$

The Equation ($C.1$) can be differentiated to obtain the equation for continuous loading or transient form.

$$\dot{\epsilon} = \dot{\epsilon^e} + \dot{\epsilon^c} = A \frac{\dot{\sigma'}}{\sigma'} + \frac{C}{\tau_C + t'} \qquad (C.4)$$

where $\tau_C + t'$ can be eliminated by means of Equation $C.3$ to obtain.

$$\dot{\epsilon} = \dot{\epsilon^e} + \dot{\epsilon^c} = A \frac{\dot{\sigma'}}{\sigma'} + \frac{C}{\tau_C} \left(\frac{\sigma_{pc}}{\sigma_p}\right)^{\frac{B}{C}} \qquad (C.5)$$

with $\sigma_p = \sigma_{p0} \exp\left(\frac{\epsilon^c}{B}\right)$.

Equation $C.5$ can be written in the form of final effective stress (σ') by eliminating τ_c and σ_{pc} taking into account $\frac{\tau}{\tau_C} = \left(\frac{\sigma'}{\sigma_{pc}}\right)^{\frac{B}{C}}$

$$\dot{\epsilon} = \dot{\epsilon^e} + \dot{\epsilon^c} = A \frac{\dot{\sigma'}}{\sigma'} + \frac{C}{\tau} \left(\frac{\sigma'}{\sigma_p}\right)^{\frac{B}{C}} \qquad (C.6)$$

where t is a standard time to which the preconsolidation pressure is referred (e.g. 24 hours).

The Vermeer & Neher (1999) model was implemented in MS Excel spreadsheet to differentiate the geochemical effects of acid from those of creep (mechanical effects). In the Excel spreadsheet, information regarding stress from the previous loading step (including the current value of the preconsolidation stress) and the final stress of the current loading step is provided. The compression indices (C_C, C_r and C_α) are used to obtain the parameters A, B, and C. During an oedometer test, when the stress is applied

to the sample, excess pore pressure develops and dissipates over time, depending on the coefficient of consolidation (C_V). The parameter (C_V) along with the height of the sample at the beginning and end of the loading step, is an input into the Excel spreadsheet. The sample is divided into three equal parts of equal height, and the elastic and plastic strains are calculated at the center of each section. The effective stress increment in the centers of each layer is evaluated according to the simulated pore pressure dissipation. The (average) total strain is then evaluated as the sum of the displacements of each layer divided by the total height of the sample.

Appendix D

This appendix documents the initial characteristics of tested samples in triaxial including void ratio, water content and degree of saturation. It also includes data of void ratios at the start and end of consolidation stage, and Skempton's B parameter value at the end of saturation. This appendix then states the volume change during the saturation of the samples in triaxial tests.

Table D.1 Initial characteristics of Clay A and Clay B samples tested triaxially.

Test ID	w (%)	e (-)	S (-)
A-R1-N-4.25	16.56	0.49	0.99
A-R1-N-7.5 (1)	14.16	0.46	0.98
A-R1-N-7.5 (2)	14.66	0.45	1.00
A-R1-T_{DCO2}S14-7.5	14.77	0.42	0.98
A-R1-T_{BCO2}S14-7.5	14.12	0.41	0.97
B-I-N-6	13.75	0.39	0.98
B-I-N-12	14.47	0.45	0.98
B-I-T_{WCO2}S30-6	13.95	0.41	0.98
B-I_{MF}-T_{WCO2}S30-6	14.11	0.43	0.92
B-I_{MF}-T_{WCO2}S30-6 (1)	13.10	0.46	0.95
B-I_{MF}-T_{WCO2}S30-12	13.33	0.42	0.92
B-R1-N-3	19.23	0.54	0.99
B-R1-N-6	17.67	0.51	0.97
B-R1.5-N-6	17.69	0.51	0.96
B-R3.0-N-6	18.35	0.53	0.97
B-R1-T_{WCO2}S30-3	18.30	0.56	0.91
B-R1-T_{WCO2}P14-6	17.72	0.55	0.96
B-R1.5-T_{WCO2}P14-6	17.14	0.55	0.97
B-R1-T_{WCO2}P30-6	16.89	0.50	0.99
B-R1.5-T_{WCO2}P30-6	17.68	0.50	0.99

Table D.2 Parameter B and void ratio data for Clay A.

Test ID	B	Void ratio (e)	
	end of saturation	*e (start of cons.)*	*e (end of cons.)*
A-R1-N-4.25	0.96	0.48	0.36
A-R1-N-7.5 (1)	0.98	0.44	0.31
A-R1-N-7.5 (2)	0.95	0.41	0.32
A-R1-T_{DCO2}S14-7.5	0.96	0.42	0.34
A-R1-T_{BCO2}S14-7.5	0.97	0.41	0.33

Table D.3 Volumetric strains during saturation of Clay A samples.

Test ID	Volumetric strains during saturation
A-R1-N-4.25	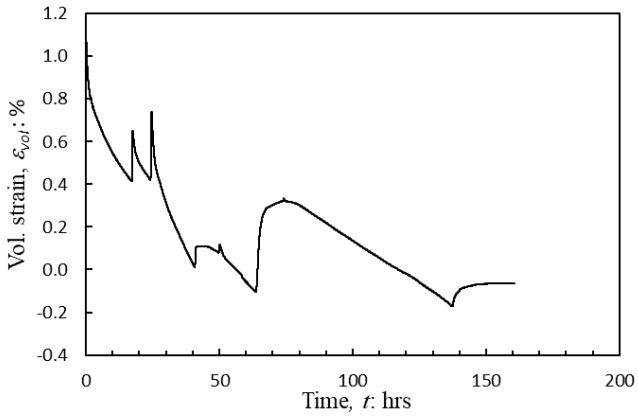
A-R1-N-7.5 (1)	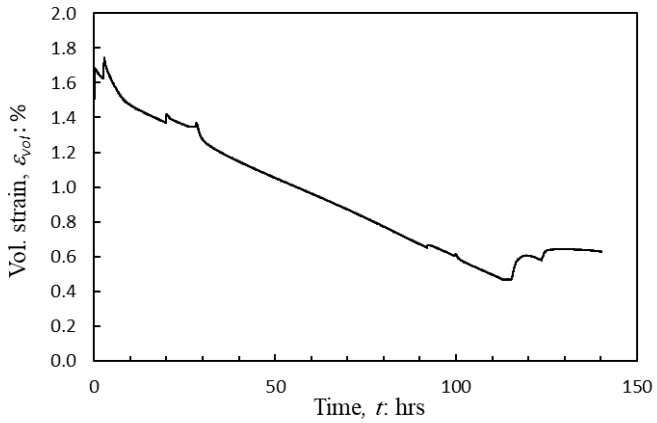
A-R1-N-7.5 (2)	N/A

A-R1-T_{DCO2}S14-7.5

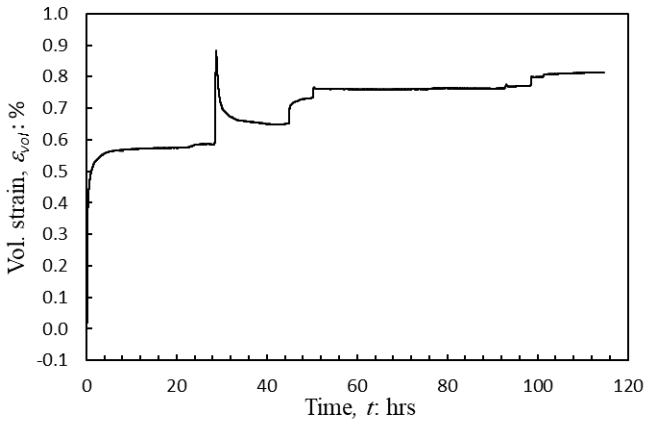

A-R1-T_{BCO2}S14-7.5

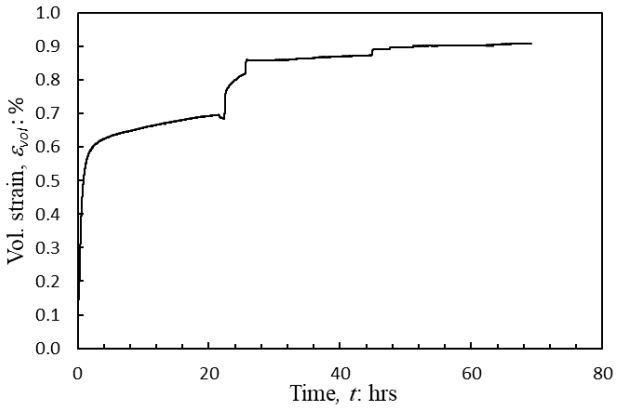

Table D.4 Parameter B and void ration data for Clay B.

Test ID	Intact specimen Depth (m)	B	e	
		end of saturation	e (start of consolidation)	e (end of consolidation)
B-I-N-6	1332.5-1332.6	0.97	0.37	0.29
B-I-N-12	1299.6-1299.8	0.98	0.41	0.30
B-I-T_{WCO2}S30-6	1331.0-1331.1	0.96	0.40	0.30
B-I_{MF}-T_{WCO2}S30-6	1299.8-1300.0	0.96	0.42	0.35
B-I_{MF}-T_{WCO2}S30-6 (1)	1299.8-1300.0	0.95	0.45	0.34
B-I_{MF}-T_{WCO2}S30-12	1299.8-1300.0	0.96	0.39	0.34
B-R1-N-3		0.95	0.48	0.46
B-R1-N-6		0.95	0.52	0.36
B-R1.5-N-6		0.95	0.50	0.31
B-R3.0-N-6		0.95	0.51	0.25
B-R1-T_{WCO2}S30-3		0.95	0.50	0.46
B-R1-T_{WCO2}P14-6		0.95	0.51	0.37
B-R1.5-T_{WCO2}P14-6		0.96	0.54	0.31
B-R1-T_{WCO2}P30-6		0.97	0.48	0.38
B-R1.5-T_{WCO2}P30-6		0.96	0.49	0.33

Table D.5 Volumetric strains during saturation of Clay B samples.

Test ID	Volumetric strains during saturation
B-I-N-6	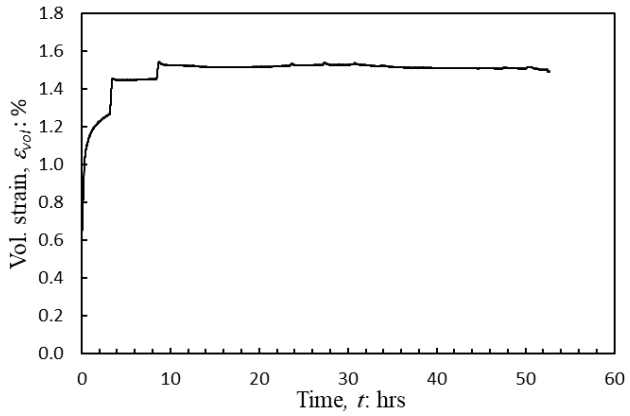

B-I-N-12

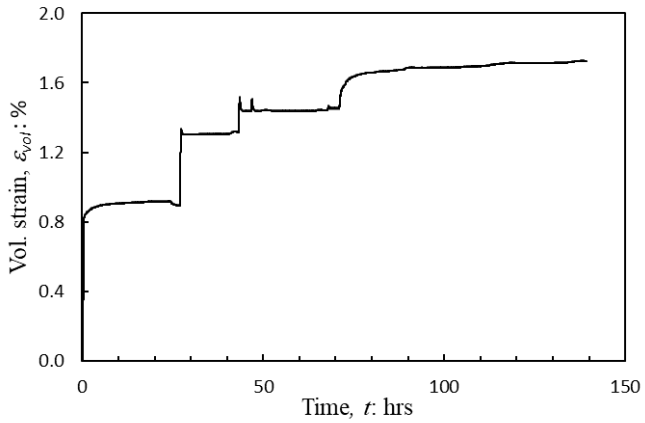

B-I-T_{WCO2}S30-6 N/A

B-I_{MF}-T_{WCO2}S30-6

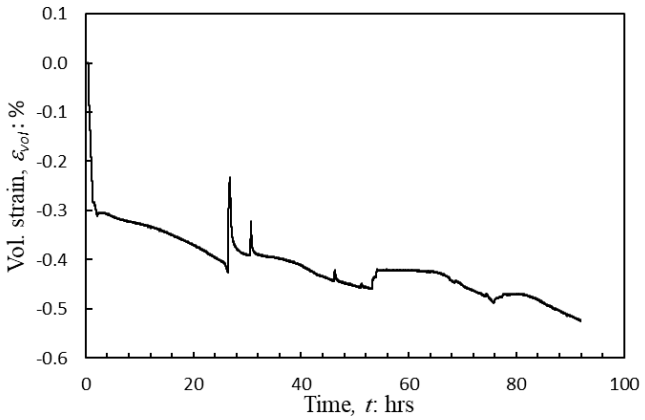

B-I_{MF}-T_{WCO2}S30-6 (1)

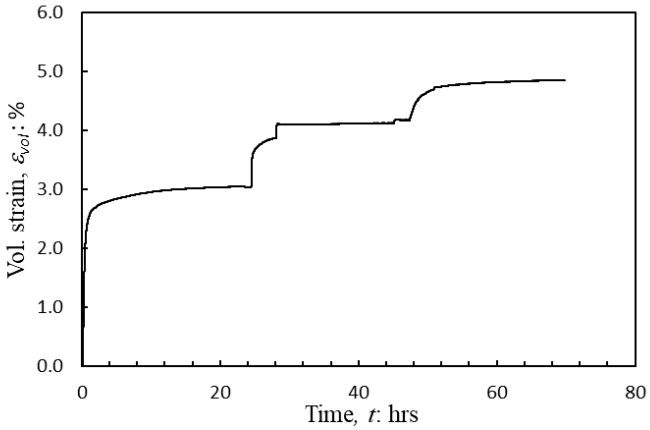

B-I_{MF}-T_{WCO2}S30-12

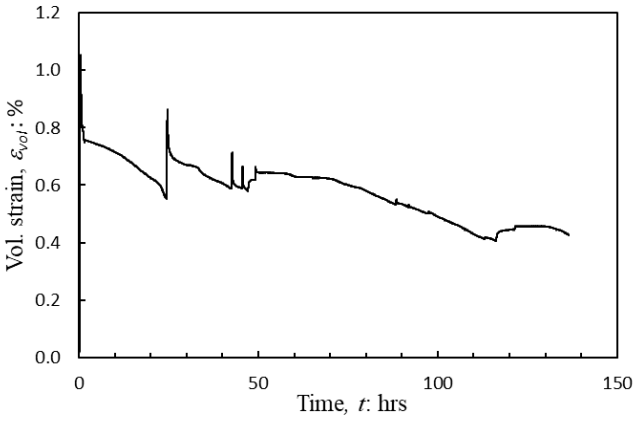

B-R1-N-3

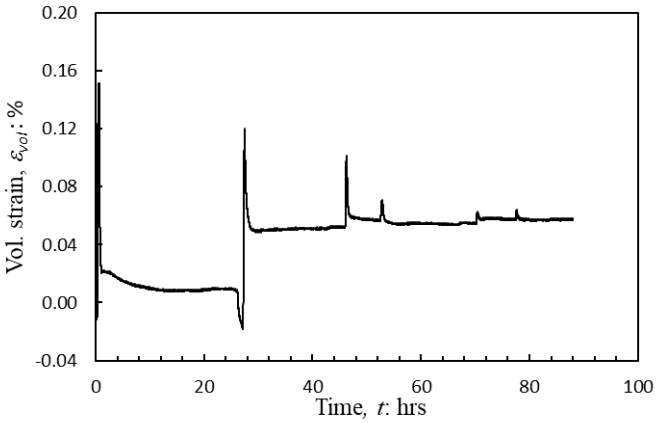

B-R1-N-6 N/A

B-R1.5-N-6

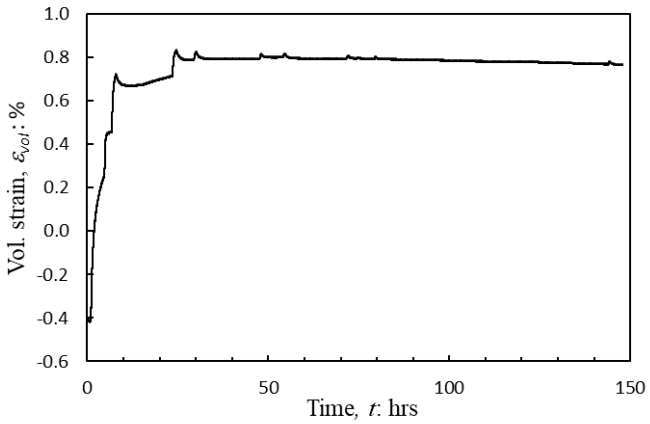

B-R3.0-N-6

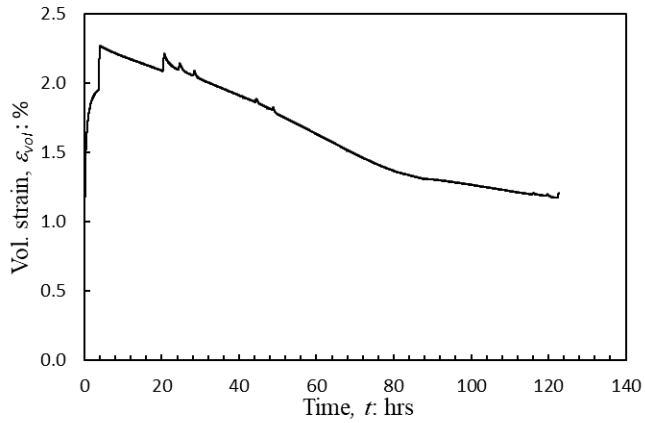

B-R1-T$_{WCO2}$S30-3

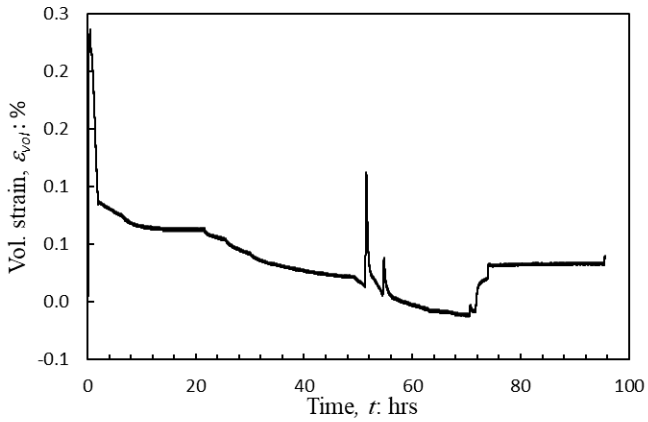

B-R1-T$_{WCO2}$P14-6

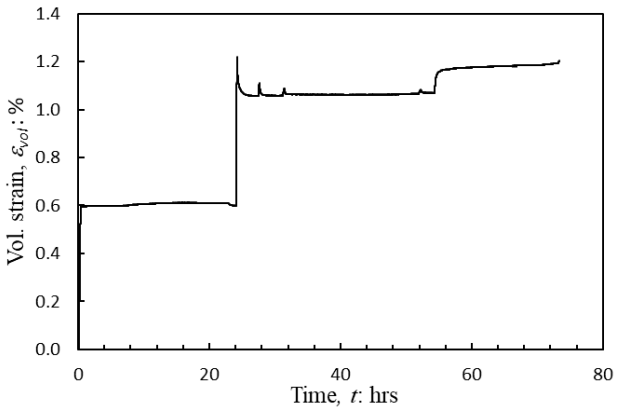

B-R1.5-T $_{WCO2}$P14-6

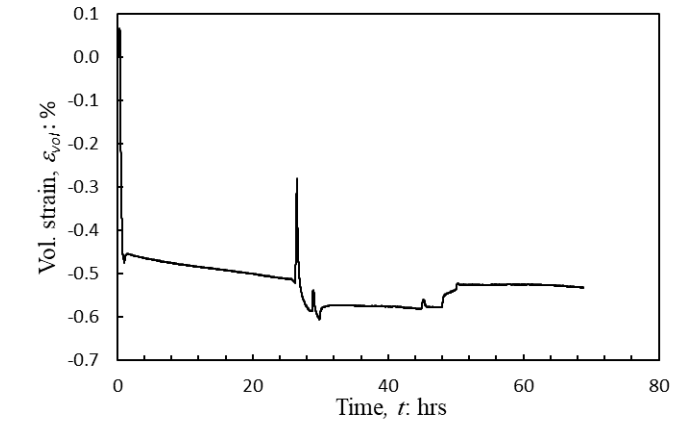

B-R1-T $_{WCO2}$P30-6

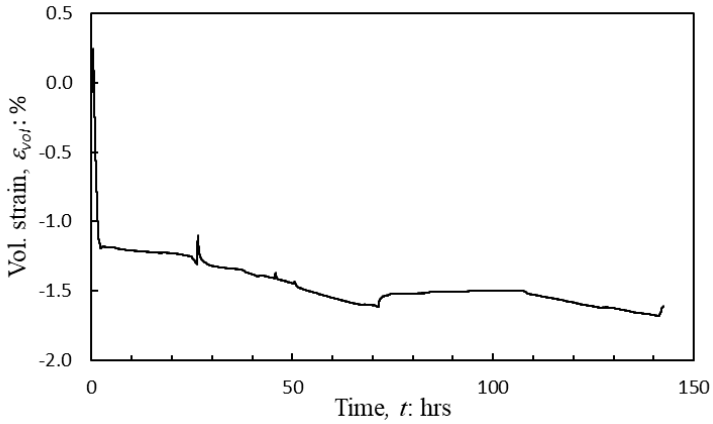

B-R1.5-T $_{WCO2}$P30-6

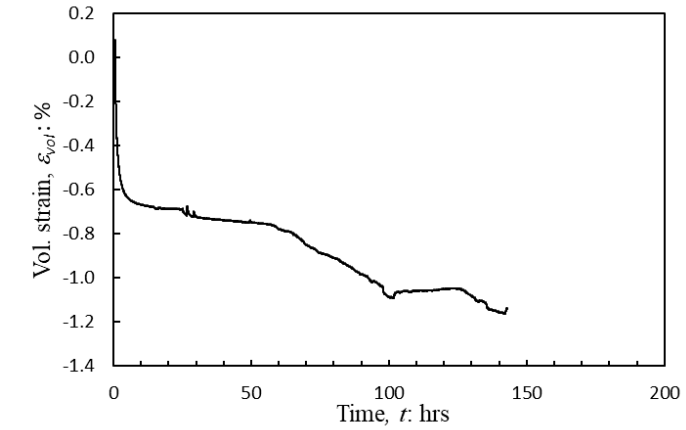

Axial and volumetric strains, induced in Clay A and Clay B samples after exposure to CO_2 are summarized in table below. Only axial strains are documented in cases where diameter of the samples were not measured after exposure.

Table D.6 Axial and volumetric strains induced due to exposure.

Test ID	ϵ_{ax} (%)	ϵ_{vol} (%)
A-R1-T_{DCO2}S14-7.5	0.58	
A-R1-T_{BCO2}S14-7.5	0.53	0.24
A-R1-T_{DCO2}S14	0.25	
A-R1-T_{BCO2}S14	Not recovered	
	Clay B samples	
B-I-T_{WCO2}S30-6	1.21	1.58
B-I_{MF}-T_{WCO2}S30-6	-1.06	-3.39
B-I_{MF}-T_{WCO2}S30-6 (1)	0.24	1.19
B-I_{MF}-T_{WCO2}S30-12	-0.95	-1.37
B-I-T_{WCO2}S30	1.78	-0.92
B-R1-T_{WCO2}S30-3	0.50	-0.14
B-R1-T_{WCO2}S30-6	2.17	1.63
B-R1.5-T_{WCO2}S30-6	2.46	4.04

References

Agofack, N., Cerasi, P., Stroisz, A., & Rørheim, S. (2019). *Sorption of CO2 and integrity of a caprock shale*. In the Proceedings of American Rock Mechanics Association Symposium, New York.

Ajayi, T., Gomes, J. S., & Bera, A. (2019). A review of CO2 storage in geological formations emphasizing modeling, monitoring and capacity estimation approaches. *Petroleum Science*, *16*(5), 1028–1063. https://doi.org/10.1007/s12182-019-0340-8

Akono, A., Druhan, J. L., Dávila, G., Tsotsis, T., Jessen, K., Fuchs, S., Crandall, D., Shi, Z., Dalton, L., Tkach, M. K., Goodman, A. L., Frailey, S., & Werth, C. J. (2019). A review of geochemical–mechanical impacts in geological carbon storage reservoirs. *Greenhouse Gases: Science and Technology*, *9*(3), 474–504. https://doi.org/10.1002/ghg.1870

Alam, M. M., Hjuler, M. L., Christensen, H. F., & Fabricius, I. L. (2014). Petrophysical and rock-mechanics effects of CO2 injection for enhanced oil recovery: Experimental study on chalk from South Arne field, North Sea. *Journal of Petroleum Science and Engineering*, *122*, 468–487. https://doi.org/10.1016/j.petrol.2014.08.008

Alemu, B. L., Aagaard, P., Munz, I. A., & Skurtveit, E. (2011). Caprock interaction with CO2: A laboratory study of reactivity of shale with supercritical CO2 and brine. *Applied Geochemistry*, *26*(12), 1975–1989. https://doi.org/10.1016/j.apgeochem.2011.06.028

Archie, G. E. (1942). The Electrical Resistivity Log as an Aid in Determining Some Reservoir Characteristics. *Transactions of the AIME*, *146*(01), 54–62. https://doi.org/10.2118/942054-G

Armitage, P. J., Faulkner, D. R., & Worden, R. H. (2013). Caprock corrosion. *Nature Geoscience*, *6*(2), 79–80. https://doi.org/10.1038/ngeo1716

Arroyo, M. (2007). Wavelet analysis of pulse tests in soil samples. *Italian Geotechnical Journal*, *30*, 26–38.

Arroyo, M., Muir Wood, D., & Greening, P. D. (2003). Source near-field effects and pulse tests in soil samples. *Géotechnique*, *53*(3), 337–345. https://doi.org/10.1680/geot.2003.53.3.337

Arroyo, M., Muir Wood, D., Greening, P. D., Medina, L., & Rio, J. (2006). Effects of sample size on bender-based axial G0 measurements. *Géotechnique*, *56*(1), 39–52. https://doi.org/10.1680/geot.2006.56.1.39

Arulnathan, R., Boulanger, R. W., & Riemer, M. F. (1998). Analysis of bender element tests. *Geotechnical Testing Journal*, *21*(2), 120–131.

ASTM. (2008). *D6836-16, Test Methods for Determination of the Soil Water Characteristic Curve for Desorption Using Hanging Column, Pressure Extractor, Chilled Mirror Hygrometer, or Centrifuge*. ASTM International. https://doi.org/10.1520/D6836-16

ASTM. (2011). *D4767-11, Test Method for Consolidated Undrained Triaxial Compression Test for Cohesive Soils*. ASTM International. https://doi.org/10.1520/D4767-11R20

ASTM. (2016). *D5298-16, Test Method for Measurement of Soil Potential (Suction) Using Filter Paper*. ASTM International. https://doi.org/10.1520/D5298-16

ASTM. (2017). *D4318−17, Standard Test Methods for Liquid Limit, Plastic Limit, and Plasticity Index of Soils*. https://doi.org/10.1520/ D4318-17E01

ASTM. (2020). *D792-20, Standard Test Methods for Density and Specific Gravity (Relative Density) of Plastics by Displacement*. https://doi.org/0.1520/ D0792-20

ASTM. (2021). *D4373-21, Test Method for Rapid Determination of Carbonate Content of Soils*. ASTM International. https://doi.org/10.1520/D4373-21

Atkinson, J. (2007). Peak strength of overconsolidated clays. *Géotechnique*, *57*(2), 127–135. https://doi.org/10.1680/geot.2007.57.2.127

Auerbach, D. I., Caulfield, J. A., Adams, E. E., & Herzog, H. J. (1997). Impacts of ocean CO2 disposal on marine life: I. A toxicological assessment integrating constant-concentration laboratory assay data with variable-concentration field exposure. *Environmental Modeling & Assessment*, *2*(4), 333–343. https://doi.org/10.1023/A:1019029931755

Bachu, S. (2008). CO2 storage in geological media: Role, means, status and barriers to deployment. *Progress in Energy and Combustion Science*, *34*(2), 254–273. https://doi.org/10.1016/j.pecs.2007.10.001

Bachu, S., & Adams, J. J. (2003). Sequestration of CO2 in geological media in response to climate change: Capacity of deep saline aquifers to sequester CO2 in solution. *Energy Conversion and Management*, *44*(20), 3151–3175. https://doi.org/10.1016/S0196-8904(03)00101-8

Bachu, S., Shaw, J. C., & Pearson, R. M. (2004). *Estimation of Oil Recovery and CO2 Storage Capacity in CO2 EOR Incorporating the Effect of Underlying Aquifers*. SPE/DOE Symposium on Improved Oil Recovery. https://doi.org/10.2118/89340-MS

Baklid, A., Korbol, R., & Owren, G. (1996, October 6). *Sleipner Vest CO2 Disposal, CO2 Injection Into A Shallow Underground Aquifer*. SPE Annual Technical Conference and Exhibition. https://doi.org/10.2118/36600-MS

Barla, G., Barla, M., & Debernardi, D. (2010). New Triaxial Apparatus for Rocks. *Rock Mechanics and Rock Engineering*, *43*(2), 225–230. https://doi.org/10.1007/s00603-009-0076-7

Bear, J., & Cheng, A. H.-D. (2010). *Modeling Groundwater Flow and Contaminant Transport*. Springer Netherlands. https://doi.org/10.1007/978-1-4020-6682-5

Bemer, E., & Lombard, J. M. (2010). From Injectivity to Integrity Studies of CO_2 Geological Storage: Chemical Alteration Effects on Carbonates Petrophysical and Geomechanical Properties. *Oil & Gas Science and Technology – Revue de l'Institut Français Du Pétrole*, *65*(3), 445–459. https://doi.org/10.2516/ogst/2009028

Benson, S. M., & Cole, D. R. (2008). CO2 Sequestration in Deep Sedimentary Formations. *Elements*, *4*(5), 325–331. https://doi.org/10.2113/gselements.4.5.325

Bernstein, L., Bosch, P., Canziani, O., Chen, Z., Christ, R., & Riahi, K. (2008). *IPCC, 2007: Climate Change 2007: Synthesis Report*. IPCC. http://www.ipcc.ch/publications_and_data/ar4/syr/en/contents.html

Bhuiyan, M. H., Agofack, N., Gawel, K. M., & Cerasi, P. R. (2020). Micro- and Macroscale Consequences of Interactions between CO2 and Shale Rocks. *Energies*, *13*(5), 1167. https://doi.org/10.3390/en13051167

Bildstein, O., Kervévan, C., Lagneau, V., Delaplace, P., Crédoz, A., Audigane, P., Perfetti, E., Jacquemet, N., & Jullien, M. (2010). Integrative Modeling of Caprock Integrity in the Context of CO2 Storage: Evolution of Transport and Geochemical Properties and Impact on Performance and Safety Assessment. *Oil & Gas Science and Technology – Revue de l'Institut Français Du Pétrole*, *65*(3), Article 3. https://doi.org/10.2516/ogst/2010006

Biot, M. A. (1956). Theory of Propagation of Elastic Waves in a Fluid-Saturated Porous Solid. II. Higher Frequency Range. *The Journal of the Acoustical Society of America*, *28*(2), 179–191. https://doi.org/10.1121/1.1908241

Bjerrum, L. (1967). Engineering Geology of Norwegian Normally-Consolidated Marine Clays as Related to Settlements of Buildings. *Géotechnique*, *17*(2), 83–118. https://doi.org/10.1680/geot.1967.17.2.83

Black, J. R., & Haese, R. R. (2014). Chlorite dissolution rates under CO2 saturated conditions from 50 to 120° C and 120 to 200 bar CO2. *Geochimica et Cosmochimica Acta*, *125*, 225–240.

Blanchy, G., Saneiyan, S., Boyd, J., McLachlan, P., & Binley, A. (2020). ResIPy, an intuitive open source software for complex geoelectrical inversion/modeling. *Computers & Geosciences*, *137*, 104423. https://doi.org/10.1016/j.cageo.2020.104423

Bonal, J., Donohue, S., & McNally, C. (2012). Wavelet analysis of bender element signals. *Géotechnique*, *62*(3), 243–252. https://doi.org/10.1680/geot.9.P.052

Bragg, W. H. (1913). The Reflection of X-Rays by Crystals. *Nature*, *91*(2280), 477–477. https://doi.org/10.1038/091477b0

Brignoli, E., Gotti, M., & Stokoe, K., II. (1996). Measurement of Shear Waves in Laboratory Specimens by Means of Piezoelectric Transducers. *Geotechnical Testing Journal*, *19*(4), 384–397. https://doi.org/10.1520/GTJ10716J

Burland, J. B. (1990). On the compressibility and shear strength of natural clays. *Géotechnique*, *40*(3), 329–378. https://doi.org/10.1680/geot.1990.40.3.329

Capilla, C. (2006). Application of the Haar wavelet transform to detect microseismic signal arrivals. *Journal of Applied Geophysics*, *59*(1), 36–46. https://doi.org/10.1016/j.jappgeo.2005.07.005

Cardarelli, E., & De Donno, G. (2019). Chapter 2 - Advances in electric resistivity tomography: Theory and case studies. In R. Persico, S. Piro, & N. Linford (Eds.), *Innovation in Near-Surface Geophysics* (pp. 23–57). Elsevier. https://doi.org/10.1016/B978-0-12-812429-1.00002-7

Cardarelli, E., Fischanger, F., & Piro, S. (2008). Integrated geophysical survey to detect buried structures for archaeological prospecting. A case-history at Sabine Necropolis (Rome, Italy). *Near Surface Geophysics*, *6*(1), 15–20. https://doi.org/10.3997/1873-0604.2007027

Carroll, S., Hao, Y., Smith, M., & Sholokhova, Y. (2013). Development of scaling parameters to describe CO2–rock interactions within Weyburn-Midale carbonate flow units. *International Journal of Greenhouse Gas Control*, *16*, S185–S193. https://doi.org/10.1016/j.ijggc.2012.12.026

Casagrande, A. (1936). The determination of the pre-consolidation load and its practical significance. *Proc. 1st Int. Conf. Soil Mech.*, 3–60.

Chambers, J. E., Kuras, O., Meldrum, P. I., Ogilvy, R. D., & Hollands, J. (2006). Electrical resistivity tomography applied to geologic, hydrogeologic, and engineering investigations at a

former waste-disposal site. *Geophysics*, *71*(6), B231–B239. https://doi.org/10.1190/1.2360184

Choi, C.-S., Kim, J., & Song, J.-J. (2021). Analysis of shale property changes after geochemical interaction under CO2 sequestration conditions. *Energy*, *214*, 118933. https://doi.org/10.1016/j.energy.2020.118933

Ciancimino, A. (2021). *Performance of caisson foundations subjected to flood-induced scour* [PhD Thesis, Politecnico di Torino]. https://iris.polito.it/handle/11583/2924992

Ciancimino, A., Cosentini, R. M., Foti, S., Messori, A., Ullah, H., Volonté, G., & Musso, G. (2024). A preliminary investigation on the mechanical behavior of a stiff Italian clay in the context of hydrogen storage. *Geomechanics for Energy and the Environment*, *38*, 100562. https://doi.org/10.1016/j.gete.2024.100562

Comina, C., Cosentini, R. M., Della Vecchia, G., Foti, S., & Musso, G. (2011). 3D-electrical resistivity tomography monitoring of salt transport in homogeneous and layered soil samples. *Acta Geotechnica*, *6*, 195–203.

Comina, C., Foti, S., Musso, G., & Romero, E. (2008). EIT Oedometer: An Advanced Cell to Monitor Spatial and Time Variability in Soil with Electrical and Seismic Measurements. *Geotechnical Testing Journal*, *31*(5), 404–412. https://doi.org/10.1520/GTJ101367

Cook, J. (1999). The Effects of Pore Pressure on the Mechanical and Physical Properties of Shales. *Oil & Gas Science and Technology*, *54*(6), Article 6. https://doi.org/10.2516/ogst:1999059

Cosentini, R. M., Della Vecchia, G., Foti, S., & Musso, G. (2012). Estimation of the hydraulic parameters of unsaturated samples by electrical resistivity tomography. Géotechnique, 62(7), 583–594. https://doi.org/10.1680/geot.10.P.066

Decagon Devices, Inc. (2010). *WP4C Dewpoint PotentiaMeter Operator's Manual*. https://www.catec.nl/uploads/pdf/DEC-WP4C-manual_766.pdf

Delage, P., Howat, M. D., & Cui, Y. J. (1998). The relationship between suction and swelling properties in a heavily compacted unsaturated clay. Engineering Geology, 50(1), 31–48. https://doi.org/10.1016/S0013-7952(97)00083-5

Demars, K., Chaney, R., & Richter, J. (1983). The Rapid Carbonate Analyzer. *Geotechnical Testing Journal*, *6*(1), 30–34. https://doi.org/10.1520/GTJ10821J

Desrues, J., Chambon, R., Mokni, M., & Mazerolle, F. (1996). Void ratio evolution inside shear bands in triaxial sand specimens studied by computed tomography. *Géotechnique*, *46*(3), 529–546. https://doi.org/10.1680/geot.1996.46.3.529

Dewhurst, D. N., Raven, M. D., Shah, S. S. B. M., Ali, S. S. B. M., Giwelli, A., Firns, S., Josh, M., & White, C. (2020). Interaction of super-critical CO2 with mudrocks: Impact on composition and mechanical properties. *International Journal of Greenhouse Gas Control*, *102*, 103163. https://doi.org/10.1016/j.ijggc.2020.103163

Dooley, J., Davidson, C., Dahowski, R., Wise, M., Gupta, N., Kim, S., & Malone, E. (2006). *Carbon Dioxide Capture and Geologic Storage: A Key Component of a Global Energy Technology Strategy to Address Climate Change*.

Doran, I. G., Sivakumar, V., Graham, J., & Johnson, A. (2000). Estimation of in situ stresses using anisotropic elasticity and suction measurements. *Géotechnique*, *50*(2), 189–196. https://doi.org/10.1680/geot.2000.50.2.189

Eaton, B. A., & Eaton, T. L. (1997). Fracture gradient prediction for the new generation. *World Oil*, *218*(10), 93–97.

Edenhofer, O., Pichs-Madruga, R., Sokona, Y., C. Minx, J., Farahani, E., & .. (2015). *IPCC Climate Change 2014: Mitigation of Climate Change. Contribution of Working Group III to the Fifth Assessment Report of the Intergovernmental Panel on Climate Change*. Cambridge University Press. https://www.ipcc.ch/report/ar5/wg3/

Egermann, P., Lombard, J.-M., & Bretonnier, P. (2006). A fast and accurate method to measure threshold capillary pressure of caprocks under representative conditions,". *International Symposium of the Society of Core Analysts,*.

Epp, J. (2016). X-ray diffraction (XRD) techniques for materials characterization. In *Materials Characterization Using Nondestructive Evaluation (NDE) Methods* (pp. 81–124). Elsevier. https://doi.org/10.1016/B978-0-08-100040-3.00004-3

Falcon-Suarez, I., Marín-Moreno, H., Browning, F., Lichtschlag, A., Robert, K., North, L. J., & Best, A. I. (2017). Experimental assessment of pore fluid distribution and geomechanical changes in saline sandstone reservoirs during and after CO2 injection. *International Journal of Greenhouse Gas Control*, *63*, 356–369. https://doi.org/10.1016/j.ijggc.2017.06.019

Falcon-Suarez, I., Papageorgiou, G., Chadwick, A., North, L., Best, A. I., & Chapman, M. (2018). CO 2 -brine flow-through on an Utsira Sand core sample: Experimental and modelling. Implications for the Sleipner storage field. *International Journal of Greenhouse Gas Control*, *68*, 236–246. https://doi.org/10.1016/j.ijggc.2017.11.019

Favero, V., & Laloui, L. (2018). Impact of CO2 injection on the hydro-mechanical behavior of a clay-rich caprock. *International Journal of Greenhouse Gas Control*, *71*, 133–141. https://doi.org/10.1016/j.ijggc.2018.02.017

Feng, G., Kang, Y., Sun, Z., Wang, X., & Hu, Y. (2019). Effects of supercritical CO2 adsorption on the mechanical characteristics and failure mechanisms of shale. *Energy*, *173*, 870–882. https://doi.org/10.1016/j.energy.2019.02.069

Fernández Lavín, A., & Ovando Shelley, E. (2020). Haar Wavelet Transform for Arrival Time Identification in Bender Element Tests. *Geotechnical Testing Journal*, *43*(4), 20180400. https://doi.org/10.1520/GTJ20180400

Fitts, J. P., & Peters, C. A. (2013). Caprock Fracture Dissolution and CO2 Leakage. *Reviews in Mineralogy and Geochemistry*, *77*(1), 459–479. https://doi.org/10.2138/rmg.2013.77.13

Flude, S., & Alcade, J. (2020). *Carbon capture and storage has stalled needlessly – three reasons why fears of CO_2 leakage are overblown*. https://theconversation.com/carbon-capture-and-storage-has-stalled-needlessly-three-reasons-why-fears-of-co-leakage-are-overblown-130747

Gaus, I. (2010). Role and impact of CO2–rock interactions during CO2 storage in sedimentary rocks. *International Journal of Greenhouse Gas Control*, *4*(1), 73–89. https://doi.org/10.1016/j.ijggc.2009.09.015

Gaus, I., Azaroual, M., & Czernichowski-Lauriol, I. (2005). Reactive transport modelling of the impact of CO2 injection on the clayey cap rock at Sleipner (North Sea). *Chemical Geology*, *217*(3), 319–337. https://doi.org/10.1016/j.chemgeo.2004.12.016

Global CCS institute. (2024). *Global status of CCS 2024—Collaborating for a net-zero future*. https://www.globalccsinstitute.com/wp-content/uploads/2024/10/2024-GSR_20241015.pdf#page=1.99

Goldstein, J. I., Newbury, D. E., Michael, J. R., Ritchie, N. W. M., Scott, J. H. J., & Joy, D. C. (2017). *Scanning Electron Microscopy and X-Ray Microanalysis*. Springer.

Green, C., & Ennis-King, J. (2009). Effect of Vertical Heterogeneity on Long-Term Migration of CO2 in Saline Formations. *Transport in Porous Media*, *82*, 31–47. https://doi.org/10.1007/s11242-009-9498-7

Grgic, D. (2011). Influence of CO2 on the long-term chemomechanical behavior of an oolitic limestone. *Journal of Geophysical Research: Solid Earth*, *116*(B7). https://doi.org/10.1029/2010JB008176

Gu, X., Zuo, K., Tessari, A., & Gao, G. (2021). Effect of saturation on the characteristics of P-wave and S-wave propagation in nearly saturated soils using bender elements. *Soil Dynamics and Earthquake Engineering*, *145*, 106742. https://doi.org/10.1016/j.soildyn.2021.106742

Gunter, W., Bachu, S., & Benson, S. (2004). The Role of Hydrogeological and Geochemical Trapping in Sedimentary Basins for Secure Geological Storage of Carbon Dioxide. *Geological Society, London, Special Publications*, *233*, 129–145. https://doi.org/10.1144/GSL.SP.2004.233.01.09

Gupta, S. C., & Hanks, R. J. (1972). Influence of Water Content on Electrical Conductivity of the Soil. *Soil Science Society of America Journal*, *36*(6), 855–857. https://doi.org/10.2136/sssaj1972.03615995003600060011x

Hangx, S. J. T., Spiers, C. J., & Peach, C. J. (2010a). Mechanical behavior of anhydrite caprock and implications for CO_2 sealing capacity. *Journal of Geophysical Research*, *115*(B7), B07402. https://doi.org/10.1029/2009JB006954

Hangx, S. J. T., Spiers, C. J., & Peach, C. J. (2010b). The effect of deformation on permeability development in anhydrite and implications for caprock integrity during geological storage of CO2: Effect of deformation on permeability development in anhydrite. *Geofluids*, *10*(3), 369–387. https://doi.org/10.1111/j.1468-8123.2010.00299.x

Hanke, R., Fuchs, T., Salamon, M., & Zabler, S. (2016). X-ray microtomography for materials characterization. In G. Hübschen, I. Altpeter, R. Tschuncky, & H.-G. Herrmann (Eds.), *Materials Characterization Using Nondestructive Evaluation (NDE) Methods* (pp. 45–79). Woodhead Publishing. https://doi.org/10.1016/B978-0-08-100040-3.00003-1

Hart, D. J., & Wang, H. F. (1999). *Pore pressure and confining stress dependence of poroelastic linear compressibilities and Skempton's B coefficient for Berea sandstone*. 365–371. Scopus.

Head, K. H., & Epps, R. (2014). *Manual of Soil Laboratory Testing: Volume III: Effective Stress Tests, Third Edition*. Whittles Publishing. https://books.google.it/books?id=6dhCnwEACAAJ

Hepple, R. P., & Benson, S. M. (2005). Geologic storage of carbon dioxide as a climate change mitigation strategy: Performance requirements and the implications of surface seepage. *Environmental Geology*, *47*(4), 576–585. https://doi.org/10.1007/s00254-004-1181-2

Hervas, F., Serra, P., Torres, C., Fernàndez, M., Queralto, D., Ribas, J., Cosp, J., Marsal, A., & Manich, A. (2006). *Study of the extraction kinetic of glycosaminoglycans from raw sheepskin trimmings*.

Hong, Z.-S., Yin, J., & Cui, Y.-J. (2010). Compression behavior of reconstituted soils at high initial water contents. *Géotechnique*, *60*(9), 691–700. https://doi.org/10.1680/geot.09.P.059

Hong, Z.-S., Zeng, L.-L., Cui, Y.-J., Cai, Y.-Q., & Lin, C. (2012). Compression behavior of natural and reconstituted clays. *Géotechnique*, *62*(4), 291–301. https://doi.org/10.1680/geot.10.P.046

Hui, D., Pan, Y., Luo, P., Zhang, Y., Sun, L., & Lin, C. (2019). Effect of supercritical CO2 exposure on the high-pressure CO2 adsorption performance of shales. *Fuel*, *247*, 57–66. https://doi.org/10.1016/j.fuel.2019.03.013

IEA. (2024). *CO2 Emissions in 2023*. IEA, Paris. https://www.iea.org/reports/co2-emissions-in-2023

Inkson, B. J. (2016). Scanning electron microscopy (SEM) and transmission electron microscopy (TEM) for materials characterization. In G. Hübschen, I. Altpeter, R. Tschuncky, & H.-G. Herrmann (Eds.), *Materials Characterization Using Nondestructive Evaluation (NDE) Methods* (pp. 17–43). Woodhead Publishing. https://doi.org/10.1016/B978-0-08-100040-3.00002-X

IPCC Special Report on Carbon Dioxide Capture and Storage Prepared by Working Group III of Intergovernmental Panel on Climate Change. (2005). Cambridge University Press. pp, 1-442

Jain, A. K., & Cao, L. (2005). Assessing the effectiveness of direct injection for ocean carbon sequestration under the influence of climate change. *Geophysical Research Letters*, *32*(9). https://doi.org/10.1029/2005GL022818

Jaky, J. (1948). Pressure in Silos. *Proc. 2nd Int. Conf. Soil Mech.*, *1*, 103–107.

Kaczmarek, M. (2001). Ultrasound—A useful tool to investigate complex materials. *Periodica Polytechnica Chemical Engineering*, *45*(2), Article 2.

Kaszuba, J., Yardley, B., & Andreani, M. (2013). Experimental Perspectives of Mineral Dissolution and Precipitation due to Carbon Dioxide-Water-Rock Interactions. *Reviews in Mineralogy and Geochemistry*, *77*(1), 153–188. https://doi.org/10.2138/rmg.2013.77.5

Katende, A. (2016). *Carbon Dioxide as refrigerant*. https://www.unilab.eu/wp-content/uploads/2016/10/1-Carbon-Dioxide-as-Refrigerant.pdf

Keller, G. V., & Frischknecht, F. C. (1966). *Electrical Methods in Geophysical Prospecting*. Elsevier Science & Technology.

Klein, K. A., & Santamarina, J. C. (2003). Electrical Conductivity in Soils: Underlying Phenomena. *Journal of Environmental and Engineering Geophysics*, *8*(4), 263–273. https://doi.org/10.4133/JEEG8.4.263

Knauss, K. G., & Wolery, T. J. (1988). The dissolution kinetics of quartz as a function of pH and time at 70°C. *Geochimica et Cosmochimica Acta*, *52*(1), 43–53. https://doi.org/10.1016/0016-7037(88)90055-5

Kumar, A., Ozah, R., Noh, M., Pope, G. A., Bryant, S., Sepehrnoori, K., & Lake, L. W. (2005). Reservoir Simulation of CO2 Storage in Deep Saline Aquifers. *SPE Journal*, *10*(03), 336–348. https://doi.org/10.2118/89343-PA

Kumar, J., & Shinde, N. S. (2019). Interpretation of bender element test results using sliding Fourier transform method. *Canadian Geotechnical Journal*, *56*(12), 2004–2014. https://doi.org/10.1139/cgj-2018-0733

Lahann, R., Mastalerz, M., Rupp, J. A., & Drobniak, A. (2013). Influence of CO2 on New Albany Shale composition and pore structure. *International Journal of Coal Geology*, *108*, 2–9. https://doi.org/10.1016/j.coal.2011.05.004

Lancellotta, R. (2008). *Geotechnical Engineering* (2nd ed.). CRC Press. https://doi.org/10.1201/9781482265934

Le Guen, Y., Renard, F., Hellmann, R., Brosse, E., Collombet, M., Tisserand, D., & Gratier, J.-P. (2007). Enhanced deformation of limestone and sandstone in the presence of high fluids. *Journal of Geophysical Research: Solid Earth*, *112*(B5). https://doi.org/10.1029/2006JB004637

Lee, J.-S., & Santamarina, J. C. (2005). Bender Elements: Performance and Signal Interpretation. *Journal of Geotechnical and Geoenvironmental Engineering*, *131*(9), 1063–1070. https://doi.org/10.1061/(ASCE)1090-0241(2005)131:9(1063)

Leung, D. Y. C., Caramanna, G., & Maroto-Valer, M. M. (2014). An overview of current status of carbon dioxide capture and storage technologies. *Renewable and Sustainable Energy Reviews*, *39*, 426–443. https://doi.org/10.1016/j.rser.2014.07.093

Liu, F., Lu, P., Griffith, C., Hedges, S. W., Soong, Y., Hellevang, H., & Zhu, C. (2012). CO2–brine–caprock interaction: Reactivity experiments on Eau Claire shale and a review of relevant literature. *International Journal of Greenhouse Gas Control*, *7*, 153–167. https://doi.org/10.1016/j.ijggc.2012.01.012

Lyu, Q., Ranjith, P., Long, X., & Ji, B. (2016). Experimental Investigation of Mechanical Properties of Black Shales after CO2-Water-Rock Interaction. *Materials*, *9*(8), 663. https://doi.org/10.3390/ma9080663

Mallat, S. G. (1989). A theory for multiresolution signal decomposition: The wavelet representation. *IEEE Transactions on Pattern Analysis and Machine Intelligence*, *11*(7), 674–693. IEEE Transactions on Pattern Analysis and Machine Intelligence. https://doi.org/10.1109/34.192463

Millington, R. J., & Quirk, J. P. (1961). Permeability of porous solids. *Transactions of the Faraday Society*, *57*, 1200. https://doi.org/10.1039/tf9615701200

Misiti, M., Misiti, Y., Oppenheim, G., & Poggi, J.-M. (1996). Wavelet toolbox user's guide. *The Math Works Ins*, 2–36.

Mitchell, J. K., & Soga, K. (2005). *Fundamentals of Soil Behavior*. Wiley.

Monfared, M., Sulem, J., Delage, P., & Mohajerani, M. (2011). A Laboratory Investigation on Thermal Properties of the Opalinus Claystone. *Rock Mechanics and Rock Engineering*, *44*(6), 735–747. https://doi.org/10.1007/s00603-011-0171-4

Morad, S., Ketzer, J., & De Ros, L. F. (2000). Spatial and temporal distribution of diagenetic alterations in siliciclastic rocks: Implications for mass transfer in sedimentary basins. *Sedimentology*, *47*, 95–120.

Mortezaei, K., Amirlatifi, A., Ghazanfari, E., & Vahedifard, F. (2021). Potential CO_2 leakage from geological storage sites: Advances and challenges. *Environmental Geotechnics*, *8*(1), 3–27. https://doi.org/10.1680/jenge.18.00041

Mouzakis, K. M., Navarre-Sitchler, A. K., Rother, G., Bañuelos, J. L., Wang, X., Kaszuba, J. P., Heath, J. E., Miller, Q. R. S., Alvarado, V., & McCray, J. E. (2016). Experimental Study of Porosity Changes in Shale Caprocks Exposed to CO_2 -Saturated Brines I: Evolution of Mineralogy,

Pore Connectivity, Pore Size Distribution, and Surface Area. *Environmental Engineering Science*, *33*(10), 725–735. https://doi.org/10.1089/ees.2015.0588

Niemi, A., Bear, J., & Bensabat, J. (Eds.). (2017). *Geological Storage of CO2 in Deep Saline Formations* (Vol. 29). Springer Netherlands. https://doi.org/10.1007/978-94-024-0996-3

NOAA. (2023). *Trends in CO2—NOAA Global Monitoring Laboratory*. https://gml.noaa.gov/ccgg/trends/mlo.html

Nooraiepour, M., Fazeli, H., Miri, R., & Hellevang, H. (2018). Effect of CO2 Phase States and Flow Rate on Salt Precipitation in Shale Caprocks—A Microfluidic Study. *Environmental Science & Technology*, *52*(10), 6050–6060. https://doi.org/10.1021/acs.est.8b00251

Nouailletas, O., Perlot, C., La Borderie, C., Rousseau, B., & Ballivy, G. (2013). Shear Behavior Evolution of a Fault due to Chemical Degradation of Roughness: Application to the Geological Storage of CO_2. In G. Pijaudier-Cabot & J.-M. Pereira (Eds.), *Geomechanics in CO2 Storage Facilities* (pp. 95–114). John Wiley & Sons, Inc. https://doi.org/10.1002/9781118577424.ch6

Osipov, V. I., & Sokolov, V. N. (1978). Relation between the microfabric of clay soils and their origin and degree of compaction. *Bulletin of the International Association of Engineering Geology - Bulletin de l'Association Internationale de Géologie de l'Ingénieur*, *18*(1), 73–81. https://doi.org/10.1007/BF02635351

Otani, J., Mukunoki, T., & Obara, Y. (2000). Application of X-Ray CT Method for Characterization of Failure in Soils. *Soils and Foundations*, *40*(2), 111–118. https://doi.org/10.3208/sandf.40.2_111

Pokrovsky, O. S., Golubev, S. V., & Schott, J. (2005). Dissolution kinetics of calcite, dolomite and magnesite at 25 °C and 0 to 50 atm *p*CO2. *Chemical Geology*, *217*(3), 239–255. https://doi.org/10.1016/j.chemgeo.2004.12.012

Pokrovsky, O. S., Golubev, S. V., Schott, J., & Castillo, A. (2009). Calcite, dolomite and magnesite dissolution kinetics in aqueous solutions at acid to circumneutral pH, 25 to 150 °C and 1 to 55 atm pCO2: New constraints on CO2 sequestration in sedimentary basins. *Chemical Geology*, *265*(1), 20–32. https://doi.org/10.1016/j.chemgeo.2009.01.013

Rezaee, R., Saeedi, A., Iglauer, S., & Evans, B. (2017). Shale alteration after exposure to supercritical CO2. *International Journal of Greenhouse Gas Control*, *62*, 91–99. https://doi.org/10.1016/j.ijggc.2017.04.004

Rimmelé, G., Barlet-Gouédard, V., & Renard, F. (2010). Evolution of the Petrophysical and Mineralogical Properties of Two Reservoir Rocks Under Thermodynamic Conditions Relevant for CO2 Geological Storage at 3 km Depth. *Oil & Gas Science and Technology – Revue de l'Institut Français Du Pétrole*, *65*(4), Article 4. https://doi.org/10.2516/ogst/2009071

Rio, J., Greening, P., & Medina, L. (2003). Influence of sample geometry on shear wave propagation using bender elements. *In the Proceedings of Deformation Characteristics of Geomaterials, Lyon.*, 963–967.

Rochelle, C., Pearce, J., & Holloway, S. (1999). The underground sequestration of carbon dioxide: Containment by chemical reactions in the deep geosphere. *Geological Society, London, Special Publications*, *157*, 117–129. https://doi.org/10.1144/GSL.SP.1999.157.01.09

Rohmer, J., Pluymakers, A., & Renard, F. (2016). Mechano-chemical interactions in sedimentary rocks in the context of CO 2 storage: Weak acid, weak effects? *Earth-Science Reviews*, *157*, 86–110. https://doi.org/10.1016/j.earscirev.2016.03.009

Romero, E., & Simms, P. H. (2008). Microstructure Investigation in Unsaturated Soils: A Review with Special Attention to Contribution of Mercury Intrusion Porosimetry and Environmental Scanning Electron Microscopy. *Geotechnical and Geological Engineering*, *26*(6), 705–727. https://doi.org/10.1007/s10706-008-9204-5

Rutqvist, J. (2012). The Geomechanics of CO2 Storage in Deep Sedimentary Formations. *Geotechnical and Geological Engineering*, *30*(3), 525–551. https://doi.org/10.1007/s10706-011-9491-0

Sanchez-Salinero, I., Roesset, J. M., Stokoe, K., & Kenneth, H. (1986). Analytical studies of body wave propagation and attenuation. *Report GR*, 86–15.

Santamarina, J. C., & Fam, M. A. (1997). Discussion: Interpretation of bender element tests. *Géotechnique*, *47*(4), 873–877. https://doi.org/10.1680/geot.1997.47.4.873

Scelsi, G., De Bellis, M. L., Pandolfi, A., Musso, G., & Della Vecchia, G. (2019). A step-by-step analytical procedure to estimate the in-situ stress state from borehole data. *Journal of Petroleum Science and Engineering*, *176*, 994–1007. https://doi.org/10.1016/j.petrol.2019.01.100

Shukla, R., Ranjith, P., Haque, A., & Choi, X. (2010). A review of studies on CO2 sequestration and caprock integrity. *Fuel*, *89*(10), 2651–2664. https://doi.org/10.1016/j.fuel.2010.05.012

Skempton, A. W. (1954). The Pore-Pressure Coefficients A and B. *Géotechnique*, *4*(4), 143–147. https://doi.org/10.1680/geot.1954.4.4.143

Smart, P., & Tovey, N. K. (1982). *Electron Microscopy of Soil and Sediments: Techniques*. Oxford University Press.

Sridharan, A., & Venkatappa rao., G. (1972). Pore Size Distributions of Soils From Mercury Intrusion Porosimeter Data. *Soil Science Society of America Journal*, *36*(6), 980–981. https://doi.org/10.2136/sssaj1972.03615995003600060046x

Sterpenich, J., Sausse, J., Pironon, J., Géhin, A., Hubert, G., Perfetti, E., & Grgic, D. (2009). Experimental ageing of oolitic limestones under CO2 storage conditions. *Chemical Geology*, *265*(1–2), 99–112. https://doi.org/10.1016/j.chemgeo.2009.04.011

Tambach, T. J., Koenen, M., Wasch, L. J., & van Bergen, F. (2015). Geochemical evaluation of CO2 injection and containment in a depleted gas field. *International Journal of Greenhouse Gas Control*, *32*, 61–80. https://doi.org/10.1016/j.ijggc.2014.10.005

Vafaie, A., Cama, J., Soler, J. M., Kivi, I. R., & Vilarrasa, V. (2023). Chemo-hydro-mechanical effects of CO2 injection on reservoir and seal rocks: A review on laboratory experiments. *Renewable and Sustainable Energy Reviews*, *178*, 113270. https://doi.org/10.1016/j.rser.2023.113270

van Schoor, M. (2002). Detection of sinkholes using 2D electrical resistivity imaging. *Journal of Applied Geophysics*, *50*(4), 393–399. https://doi.org/10.1016/S0926-9851(02)00166-0

Vermeer, P., & Neher, H. (1999). A soft soil model that accounts for creep. *Beyond 2000 in Computational Geotechnics*, 249–261.

Vespo, V. S. (2024). *Chemo-hydro-mechanical effects of CO2 storage on Italian reconstituted caprock* [PhD Thesis, Politecnico di Torino]. https://iris.polito.it/handle/11583/2993910

Vespo, S. V., Gramegna, L., Fiorucci, A., Della Vecchia, G., & Musso, G. (2025). Geochemical calibration for carbonate clay caprock under acidic conditions: Experimental and numerical insights. *Submitted to Géotechnique Letters*.

Vialle, S., & Vanorio, T. (2011). Laboratory measurements of elastic properties of carbonate rocks during injection of reactive CO2-saturated water. *Geophysical Research Letters*, *38*(1). https://doi.org/10.1029/2010GL045606

Vlassenbroeck, J., Masschaele, B., Cnudde, V., Dierick, M., Pieters, K., Van Hoorebeke, L., & Jacobs, P. (2006). *Advances in X-ray Tomography for Geomaterials*. 167–173.

Washburn, E. W. (1921). The Dynamics of Capillary Flow. *Physical Review*, *17*(3), 273–283. https://doi.org/10.1103/PhysRev.17.273

Xie, S. Y., Shao, J. F., & Xu, W. Y. (2011). Influences of chemical degradation on mechanical behavior of a limestone. *International Journal of Rock Mechanics and Mining Sciences*, *48*(5), 741–747. https://doi.org/10.1016/j.ijrmms.2011.04.015

Zhang, S., Xian, X., Zhou, J., & Zhang, L. (2017). Mechanical behavior of Longmaxi black shale saturated with different fluids: An experimental study. *RSC Advances*, *7*(68), 42946–42955. https://doi.org/10.1039/C7RA07179E

Zinsmeister, L., Dautriat, J., Dimanov, A., Raphanel, J., & Bornert, M. (2013, June 23). *Mechanical Evolution of an Altered Limestone Using 2D and 3D Digital Image Correlation (DIC)*. 47th U.S. Rock Mechanics/Geomechanics Symposium. https://dx.doi.org/

Zou, Y., Li, S., Ma, X., Zhang, S., Li, N., & Chen, M. (2018). Effects of CO2–brine–rock interaction on porosity/permeability and mechanical properties during supercritical-CO2 fracturing in shale reservoirs. *Journal of Natural Gas Science and Engineering*, *49*, 157–168. https://doi.org/10.1016/j.jngse.2017.11.004